

The influence of surface defects on the degradation behaviour of magnesium alloys for medical applications

Dissertation

zur Erlangung des akademischen Grades

Doktor der Ingenieurwissenschaften

(Dr.-Ing.)

der Technischen Fakultät

der Christian-Albrechts-Universität zu Kiel

vorgelegt von

Marcjanna Maria Gawlik

Kiel 2019

Erstgutachterin: Prof. Dr. Regine Willumeit-Römer

Zweitgutachter: Prof. Dr. Rainer Adlung

Termin der Disputation: 24.06.2019

Eidesstattliche Erklärung

Hiermit erkläre ich, dass die beigefügte Dissertation, abgesehen von der Beratung durch die Betreuer, nach Inhalt und Form meine eigene Arbeit ist.

Die Arbeit, ganz oder zum Teil, wurde nie schon einer anderen Stelle im Rahmen eines Prüfungsverfahrens vorgelegt und ist, abgesehen von den im Anhang angegebenen Veröffentlichungen, nicht anderweitig zur Veröffentlichung vorgelegt worden.

Außerdem ist die Arbeit unter Einhaltung der Regeln guter wissenschaftlicher Praxis der Deutschen Forschungsgemeinschaft entstanden.

Geesthacht, den

Zusammenfassung

Die Degradation von Mg Legierungen reagiert sehr empfindlich auf Verunreinigungen und Mikrostrukturänderungen. Somit ist die Reinigung der Oberfläche nach der Herstellung für alle Anwendungen in korrosiver Umgebung erforderlich. Insbesondere ist eine gleichmäßige Degradation bei medizinischer Anwendung essentiell. In früheren Studien stellte sich eine Ätzung mit Essigsäure (HAc) in Bezug auf Herabsetzung der Korrosionsrate als vielversprechend heraus. Zur Oberflächenbehandlung mittels HAc-Ätzung von Mg-Gd Legierungen, die speziell im biologischen Bereich interessant sind, gibt es bislang keine systematischen Untersuchungen. Das Ziel dieser Arbeit ist es daher, den Zusammenhang zwischen verschiedenen Ätzzuständen und der oberflächennahen Morphologie und Mikrostruktur von Mg-Gd-Legierungen sowie deren Einfluss auf das Degradationsverhalten zu bestimmen. Dem Ausgangszustand (AR) entsprechende Mg-xGd-Legierungen ($x = 2, 5$ und 10) wurden in 5 oder 10 mL Ätzlösung (250 g/L) für 15 oder 150 s geätzt. Händisch geschliffene Proben wurden zum Vergleich untersucht. Das Degradationsverhalten aller Zustände wurden mittels Immersionsversuch in 2 mL Zellkulturmedium „cell culture medium“ (CCM) als halb stationärer Test unter physiologischen Bedingungen bestimmt. Die Mikrostruktur von AR und geätzten Proben wurde mit dem Lichtmikroskop untersucht und u.a. durch einen von der Herstellung bedingten Deformations- und Zwillingsbereich charakterisiert. Die Morphologie der geätzten und korrodierten Oberflächen wurde mittels Sekundärelektronenmikroskopie (SEM) und Weißlichtinterferometrie (WLI) bestimmt. Flugzeit-Sekundärionen-Massenspektrometrie „Time of flight secondary ion mass spectrometry“ (ToF-SIMS) wurde vor und nach dem Ätzen angewandt, um den Fe-Gehalt an der Oberfläche zu analysieren. Das Abbauverhalten wurde in Bezug auf Abbaurrate, Linearität und Homogenität mit Partikel induzierter mikro-galvanischer Degradation (PID) bewertet. Ein neues Konzept für die Charakterisierung von homogener Degradation wurde mittels des leeren Volumens der Täler „Valley void volume“ (V_{vv}) entwickelt. Diese Arbeit zeigt, dass sich die Parameter des Ätzprozesses auf die Homogenität und die Rate der Degradation auswirken. Vor allem ist die Entfernung von Kontamination wie Fe-Partikeln zu nennen. Die Entfernung von Deformations- und Zwillingszone spielt eine im Verhältnis untergeordnete Rolle. Die Oberflächenmorphologie ist ebenfalls im Vergleich unbedeutend. Der größte Einfluss auf die Homogenität der Degradation rührt von Partikeln im Materialinneren her, in dieser Arbeit vorwiegend Fe-Partikel und Gd-reiche Ausscheidungen, z.B. Hydride. Die Freilegung dieser Partikel durch das Ätzen oder die spätere Degradation fördert die Bildung von größeren Löchern und eine inhomogene Degradation. Hier ist eine Abhängigkeit vom Gd-Gehalt zu beobachten: Die Degradation über die Zeit der Mg-10Gd-Legierung wird zwar durch die Ätzung gleichmäßiger, tendiert aber zu späteren Zeiten trotzdem zur Inhomogenität. Diese Inhomogenität ist bei den anderen beiden Legierungen nicht zu beobachten. Insgesamt konnte gezeigt werden, dass die HAc-Ätzung eine erfolgreiche Methode ist um Oberflächenverunreinigungen wie Fe zu entfernen und damit die Reproduzierbarkeit der Abbaurrate für alle Legierungen zu verbessern. Die Bestimmung der Degradationsrate und der Homogenität ist nötig, um zuverlässige Vorhersagen für Legierungen oder Oberflächenbehandlungen von abbaubaren Implantaten zu machen.

Abstract

The degradation of Mg alloys is very sensitive to impurities and microstructure changes. Thus, surface cleaning after manufacturing is essential for all applications under a corrosive environment. In particular for biomedical applications, controlled degradation is crucial. Several studies have turned out that HAc etching is a promising surface treatment to decrease the degradation rate. To date, there have been no systematic investigations concerning the effect of surface treatment on Mg-Gd alloys, which are of particular interest in the field of biology. The aim of this work is to determine the relationship between different HAc etching conditions and the morphology and microstructure of Mg-Gd alloys in the near-surface region as well as the impact on the degradation behaviour. As-received (AR) Mg-xGd ($x = 2, 5, 10$) samples were etched in 5 or 10 mL of 250 g/L HAc solution for 15 or 150 s. Manually ground samples were prepared for comparison. The degradation behaviour of all specimens with different surface treated conditions were determined by an immersion test in 2 mL cell culture medium (CCM). The degradation tests were performed as semi-static test under physiological conditions. The microstructure of the AR and etched conditions were analysed by optical microscopy and characterized by a machining-related deformation and twinning region. The etched and degraded surface morphologies were examined using scanning electron microscopy (SEM) and white light interferometry (WLI). Time-of-Flight secondary ion mass spectrometry (ToF-SIMS) investigations were carried out before and after etching to determine the amount of Fe on the surface. The degradation behaviour was evaluated in terms of rate, linearity, and homogeneity and with respect to particle induced micro-galvanic degradation (PID). A new approach for the characterization of homogenous degradation behaviour was developed by use of a valley void volume (V_{vv}) method. This work shows, that different etching conditions have an influence on the homogeneity of the degradation and the degradation rate. In particular, the removal of Fe surface contaminations has to be mentioned. The removal of the deformation and twinning zone plays only a relatively minor role. The influence of surface morphology is compared to that insignificant. The strongest impact on the homogeneity of degradation arose from particles inside the bulk, like Fe impurities or Gd rich precipitations, e.g. hydrides. The exposure of these particle by etching or later degradation supports the formation of bigger pits and non-homogenous degradation. A dependency of Gd content and degradation behaviour is observed: The degradation over time for Mg-10Gd have been shown to be linear, despite a non-homogenous degradation at a later degradation time. This non-homogeneity in later stage have not been observed for Mg-2Gd and Mg-5Gd. It has been shown, that HAc etching is an effective method to remove contaminations such as Fe from the surface and improve the reproducibility of the degradation rate for all alloys. However, the determination of the degradation rate and the homogeneity is necessary to make reliable predictions about the suitability of an alloy or treatment for degradable implants.

Table of contents

1	Introduction	1
2	State of the Art	2
2.1	Mg and its Mg-Gd alloys	2
2.2	Degradation influencing factors	3
2.2.1	Degradation characteristics and mechanism	3
2.2.2	Mg-REE alloy degradation	5
2.2.3	Influence of particles and impurities	5
2.2.4	Influence of microstructural features	6
2.3	Surface characterization	8
2.3.1	Degradation homogeneity	8
2.3.2	Non-destructive surface measurement	9
2.3.3	Quantification of surface defects	10
2.3.4	Time-of-flight secondary ion mass spectrometry	10
2.4	Surface treatments	12
2.4.1	Mechanical surface treatments	12
2.4.2	Surface modification on Mg-REE alloys	12
2.4.3	Magnesium in acetic solution	12
2.4.4	Acid etching	13
2.4.5	The effect of surface treatments on the degradation behaviour	13
3	Motivation and objectives	43
4	Materials and Methods	43
4.1	Material	43
4.2	Etching procedure	44
4.3	Ground samples for comparison	45
4.4	Calculation of material removal	45
4.5	Metallographic investigation	45
4.5.1	Sample preparation	45
4.5.2	Optical microscopy	45
4.5.3	Scanning electron microscopy	46
4.6	ToF-SIMS	46
4.7	Interferometry	47
4.7.1	White light interferometry	47
4.7.2	Etching pit	47
4.7.3	Homogeneity of the surface	48
4.7.4	Depth calibration of ToF-SIMS	48

4.8	Degradation test.....	49
5	Results	50
5.1	As-received microstructure.....	50
5.2	Microstructure and material removal after surface treatments	52
5.3	Morphology after etching	54
5.4	Analysis of Fe surface impurities	56
5.5	Additional etching results.....	57
5.6	Degradation test.....	77
5.7	Homogeneity after degradation	78
5.7.1	Homogeneity of all conditions.....	78
5.7.2	Selected topographies.....	83
5.8	Particle induced micro-galvanic degradation	85
5.9	Effect of HAc etching on the degradation behaviour	89
6	Discussion	94
6.1	Origin of influencing factors	94
6.1.1	Fe surface impurities	94
6.1.2	Gd rich particles	94
6.1.3	Deformation.....	95
6.2	Effect of etching on the morphology and microstructure	95
6.3	Factors influencing the degradation behaviour	97
6.3.1	Particle induced micro-galvanic degradation	97
6.3.2	Effect on homogeneity.....	98
6.3.3	Effect on degradation rate and reproducibility.....	99
6.4	Summary of influencing factors	103
7	Conclusion.....	104
	References.....	106
	Figures	116
	Tables.....	119
	Appendix.....	120
	Acknowledgements.....	124
	Lists of publications and conferences.....	125

1 Introduction

In recent years, there has been an increasing interest in Mg alloys as a biodegradable material for medical applications [1–6]. A key aspect of using magnesium is the biocompatibility and biodegradability [7–10]. The degradability of an implant is a fundamental property to avoid secondary surgeries. This concept is useful for the younger population and older people, where surgery becomes more dangerous with advancing age. Pure Mg is a trace element of the human body [11], excess of Mg ions can be excreted naturally through the kidneys [12,13]. The initial degradation plays a critical role in the design of Mg implants [14]. An initial fast degradation has to be avoided due to the strong evolution of hydrogen that results from Mg in a neutral solution [15–17], which was reported to high rates of postimplantation mortality *in vivo* [18]. Kraus et al. [19] reported no detrimental effects on the mechanical integrity of the implants *in vivo*, despite massive hydrogen evolution [19]. However, a strong hydrogen evolution in the initial stage of degradation might hinder cell adherence and bone-implant interlocking [14].

A uniform dissolution of the implant material with a degradation rate, which is adjusted to the use of the implant, is important to ensure a feasibility of Mg implants. Several attempts have been made to increase the degradation resistance of Mg alloys. By alloying, it is possible to improve the mechanical properties and the degradation behaviour of implants, depending on the element and the level of alloying. There is a growing body of literature that has investigated the alloying of Mg with rare earth elements (REE) [20–31]. Previous research has established that REE hydrides or REE phases are formed inside Mg-REE alloys [31–40]. The result of these phases on the degradation behaviour is not fully understood. There is little published data on the effect of REE rich phases on the degradation morphology [34,35].

Researchers have shown an increased interest in the surface modification of Mg alloys to modify the degradation behaviour. Recently, a large amount of literature has been published around the theme of coatings [41–50]. A search through this literature has revealed a few studies that used etching or acid pickling to improve degradation resistance [51–57]. A full understanding of the impact of etching on the microstructure and morphology is still lacking. Although investigations have been carried out on the deformation area near to the surface region, only a few studies have considered its influence on degradation [58–60]. Previous studies have not dealt with the etching morphology. It is now well established that Fe impurities can impair the degradation resistance [15,61–63]. However, some of the studies failed to specify whether the removal of Fe or impurities was the only reason for the improved degradation resistance. The research to date has tended to focus on a degradation rate. Up to now, far too little attention has been paid to the overall homogeneity of the degradation process.

The aim of this thesis is to explore the effect of different surface treatments on the morphology and degradation behaviour of Mg-Gd alloys. This work will examine the way in which the microstructural features influence the dissolution of Mg in acidic and cell culture solutions. New insights into the effect of Gd rich particles on the dissolution of Mg-Gd alloys in HAc and cell culture medium (CCM) are provided. One purpose was to analyse the impact of Fe on the degradation behaviour in terms of degradation rate and homogeneity.

Data for this study was collected using etching experiments in HAc solution and immersion tests in cell culture medium. Quantitative methods were used to provide information about the overall pit depth distribution and to compare the homogeneity of degradation for different surface treated conditions. Understanding the link between the surface condition and degradation behaviour will help in the development and processing of Mg based alloy implants for biomedical application.

2 State of the Art

2.1 Mg and its Mg-Gd alloys

Magnesium (Mg) is a biodegradable and biocompatible element [64], which is suitable to use for implant in orthopaedic [65] and cardiovascular applications [66,67]. Mg can dissolve completely when immersed in an aqueous solution. The Mg ions from the degradation process are reported to support osseointegration and osteoconduction [2,68–72]. Previous research has established antibacterial properties of pure Mg, both *in vitro* and *in vivo* [73,74], that can be further improved by alloying for example with Ag [75].

Mg has a hexagonal closed packed (hcp) lattice structure which is shown in Figure 2.1. The formability of polycrystals is very poor at room temperature [76]. Von Mises [77] reported that uniform deformation was possible only for polycrystals which have more than five separate slip systems [77]. In the case of pure Mg the basal (0001) plane is the only available slip plane up to 225 °C. Dislocation motion is only possible for certain directions on the slip plane, as shown in Figure 2.1. Another mechanism for deformation at room temperature is twinning [76]. Twinning is defined as a shear deformation, in which atoms are shifted parallel to the twin plane [78]. The plastic deformation changes the orientation of the original lattice structure but without modifying the atomic structure [79]. The use of higher temperatures leads to a higher atom diffusivity, which activates pyramidal or prismatic slip [76,80,81].

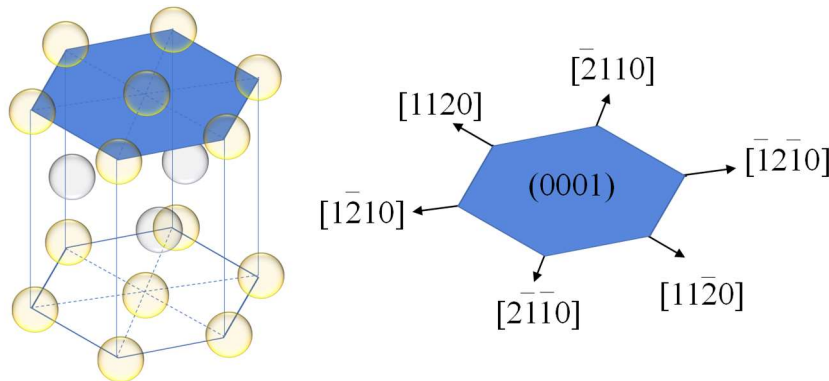


Figure 2.1 Mg lattice structure. The illustration is drawn and modified after [76].

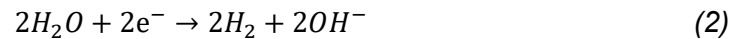
Gd is a suitable element for alloying, due to a high solubility of ~23.5 wt.% in magnesium at the eutectic point [82]. The high solubility prevents the development of secondary phases [82], which are reported to negatively influence the degradation resistance [83–85]. An increase in tensile strength is observed with increase in Gd up to 10 wt.% [25,86]. The distortion of the Mg lattice becomes severe with more Gd atoms in solid solution, due to the difference in atomic size between Gd and Mg [26]. As a result, dislocation movement is impaired and the material consolidated. Gao et al. [26], suggested the solid solution strengthening by Gd was more effective compared to Al and Zn, due to the mismatching atomic size and valency effects [26]. Kim et al. [25] demonstrated an increasing grain size with increasing Gd content up to 10 wt.%. An unexpected decrease in grain size was observed by alloying Mg with 15 wt.% Gd. They explain this phenomenon by the formation of Mg₅Gd precipitates, which inhibit grain growth by grain boundary pinning. Kim et al. [25] identified an increased tensile strength with 15 wt.% Gd, that was associated with a reduced grain size and precipitation formation [25]. According to Stanford and Barnett [27], the formability of Mg can be improved by alloying REE. Additions of Gd lead to an increase of ductility, this results from stronger grain refinement and texture weakening compared to REE free alloys or pure Mg after extrusion [27].

Jung et al. [28] assumed the change in stacking fault energy (SFE) of the matrix or the solute drag pinning effect as reasons for texture weakening [28]. Al-Samman and Li [29] reported a lower grain refinement when alloying ZEK100 with Gd in contrast with other REE like Ce, La and Nd. However, alloying with Gd exhibited a strong improvement in room temperature ductility [29]. Xu et al. [30] revealed a correlation between amount of Gd in Mg alloys and hardness or yield strength. They produced Mg-xGd ($x = 2, 5, 10, 15$) samples after permanent mold direct chill casting and solid solution strengthening or hot extrusion. A linear increase of hardness with additional Gd and an linear increase with $x^{1/2}$ or $x^{1/3}$ for tension and compression yield strength was observed [30]. Detailed examination of binary Mg-Gd alloys by Hort et al. [31] showed that the use of different Gd amounts allows to tailor the mechanical properties in a broad range. Especially the fracture strain is found to be more suitable with values for the cortical bone compared to Ti alloys and stainless steel [31]. Different theories exist in the literature [31–33,36,40] regarding Gd rich particles, when alloyed Mg with Gd. These particles are often determined as hydrides, formed by surface deformation and with contact to aqueous solutions, which may explain the formation of GdH_2 on the alloys due to the higher affinity of Gd to H_2 compared to Mg. Due to a higher electronegativity discrepancy of Gd to H, compared to Mg and H, the incurrence of GdH_2 is favoured. The formation of GdH_2 has also more negative Gibbs free energy compared to the building of H_2 at room temperature. It is assumed that the formation of GdH_2 in a Mg-Gd-H system is most probable as opposed to formation of H_2 and MgH_2 [40]. Peng et al. [40] suggests rectangular shaped and Gd rich particles as GdH_2 . They investigated, that water-free electropolishing does not emerge hydrides on the surface, while polishing in aqueous environment does. A study of Huang et al. [32] affirms the formation of REE hydrides in Mg after polishing in watery environment as well. These studies clearly indicate that there is a relationship between aqueous solution and hydride formation. A broader perspective has been adopted by Vlček et al. [33] who studied hydrogen absorption in Mg-22Gd. They suggested a formation of Gd rich particles to GdH_2 during solidification and a formation of hydrides caused by grinding, polishing in watery environments. Vlček et al. [33] identifies the dissolution of the $Mg_{46}Gd_9$ known also as Mg_5Gd phase caused by a 530 °C solution treatment as major cause for the formation of GdH_2 particles. This can be explained by hydrogen being released from Mg as it is heated, which then pushes Gd particles to accumulate into deformed areas of the material [33]. By drawing on the concept of Vlček et al. [33], Peng et al. [40] has been able to show a higher accumulation of hydrides at grain boundaries and an influence of deformation and dislocation movement on formation of GdH_2 . They explained a highly Gd segregation at grain boundaries during solidification. Hydrogen is moved by deformation and relocated at grain boundaries, where the building of GdH_2 is enabled [40]. Unlike previous mentioned studies, Kubásek and Vojtěch [87] found Gd oxides, which are assumed as Gd_2O_3 or $GdMg_2O_4$, formed during melting and casting. This view is supported by Hort et al. [31], who ascertain a formation of Gd_2O_3 or $GdMg_2O_4$ during casting, due to a higher affinity of Gd to O [31,88]. Brar et al. [89], however, who have looked at the oxidation of Mg-3Gd with pure oxygen, have found MgO and Gd_2O_3 on the surface [89]. In view of all that has been mentioned so far, one may suppose that the affinity of Gd with hydrogen or oxygen is higher compared to Mg.

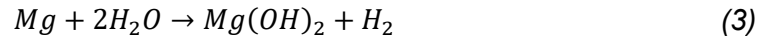
2.2 Degradation influencing factors

2.2.1 Degradation characteristics and mechanism

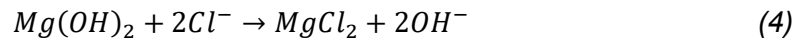
There is a larger volume of published studies describing the mechanism of Mg degradation [1,11,90–95]. Mg in aqueous solution is an electrochemical reaction and is described as follows:



The anodic reaction is the dissolution of Mg in Equation (1) and the cathodic reaction is the dissociation of water into hydrogen and hydroxide ions in Equation (2) [94]. In total a formation of Mg(OH)₂ layer and hydrogen evolution is reported:

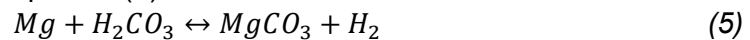


In the case of a chloride containing aqueous solution, chloride is able to destroy the protective Mg(OH)₂ layer by the formation of MgCl₂ and accelerate the degradation process [11]:

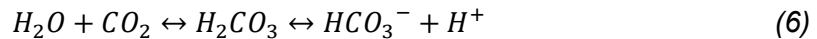


Severe pitting degradation was reported, when the chloride concentrations amounts to 150 mmol/l in the fluid [11,96,97].

In vitro degradation experiments under cell culture conditions are performed at 37 °C, 5 % CO₂, 20 % O₂, 95 % relative humidity inside an incubator. The cell culture medium (CCM) DMEM as corrosive medium contains inorganic salts like e.g. sodium bicarbonate (NaHCO₃), calcium chloride (CaCl₂·2H₂O), sodium chloride (NaCl) and sodium phosphate monobasic (NaH₂PO₄·2H₂O) [98,99]. Next to the formation of Mg(OH)₂, as shown in Equation (3), MgCO₃ and possible Ca compounds like hydroxyapatite or tricalcium phosphates are formed [98]. The formation of MgCO₃ is described by the reaction of solid Mg with carbonic acid H₂CO₃ in Equation (5):



H₂CO₃ originates from the combination of carbon dioxide CO₂ and water as shown in Equation (6):



NaHCO₃ from DMEM dissociate in bicarbonate HCO₃⁻ and Na⁺ represented in Equation (7). Bicarbonate can react with H⁺ to form H₂CO₃.



The combination of HCO₃⁻ and CO₂ builds the bicarbonate buffer system, which sustain the pH. Due to an ambient CO₂ supply, the equilibrium is shifted to the formation of carbonic acid H₂CO₃. With increasing H₂CO₃, the content on MgCO₃ increases [98].

Mg dissolving in neutral solution shows an unusual reaction in terms of hydrogen evolution, when compared with other base metals reaction. In the case of oxygen degradation, more hydrogen is evolved as expected. This phenomenon is called negative difference effect. To date several studies revealed explanations for the negative difference effect [15–17].

The combination of Mg and Fe or another impurity with high potential difference to Mg inside an electrolyte is called degradation cell and leads to galvanic degradation. Mg with more negative potential acts as anode and is oxidized. The element with less negative potential acts as cathode and is reduced. In addition to different metal combinations, there are other possibilities for degradation cell forming. Further reasons are various tension or residual level stress from machining or processing and different metallographic constituents in a heterogeneous alloy [100].

2.2.2 Mg-REE alloy degradation

One study by Birbilis et al. [101] found an increase in the corrosion rate of as cast Mg on increased alloying with La, Ce and Nd (up to 6 wt.%) resulting from the formation of intermetallic phases [101]. In contrast to Birbilis et al. [101], Jiang et al. [102] asserted that an increase in Nd addition in as cast Mg-7Y-xNd leads to a decrease in weight loss and current density I_{corr} . A decrease in the content of $\text{Mg}_{24}(\text{Y,Nd})_5$ phase with increasing Nd was mentioned as one key factor [102].

Tiyyagura et al. [103] tested the degradation behaviour of T4 heat treated and as-extruded Mg-5Gd under *in vitro* conditions in simulated body fluid (SBF). In comparison to pure Mg, the corrosion rate of Mg-5Gd is halved after 28 days immersion. After the degradation process, the degradation products and morphology vary widely for both alloys. Pure Mg showed formation of hydroxyapatite (HAp) and MgO, while $\text{Mg}(\text{OH})_2$ is formed on Mg-5Gd [103].

Zidane et al. [104] carried out weight loss and EIS experiments with as cast Mg-xGd alloys ($x = 2, 5, 10, 15$) in 1 wt.% NaCl solution. The corrosion rate is significantly reduced with more Gd addition. The lowest corrosion rate is determined for Mg-10Gd. Surprisingly a higher corrosion rate was detected for Mg-15Gd [104]. This view is supported by Hort et al. [31] who described exactly the same corrosion rate development in as cast Mg-xGd alloys.

2.2.3 Influence of particles and impurities

Influence of Fe-impurities

Matsubara et al. [61] performed immersion tests in 5 % NaCl, using AM50 and AM60 alloys. A variation of Fe impurities in both alloys set up five different testing conditions. They identified that Fe inclusions initiated a corrosive attack [61].

In a study conducted by Höche et al. [63], a cathodic active surface film ($\text{Mg}(\text{OH})_2$ and Fe rich film) formation labelled as dark film was reported (Figure 2.2). The dark film arose from redeposited Fe from the Fe reduction process, after the anodic dissolution of Mg [105]. The dark area was mentioned as one reason for intensified excess of hydrogen evolution [63], based on the study of Curioni et al. [106]. Possible reaction steps after Volmer, Tafel and Heyrovski mechanism [107] are suggested.

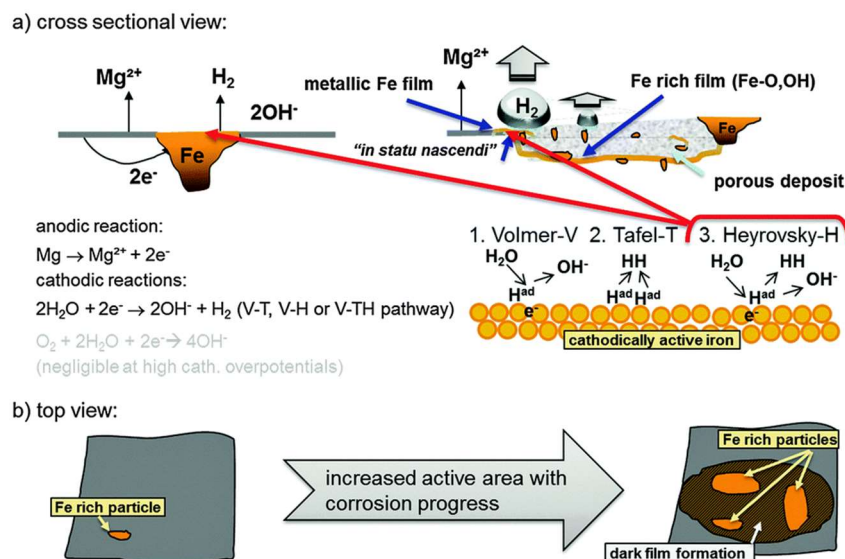


Figure 2.2 A reduction of Fe particles leads to a formation of cathodic active dark area, which increases the hydrogen evolution reaction: a) cross sectional view; b) top view. (obtained from [63], published by the PCCP Owner Societies CC by 3.0)

Yang et al. [62] varied the content of Fe in pure Mg to study the degradation behaviour. They investigated a formation of a surface film initiated by micro galvanic degradation between cathodic Fe particles and Mg matrix as anode when reaching a tolerance level of Fe. The tolerance level is reached with high population density of Fe particles. They concluded that, the pure existence of Fe particles does not induce severe degradation [62]. This view is supported by Song et al. [15] who illustrated an acceleration in degradation after a specific tolerance level. Moreover, a high number of Fe particles, relating thereto surface film formation, increased the degradation potential. With higher degradation potential, localized degradation is activated due to a local breakdown of the surface film [62].

Particle induced micro-galvanic degradation

Most research in the area of REE particle induced micro-galvanic degradation has been carried out in the study of Cao et al. [34]. They suggest that the galvanic degradation influence of Y rich particles depends on the activity of the particles which act as a cathode. Activity is controlled by the protectiveness of a surface film on the matrix. Cao et al. [34] offered an explanatory theory for degradation attack, which does not take place directly at the particle. Mg hydroxide is formed on the surface around the particle due to a combination of H_2 and OH^- . Hydrogen is released after a cathodic reaction of the particle, while OH^- ions are a by-product of the matrix degradation. This results in protection of the particle and surrounding area, which could cause material degradation around the protective film [34]. This view is supported by Kalb et al. [108] who described a similar mechanism of micro-galvanic degradation for pure Mg and WE43. Instead of particles being present on the volcano shaped residue, Kalb et al. [108] found the particles at the bottom of the volcano shaped residue. In contrast to Cao et al. [34], Kalb et al. [108] found Fe rich particles inside pure Mg and Zr rich particles inside WE43. A broader perspective has been adopted by Kalb et al. [108] who argues that the surrounding pH is a key factor for micro-galvanic degradation.

2.2.4 Influence of microstructural features

Deformation and twinning

Aung and Zhou [109] investigated the influence of grain size and twinning on the degradation of AZ31B-H24 alloy sheets. They performed hydrogen evolution tests by immersing the samples into 3.5 wt.% NaCl and also confirmed their results using potentiodynamic polarisation. As-received and four heat treated conditions (200 °C, 300 °C, 400 °C, 500 °C) were examined. With increasing heat treatment temperature, the grain size increased, and the twins dissipated at 300 °C. After 10 h of immersion, the lowest hydrogen content was measured for samples heat treated at 200 °C and 300 °C. As-received samples and samples with a larger grain size than the samples treated at 300 °C showed higher hydrogen evolution and an increase in current density. Aung and Zhou [109] reported that grain boundaries prevents corrosion, which is why 300 °C heat treated samples showed the slightest degradation rate with smaller grain size compared to 400 °C and 500 °C samples. SEM micrographs showed that intragranular corrosion had taken place at twins during immersion testing [109]. An anodic dissolution of the matrix surrounding the twins is assumed to have taken place [110]. It is expected that twinning affects the homogeneity of corrosion with stronger intragranular corrosion preferential compared to the influence of grain size [109].

One study by Zou et al. [111] examined the effect of twinning on the degradation morphology and degradation rate of Mg-1Y. Extruded samples were used as non-deformed samples. Deformed material was compressed after extrusion and included twinning. Deformed samples resulted in a current density which is over three times lower in contrast to non-

deformed samples. In their analysis, the influence of secondary phases, grain size and texture difference can be neglected, which assumes that the lower degradation density and higher degradation resistance arise from twinning. Zou et al. [111] explained, that extension twinning lead to more homogenous and accelerated formation of an oxide film compared to the non-deformed material. Microcracks and pitting occurred for both materials, but a higher tendency for pitting is reported for non-deformed material [111].

This view is supported by Wang et al. [112] who writes that Mg-3Al-1Zn sheets with less twin density show more advanced degradation with deeper pits compared to samples with higher twin density. Wang et al. proposes galvanic degradation between twinned and non-twinned regions emerged from crystallographic orientation difference. A broader perspective has been adopted by comparison of the crystallographic orientation inside the twinned area toward the matrix for both conditions. They point out, that inside the less twinned sheets, planes inside twinned areas are perpendicular to the matrix, which promotes galvanic degradation. The stronger twinned regions showed a preferential crystallographic orientation of twinning area to the matrix [112]. The crucial factor is not the amount of twins, moreover the crystallographic orientation to the matrix is determining.

Lu et al. [113] showed a stress layer in surface near region in the micrographs after high speed cutting of AZ31 alloys, where the grain size was not apparent. The stress layer showed a dependence from the cutting speed with a reduction from 40 μm to 25 μm , when increasing the cutting speed [113]. Pu et al. [58,114,115] published studies investigating the dependence of deformation layer depth on the machining parameters for AZ31. One study from Pu et al. [58] investigated the difference in degradation for different machined surfaces. Hydrogen evolution tests were performed in SBF for dry and cryogenic machined samples. Pu et al. [58] suggest a possible enhancement in degradation resistance through the use of cryogenic machining in contrast to dry machining as less hydrogen evolution took place in the time range between 2 – 7 days. These results however need to be interpreted with caution. One source of uncertainty is that only a minor decrease in hydrogen evolution was observed, while there was no difference in hydrogen evolution within the first two days. Pu et al. [58] suggested a possible passivation layer on both surfaces, which inhibits the initial degradation. The progress of hydrogen evolution for both surface finishes assimilated again after 10 days testing. The reason for this is not clear but it may have something to do with the complete removal of the deformation layer after several days testing [58].

Grain size and secondary phases

One study by Mostaed et al. [116] examined the effect of equal channel angular pressing (ECAP) on the degradation of Mg and ZK60. The intended grain size reduction had an insignificant effect on the degradation potential. In their conclusion, Mostaed et al. [116] identified a homogenous second phase distribution in material processed by ECAP as a reason for the decrease in pitting degradation [116]. Conversely, Argade et al. [117] reported a significant difference in the degradation resistance of Mg-4Y-3Nd with grain sizes of 70 μm and 0.7 μm . They performed heat treatment at 520 °C for 4 h or friction stir processing (FSP) and obtained four different grain sizes (70 \pm 58 μm , 20 \pm 12 μm , 2.4 \pm 2 μm , and 0.65 \pm 0.44 μm). After a three weeks immersion test the weight loss measurements showed a reduction in weight loss with decreasing grain size. In addition, the smallest grain size resulted in the highest passivation and positive pitting potential, which is an indication for a higher resistance to pit formation. From the biggest to the smallest grain size, the degradation rate reduced by one order of magnitude [117]. An investigation by Lu et al. [118] reached different conclusions, finding the lowest degradation rate for a well-balanced combination of grain size and secondary phases in Mg-3Zn-0.3Ca. They varied the volume fraction of secondary phases and grain size by use of different heat treatments.

Temperatures were adjusted between 310 and 450 °C for 24 or 48 h. Overall, eight different grain sizes (97 µm – 214 µm) with corresponding secondary phases volume fractions were examined. The lowest grain size was determined for as cast samples which also contained the highest volume fraction of secondary phases. The highest heat treatment temperature for 48 h resulted in the largest grain size and lowest number of secondary phases [118]. In contrast to Argade et al. [117], Lu et al. [118] argued that the smallest grain size did not result in the lowest degradation rate. Moreover, secondary phases induced galvanic degradation, which resulted in the highest degradation rate of all conditions. The heat-treated condition with the largest grain size did not result in the highest degradation rate, due to it having the lowest number of secondary phases. Both the secondary phases and the grain size were reported to be crucial for the degradation rate [118]. A recent systematic literature review [119] summarized the reasons for an improvement of the degradation resistance by grain size reduction. Ahmadkhaniha et al. [119] concluded that grain refinement effects positively influenced the formation of a passivation layer (MgO + Mg(OH)₂) or reduced pit initiation.

2.3 Surface characterization

2.3.1 Degradation homogeneity

Severe pit forming on the surface of the implant has to be avoided in order to obtain uniform degradation. Uniform degradation over the entire surface is necessary to conserve the mechanical integrity of the implant and to encourage strong bone-implant interlocking. To reach this aim, the characterization of localized and general degradation has been subject to several different analyses.

A large and growing body of literature has investigated the morphology of degraded samples using SEM [51,120–130] and/or optical microscopy [52,131] without a standard objective criterion. A calculated pitting factor has been reported by Maier et al. [132–134]. In order to calculate this factor, the deepest point of the surface must be found. This is obtained by use of cross section micrographs. The average degradation depth is also necessary and is determined either by mass loss or by dividing the corroded cross sections by the diameter of the exposed area [134]. Maier et al. [133] introduced a method where the original surface was partly retained in order to calculate the depth difference between the original and the degraded surface [133]. Trend analyses of different studies [135–138] were performed on pit volumes, pit areas, pit densities and the nearest-neighbour pit distances. These trends were obtained through use of a laser profilometry by observing pit growth and surface changes over time from a salt spray exposure and an immersion test in 3.5 wt.% NaCl [135–138]. Chen and Ju [139] developed a four-phase diagram from the average pit depth and pitted area percentage and used this to predict the risk of pitting occurring. These depths and percentages were measured using infinite focus microscopy. Parameters from the Abbot-Firestone curve were also reported as being suitable to characterize surfaces [139]. Chen and Ju [139] correlated pit depths and the respective pitted area percentages to the functional surface parameters. Comparing different Power Spectral Densities (PSD) was also reported as a viable method for degradation behaviour analysis [140–142]. Holme and Lunder [143] identified pit depth, area and volume using white light interferometry (WLI). They also created semi-logarithmic depth distribution diagrams and fitted curves based on the defined geometrical shape of the pits [143]. These techniques helped in describing the pitting behaviour, but not the overall surface homogeneity, which is defined as uniform distribution of pits over the complete sample surface.

2.3.2 Non-destructive surface measurement

White light interferometry (WLI) which was used in this study works according to the principle of the Michelson interferometer. White light is separated inside a beam splitter into two beams (Figure 2.3). One beam is reflected on the sample the so called “sample beam”, while the other one is reflected on a mirror, the “reference beam”. The combined beams generate an interferogram with constructive (light fringes) and destructive (dark fringes) interference [144]. Maximum interference with highest fringe contrast occurs when the optical path length of the sample beam is identical with the optical path length of the reference beam [145]. The head including the beam splitter and mirror is movable and can be adjusted in height from -z to +z. The sample is fixed on the stage. Stage knobs are used to compensate for a strong tilt of the sample. A sample surface is completely scanned with an adjusted height difference (“stitching”). The signal of maximum interference as a function of scan position is determined as height data to calculate a 3D surface topography [146].

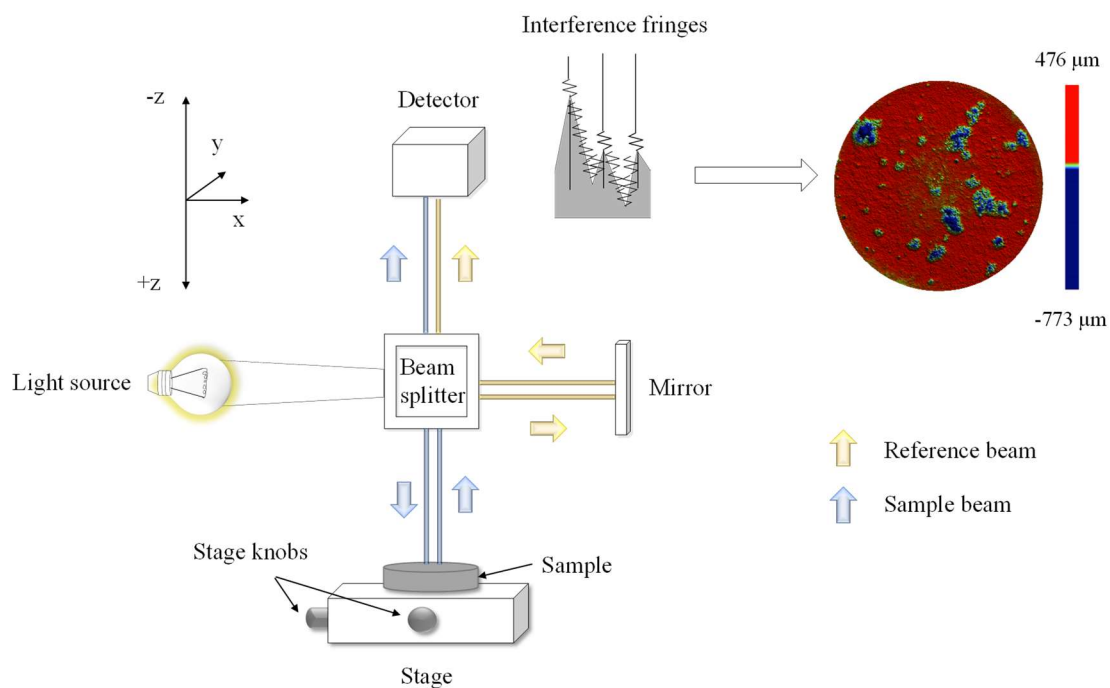


Figure 2.3 Drawing showing the principle of the Michelson interferometer.

The surface of samples is laterally separated into three different types, dependent on the surface spatial wavelength. The highest spatial wavelength is assigned for the form of a surface. The next smaller medium spatial wavelength range describes the waviness of the sample. The smallest spatial wavelength range is referred to the roughness of the sample [147]. For surface areal parameters the waviness and roughness were determined by the parameter Sa. Sa is defined as follows [148]:

$$Sa = \frac{1}{A} \iint |z(x, y)| dx dy \quad (8)$$

Where Sa is the arithmetic mean of the height within a surface area in μm, A the surface area in μm² and z in μm the surface height at points within the area.

In the degradation test of this research, the samples were completely immersed. As such, it is not possible to determine the depth difference between the initial and the corroded surface and, thus, a different technique has had to be developed.

2.3.3 Quantification of surface defects

Functional parameters are calculated from the Abbot-Firestone curve [149,150], which describes the material fraction found at each height difference ranging from the highest peak = 0 % material fraction to the deepest valley = 100 % material fraction (Figure 2.4) [151]. The volume parameter for 3D surfaces are defined from the curve in ISO 25178-2 [152] as V_{mp} (peak material volume), V_{mc} (core material volume), V_{vc} (core void volume) and V_{vv} (valley void volume) [152].

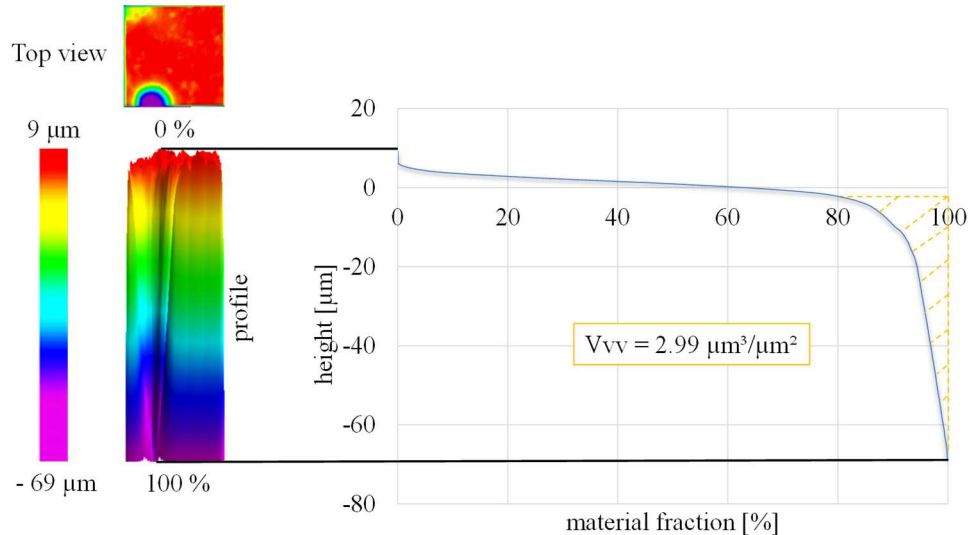


Figure 2.4 Top view and profile of a surface with a single pit and the corresponding Abbot-Firestone curve.

Void volumes are commonly used in engineering, when for example lubrication, adhesion, friction and wear are analysed. It is reported that the progression of the Abbot-Firestone curve and the void volume V_{vv} are representative for every processed surface. The V_v (void volumes) are defined as volume of voids per unit area and are calculated by integrating the volume between two heights x_1 and x_2 in the material ratio curve [153]. In ISO 25178-3 [154] the heights are set by standard at $x_1 = 80\%$ material fraction and $x_2 = 100\%$ material fraction for V_{vv} [148,154]. V_{vv} in particular is stated to quantitatively characterize damage to the surface [151]. Thus, V_{vv} is used to describe damage to the surface by degradation. Figure 2.4 shows the top view of a surface with a single pit. The pit is chopped to present the pit progress in the profile. Next to the profile the corresponding Abbot-Firestone curve for this topography is shown. The highest point of the surface is $9\ \mu\text{m}$ above the zero level. The deepest point inside the pit is $69\ \mu\text{m}$ below the zero level. The curved shape between 80% and 100% material fraction show a V_{vv} of $2.99\ \mu\text{m}^3/\mu\text{m}^2$.

2.3.4 Time-of-flight secondary ion mass spectrometry

One of the most well-known procedure for assessing the chemical composition within the outermost surface layers is Time-of-flight secondary ion mass spectrometry (ToF-SIMS) (Figure 2.5). Bi^+ is used as primary ion beam, because Bi has only one stable isotope allowing for straightforward beam pulsing, additionally because of its high atomic weight the sputter yields are high. On organic samples low fragmentation of the secondary ions is observed, especially for larger Bi clusters. Short pulse lengths allow for good mass resolution [155]. For metal depth profiling oxygen erosion and positive secondary ion polarity was used due to the reason that electronegative O_2^+ is implanted in the top layer of the sample, by what the ionization of the metals (M^+) is increased. Cs^+ for example would

decrease the positive signals of metals [156]. Static SIMS is used for high resolution mass analysis, where a maximum of 1% of the surface area is affected [157]. The primary ion beam is rasterized across a field of view on the sample. The energy from the primary ion is transferred to the atoms and molecules in the first 2-3 atom layers [157]. An atom receiving higher energy than binding forces to the surface is ejected as a neutral species or being usually single charged as a secondary ion.

The secondary ions are mass separated and detected by a reflectron type time-of-flight analyzer with an ultra-high vacuum base pressure of below 5×10^{-10} mbar. Ultra-high vacuum is necessary to preserve a clean surface area and avoid collisions of secondary ions with residual gas molecules thereby the highest mean free path is found inside the drift tube [155]. Inside the tube, all secondary ions are accelerated through an extraction plate, so that all ions have the same kinetic energy. Ions with lowest mass arrive sooner at the end of the tube, compared to heavier ions. The following equation is necessary to calculate a mass spectrum:

$$E = \frac{1}{2} \cdot m \cdot v^2 \quad (9)$$

Where E is the kinetic Energy in keV, m the mass and v the velocity of the ions. The mass to charge ratio called m/z of the ions can be then calculated as follows [155]:

$$\frac{m}{z} = \frac{2 \cdot U}{v^2} \quad (10)$$

Where m/z is the mass to charge ratio, U the acceleration potential in eV and v the velocity of the ions that pass the drift tube length in m/s.

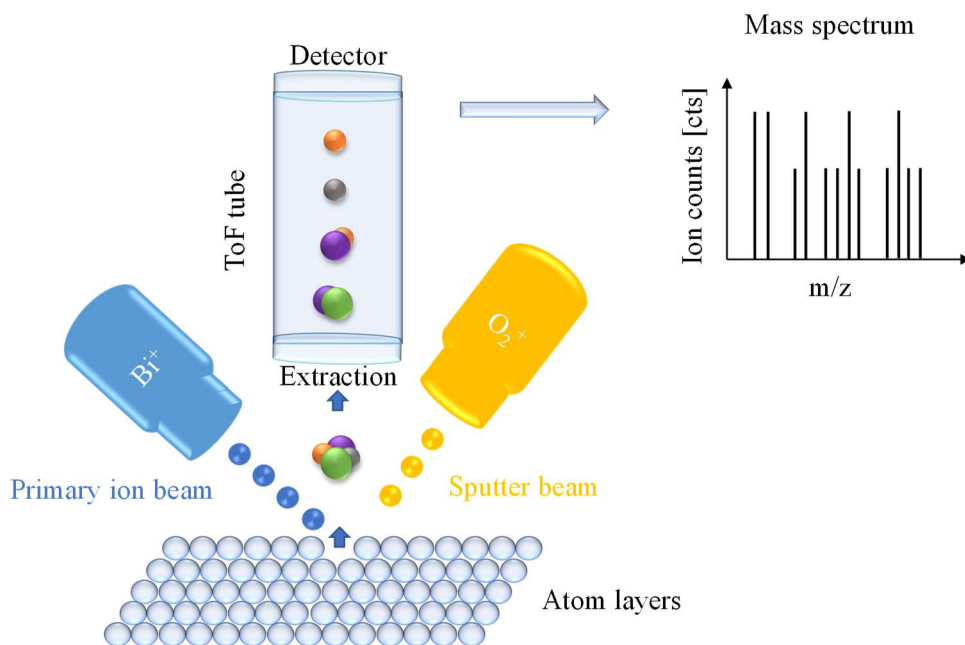


Figure 2.5 Setup of ToF-SIMS analysis in this study.

By knowing the length of the drift tube s and the time to traverse the tube, the velocity of each ion is calculated by $v = s/t$. A dependence between ion flight time and m/z is used to plot a mass spectrum, where faster time-of-flight of ions result from a lower m/z and slower ions have higher m/z ratios. Using this method the number of ions resulting from every pulse is recorded for each m/z [155].

Dynamic SIMS is used for depth profiling and 3D visualization of ion images. The O_2^+ sputter gun erodes material from the surface over a defined area followed by a Bi^+ primary ion analysis in a smaller area. The sputter yield is the amount of material removal during erosion [155]. Yamamura et al. [158] provided a semi-empirical calculation for pure Mg and determined a sputter yield of 5.38. The erosion rate is dependent on the material, the kinetic energy of ions, the angle of incidence, current, measured area and the ion type [158].

2.4 Surface treatments

2.4.1 Mechanical surface treatments

One study by Walter and Kannan [129] examined a trend of decreasing current density i_{corr} with decreasing roughness for AZ91 produced by different grit sizes of grinding papers [129]. In an analysis of Song and Xu [52] it is shown, that removing impurities from the surface by grinding decreased the hydrogen evolution compared to AR AZ31 condition [52]. The studies [52,129] presented provide evidence that grinding is an effective method to improve the degradation behaviour. However, mechanical surface treatments like grinding are not suitable for implant geometries like stents, screws and rods [14]. Surface treatments over the entire surface come rather into consideration, when using biodegradable Mg implants.

2.4.2 Surface modification on Mg-REE alloys

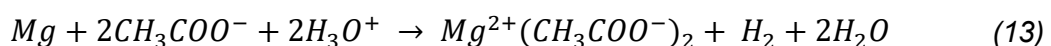
Work on surface treated WE43 was undertaken by Jin et al. [159]. Reactive magnetron sputtering was used to form niobium nitride (NbN) on the surface of as cast Mg-Y-REE alloy. The degradation resistance increased after deposition compared to a non-coated surface, as confirmed by electrochemical impedance spectroscopy (EIS), polarization tests and immersion tests in simulated body fluid (SBF) [159]. This view was supported by Jamesh et al. [160] who wrote that a surface modification by silicon ion implantation diminished the current density I_{corr} [160]. In a follow-up study, Jamesh et al. [161] found that Zr and N plasma immersion ion implantation, increased the degradation resistance in SBF and cell culture medium (cDMEM) [161]. Similarly, Li et al. [162] found that a SiC coating deposited by Plasma enhanced chemical vapour deposition (PECVD) on WE43, led to a reduction of the degradation rate for immersion in SBF, when compared to uncoated samples [162]. In all the studies reviewed above, surface treatments were recognised as an effective method to decrease the degradation rate.

2.4.3 Magnesium in acetic solution

The main reaction of base metals in acid solutions with a pH below 4 is called “acid corrosion” or “hydrogen corrosion” [100]. H_3O^+ ions from dissolved HAc react with Mg, dissolving into Mg^{2+} , water and hydrogen. A decrease of $[H_3O^+]$ lead to an increase in pH [163].



In general, the reaction of metals and acids lead to the formation of salts and hydrogen [164]. Salt is defined as a product of metal and acid residue [165], here magnesium acetate.



2.4.4 Acid etching

Nwaogu et al. [53,54] carried out etching experiments with both inorganic acids (nitric acid, phosphoric acid, sulphuric acid) and organic acids (acetic acid, citric acid, oxalic acid) on rolled sheets. With increasing etching time, a trend of more material removal was shown. The highest material removal of $21.23 \pm 1.52 \mu\text{m}$ was reached by use of 300 g/L HAc for 120 s, when compared to the other organic and inorganic etching solutions [53,54]. The highest material removal ($21.23 \pm 1.52 \mu\text{m}$) led to the lowest Fe surface content (18 ppm) and corrosion rate ($0.34 \pm 0.04 \text{ mm/year}$) for acetic acid etching in 5 wt.% NaCl, determined by salt spray testing. However, a removal of around $4 \mu\text{m}$ material was sufficient to reduce the Fe level $< 20 \text{ ppm}$ and decrease the corrosion rate to less than 1 mm/year compared to an as-received corrosion rate around 15 mm/year [53]. However, no trend between material removal, Fe elimination and degradation rate were observed when comparing different inorganic and organic etching solution experiments. Similarly, Supplit et al. [55] found the lowest corrosion rate ($0.70 \text{ mg cm}^{-2} \text{ d}^{-1}$) [14,55] in 5 wt.% NaCl for acetic acid (200 g/L for 30 s) treated AZ31 sheets after hydrogen evolution testing when compared to nitric, phosphoric, and hydrofluoric acid pre-treated samples [55]. The corrosion rates of both studies are not comparable, due to different corrosion experiment set-ups. However, both studies clearly showed, that acetic acid etching resulted in lowest corrosion rates when compared with other etching treatments.



A study by Gawlik et al. [56] involved the effect of acetic acid etching of Mg-5Gd on the degradation behaviour in a cell culture medium. To determine the effects of concentration and immersion times, Gawlik et al. [56] compared the mean degradation depth of six as-received and etched samples after 24 h degradation. For this different etching concentrations and times were used and decided after this short period degradation to take the condition with lowest mean degradation depth and standard deviation. The best conditions were used for a long-term testing of 30 days. All etched conditions showed a lower degradation rate in comparison to the as-received samples. Due to a linear regression of the plotted results, Gawlik et al. [56] ascertained more reliable and reproducible results by etching. They found a deformation and twinning zone in the near-surface region, which was eliminated, by removing around $150 \mu\text{m}$ of material. All etching conditions resulted in the formation of etching pits containing Gd-rich particles. A GdH_2 phase was confirmed by XRD. In a follow-up study, Gawlik et al. [57] showed that Fe contamination were removed from the surface of Mg-xGd alloys by etching for 15 s. A direct connection of Fe and degradation rate was not shown yet.

2.4.5 The effect of surface treatments on the degradation behaviour

A review of mechanical and chemical surface treatments, including their influence on roughness and morphology with correlated degradation behaviour is shown in following publication: “**The Effect of Surface Treatments on the Degradation of Biomedical Mg Alloys – A Review Paper**” [14].

Review

The Effect of Surface Treatments on the Degradation of Biomedical Mg Alloys—A Review Paper

Marcjanna Maria Gawlik ^{1,*}, Björn Wiese ¹ , Valérie Desharnais ^{1,2}, Thomas Ebel ¹ and Regine Willumeit-Römer ¹ 

¹ Helmholtz-Zentrum Geesthacht, Max-Planck-Straße 1, 21502 Geesthacht, Germany; bjoern.wiese@hzg.de (B.W.); valerie.desharnais@sympatico.ca (V.D.); thomas.ebel@hzg.de (T.E.); regine.willumeit@hzg.de (R.W.-R.)

² School of Computer Science, McGill University, 845 Sherbrooke Street West, Montréal, QC H3A 2T5, Canada

* Correspondence: marcjanna.gawlik@hzg.de

Received: 19 November 2018; Accepted: 14 December 2018; Published: 16 December 2018



Abstract: This report reviews the effects of chemical, physical, and mechanical surface treatments on the degradation behavior of Mg alloys via their influence on the roughness and surface morphology. Many studies have been focused on technically-used AZ alloys and a few investigations regarding the surface treatment of biodegradable and Al-free Mg alloys, especially under physiological conditions. These treatments tailor the surface roughness, homogenize the morphology, and decrease the degradation rate of the alloys. Conversely, there have also been reports which showed that rough surfaces lead to less pitting and good cell adherence. Besides roughness, there are many other parameters which are much more important than roughness when regarding the degradation behavior of an alloy. These studies, which indicate the relationship between surface treatments, roughness and degradation, require further elaboration, particularly for biomedical Mg alloy applications.

Keywords: surface treatments; roughness; Mg-alloys; degradation behavior

1. Introduction

The study of Mg as degradable biomaterial for implants is an advanced research area. A second operation to remove the implant after bone healing can be avoided [1–6]. Mg is naturally available as trace element in the body, and is thus non-toxic and biocompatible [7–9]. Implant processing is feasible due to the ductility and workability of Mg [10]. Strength and toughness are higher than of polymer implants, which is beneficial for load-bearing implants [11,12]. Mg alloys are reported to show improved osseointegration and bone implant strength compared to permanent Ti alloys [13,14]. In particular, Mg alloys are suitable as biodegradable implant materials [1,15–19]. Mg is able to degrade in aqueous solutions with the formation of magnesium hydroxide and hydrogen [20–24]. In particular, aqueous salt solutions containing ions including chlorides or sulphates, with the exception of alkali metals or alkaline metal containing solutions, are able to dissolve the protective magnesium hydroxide layer, leading to enhanced degradation [24–28]. In order to improve the mechanical properties of Mg, elements are added to tailor, for example, its tensile strength and ductility. Thus, it is possible to produce implants that have tailored mechanical properties to use it as temporary bone fixation. However, when alloying and processing the material, impurities like Fe, Ni, and Cu or phases with a high electrochemical potential difference are found at or near to the surface of the material, which increases the degradation rate through galvanic corrosion [23,29]. For the application of biodegradable Mg implants to become feasible in the future, two different objectives must be met in order to achieve usable degradation behavior.

One objective is limiting the degradation rate of the initial state of the alloy, which, as explained later, is related to the amount of hydrogen evolution. The deeper and rougher the surface morphology, the more hydrogen gas will be produced [9]. An overly fast degradation with gas evolution in the initial state leads to degradation of the mechanical integrity. Excessive gas evolution can also modify the bone remodeling process and impair the consolidation of bones [30]. However, relatively strong hydrogen evolution is crucial for cell adherence and implant-bone integration [21,31,32]. Aqueous salt solutions including chloride ions, like those found in the human body fluids [33], increasing decomposing of $\text{Mg}(\text{OH})_2$, release OH^- and raise the pH [34]. Besides hydrogen production, a local alkalization might provoke necrosis [9].

The second objective is to control the degradation rate of implants during the healing time. The required degradation rate depends on the application with lifetime and stability of the implant and the potential of the surrounding tissue to tolerate pH changes and high ion concentrations. It is reported that the properties of the material, e.g., crystallographic orientation [35–37], microstructure [21,38–48], grain size [41,49–53], secondary phases [51,54,55], contamination [38,40,56], and deformation [38,41,57–60], affect the degradation behavior, as well the environment, e.g., the immersion medium [61–64]. It is possible to control the degradation behavior of Mg alloys using chemical, physical, and mechanical surface treatments [27,32,65–69]. Additionally, surface uniformity has been shown to decelerate degradation [70]. Surface morphology can differ despite identical roughness parameters, and also affects the degradation process [39]. Studies have shown that surface roughness can affect the initial degradation [71], the degradation rate [38,71–77], degradation resistance [73,78–82], pitting behavior [38,71,72,83], bone integration [84–86], cell adherence [21,74,87,88], cell proliferation [88–91], and cell differentiation [92]. Besides roughness, surface unevenness can also influence the adhesion of cells [73]. In some cases, a smoother surface will reduce the degradation rate [72,74,93]. However, this behavior has been contradicted in other studies [73,79,81,82,94,95].

The aim of this review is to show the correlation between surface treatment, roughness, and the degradation behavior of Mg alloys in order to define meaningful roughness values and suitable surface treatments for biodegradable Mg implants. An overview of studies mentioning surface treatments, roughness, and degradation is given in Tables 1–5.

2. Mechanical Surface Treatments

2.1. Grinding and Polishing

The degradation behavior of sand-cast, ground, and polished AZ91 alloys were investigated by Walter and Kannan [96]. The use of a grinding paper with increased grit size decreased the surface roughness (Table 1, Ref. [96]). Three methods were used to evaluate the relationship between pitting and roughness: a 24 h immersion test in a 0.5 wt.% NaCl solution, 1 h of potentiodynamic polarization (PDP) and 1 h of Electrochemical Impedance Spectroscopy (EIS). For the polished samples, no inductive loop after EIS was observed. A low inductive loop is related to a low or negligible amount of surface pitting. This was found for all ground samples. Thus, it is suspected that no pitting will occur on polished surfaces due to a higher passivation. As a consequence, passivation is reduced for higher surface roughness values. The polarization curves in Ref. [96] show that a higher anodic current, as indicated by the current density i_{corr} , is produced with greater surface roughness (Table 1, Ref. [96] and Figure 1).

In particular, the polarization curve of material ground with 320 grit paper in Ref. [96] exhibits a strong increase in anodic current, which suggests a high number of pits being formed. The surface appearance was analyzed by scanning electron microscope (SEM) after immersion for 24 h and after galvanostatic testing. Numerous pits were observed after immersion when the 320 grit size paper was used, which confirms the results from the electrochemical testing. Less pitting was seen to occur when using a finer grinding paper. In the case of paper with a 1200 grit size, no localized pitting was found after testing. Surprisingly, more pits were observed on polished samples after galvanostatic testing.

This is likely to have been caused by a high anodic current which reduces passivation for all surface treatments. Walter and Kannan [96] concluded from these experiments that roughness does affect the passivation layer, but does not directly affect the likelihood of pitting. After removing the passivation layer, pitting occurred for all surface roughness values as seen by SEM [96].

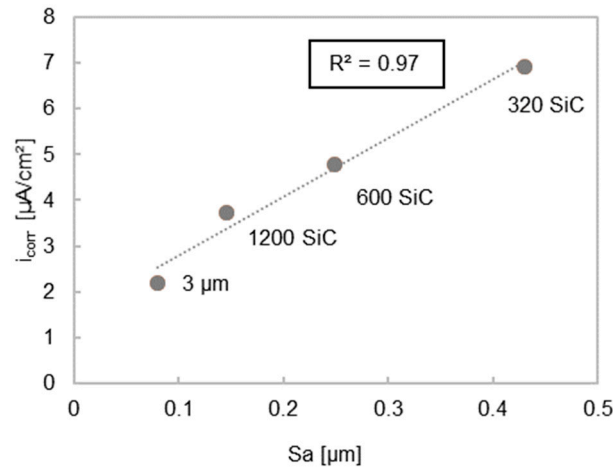


Figure 1. Graph shows a linear relationship between S_a and i_{corr} after grinding and polishing. R^2 is the coefficient of determination, which assesses the linear mutual dependence of x and y . $R^2 = 1$ defines the highest linearity [97]. S_a and i_{corr} values were obtained from [96].

Walter et al. [71] also investigated the correlation between the degradation and surface roughness S_a (the arithmetic mean height within a sample area, three dimensionally determined roughness) [98] for samples which were ground using 120 SiC grit size paper ($S_a = 973$ nm) and samples that had been ground using 2500 grit size paper, followed by polishing with a 3 μm diamond paste ($S_a = 22$ nm). The samples were cleaned with acetone and ethanol. The degradation behavior was characterized under simulated body fluid (SBF) using EIS. The results for both surface finishes exhibited similar tendencies. The ground and the polished samples showed a mid-frequency capacitive loop at the beginning of testing [71]. A mid-frequency capacitive loop corresponds to a passivation layer [96]. For the ground sample, a mid-frequency capacitive loop was observed for the first 2 h and was then followed by an inductive loop at low frequencies. The polished samples had inductive loops at low frequencies after 4 h, which confirms that passivation layers on smoother surfaces last longer [71]. In general, an inductive loop implies surface pitting [99]. The polarization resistance was present for a maximum of 3 h for the polished sample in contrast to a maximum of 2 h for rougher ground surface. This observation agrees with the assumption that polished samples have a higher passivation. Thus polishing samples reduces the degradation behavior, especially at the beginning of immersion. The SEM results support these findings. After 2 h immersion, a general degradation for both finishes was observed. After 6 h, the rougher surface clearly showed more pitting, while the few pits seen on the polished surface indicated the start of pit formation. Pitting was studied for both surfaces after 12 h immersion. The initial pitting of the ground surface had progressed further compared to the polished finish. Walter et al. [71] explained this observation as a local pH drop caused by deep valleys in the rough surface. Additionally, the passivation layer of the rough surface broke up earlier than the smooth surface [71].

Alvarez et al. [94] found that polished AE44 samples encouraged more pitting compared to semi-polished samples in an immersion test. At the beginning of degradation, polished samples exhibited a higher pit volume compared to semi-polished samples. However, semi-polished samples had higher pit radii. The smoother surface of the polished sample and its related chlorine absorption capacity is given as a possible explanation. This behavior is distinct from reports that report that rougher surfaces on steel [75,76] and aluminum [77] lead to faster degradation and more pitting.

Walter and Kannan [96] suggested a change of the passivation layer provoked by shifting the local pH, initiated by aeration of the solution, as a reason for this behavior [96]. Pitting for both conditions leads to intergranular degradation after several hours. However, the start of intergranular degradation of the polished samples started earlier than for semi-polished samples [94].

Lorenz et al. [74] showed that surface roughness does not only influence the degradation resistance of pure magnesium; it also affects the cell (HeLa cells/GSP-C12 mouse fibroblasts) adhesion on the surface of Mg. For this study, discs were prepared with 600 paper grit size, a combination of 6 μm diamond paste, and an ethanol/glycerol solution. Sample cleaning was performed using an ultrasonic bath filled with ethanol for 3 min. In order to analyze the effects of surface morphology on cell adherence, one series of samples was immersed in 1 mol NaOH for 24 h and another series in modified simulated body fluid (M-SBF) at 37 °C for 5 d. Afterwards, the samples were flushed with ethanol and dried in air. The roughness increased after immersion in both solutions, but especially for the modified simulated body fluid (M-SBF) solution. pH measurements were also carried out on Mg samples degrading in a Minimum Essential Media (MEM) that included fetal bovine serum (FBS). A pH of 8.96 was observed for the M-SBF treated Mg samples and was higher compared to the other treatments after 2 h (Tables 1 and 4, Ref. [74]). The thicker Ca/Mg phosphate layer after M-SBF immersion does not protect the Mg sample due to its porosity, but the corrosion resistance increased by a factor of five compared to the untreated samples. In contrast, the cell density is higher compared to the polished and NaOH treated samples. The increase of the roughness by immersing in M-SBF improved the cell adhesion. The medium alkalization of the M-SBF samples is only suitable for short term applications. The smooth surface of the polished samples exhibits nearly no cell adherence and degrades very quickly. The passivation of Mg with NaOH reduces degradation, but cell adhesion is lower compared to M-SBF immersion [74].

Liu [61] compared the cell adherence of rolled pure Mg foils with an oxide layer and on ground foils without an oxide layer. He also studied the effects of roughness and degradation in Dulbecco's Modified Eagle's Medium (DMEM) and deionized (DI) water. The smoother ground samples varied by only 1.2% (oxide layer 13.6% and on ground foils 14.8%) in cell density from the rough oxidized samples (Tables 1 and 2, Ref. [61]). As such, it can be assumed, that surface roughness did not affect the cell density. No correlation between roughness and degradation rate was found, though ground samples in DMEM showed a slower degradation rate compared to oxidized samples. The opposite behavior was observed in DI water [61].

In contrast to the studies carried out by Liu [61] and Lorenz et al. [74], it was reported by Johnson et al. [21] that ground Mg-4Y samples demonstrated a better cell attachment than samples with an electrical discharged machined (EDM) surface. The roughness of the surfaces could be a possible explanation, as it was found that rough surfaces degrade faster than smooth surfaces [21,72,93]. Mg-4Y exhibits a contrary degradation behavior as pure Mg [61]. The ground surface leads to a lower mass loss in DI water which is opposite to the higher mass loss in DMEM (Tables 1 and 2, Ref. [21]). This effect is not thought to be due to roughness, but rather, from a different evolution of the pH under the different testing conditions.

Song and Xu [38] investigated the effect of tempering (HT), sandblasting, grinding, and etching on the degradation resistance of the alloy AZ31. Tempering and sandblasting reduced degradation resistance, while grinding or acid etching as a cleaning procedure decreased weight loss and hydrogen evolution. Heat treatment led to the precipitations of large Al-Mn-Fe particles which deteriorated the degradation resistance [38]. In addition to impurities, it is also known that roughness influences the degradation rate [100]. The roughness R_a (two-dimensionally determined roughness, arithmetic mean deviation of the roughness profile) and the hydrogen evolution of ground samples were very low compared to sandblasted samples (Tables 1 and 2, Ref. [38]). Sandblasting led to a very rough surface, accompanied by micro stresses in the surface layer. The Fe impurities rather than this surface roughening increased the degradation rate. Grinding the surface removes contaminations and leads

to a slower degradation rate. Though ground surfaces are smoother than etched, the effect on the degradation is not as significant as removing a significant amount of Fe [38].

Zhao and Zhu [6] investigated, in addition to collagen monomer concentration, pH, and assembly time, the influence of ground surfaces on collagen fibril formation. They tested different surface finishes and the collagen formation with subsequent cell attachment. They ground Mg and AZ31 discs with 180 ($R_a = 1.89 \mu\text{m}$), 800 ($R_a = 0.29 \mu\text{m}$) and 1200 ($R_a = 0.15 \mu\text{m}$) SiC paper and apply 50 μL of 200 $\mu\text{g}/\text{mL}$ D-phosphate-buffered solution (DPBS) diluted collagen solution for 2 h on the samples. By SEM they observed the morphology of collagen fibers for every surface finish and alloy. A clear difference of collagen formation was visible from roughest to smoothest surface for both alloys. While the collagen formation on both alloys for both smoothest surfaces was comparable, the roughest surface of AZ31 showed less dense structure in contrast to Mg. The roughest surface of both alloys adsorbed the highest amount of collagen after 2 h, while the smoothest surface showed the lowest adsorbed amount. This trend was more distinct for Mg compared to AZ31. Cell attachment observations after 2 h lead to the assumption that cells were more attached on collagen treated and smoother samples in contrast to the roughest surface finish. The roughest surface finish with a more fiber woven structure and highest collagen adsorption also showed in another Fluorescent live/dead cell analysis that, after one day, the collagen structure on a rough surface is more detrimental to cell density, independent of the alloy [6]. Nudelman et al. [101], reported a correlation between collagen and cell attachment [101]. In contrast to Nudelman et al. [101], Zhao and Zhu [6] evidenced a decrease in cell density with higher collagen adsorption. For this reason, it is assumed, that more collagen does not always result in a stronger cell attachment. In reference to roughness, this study shows an effect on the collagen formation which influences the cell density indirectly [6].

2.2. Burnishing

A comparison between ground and burnished sample degradation was performed using hydrogen evolution, PDP, and white light interferometry on the AZ31B alloy [39]. Ground and burnished (dry and cryogenic) samples had a very similar roughness before degradation. Burnishing was performed using a severe plasticity burnishing (SPB) process. Cryogenic burnishing is distinguished from dry burnishing by the use of liquid nitrogen. After degradation, the morphology of the ground samples differed from the burnished samples. Thus, roughness will not be the only factor to influence the degradation behavior. In addition, grain size and basal texture had an influence on the uniformity and amount of degradation. Dry and cryogenic burnishing decreased hydrogen evolution over a 7 h period with respect to ground surfaces. Both burnishing processes lead to a smoother finish with reduced pit depth and pit volume compared to the 4000 grit size paper treatment immersion test. The PDP analysis shows the same trend for both burnished surfaces with a higher degradation resistance, indicated by a broader capacitive loop [39]. The crystallographic orientation and grain refinement has to be considered, as well as the surface roughness [38]. In this report, the surface roughness did not affect the degradation, in disagreement with the prediction of Song and Xu [38]. Moreover, a small grain size and a strong basal texture led to a higher degradation resistance [39].

Table 1. Overview of different studies concerning grinding and polishing that consider roughness and degradation behavior. * Values were determined from the diagram with the corresponding reference.

Alloy	Sample	Experiment	Solution	Time	Grinding/ Polishing	Initial Roughness	Results	Ref
Mg	Disk	pH	MEM ¹	2 h	Polishing: 6 µm + lubricant	Ra = 0.10 µm	pH = 8.01 * CD ³ = 10 cells/mm ²	[74]
		Cell viability	MEM ¹ + FBS ²	24 h				
	Foil	Mass loss	DMEM ⁴ + 10% FBS ²	up to 80 d	1200 grit	-	Max DR ⁵ = 0.09 mg cm ⁻² d ⁻¹ Max DR ⁵ = 0.28 mg/cmWitt ² /d	[61]
AZ31	Disk	Cell adhesion	DMEM ⁴ + 10% FBS ²	24 h	1200 grit	-	14.8% cell adhesion	[6]
		Collagen quantification, cell attachment	-	2 h	180 grit 800 grit 1200 grit	Ra = 1.89 µm Ra = 0.29 µm Ra = 0.15 µm	Trend of higher collagen adsorption with higher Ra, lowest CD ³ for highest Ra.	
		Immersion	3.5 wt.% NaCl	4 and 12 h, 1.5 and 2.5 d	1400 grit	-	intergranular degradation started earlier after polishing	
AZ31	Sheet	PDP ⁷ EIS ⁸	0.9 wt.% NaCl	-	P1000 emery Paper	Ra = 0.33 µm	i _{corr} = 3.64 µAcm ⁻² Rp = 934 Ωcm ²	[102]
		Hydrogen	5 wt.% NaCl	24 h	1200 grit	Ra = 0.07 µm	1.11 mg/dcm ²	[38]
		PDP ⁷ (1 cm ²)	PBS ⁹	-	1200 grit	Sa = 48.58 ± 23.45 nm	i _{corr} = 34.5 ± 3.5 µA cm ⁻² CR ¹⁰ = 0.76 ± 0.06 mm/y	[103]
AZ31	Disk	Cytotoxicity	α-MEM ¹¹	21 d	1200 grit	Sa = 48.58 ± 23.45 nm	* Cell survival: 92 %	[39]
		Immersion, Hydrogen, PDP ⁷	5 wt.% NaCl	30, 200 h Immersion, 7 h Hydrogen	4000 grit Dry Burnishing Cryogenic Burnishing	Ra = 0.2 µm	Burnishing lead to a better corrosion behavior	
		Collagen quantification, cell attachment	-	2 h	180 grit 800 grit 1200 grit	Ra = 1.89 µm Ra = 0.29 µm Ra = 0.15 µm	Trend of higher collagen adsorption with higher Ra, lowest CD ³ for highest Ra.	

Table 1. Cont.

Alloy	Sample	Experiment	Solution	Time	Grinding/ Polishing	Initial Roughness	Results	Ref
AZ91	-	EIS ⁸ (0.785 cm ²)	SBF ¹²	12 h	120 grit Polishing: 3 µm	Sa = 0.022 µm Sa = 0.973 µm	passivation layers on smoother surfaces last longer	[71]
	-	PDP ⁷ (0.75 cm ²)	0.5 wt.% NaCl	-	320 grit 600 grit 1200 grit Polishing: 3 µm	Sa = 0.430 µm Sa = 0.248 µm Sa = 0.145 µm Sa = 0.08 µm	$i_{\text{corr}} = 6.92 \mu\text{A cm}^{-2}$ $i_{\text{corr}} = 4.79 \mu\text{A cm}^{-2}$ $i_{\text{corr}} = 3.73 \mu\text{A cm}^{-2}$ $i_{\text{corr}} = 2.19 \mu\text{A cm}^{-2}$	[96]
	Disk	PDP ⁷ (1 cm ²)	PBS ⁹	-	1200 grit	Sa = 29.76 ± 12.69 nm	$i_{\text{corr}} = 36.6 \pm 3.2 \mu\text{A cm}^{-2}$ CR ¹⁰ = 0.78 ± 0.07 mm/y	[103]
	Disk	Cytotoxicity	α-MEM ¹¹	21 d	1200 grit	Sa = 29.76 ± 12.69 nm	* Cell survival: 87 %	
M-4y		Mass loss	DMEM ⁴ + 10% FBS ² DI ⁶ Water	9.04 d	1200 grit	Ra = 65 ± 31 nm	* 89.7 % * 0.33 %	
	Disk	pH	DMEM ⁴ + 10% FBS ² DI ⁶ Water	24 h	1200 grit	Ra = 65 ± 31 nm	* pH = 8.32 * pH = 9.00	[21]
	Disk	Cell adhesion	DMEM ⁴ + 10% FBS ²		1200 grit	Ra = 65 ± 31 nm	* 22.4 %	
ZK60A		PDP (1 cm ²)	PBS ⁹	-	1200 grit	Sa = 78.30 ± 21.63 nm	$i_{\text{corr}} = 32.3 \pm 2.6 \mu\text{A cm}^{-2}$ CR ¹⁰ = 0.68 ± 0.01 mm/y	[103]
	Disk	Cytotoxicity	α-MEM ¹¹	21 d	1200 grit	Sa = 78.30 ± 21.63 nm	* Cell survival: 32 %	
Mg-0.5Ca-6Zn	Rectangular prism	PDP ⁷ (1 cm ²)	Kokubo	-	2000 grit	Rq = 210 nm	$i_{\text{corr}} = 365 \mu\text{A cm}^{-2}$ CR ¹⁰ = 8.34 mm/y	[104]
		Hydrogen		10 d	2000 grit	Rq = 210 nm	4.92 mL/cm ² /d	
WE43	Plate		SBF ¹²	-	Polishing: 1 µm	-	$i_{\text{corr}} = 642 \pm 125 \mu\text{A cm}^{-2}$	[105]

Table 1. Cont.

Alloy	Sample	Experiment	Solution	Time	Grinding/ Polishing	Initial Roughness	Results	Ref
Mg-1.0Ca		Mass loss	SBF ¹²	3 d	1200 grit	Sa = 4.67 nm	* 9.63 mg	
		Cell viability	Extract DMEM ⁴ + 10% FBS ²	3 d + 4 h	1200 grit	Sa = 4.67 nm	* 100%	
Mg-0.5Sr	Rectangular prism	EIS ⁸ (10 × 10 mm ²)	SBF ¹²	-	1200 grit	Sa = 4.67 nm	$i_{corr} = 2.3 \times 10^2 \mu A cm^{-2}$	[88]
		Mass loss	SBF ¹²	3 d	1200 grit	Sa = 2.16 nm	* 14.3 mg	
Mg-0.5Sr		Cell viability	Extract DMEM ⁴ + 10% FBS ²	3 d + 4 h	1200 grit	Sa = 2.16 nm	* 100 %	
		EIS ⁸ (10 × 10 mm ²)	SBF ¹²	-	1200 grit	Sa = 2.16 nm	$i_{corr} = 1.0 \times 10^3 \mu A cm^{-2}$	

¹ MEM: Minimum Essential Media; ² FBS: fetal bovine serum; ³ CD: Cell density; ⁴ DMEM: Dulbecco's Modified Eagle's Medium; ⁵ DR: degradation rate; ⁶ DI: deionized; ⁷ PDP: potentiodynamic polarization; ⁸ EIS: Electrochemical Impedance Spectroscopy; ⁹ PBS: phosphate buffered saline; ¹⁰ CR: corrosion rate; ¹¹ α-MEM: MEM alpha modification Media; ¹² SBF: simulated body fluid.

2.3. Machining

Turned, threaded and sandblasted Mg-0.8Ca samples were examined and tested in vivo [93]. Smooth ($R_a = 3.65 \mu\text{m}$) turned and threaded samples exhibited the best interlocking connection between the bone and implant. Rough ($R_a = 32.7 \mu\text{m}$) sandblasted rods degraded most rapidly with the highest number of visible gas bubbles. Turned surfaces led to the lowest gas evolution and decomposition in these studies [87,93]. Despite a similar integration of threaded and turned implants into the bone tissue, threaded implants showed a non-uniform bone resorption at the thread edges [93]. This is in agreement with the findings of Walter et al. [71], which may be explained by local variations in pH.

Mhaede et al. [102] reported a relationship between roughness and corrosion resistance. For the degradation test in 0.9 wt.% NaCl solution, eight different conditions of AZ31 alloy were prepared. Samples were either ground or shot-peened with 3 different Almen intensities (saturation value of residual arc height of an Almen strip, established by John Almen) [102,106,107], ground and coated, or shot-peened with 3 different Almen intensities and coated without prior grinding. Shot peening was performed with ceramic shot which had a diameter of $850 \mu\text{m}$ (Z850). The dicalcium phosphate dihydrate (DCPD) coating used was produced by electro-deposition of samples in a $0.1 \text{ mol Ca}(\text{NO}_3)_2 \cdot 4\text{H}_2\text{O} + 0.06 \text{ mol NH}_4\text{HPO}_4$ solution. In Table 2, Ref. [102] it is shown that the current density i_{corr} for the shot-peened (SP) samples was increased compared to the other conditions in Table 4, Ref. [102]. It has been shown that having a rough surface after shot-peening affects i_{corr} (Table 2, Ref. [102] and Figure 2), as the resulting greater surface area increases the surface reactivity [102]. However, it is not possible to relay R_a linear to i_{corr} (Tables 1, 2 and 4, Ref. [102] and Figure 2) for all surface finishes due to the protective properties of the DCPD coating compared to only shot peened samples. The linear relationship between R_a and i_{corr} for the shot-peened and shot-peened/coated samples (Figure 2) agrees with the study of Walter and Kannan [96], whereas linear correlation was observed for only the ground samples. However, it should be noted that higher deformation and internal stress, arising from higher Almen intensities, could also affect the degradation behavior.

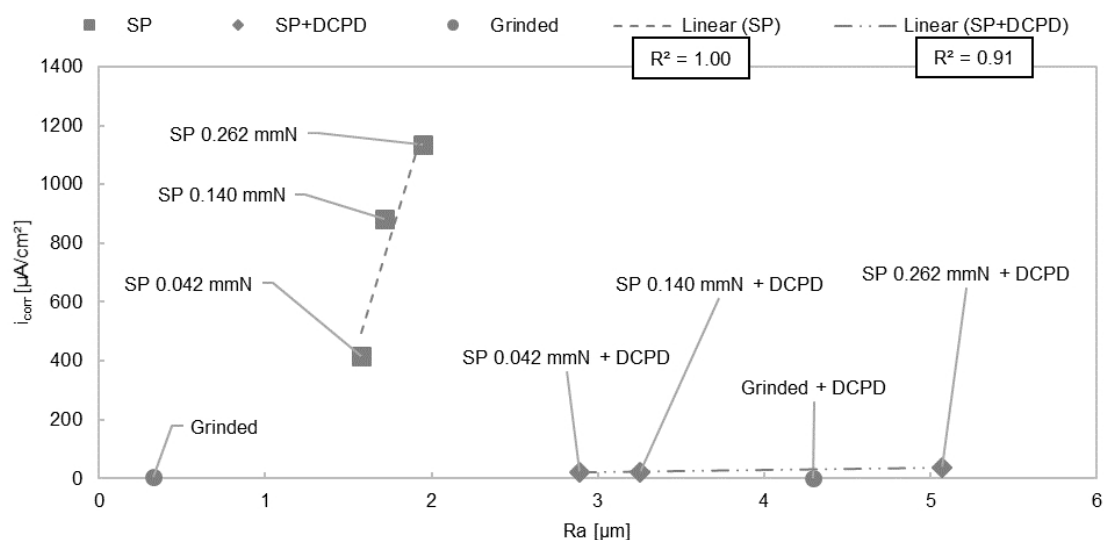


Figure 2. Diagram current density i_{corr} against roughness R_a for ground, shot peened, and shot peened + DCPD coated samples. A non-linear R^2 relationship between R_a and i_{corr} is shown by comparing all conditions (ground/SP/SP+DCPD) together. Linear R^2 is plotted for only shot peened or only shot peened and coated samples. A trend of linearity can be seen only for roughness values arising from same surface treatments. R_a and i_{corr} values were obtained from [102].

Denkena and Lucas [108] studied the surface and subsurface properties after turning and deep rolling a Mg-3Ca alloy. Three different conditions for each machining process were investigated. With

regard to turning, the roughness Rz (distance from deepest valley to highest peak within sample length from a linear measurement) [109] decreased from around Rz ~ 4.48 μm to Rz ~ 3.75 μm after increasing the cutting speed from 10 m/min to 100 m/min at constant cutting depth and feed rate. By reducing the feed rate from 0.1 mm to 0.05 mm at a constant cutting speed (100 m/min) and cutting depth (0.5 mm), the roughness (Rz ~ 2.17 μm) was reduced (Table 2, Ref. [108]). After deep rolling with different rolling forces ($F = 50\text{ N}, 200\text{ N}, 500\text{ N}$) and constant rolling speed (25 m/min) and feed rate (0.1 mm), no significant change in roughness (Rz ~ 0.91–1.26 μm) occurred (Table 2, Ref. [108]). Degradation tests were performed in 0.9 wt.% NaCl solution and the hydrogen gas evolution was measured. The mass loss was calculated from the amount of hydrogen produced and a correction factor. The degradation rates for turning with higher roughness were greater compared to the degradation rates after rolling. However, for turning, the condition with the highest roughness showed the lowest mass loss compared to the smoother samples. For deep rolling, the condition with the lowest rolling force led to the highest, while not signifying mass loss (calculated from hydrogen generation) after around 240 h exposure time compared to conditions with higher rolling forces and comparable Rz values. No significant correlation between roughness and mass loss was found. High residual compressive stress was reported to reduce the degradation rate by about 100 times [108], and the degradation results were comparable with the results from high speed dry milled Mg-0.8Ca with the lowest roughness [110].

The influence of machining and deep rolling on Mg-3Ca and Mg-0.8Ca was analyzed by Denkena et al. [111], and the results were compared to those of Denkena and Lucas [108]. Only 3 conditions per alloy were tested. The turning was carried out with a cutting speed of 100 m/min, cutting depth of 200 μm , and a feed rate of 0.1 mm. Two deep rolling conditions were studied with rolling forces of 50 N and 200 N and the same cutting speed and feed as described by Denkena and Lucas [108]. The roughness Rz after turning and deep rolling was comparable for each alloy for every machining process. The roughness Rz after turning was about 4 μm , while Rz for deep rolling resulted in a lower Rz of between 0.44–0.76 μm (Table 2, Ref. [111],[108]) compared to Denkena and Lucas [108]. The corrosion behavior was tested by hydrogen evolution and performed in a 0.9 wt.% NaCl solution and $\mu\text{-CT}$. It was shown that turned Mg-3Ca with the highest Rz resulted in the highest hydrogen evolution (~ 20.2 mL/cm² after 29 h) and greatest degradation in $\mu\text{-CT}$ compared to deep rolled samples (~0.76–1.27 mL/cm² after 29 h). For the Mg-0.8Ca alloy the hydrogen evolution (~5.42–6.22 mL/cm² after 29 h) showed no significant dependence on the method of machining. From these investigations, it is possible to say that roughness had no influence on the degradation behavior. Rather than roughness, a high compressive stress and the Mg₂Ca phase in the Mg-3Ca alloy was reported to affect the degradation behavior [111].

Table 2. Overview of different studies investigating SFF and machining and their influence on the degradation behavior. * Values were determined from the diagram with the corresponding reference.

Alloy	Sample	Experiment	Solution	Time	Machining	Initial Roughness	Results	Ref	
Mg	-	PDP ¹	HBSS ² + HEPES ³	6 h	SFF ⁴	Ra = 0.59 ± 0.04 μm	i _{corr} = 94.52 μAcm ⁻²	[72]	
						Ra = 2.68 ± 0.74 μm	i _{corr} ~ 189.04 μAcm ⁻²		
						Ra = 9.12 ± 0.44 μm	i _{corr} ~ 567.12 μAcm ⁻²		
						Ra = 0.59 ± 0.04 μm	2.74 mg cm ⁻² d ⁻¹		
		Mass loss					Ra = 2.68 ± 0.74 μm	28.43 mg cm ⁻² d ⁻¹	
							Ra = 9.12 ± 0.44 μm	130.12 mg cm ⁻² d ⁻¹	
	Foil	Mass loss	DMEM ⁵ + 10% FBS ⁶ + P/S ⁷ DI ⁹ Water	80 d	Rolling	-	Max DR ⁸ = 1.2 mg cm ⁻² d ⁻¹ Max DR ⁸ = 0.14 mg cm ⁻² d ⁻¹	[61]	
AZ31	Sheet	Hydrogen	5 wt.% NaCl	1.5 h 0.25 h	Milling HT ¹⁰ + SB60 ¹¹	Ra = 2.02 μm	54.23 mg/dcm ² 563.49 mg/dcm ²	[38]	
		PDP ¹		0.9 wt.% NaCl	-	SP ¹² 0.042 mmN SP ¹² 0.140 mmN SP ¹² 0.262 mmN	Ra = 1.58 μm Ra = 1.72 μm Ra = 1.95 μm	i _{corr} = 416.17 μAcm ⁻² i _{corr} = 882.77 μAcm ⁻² i _{corr} = 1136.5 μAcm ⁻²	[102]
	Sheet	Hydrogen	5 wt.% NaCl	6.55 h	Rolling	-	* CR ¹³ = 7.17 mg cm ⁻² d ⁻¹	[95]	
	Plate	PDP ¹	3.5 wt.%	-	SB40 ¹⁴	-	i _{corr} = 2.1 μA cm ⁻²	[80]	
				DI ⁹ Water	217 h	EDM ¹⁵	Ra = 196 ± 47 nm	* 75.2 % * 45.9 %	
M-4Y	Disk	Cell adhesion	DI ⁹ Water	24 h	EDM ¹⁵	Ra = 196 ± 47 nm	* pH = 8.48 * pH = 8.98	[21]	
		Cell adhesion	DMEM ⁵ + 10% FBS ⁶ + P/S ⁷		EDM ¹⁵	Ra = 196 ± 47 nm	* 7.82 %		

Table 2. Cont.

Alloy	Sample	Experiment	Solution	Time	Machining	Initial Roughness	Results	Ref
Mg-3.0Ca	Cylinder	Mass loss From hydrogen generation	0.9 wt.% NaCl	93 h	Turning: ap = 0.5 mm, vc = 10 m/min, f = 0.1 mm	* Rz = 4.48 μm	* 0.89 g/cm ²	[108]
					Turning: ap = 0.5 mm, vc = 100 m/min, f = 0.1 mm	* Rz = 3.75 μm	* 1.35 g/cm ²	
					Turning: ap = 0.5 mm, vc = 100 m/min, f = 0.05 mm	* Rz = 2.17 μm	* 1.29 g/cm ²	
	Cylinder	Hydrogen evolution	0.9 wt.% NaCl	240 h	Deep Rolling ¹⁶ : Fr = 50 N	* Rz = 1.26 μm	* 0.07 g/cm ²	[111]
					Deep Rolling ¹⁶ : Fr = 200 N	* Rz = 0.91 μm	* 0.02 g/cm ²	
					Deep Rolling ¹⁶ : Fr = 500 N	* Rz = 1.26 μm	* 0.02 g/cm ²	
Cylinder	Hydrogen evolution	0.9 wt.% NaCl	29 h	Turning: ap = 200 μm , vc = 100 m/min, f = 0.1 mm	* Rz = 3.98 μm	* 20.2 mL/cm ²	[111]	
				Deep Rolling ¹⁶ : Fr = 50 N	* Rz = 0.63 μm	* 1.27 mL/cm ²		
				Deep Rolling ¹⁶ : Fr = 200 N	* Rz = 0.47 μm	* 0.76 mL/cm ²		
	Cylinder	μ -CT	0.9 wt.% NaCl	29 h	Turning: ap = 200 μm , vc = 100 m/min, f = 0.1 mm	* Rz = 3.98 μm	* PV ¹⁷ = 19.6 mL	[111]
					Deep Rolling ¹⁶ : Fr = 50 N	* Rz = 0.63 μm	* PV ¹⁷ = 1.44 mL	
					Deep Rolling ¹⁶ : Fr = 200 N	* Rz = 0.47 μm	* PV ¹⁷ = 1.05 mL	

Table 2. Cont.

Alloy	Sample	Experiment	Solution	Time	Machining	Initial Roughness	Results	Ref	
Mg-0.8Ca	Cylinder	Hydrogen evolution	0.9 wt.% NaCl	29 h	Turning: ap = 200 µm, vc = 100 m/min, f = 0.1 mm	* Rz = 4.00 µm	* 6.18 mL/cm ²	[111]	
					Deep Rolling ¹⁶ : Fr = 50 N	* Rz = 0.44 µm	* 5.42 mL/cm ²		
		µ-CT	0.9 wt.% NaCl	29 h	Deep Rolling ¹⁶ : Fr = 200 N	* Rz = 0.76 µm	* 6.22 mL/cm ²	[111]	
					Turning: ap = 200 µm, vc = 100 m/min, f = 0.1 mm	* Rz = 4.00 µm	* PV ¹⁷ = 16.3 mL		
Mg-0.5Ca	Disk	Rabbit, µ-CT	-	3 and 6 months	Deep Rolling ¹⁶ : Fr = 50 N	* Rz = 0.44 µm	* PV ¹⁷ = 12.1 mL	[93]	
					Deep Rolling ¹⁶ : Fr = 200 N	* Rz = 0.76 µm	* PV ¹⁷ = 6.71 mL		
		Mass loss	DMEM ⁵ + 10% FBS ⁶ + P/S ⁷	30 d	Turning	Ra = 3.65 µm	Turning lead to the lowest gas evolution and decomposition	CR ¹³ = 0.50 µm/d	[57]
					Sand milling	Ra = 32.7 µm			
				Threading	-				

¹ PDP: potentiodynamic polarization; ² HBBS: Hank's Balanced Salt Solution; ³ HEPES: Biological buffer for cell culture media; ⁴ SFF: indirect solid free-form fabrication; ⁵ DMEM: Dulbecco's Modified Eagle's Medium; ⁶ FBS: fetal bovine serum; ⁷ P/S: Penicillin/Streptomycin; ⁸ DR: degradation rate; ⁹ DI: deionized; ¹⁰ HT: heat treated at 450 °C for 10 min (tempering); ¹¹ SB60: sandblasting with glass bead type MS-6 at 60 psi; ¹² SP: shot peening; ¹³ CR: corrosion rate; ¹⁴ SB40: sand blasting by #40 SiO₂; ¹⁵ EDM: wire electrical discharge machining; ¹⁶: Deep Rolling: with vr = 25 m/min and Fr = 0.1 mm.

3. Chemical Surface Treatments and Coatings

3.1. Acid Etching

The treatments reported by Supplit et al. [95] indicated that it was possible to improve the degradation resistance of rolled AZ31 alloy by pickling with different acids like acetic acid, phosphoric acid, nitric acid, and hydrofluoric acid [95]. Acid pickling, especially with acetic acid decreased the degradation rate from $7.17 \text{ mg cm}^{-2} \text{ d}^{-1}$ (rolled condition) to $0.70 \text{ mg cm}^{-2} \text{ d}^{-1}$. The second best etching method was found to be phosphoric acid. The degradation rates were determined by measuring hydrogen gas evolution in 5 % NaCl. A rougher surface after pickling with acetic acid was observed when compared to the other etching solutions. The samples with the lowest degradation rates had rougher surfaces, an observation that contradicts the findings of Nguyen et al. [72].

Organic acids like acetic, citric, or oxalic, and inorganic acids like phosphoric, nitric, and sulfuric acid were used to treat AZ31 alloy by Nwaogu et al. [40]. The aim was to remove contamination and impurities from resulting from rolling. After etching, 1–20 μm was removed from the surface. It was observed that more material was removed as the etching time increased. A roughness analysis showed that the roughness value R_a after etching is higher than R_a of rolled samples. Removing 5 μm of material generally reduced the number of Ni impurities. However, Fe impurities still remained at the surface even after material had been removed. To determine the degradation behavior, a 48 h salt spray test was used as a screening test. The lowest degradation rates were obtained from samples with the lowest impurity levels which had the greatest amount of material removed. Acetic acid-etched samples had the slowest degradation rates. EIS measurements supported the finding that acetic acid etching leads to the resistance, due to having the highest polarization resistance (R_p) [40]. This finding is in agreement with the results obtained by Supplit et al. [95] and Nwaogu et al. [40], who showed that a low impurity level and a 5 μm etching depth improved the degradation behavior. When more than 5 μm of material was removed, the surface became rougher [40].

The change in roughness after inorganic acid etching confirmed this finding [56]. For sulfuric acid etching, R_a ($>2 \mu\text{m}$) was much higher compared to other inorganic etching solutions when 7 μm of material had been removed. In addition, sulfuric acid etching leads to a lower degradation resistance in spite of the resulting low level of impurities. Degradation of sulfuric acid-etched material mostly results from galvanic degradation initiated by second phases. Though the effect of roughness were not the main focus in these investigations, nitric acid etching showed a high degradation resistance for a surface with an initially uniform roughness distribution and low roughness value [56]. Thus, the roughness of a sample after etching could also be a parameter which has to be considered in order to determine the full degradation behavior.

Gawlik et al. [57] measured the roughness after acetic acid etching with various combinations of acid concentration and immersion time. The surface roughness S_a increased after etching compared to the milled surface and varies with different conditions. After 30 days immersion, the same degradation rate was determined for all etched conditions (Table 3, Ref. [57]), in spite of different S_a and S_q (root mean square value of surface deviations) [98] values after etching. This leads to the conclusion that the initial roughness of the sample has no long-term effect on degradation. The varying surface morphology and near-surface deformation arising from milling also affected the degradation rate [57].

Similarly to Nwaogo et al. [40,56], Song and Xu [38] described that Fe impurities accelerate the degradation of the AZ31 alloy. As such, as-received samples and heat-treated samples have lower degradation resistance compared to ground and sulfuric acid etched samples, due to Fe particles remaining on the surface. Sulfuric acid etching roughens the surface much more than grinding, but both conditions lead to a similar degradation rate. Thus, the roughness of the etched samples itself does not contribute to the degradation rate. Acid cleaning removes contamination and the deformation zone arising from processing, and thus directly impacts the degradation behavior [38].

Table 3. List of different studies on acid etching being used as a surface treatment. * Values were determined from the diagram with the corresponding reference.

Alloy	Sample	Experiment	Solution	Time	Acid Etching	Initial Roughness	Results	Ref	
AZ31	Sheet	SST ¹	5 wt.% NaCl	48 h	50 g/L H ₂ SO ₄ ² , 15s	* Ra = 0.98 μm	CR ³ = 2.20 ± 0.18 mm/y	[56]	
					80 g/L HNO ₃ ⁴ , 120 s	* Ra = 0.23 μm	CR ³ = 0.51 ± 0.10 mm/y		
					80 g/L H ₃ PO ₄ ⁵ , 60s	* Ra = 0.49 μm	CR ³ = 0.74 ± 0.31 mm/y		
	Sheet	SST ¹	5 wt.% NaCl	48 h	300 g/L CH ₃ COOH ⁶ , 120s	* Ra = 0.61 μm	CR ³ = 0.34 ± 0.08 mm/y	[40]	
					80 g/L C ₂ H ₂ O ₄ ⁷ , 30s	* Ra = 0.48 μm	CR ³ = 0.59 ± 0.11 mm/y		
					80 g/L C ₆ H ₈ O ₇ ⁸ , 60s	* Ra = 0.34 μm	CR ³ = 0.72 ± 0.07 mm/y		
	AZ31	Hydrogen	5 wt.% NaCl	~48 h	20% CH ₃ COOH ⁶ , 30 s		* CR ³ = 0.70 mg cm ⁻² d ⁻¹	[95]	
					50% H ₃ PO ₄ ⁵ , 30 s	-	* CR ³ = 1.58 mg cm ⁻² d ⁻¹		
					3.3% HNO ₃ ⁴ , 20 s		* CR ³ = 4.59 mg cm ⁻² d ⁻¹		
					12% HF ⁹ , 1200 s		* CR ³ = 1.68 mg cm ⁻² d ⁻¹		
AZ31	Foil	Immersion	5 wt.% NaCl	24 h	HT ¹⁰ + 10 % H ₂ SO ₄ ² , 20 s	Ra = 2.50 μm	0.97 mg/dcm ²	[38]	
					14 d			* CR ³ = 8.27 mg/d	[70]
					30 d				
Mg-5Gd	Disk	Mass loss	DMEM ¹² + 10% FBS ¹³ + P/S ¹⁴	30 d	150 g/L CH ₃ COOH ⁶ , 150 s	Sa = 6.3 μm	CR ³ = 0.31 μm/d	[57]	
					250 g/L CH ₃ COOH ⁶ , 150s	Sa = 5.6 μm	CR ³ = 0.30 μm/d		
					300 g/L CH ₃ COOH ⁶ , 90 s	Sa = 2.3 μm	CR ³ = 0.30 μm/d		

¹ SST: salt spray test; ² H₂SO₄: sulfuric acid; ³ CR: corrosion rate; ⁴ HNO₃: nitric acid; ⁵ H₃PO₄: phosphoric acid; ⁶ CH₃COOH: acetic acid; ⁷ C₂H₂O₄: oxalic acid; ⁸ C₆H₈O₇: citric acid; ⁹ HF: hydrofluoric acid; ¹⁰ HT: heat treated at 450 °C for 10 min (tempering); ¹¹ SBF: simulated body fluid; ¹² DMEM: Dulbecco's Modified Eagle's Medium; ¹³ FBS: fetal bovine serum; ¹⁴ P/S: Penicillin/Streptomycin.

Gray-Munro et al. [70] also tested acetic treatments on AZ31 alloy. Gray and Luan's study [68] described that a strong passive oxide layer was formed during the etching process when compared to the as-received state. Gray-Munro et al. [70] found that as-received samples have a greater non-uniform morphology in comparison with phosphoric acid etched samples. Phosphoric acid treated samples showed a lower degradation rate of 8.27 mg/d compared to non-etched samples (~31 mg/d). Additionally, the modified surface after etching improves adhesion and minimizes the porosity of coatings [70].

3.2. Coatings

Gray-Munro et al. [70] discovered that biomimetic calcium phosphate coatings (Ca/P) and polymer coatings after phosphoric etching led to a uniform morphology, which in turn led to a uniform degradation over the surface of the AZ31 alloy. The degradation rates of 6.17 mg/d (Table 4, Ref. [70]) for a polymer poly(L-lactic acid) (PLA) coating and of 3.83 mg/d for a poly (desaminotyrosyl tyrosine hexyl) (DTH) carbonate coating are compared to etched samples with rates of 8.27 mg/d (Table 3, Ref. [70]) (sample size: 1 mm thick foil, 10 mm × 20 mm). The degradation rate (7.27 mg/d) resulting from the Ca/P coated samples did not strongly differ from the only etched alloys [70]. However, the Ca/P-coated Mg alloy exhibited non-toxic and biocompatible properties. Ca/P enhanced the osseointegration and bioresorption of the alloy in a physical environment [112–116], which is why a Ca/P coating is more favorable compared to phosphoric etching.

Bakhsheshi-Rad et al. [104] performed potentiodynamic polarization (PDP) tests and immersion tests in SBF (Kokubo solution) on polished Mg-0.5Ca-6Zn samples with and without a coating. The coatings tested were a fluoride conversion coating, a dicalcium phosphate dihydrate/magnesium fluoride (DCPD/MgF₂) coating, and a nano-hydroxyapatite/magnesium fluoride (nano-HA/MgF₂) coating. A higher root mean square roughness (Rq) was measured for polished Mg-0.5Ca-6Zn samples with either a DCPD/MgF₂ coating (Rq = 395 nm) or a nano-HA/MgF₂ coating (Rq = 468 nm). The Rq for polished Mg-0.5Ca-6Zn (Rq = 210 nm) samples without coating and polished Mg-0.5Ca-6Zn samples with a fluoride coating (Rq = 280 nm) were somewhat lower. As seen in Table 4, Ref. [104], hydrogen evolution, i_{corr} and the degradation rate declined as the surface roughness increased, in contrast to studies of Walter and Kannan [96] and Mhaede et al. [102]. As shown in Table 4, Ref. [104], the degradation rate after coating compared to non-coated Mg alloy in Table 1, Ref. [104] is about a factor of 60 smaller, even though Rq only differs by 70 nm [104]. Thus, the protective coatings have a greater influence on corrosion than the Rq values.

Pompa et al. [103] investigated the morphology, surface roughness, cell viability, and degradation rate of ground and anodized AZ31B, AZ91E, and ZK60A alloys. Grinding was performed with a 1200 grit size grinding paper. Anodization was carried out using a mixture of alcohol and organic acid. The surface roughness increased dramatically from Sa = 29.76 nm to Sa = 204.81 nm after anodization for the AZ91E alloy. The anodization of AZ31B (Sa = 48.58 μm) and ZK60A (Sa = 78.30 μm) did not change the roughness significantly. It was shown that anodizing decreased the degradation rate compared to a ground surface. No correlation between surface roughness and degradation rate was found. This may be due to corrosion resistances being similar for all anodized surfaces despite their variation in roughness [103].

In the study of Chiu et al. [80], AZ31 plates were arc sprayed and hot pressed. Anodizing with oxalic acid was then performed [80]. The current density i_{corr} decreased after a combination of spraying and hot pressing or additional anodizing (Table 4, Ref. [80]) as compared to uncoated sandblasted samples (Table 2, Ref. [80]). Hot pressing decreased the surface roughness, which seems to improve the acid treatment afterwards. No correlation between roughness and degradation resistance was reported [80].

Table 4. Overview of different Coatings studies involving roughness and degradation behavior. * Values were determined from the diagram with the corresponding reference.

Alloy	Sample	Experiment	Solution	Time	Coatings	Initial Roughness	Results	Ref
Mg	Disk	pH	MEM ¹	2 h	Polished + NaOH	Ra = 0.23 µm	pH = 7.88	[74]
					Polished + M-SBF ²	Ra = 1.12 µm	pH = 8.96	
	Cell viability	MEM ¹ + FBS ³	24 h	Polished + NaOH	Ra = 0.23 µm	* CD ⁴ = 177 cells/mm ²		
				Polishing + M-SBF ²	Ra = 1.12 µm	* CD ⁴ = 838 cells/mm ²		
AZ31	Foil	Immersion	SBF ⁴	2 weeks	90% H ₃ PO ₄ ⁵ , 30 s + Ca/P		* CR ⁶ = 7.27 mg/d	[70]
					90% H ₃ PO ₄ ⁵ , 30 s + PLA ⁷	-	* CR ⁶ = 6.17 mg/d	
					90% H ₃ PO ₄ ⁵ , 30 s + poly (DTH ⁸ carbonate)		* CR ⁶ = 3.83 mg/d	
					P1000 Ground + DCPD ¹⁰	Ra = 4.29 µm	i _{corr} = 1.57 µA cm ⁻²	
disk	PDP ⁹	0.9 wt.% NaCl	PBS ¹²	-	SP ¹¹ 0.042 mmN + DCPD ¹⁰	Ra = 2.89 µm	i _{corr} = 20.03 µA cm ⁻²	[102]
					SP ¹¹ 0.140 mmN + DCPD ¹⁰	Ra = 3.25 µm	i _{corr} = 21.96 µA cm ⁻²	
					SP ¹¹ 0.262 mmN + DCPD ¹⁰	Ra = 5.07 µm	i _{corr} = 38.12 µA cm ⁻²	
					1200 grit + anodizing	Sa = 49.0 ± 10.2 nm	i _{corr} = 2.72 ± 0.8 µA cm ⁻² CR ⁶ = 0.06 ± 0.01 mm/y	
Plate	PDP ⁹	3.5 wt.%	MEM ¹ alpha modification Media	21 d	1200 grit + anodizing	Sa = 49.0 ± 10.2 nm	* Cell survival: 67 %	[80]
					SB ¹³ + Al ASC ¹⁴	Ra = 11.6 µm	i _{corr} = 2.4 × 10 ⁻² µA cm ⁻²	
					SB ¹³ + Al ASC ¹⁴ + PHP ¹⁵ (800 MPa)	Ra = 4.89 µm	-	
					SB ¹³ + Al ASC ¹⁴ + PHP ¹⁵ (1600 MPa)	-	i _{corr} = 0.8 µA cm ⁻²	
					SB ¹³ + Al ASC ¹⁴ + PHP ¹⁵ (2000 MPa)	Ra = 1.12 µm	-	
					SB ¹³ + Al ASC ¹⁴ + PHP ¹⁵ + 7 wt.% oxalic acid anodizing	-	i _{corr} = 3.7 × 10 ⁻² µA cm ⁻²	

Table 4. Cont.

Alloy	Sample	Experiment	Solution	Time	Coatings	Initial Roughness	Results	Ref
AZ91	Plate	PDP ⁹	3.5 wt.% NaCl	-	PEO ¹⁶ without K ₄ P ₂ O ₇		$i_{\text{corr}} = 19.6 \mu\text{A cm}^{-2}$	[73]
					PEO ¹⁶ + 0.03 mol/L K ₄ P ₂ O ₇	-	$i_{\text{corr}} = 1.22 \times 10^{-2} \mu\text{A cm}^{-2}$	
					PEO ¹⁶ + 0.06 mol/L K ₄ P ₂ O ₇		$i_{\text{corr}} = 2.27 \mu\text{A cm}^{-2}$	
					PEO ¹⁶ + 0.15 mol/L K ₄ P ₂ O ₇		$i_{\text{corr}} = 4.77 \mu\text{A cm}^{-2}$	
Plate	PDP ⁹	3.5 wt.% NaCl	-	Polishing 0.5 $\mu\text{m Al}_2\text{O}_3$ + PEO ¹⁶	Ra = 0.5 μm	$i_{\text{corr}} = 7.26 \times 10^{-3} \mu\text{A cm}^{-2}$	[81]	
				1000 grit + PEO ¹⁶	Ra = 1.0 μm	$i_{\text{corr}} = 5.17 \times 10^{-2} \mu\text{A cm}^{-2}$		
				100 grit + PEO ¹⁶	Ra = 2.5 μm	$i_{\text{corr}} = 0.38 \mu\text{A cm}^{-2}$		
Plate				1000 grit + PEO ¹⁶ without KF ¹⁷		$R_p = 8.28 \times 10^3 \text{ m}\Omega\text{cm}^2$	[79]	
				1000 grit + PEO + KF ¹⁷		$R_p = 4.67 \times 10^3 \text{ m}\Omega\text{cm}^2$		
disk		PDP ⁹ (1 cm ²)	PBS ¹²	-	1200 grit + anodized	Sa = 204.8 \pm 62.7 nm	$i_{\text{corr}} = 2.50 \pm 0.5 \mu\text{A cm}^{-2}$	[103]
					1200 grit + anodized	Sa = 204.8 \pm 62.7 nm	* Cell survival: 102 %	
disk		PDP ⁹ (1 cm ²)	PBS ¹²	-	1200 grit + anodizing	Sa = 75.88 \pm 34.49 nm	$i_{\text{corr}} = 1.86 \pm 0.2 \mu\text{A cm}^{-2}$	[103]
					1200 grit + anodizing	Sa = 75.88 \pm 34.49 nm	* Cell survival: 30 %	
Mg-0.5Ca-6Zn	Rectangular prism	PDP ⁹ (1 cm ²)	Kokubo	-	2000 grit + DCPD ¹⁰ /MgF ₂	Rq = 395 nm	$i_{\text{corr}} = 5.72 \mu\text{A cm}^{-2}$	[104]
					2000 grit + HA/MgF ₂	Rq = 468 nm	$i_{\text{corr}} = 5.23 \mu\text{A cm}^{-2}$	
					2000 grit + 40% HF ¹⁸	Rq = 280 nm	$i_{\text{corr}} = 6.20 \mu\text{A cm}^{-2}$	
					2000 grit + DCPD ¹⁰ /MgF ₂	Rq = 395 nm	$i_{\text{corr}} = 5.23 \mu\text{A cm}^{-2}$	
Hydrogen			Kokubo	240 h	2000 grit + nano-(HA ¹⁹ /MgF ₂)	Rq = 468 nm	CR ⁶ = 0.14 mm/y	
					2000 grit + 40% HF ¹⁸	Rq = 280 nm	CR ⁶ = 0.14 mm/y	
					2000 grit + DCPD ¹⁰ /MgF ₂	Rq = 395 nm	CR ⁶ = 0.13 mm/y	

¹ MEM: Minimum Essential Media; ² M-SBF: modified simulated body fluid; ³ FBS: fetal bovine serum; ⁴ CD: Cell density; ⁵ H₃PO₄: phosphoric acid; ⁶ CR: corrosion rate; ⁷ PLA: polymer poly(L-lactic acid); ⁸ DTH: desaminotyrosyl tyrosine hexyl; ⁹ PDP: potentiodynamic polarization; ¹⁰ DCPD: dicalcium phosphate dihydrate; ¹¹ SP: Shot peening; ¹² PBS: phosphate buffered saline; ¹³ SB: Sand blasting; ¹⁴ ASC:arc-spray coating; ¹⁵ PHP: post hot pressing; ¹⁶ PEO: plasma electrolytic oxidation; ¹⁷ KF: potassium fluoride; ¹⁸ HF: hydrofluoric acid; ¹⁹ HA: hydroxyapatite.

Yoo et al. [81] studied the effect of roughness on the degradation resistance of a plasma electrolytic oxidation (PEO) layer on a AZ91 alloy. Surfaces with various Ra were prepared by grinding and polishing. Afterwards, all samples were coated using the same PEO process. Due to the differing roughness values of the ground and polished surfaces, the coating differentiated in pore size as well. This affects the degradation process. The current density increased with higher initial Ra (Table 4, Ref. [81]). A salt spray test also showed that the amount of pitting increased with higher Ra after 120 h, which indicates that the surface roughness before PEO indirectly influences the degradation resistance [81].

Cho et al. [73] compared the degradation resistance of PEO coatings on AZ91 alloy for different amounts of potassium pyrophosphate in the electrolyte. The size of the pores increased as the amount of potassium pyrophosphate was increased. It was also reported that the surface roughness increased with increasing pore size. There was a trend between pore size, surface roughness, and i_{corr} for additions of potassium pyrophosphate (Table 4, Ref. [73]). The PEO coating for the potassium pyrophosphate-free electrolyte exhibited the lowest degradation resistance compared to the rougher coatings [73].

In contrast to Cho et al. [73], Hwang et al. [79] compared PEO coatings on AZ91 alloy with and without potassium fluoride in the electrolyte. In addition to varying the surface roughness, the evolution of the degradation resistance with coating time was also examined. The surface roughness increased for longer coating times. The roughness of the coated samples, after dipping in the potassium fluoride containing electrolyte, was higher compared to coatings dipped into potassium fluoride free electrolyte. The roughness increases due to pore size enlargement as reported by Cho et al. [73]. The degradation resistance of the coatings when exposed to potassium fluoride-containing electrolyte was higher than for potassium fluoride-free electrolyte. Hwang et al. [79] explained that the oxide thickness is the reason for the improved degradation resistance, and did not assess the influence of roughness on the degradation resistance, as investigated in Hwang et al. [82]. The effect of the PEO coating roughness on the degradation behavior was examined in Hwang et al. [82] with PDP and three different coating surface roughness Ra values. The surface roughness increased with increased pore size, as was also seen in Hwang et al. [79] and by Cho et al. [73].

3.3. Ion Implantation

Jamesh et al. [105] implanted Si ions from a plasma on polished WE43 plates. Atomic force microscope (AFM) measurements after polishing and Si implantation showed that the surface became smoother after the ion implantation process. The smoother Si-implanted surfaces had improved degradation resistance. However, the roughness did not vary enough between the polished and Si-implanted surface types to obtain a correlation between roughness and degradation [105].

Zhao et al. [88] reported a slower degradation rate for Mg-Ca and Mg-Sr alloys after ion implantation (Zr and O ions) onto their surfaces. After the surfaces were implanted, measurements determined that the surfaces were uniformly rough. The roughness increased after implantation for both alloys (compare Tables 1 and 5, Ref. [88]). The current density i_{corr} decreased for surfaces with higher roughness, and the cell adherence and proliferation improved [88].

Table 5. Summary of different studies concerning the influence of ion implantation on the degradation behavior. * Values were determined from the diagram with the corresponding reference.

Alloy	Sample	Experiment	Solution	Time	Implantation	Initial Roughness	Results	Ref
WE43	Plate	PDP ¹	SBF ²	-	Polishing: 1 μm + Si ion plasma	-	$i_{\text{corr}} = 27 \pm 32 \mu\text{A cm}^{-2}$	[105]
		Mass loss	SBF ²	3 d	1200 grit + Zr 1200 grit + ZrO	Sa = 5.34 nm Sa = 9.42 nm	* 8.03 mg * 6.77 mg	
Mg-1.0Ca	Rectangular prism	Cell viability	Extract assay (DMEM ³)	24 h + 72 h + 4 h	1200 grit + Zr 1200 grit + ZrO	Sa = 5.34 nm Sa = 9.42 nm	* 101 % * 103 %	[88]
		EIS ⁴ ($10 \times 10 \text{ mm}^2$)	SBF ²	-	1200 grit + Zr 1200 grit + ZrO	Sa = 5.34 nm Sa = 9.42 nm	$i_{\text{corr}} = 1.2 \times 10^2 \mu\text{A cm}^{-2}$ $i_{\text{corr}} = 2.6 \times 10^1 \mu\text{A cm}^{-2}$	
		Mass loss	SBF ²	3 d	1200 grit + Zr 1200 grit + ZrO	Sa = 4.61 nm Sa = 7.29 nm	* 13.7 mg * 8.52 mg	
		Cell viability	Extract assay (DMEM ³)	24 h + 72 h + 4 h	1200 grit + Zr 1200 grit + ZrO	Sa = 4.61 nm Sa = 7.29 nm	* 110 % * 126 %	[88]
Mg-0.5Sr	Rectangular prism	EIS ⁴ ($10 \times 10 \text{ mm}^2$)	SBF ²	-	1200 grit + Zr 1200 grit + ZrO	Sa = 4.61 nm Sa = 7.29 nm	$i_{\text{corr}} = 2.5 \times 10^2 \mu\text{A cm}^{-2}$ $i_{\text{corr}} = 1.7 \times 10^2 \mu\text{A cm}^{-2}$	

¹ PDP: potentiodynamic polarization; ² SBF: simulated body fluid; ³ DMEM: Dulbecco's Modified Eagle's Medium; ⁴ EIS: Electrochemical Impedance Spectroscopy

4. Summary of the Influence of Roughness on Degradation

4.1. Mechanical Surface Treatments

Using grinding papers with higher grit size and/or polishing reduced surface roughness and reduced pitting during the degradation tests [71,96]. These results differ from those in studies by Alvarez et al. [94], where polished samples encouraged pitting compared to semi polished surfaces [94]. Some papers reported that roughness affects cell adherence to the surface [21,74]. However, one study showed that cell adherence was not influenced by surface roughness [61]. Some studies showed that roughness did not affect degradation [39,102,108,111]. In contrast, it was demonstrated that a linear relationship existed between roughness and degradation if the surface treatments were comparable (Figures 1 and 2) [72,96,102].

4.2. Chemical Surface Treatments and Coatings

Some studies investigated the correlation between etched AZ31 alloy samples and degradation behavior [38,40,56,70,80,95,103]. In studies by Chiu et al. [80], Supplit et al. [95], Nwaogu et al. [40,56], and Gray Munro et al. [70], it was found that acetic, nitric, and phosphoric acid surface treatment improved the degradation resistance. In a report by Song and Xu [38], sulfuric acid was shown to enhance degradation, contrasting the study by Nwaogu et al. [56]. The roughness after etching was not reported to affect degradation. Etching had positive effects on the surface as it removed contamination and manufacturing marks, resulting in a homogenous morphology [38,40,56,70]. Ca/P- and polymer coatings also led to a more uniform morphology which improved the overall degradation resistance compared to as-received samples [70]. Further investigations of the correlation between coatings and degradation behavior were performed by Yoo et al. [81], Cho et al. [73], and Hwang et al. [79,82]. They studied the influence of PEO on AZ91. They found that a PEO coating increased the surface roughness. In all reports except for that of Yoo et al. [81], the rougher surface resulted in a greater degradation resistance. Guo and An [78] reported, as did as Yoo et al. [81], Cho et al. [73], Hwang et al. [79,82], and Duan et al. [117], that coatings affect the surface roughness. Additionally, ion implantation is one technique that can be used to smooth the surface and increase the degradation resistance [105]. However, Zhao et al. [88] determined that the degradation rate slowed as the roughness increased after ion implantation.

5. Discussion

5.1. Suitable Roughness Values for Biodegradable Mg Implants

Nguyen et al. [72] investigated the influence of roughness on i_{CORR} after 6 hours degradation in HBSS (Hank's Balanced Salt Solution) of pure Mg with indirect solid free form fabrication (SFF). After SFF, no postprocessing is necessary, which enables the production of different degrees of surface roughness with the same surface properties. They avoided the influence of different alloy compositions and surface treatments. It was shown that an increase in R_a led to an increase in i_{CORR} and mass loss (Table 2, Ref. [72] and Figure 3a). Some reports concerning surface treatments established that there was no direct influence from the roughness on the degradation behavior. The roughness values from these reports are described using two-dimensional values such as R_a , R_q , and R_z , or three-dimensional parameters like S_a , which cannot be compared directly. The difference between macro-roughness and micro-roughness is also not defined. Macro roughness describes the height distribution which comes from a production process like sawing. As such, the macro-roughness of the sample is not going to influence the degradation process in the same way as micro-roughness. Macro-roughness is accompanied by the subsurface stress that results from production and machining, and which has also been reported to affect degradation [38]. Rougher surfaces influenced the pore enlargement of PEO coatings (Figure 3a) which indirectly controls the degradation rate [81].

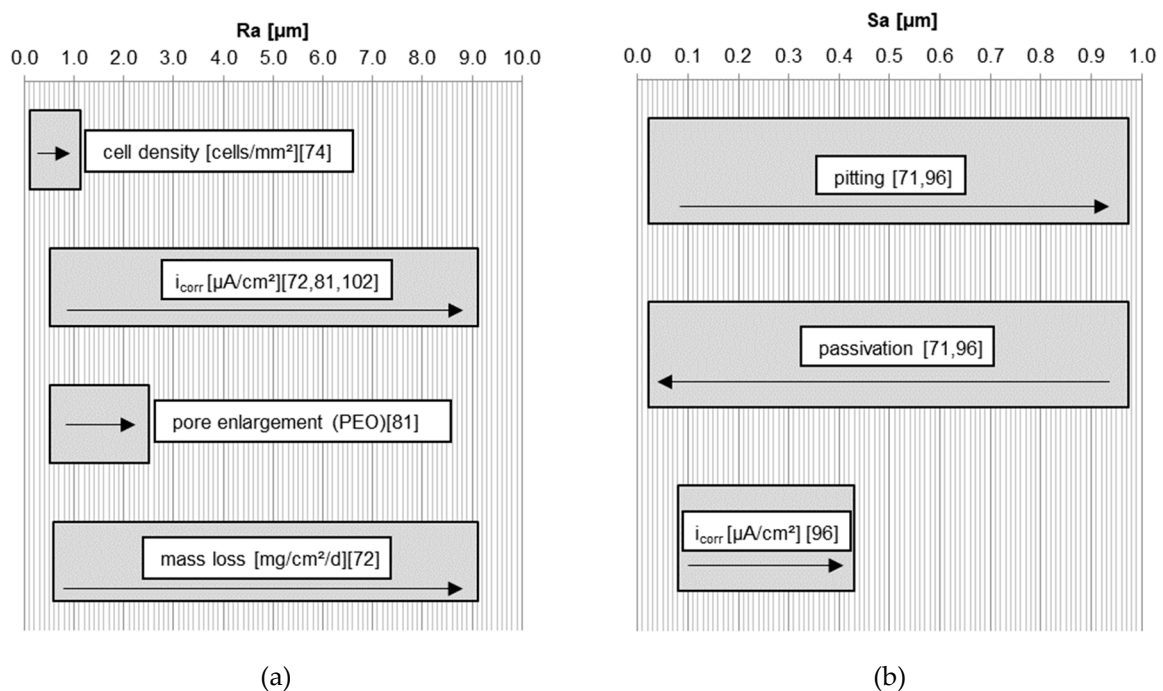


Figure 3. Trend of properties: (a) in relation to roughness Ra. The arrow shows the change of properties depending on the roughness according to [72,74,81,102]; (b) in relation to roughness Sa. The arrow shows the change of properties depending on the roughness according to [71,96].

There was also a trend of increasing current density when using different grinding papers as seen by Walter and Kannan [96] (Figures 1 and 3b) and using different Almen intensities during shot peening (Figure 2, Figures 1 and 3a) [96,102]. In general, higher roughness diminishes the passivation layer and raises the probability of pitting (Figure 3b). Initial pitting effects are only noticeable within the first six hours [71]. As such, it is suggested that roughness has no long-term effects on the degradation as the morphology changes during immersion in aqueous solutions. However, roughness can influence the initial degradation due to greater peak-to-valley height differences, which results in a higher anodizing surface area [102] with a lower pH solution inside the valleys [71]. This roughness effect fades after a short time as the higher surface peaks are eroded away. A more rapid degradation accelerates this process. Even if roughness has a noticeable effect at the start of degradation, as the surface flattens with time it will quickly become insignificant, as seen in the long-term experiments of Gawlik et al. [57]. A correlation of higher cell adherence with higher roughness for pure Mg was reported in [74] (Figure 3a). Cell toxicity and cell adherence have been mainly tested for Sa and Ra values around 1 μm and below. Some reports about osseointegration showed that the connection between dental implants and bone improves when using implants with rougher surfaces introduced by surface modifications [84,118]. One study reported that a roughness between 1–2 μm led to the best connection between a permanent Ti dental implant and bone [119]. Höh et al. [93] could not confirm a trend relating higher roughness to greater bone implant connectivity for biodegradable Mg-0.8Ca alloys. However, in vivo experiments in rabbits showed that sandblasted cylinders with a higher magnitude of roughness ($R_a = 32.7 \mu\text{m}$) led to strong gas evolution and material decomposition [93]. Mechanical integrity cannot be obtained if the initial degradation is too rapid. Significant hydrogen evolution hinders cell adherence and thus the formation of a good bond between the bone and implant. The required roughness for cell adherence depends on the kind of cells and the necessity of cell adherence. Stronger cell adherence resulting from higher roughness is needed for osseointegration for example, whereas smoother surfaces are preferred in stent applications where cell adhesion is less important. The influence of roughness on the degradation and cell adherence in in vitro and in vivo experiments is not possible either, due to different experimental set-ups and durations. The difficulty

in comparing data of in vitro and in vivo testing is reviewed by Sanchez et al. [120]. From all of these studies, depending on the application, roughness values above Sa or Ra = 0.2 μm are suggested for Mg implants in relation to cell adherence, cell density, and cell survival. Generally, most surface roughness in the studies were in the nm range. Some of the roughness values investigated in the reviewed studies were within the range of 1–2 μm [38,56,71,74,102], or had roughness values below 10 μm [38,71,72,74,81,93,96]. Greatly higher roughness values should be avoided, due to strong initial degradation and gas evolution.

5.2. Suitable Treatments for Biodegradable Mg Implants

Etching is a chemical surface treatment which is highly suitable for biodegradable Mg implants. Depending on the etching solution and the alloy used, chemical etching can vary the surface properties of the alloy. Thus, it is possible to tailor the surface roughness depending on the etching conditions. Even a minor increase in roughness (nm) showed an influence on cell adhesion [74]. Smoother surfaces were also reported to minimize the porosity of coatings. A smaller pore size in a PEO coating decreases the degradation resistance [81]. As such, etching can be used as a pre-treatment for additional coatings or as a surface modification. In addition, etched material is reported to form a stronger passivation layer compared to non-etched material, thus slowing the degradation rate [70]. Etching enables a uniform treatment over the entire surface. It can possibly be used to homogenize the surface, change the surface roughness and morphology, and remove near surface material including contamination and impurities [38,40,56]. It is suspected that it increases the degradation resistance for specific implants such as stents, rods, tubes, and screws; this is very advantageous, as it is not possible to use mechanical surface treatments such as grinding, polishing, and burnishing on these geometries.

6. Conclusions

In general, this review shows that it is difficult to make reliable and clear comparisons between different studies, because several parameters and mechanisms influence the degradation behavior. One of these parameters is the amount and distribution of impurities, a factor that was not assessed in all of the investigations, although it is of critical importance. However, from this review, some rough rules can be derived:

- Considering different roughness values arising from the same type of surface treatment, especially mechanical surface treatments, a trend of increased degradation rate can be seen with higher surface roughness.
- Roughness values arising from different surface treatments are non-comparable, and thus, cannot be compared against a degradation result.
- The roughness of a Mg implant is thought to have a greater influence on initial degradation, compared to long-term degradation. The duration for implant acceptance by the body is negligibly affected by the implant's surface roughness.
- Implant surfaces with roughness values above Sa or Ra = 0.2 μm are unsuitable for initial cell adherence and cell viability. Higher roughness should be avoided, as increased degradation is expected, and consequently, greater local alkalization will occur.
- Ca/P coatings lead to a uniform surface morphology which results in a more uniform degradation over the surface, and decreases the degradation rate compared to uncoated material. Ca/P coated Mg alloys exhibited non-toxic and biocompatible properties.
- Differences in surface roughness and additions of $\text{K}_4\text{P}_2\text{O}_7$ or KF into the electrolyte varied the pore size of PEO coatings, which, in turn, affected the degradation rate of implant materials. A smaller pore size of the PEO coating resulted in higher degradation.
- Acid etching provides a treatment over the entire surface, removing contamination and impurities by removing surface material. In particular, acetic acid and phosphoric acid etching improved the

degradation behavior, i.e., by reducing the degradation rate. Etching allows the surface properties to be tailored in order to adjust the initial and long-term degradation.

Author Contributions: Conceptualization, M.M.G.; Data Curation, M.M.G., V.D., B.W.; Writing—Original Draft Preparation, M.M.G.; Writing—Review and Editing, M.M.G., V.D., B.W., T.E., R.W.R.; Visualization, M.M.G., V.D., B.W.; Supervision, B.W., T.E., R.W.-R.

Funding: This research was funded by the Helmholtz Virtual Institute VH-VI-523 (In vivo studies of biodegradable magnesium-based implant materials).

Conflicts of Interest: The authors declare no conflict of interest. The funders had no role in the design of the study; in the collection, analyses, or interpretation of data; in the writing of the manuscript, or in the decision to publish the results.

References

1. Kraus, T.; Fischerauer, S.; Treichler, S.; Martinelli, E.; Eichler, J.; Myrissa, A.; Zötsch, S.; Uggowitzer, P.J.; Löffler, J.F.; Weinberg, A.M. The influence of biodegradable magnesium implants on the growth plate. *Acta Biomater.* **2018**, *66*, 109–117. [[CrossRef](#)] [[PubMed](#)]
2. Li, G.; Zhang, L.; Wang, L.; Yuan, G.; Dai, K.; Pei, J.; Hao, Y. Dual modulation of bone formation and resorption with zoledronic acid-loaded biodegradable magnesium alloy implants improves osteoporotic fracture healing: An in vitro and in vivo study. *Acta Biomater.* **2018**, *65*, 486–500. [[CrossRef](#)] [[PubMed](#)]
3. Rahim, M.; Ullah, S.; Mueller, P. Advances and Challenges of Biodegradable Implant Materials with a Focus on Magnesium-Alloys and Bacterial Infections. *Metals* **2018**, *8*, 532. [[CrossRef](#)]
4. Choo, J.T.; Lai, S.H.S.; Tang, C.Q.Y.; Thevendran, G. Magnesium-based bioabsorbable screw fixation for hallux valgus surgery—A suitable alternative to metallic implants. *Foot Ankle Surg.* **2018**. [[CrossRef](#)] [[PubMed](#)]
5. Höhn, S.; Virtanen, S.; Boccaccini, A.R. Protein adsorption on magnesium and its alloys: A review. *Appl. Surf. Sci.* **2019**, *464*, 212–219. [[CrossRef](#)]
6. Zhao, N.; Zhu, D. Collagen Self-Assembly on Orthopedic Magnesium Biomaterials Surface and Subsequent Bone Cell Attachment. *PLoS ONE* **2014**, *9*, e110420. [[CrossRef](#)] [[PubMed](#)]
7. Zeng, R.; Dietzel, W.; Witte, F.; Hort, N.; Blawert, C. Progress and Challenge for Magnesium Alloys as Biomaterials. *Adv. Eng. Mater.* **2008**, *10*, B3–B14. [[CrossRef](#)]
8. Vormann, J. Magnesium: nutrition and metabolism. *Mol. Aspects Med.* **2003**, *24*, 27–37. [[CrossRef](#)]
9. Song, G. Control of biodegradation of biocompatible magnesium alloys. *Corros. Sci.* **2007**, *49*, 1696–1701. [[CrossRef](#)]
10. Echeverry-Rendon, M.; Duque, V.; Quintero, D.; Robledo, S.M.; Harmsen, M.C.; Echeverria, F. Improved corrosion resistance of commercially pure magnesium after its modification by plasma electrolytic oxidation with organic additives. *J. Biomater. Appl.* **2018**, *33*, 725–740. [[CrossRef](#)]
11. Gao, Y.; Wang, L.; Li, L.; Gu, X.; Zhang, K.; Xia, J.; Fan, Y. Effect of stress on corrosion of high-purity magnesium in vitro and in vivo. *Acta Biomater.* **2018**, *83*, 477–486. [[CrossRef](#)] [[PubMed](#)]
12. Gu, X.-N.; Li, S.-S.; Li, X.-M.; Fan, Y.-B. Magnesium based degradable biomaterials: A review. *Front. Mater. Sci.* **2014**, *8*, 200–218. [[CrossRef](#)]
13. Castellani, C.; Lindtner, R.A.; Hausbrandt, P.; Tschegg, E.; Stanzl-Tschegg, S.E.; Zanoni, G.; Beck, S.; Weinberg, A.-M. Bone-implant interface strength and osseointegration: Biodegradable magnesium alloy versus standard titanium control. *Acta Biomater.* **2011**, *7*, 432–440. [[CrossRef](#)] [[PubMed](#)]
14. Li, Z.; Gu, X.; Lou, S.; Zheng, Y. The development of binary Mg-Ca alloys for use as biodegradable materials within bone. *Biomaterials* **2008**, *29*, 1329–1344. [[CrossRef](#)] [[PubMed](#)]
15. Ma, J.; Zhao, N.; Betts, L.; Zhu, D. Bio-Adaption between Magnesium Alloy Stent and the Blood Vessel: A Review. *J. Mater. Sci. Tech.* **2016**, *32*, 815–826. [[CrossRef](#)]
16. Song, G.; Song, S. A Possible Biodegradable Magnesium Implant Material. *Adv. Eng. Mater.* **2007**, *9*, 298–302. [[CrossRef](#)]
17. Lu, Y.; Huang, Y.; Feyerabend, F.; Willumeit-Römer, R.; Kainer, K.U.; Hort, N. Microstructure and Mechanical Properties of Mg-Gd Alloys as Biodegradable Implant Materials. In *TMS 2018 147th Annual Meeting & Exhibition Supplemental Proceedings*; Materials Society, T.M., Ed.; Springer International Publishing: Cham, Switzerland, 2018; ISBN 978-3-319-72525-3.

18. Li, P.; Zhou, N.; Qiu, H.; Maitz, M.F.; Wang, J.; Huang, N. In vitro and in vivo cytocompatibility evaluation of biodegradable magnesium-based stents: A review. *Sci. Chin. Mater.* **2018**, *61*, 501–515. [[CrossRef](#)]
19. Kim, B.J.; Piao, Y.; Wufuer, M.; Son, W.-C.; Choi, T.H. Biocompatibility and Efficiency of Biodegradable Magnesium-Based Plates and Screws in the Facial Fracture Model of Beagles. *J. Oral Maxillofac. Surg.* **2018**, *76*, 1055. [[CrossRef](#)]
20. Ferrando, W.A. Review of corrosion and corrosion control of magnesium alloys and composites. *J. Mater. Eng.* **1989**, *11*, 299–313. [[CrossRef](#)]
21. Johnson, I.; Perchy, D.; Liu, H. In vitro evaluation of the surface effects on magnesium-yttrium alloy degradation and mesenchymal stem cell adhesion. *J. Biomed. Mater. Res. Part A* **2012**, *100*, 477–485. [[CrossRef](#)]
22. Xin, Y.; Liu, C.; Zhang, X.; Tang, G.; Tian, X.; Chu, P.K. Corrosion behavior of biomedical AZ91 magnesium alloy in simulated body fluids. *J. Mater. Res.* **2007**, *22*, 2004–2011. [[CrossRef](#)]
23. Ghali, E. Corrosion and Protection of Magnesium Alloys. *Mater. Sci. Forum* **2000**, *350–351*, 261–272. [[CrossRef](#)]
24. Makar, G.L.; Kruger, J. Corrosion of magnesium. *Int. Mater. Rev.* **1993**, *38*, 138–153. [[CrossRef](#)]
25. Song, G.; Atrens, A.; Stjohn, D.; Nairn, J.; Li, Y. The electrochemical corrosion of pure magnesium in 1 N NaCl. *Corros. Sci.* **1997**, *39*, 855–875. [[CrossRef](#)]
26. *Corrosion*; ASM International; Korb, L.J. (Eds.) ASM handbook; [10. ed.], 7. print; ASM International: Materials Park, OH, USA, 2001; ISBN 978-0-87170-019-3.
27. Hu, H.; Nie, X.; Ma, Y. Corrosion and Surface Treatment of Magnesium Alloys. In *Magnesium Alloys—Properties in Solid and Liquid States*; Czerwinski, F., Ed.; Intech Open: London, UK, 2014; ISBN 978-953-51-1728-5.
28. Baboian, R.; Dean, S.; Hack, H.; Haynes, G.; Scully, J.; Sprowls, D. *Corrosion Tests and Standards: Application and Interpretation*; ASTM Manual Series: Philadelphia, PA, USA, 1995.
29. Song, G.L.; Atrens, A. Corrosion Mechanisms of Magnesium Alloys. *Adv. Eng. Mater.* **1999**, *1*, 11–33. [[CrossRef](#)]
30. Iglesias, C.; Bodelón, O.G.; Montoya, R.; Clemente, C.; Garcia-Alonso, M.C.; Rubio, J.C.; Escudero, M.L. Fracture bone healing and biodegradation of AZ31 implant in rats. *Biomed. Mater.* **2015**, *10*, 025008. [[CrossRef](#)]
31. Shalabi, M.M.; Gortemaker, A.; Hof, M.A.V.; Jansen, J.A.; Creugers, N.H.J. Implant Surface Roughness and Bone Healing: a Systematic Review. *J. Dent. Res.* **2006**, *85*, 496–500. [[CrossRef](#)]
32. Wang, J.; Tang, J.; Zhang, P.; Li, Y.; Wang, J.; Lai, Y.; Qin, L. Surface modification of magnesium alloys developed for bioabsorbable orthopedic implants: A general review. *J. Biomed. Mater. Res. B Appl. Biomater.* **2012**, *100*, 1691–1701. [[CrossRef](#)]
33. Kaesel, V.; Tai, P.-T.; Bach, F.-W.; Haferkamp, H.; Witte, F.; Windhagen, H. Approach to Control the Corrosion of Magnesium by Alloying. In *Magnesium*; Kainer, K.U., Ed.; Wiley-VCH Verlag GmbH & Co. KGaA: Weinheim, Germany, 2005; pp. 534–539. ISBN 978-3-527-60356-5.
34. Yun, Y.; Dong, Z.; Lee, N.; Liu, Y.; Xue, D.; Guo, X.; Kuhlmann, J.; Doepke, A.; Halsall, H.B.; Heineman, W.; et al. Revolutionizing biodegradable metals. *Mater. Today* **2009**, *12*, 22–32. [[CrossRef](#)]
35. Bland, L.G.; Gusieva, K.; Scully, J.R. Effect of Crystallographic Orientation on the Corrosion of Magnesium: Comparison of Film Forming and Bare Crystal Facets using Electrochemical Impedance and Raman Spectroscopy. *Electrochim. Acta* **2017**, *227*, 136–151. [[CrossRef](#)]
36. Zhao, Y.-C.; Huang, G.-S.; Wang, G.-G.; Han, T.-Z.; Pan, F.-S. Influence of Grain Orientation on the Corrosion Behavior of Rolled AZ31 Magnesium Alloy. *Acta Metall. Sin.* **2015**, *28*, 1387–1393. [[CrossRef](#)]
37. Liu, M.; Qiu, D.; Zhao, M.-C.; Song, G.; Atrens, A. The effect of crystallographic orientation on the active corrosion of pure magnesium. *Scr. Mater.* **2008**, *58*, 421–424. [[CrossRef](#)]
38. Song, G.-L.; Xu, Z. The surface, microstructure and corrosion of magnesium alloy AZ31 sheet. *Electrochim. Acta* **2010**, *55*, 4148–4161. [[CrossRef](#)]
39. Pu, Z.; Song, G.-L.; Yang, S.; Outeiro, J.C.; Dillon, O.W.; Puleo, D.A.; Jawahir, I.S. Grain refined and basal textured surface produced by burnishing for improved corrosion performance of AZ31B Mg alloy. *Corros. Sci.* **2012**, *57*, 192–201. [[CrossRef](#)]
40. Nwaogu, U.C.; Blawert, C.; Scharnagl, N.; Dietzel, W.; Kainer, K.U. Effects of organic acid pickling on the corrosion resistance of magnesium alloy AZ31 sheet. *Corros. Sci.* **2010**, *52*, 2143–2154. [[CrossRef](#)]

41. Aung, N.N.; Zhou, W. Effect of grain size and twins on corrosion behaviour of AZ31B magnesium alloy. *Corros. Sci.* **2010**, *52*, 589–594. [[CrossRef](#)]
42. Pardo, A.; Merino, M.C.; Coy, A.E.; Arrabal, R.; Viejo, F.; Matykina, E. Corrosion behaviour of magnesium/aluminium alloys in 3.5 wt.% NaCl. *Corros. Sci.* **2008**, *50*, 823–834. [[CrossRef](#)]
43. Ambat, R.; Aung, N.N.; Zhou, W. Evaluation of microstructural effects on corrosion behaviour of AZ91D magnesium alloy. *Corros. Sci.* **2000**, *42*, 1433–1455. [[CrossRef](#)]
44. Zheng, X.; Dong, J.; Xiang, Y.; Chang, J.; Wang, F.; Jin, L.; Wang, Y.; Ding, W. Formability, mechanical and corrosive properties of Mg-Nd-Zn-Zr magnesium alloy seamless tubes. *Mater. Des.* **2010**, *31*, 1417–1422. [[CrossRef](#)]
45. Liu, Z.; Schade, R.; Luthringer, B.; Hort, N.; Rothe, H.; Müller, S.; Liefeth, K.; Willumeit-Römer, R.; Feyerabend, F. Influence of the Microstructure and Silver Content on Degradation, Cytocompatibility, and Antibacterial Properties of Magnesium-Silver Alloys In Vitro. *Oxidat. Med. Cell. Longev.* **2017**, *2017*, 1–14. [[CrossRef](#)]
46. Stellwagen, E.; Babul, J. Stabilization of the globular structure of ferricytochrome c by chloride in acidic solvents. *Biochemistry* **1975**, *14*, 5135–5140. [[CrossRef](#)] [[PubMed](#)]
47. Jönsson, M.; Persson, D. The influence of the microstructure on the atmospheric corrosion behaviour of magnesium alloys AZ91D and AM50. *Corros. Sci.* **2010**, *52*, 1077–1085. [[CrossRef](#)]
48. Ben-Haroush, M.; Ben-Hamu, G.; Eliezer, D.; Wagner, L. The relation between microstructure and corrosion behavior of AZ80 Mg alloy following different extrusion temperatures. *Corros. Sci.* **2008**, *50*, 1766–1778. [[CrossRef](#)]
49. Ralston, K.D.; Birbilis, N. Effect of Grain Size on Corrosion: A Review. *Corrosion* **2010**, *66*, 075005. [[CrossRef](#)]
50. Liu, Y.; Liu, D.; You, C.; Chen, M. Effects of grain size on the corrosion resistance of pure magnesium by cooling rate-controlled solidification. *Front. Mater. Sci.* **2015**, *9*, 247–253. [[CrossRef](#)]
51. Lu, Y.; Bradshaw, A.R.; Chiu, Y.L.; Jones, I.P. Effects of secondary phase and grain size on the corrosion of biodegradable Mg-Zn-Ca alloys. *Mater. Sci. Eng. C* **2015**, *48*, 480–486. [[CrossRef](#)]
52. Kutniy, K.V.; Papirov, I.I.; Tikhonovsky, M.A.; Pikalov, A.I.; Sivtsov, S.V.; Pirozhenko, L.A.; Shokurov, V.S.; Shkuropatenko, V.A. Influence of grain size on mechanical and corrosion properties of magnesium alloy for medical implants. *Materialwiss. Werkstofftech.* **2009**, *40*, 242–246. [[CrossRef](#)]
53. Ullmann, B.; Reifenrath, J.; Seitz, J.-M.; Bormann, D.; Meyer-Lindenberg, A. Influence of the grain size on the in vivo degradation behaviour of the magnesium alloy LAE442. *Proc. Inst. Mech. Eng. H* **2013**, *227*, 317–326. [[CrossRef](#)]
54. Zeng, R.-C.; Chen, J.; Dietzel, W.; Zettler, R.; dos Santos, J.F.; Lucia Nascimento, M.; Kainer, K.U. Corrosion of friction stir welded magnesium alloy AM50. *Corros. Sci.* **2009**, *51*, 1738–1746. [[CrossRef](#)]
55. Zhang, T.; Li, Y.; Wang, F. Roles of β phase in the corrosion process of AZ91D magnesium alloy. *Corros. Sci.* **2006**, *48*, 1249–1264. [[CrossRef](#)]
56. Nwaogu, U.C.; Blawert, C.; Scharnagl, N.; Dietzel, W.; Kainer, K.U. Influence of inorganic acid pickling on the corrosion resistance of magnesium alloy AZ31 sheet. *Corros. Sci.* **2009**, *51*, 2544–2556. [[CrossRef](#)]
57. Gawlik, M.M.; Steiner, M.; Wiese, B.; González, J.; Feyerabend, F.; Dahms, M.; Ebel, T.; Willumeit-Römer, R. The Effects of HAc Etching on the Degradation Behavior of Mg-5Gd. *J. Med. Mater. Tech.* **2017**, *1*, 22–25.
58. Snir, Y.; Ben-Hamu, G.; Eliezer, D.; Abramov, E. Effect of compression deformation on the microstructure and corrosion behavior of magnesium alloys. *J. Alloys Compd.* **2012**, *528*, 84–90. [[CrossRef](#)]
59. Wang, B.J.; Xu, D.K.; Dong, J.H.; Ke, W. Effect of the crystallographic orientation and twinning on the corrosion resistance of an as-extruded Mg-3Al-1Zn (wt.%) bar. *Scr. Mater.* **2014**, *88*, 5–8. [[CrossRef](#)]
60. Zou, G.; Peng, Q.; Wang, Y.; Liu, B. The effect of extension twinning on the electrochemical corrosion properties of Mg-Y alloys. *J. Alloys Compd.* **2015**, *618*, 44–48. [[CrossRef](#)]
61. Liu, H. The effects of surface and biomolecules on magnesium degradation and mesenchymal stem cell adhesion. *J. Biomed. Mater. Res. Part A* **2011**, *99*, 249–260. [[CrossRef](#)]
62. Kieke, M.; Feyerabend, F.; Lemaitre, J.; Behrens, P.; Willumeit-Römer, R. Degradation rates and products of pure magnesium exposed to different aqueous media under physiological conditions. *BioNanoMaterials* **2016**, *17*, 131–143. [[CrossRef](#)]
63. Xin, Y.; Hu, T.; Chu, P.K. Influence of Test Solutions on In Vitro Studies of Biomedical Magnesium Alloys. *J. Electrochem. Soc.* **2010**, *157*, C238. [[CrossRef](#)]

64. Agha, N.A.; Feyerabend, F.; Mihailova, B.; Heidrich, S.; Bismayer, U.; Willumeit-Römer, R. Magnesium degradation influenced by buffering salts in concentrations typical of in vitro and in vivo models. *Mater. Sci. Eng. C* **2016**, *58*, 817–825. [[CrossRef](#)]
65. Uddin, M.S.; Hall, C.; Murphy, P. Surface treatments for controlling corrosion rate of biodegradable Mg and Mg-based alloy implants. *Sci. Tech. Adv. Mater.* **2015**, *16*, 053501. [[CrossRef](#)]
66. Yang, J.; Cui, F.; Lee, I.S. Surface Modifications of Magnesium Alloys for Biomedical Applications. *Ann. Biomed. Eng.* **2011**, *39*, 1857–1871. [[CrossRef](#)] [[PubMed](#)]
67. *Surface Modification of Magnesium and Its Alloys for Biomedical Applications*; Sankara Narayanan, T.S.N.; Park, I.-S.; Lee, M.-H. (Eds.) Woodhead Publishing series in biomaterials; Elsevier/Woodhead Publishing: Cambridge, UK; Waltham, MA, USA, 2015; ISBN 978-1-78242-077-4.
68. Gray, J.E.; Luan, B. Protective coatings on magnesium and its alloys—A critical review. *J. Alloys Compd.* **2002**, *336*, 88–113. [[CrossRef](#)]
69. Hornberger, H.; Virtanen, S.; Boccaccini, A.R. Biomedical coatings on magnesium alloys—A review. *Acta Biomater.* **2012**, *8*, 2442–2455. [[CrossRef](#)] [[PubMed](#)]
70. Gray-Munro, J.E.; Seguin, C.; Strong, M. Influence of surface modification on the in vitro corrosion rate of magnesium alloy AZ31. *J. Biomed. Mater. Res. Part A* **2009**, *91A*, 221–230. [[CrossRef](#)] [[PubMed](#)]
71. Walter, R.; Kannan, M.B.; He, Y.; Sandham, A. Effect of surface roughness on the in vitro degradation behaviour of a biodegradable magnesium-based alloy. *Appl. Surf. Sci.* **2013**, *279*, 343–348. [[CrossRef](#)]
72. Nguyen, T.L.; Blanquet, A.; Staiger, M.P.; Dias, G.J.; Woodfield, T.B.F. On the role of surface roughness in the corrosion of pure magnesium in vitro. *J. Biomed. Mater. Res. B Appl. Biomater.* **2012**, *100*, 1310–1318. [[CrossRef](#)]
73. Cho, J.-Y.; Hwang, D.-Y.; Lee, D.-H.; Yoo, B.; Shin, D.-H. Influence of potassium pyrophosphate in electrolyte on coated layer of AZ91 Mg alloy formed by plasma electrolytic oxidation. *Trans. Nonferr. Met. Soc. China* **2009**, *19*, 824–828. [[CrossRef](#)]
74. Lorenz, C.; Brunner, J.G.; Kollmannsberger, P.; Jaafar, L.; Fabry, B.; Virtanen, S. Effect of surface pre-treatments on biocompatibility of magnesium. *Acta Biomater.* **2009**, *5*, 2783–2789. [[CrossRef](#)]
75. Laycock, N.J.; Noh, J.S.; White, S.P.; Krouse, D.P. Computer simulation of pitting potential measurements. *Corros. Sci.* **2005**, *47*, 3140–3177. [[CrossRef](#)]
76. Burstein, G.T.; Vines, S.P. Repetitive Nucleation of Corrosion Pits on Stainless Steel and the Effects of Surface Roughness. *J. Electrochem. Soc.* **2001**, *148*, B504. [[CrossRef](#)]
77. Suter, T.; Müller, Y.; Schmutz, P.; von Trzebiatowski, O. Microelectrochemical Studies of Pit Initiation on High Purity and Ultra High Purity Aluminum. *Adv. Eng. Mater.* **2005**, *7*, 339–348. [[CrossRef](#)]
78. Guo, H.F.; An, M.Z. Growth of ceramic coatings on AZ91D magnesium alloys by micro-arc oxidation in aluminate–fluoride solutions and evaluation of corrosion resistance. *Appl. Surf. Sci.* **2005**, *246*, 229–238. [[CrossRef](#)]
79. Hwang, D.Y.; Kim, Y.M.; Shin, D.H. Corrosion Resistance of Plasma-Anodized AZ91 Mg Alloy in the Electrolyte with/without Potassium Fluoride. *Mater. Trans.* **2009**, *50*, 671–678. [[CrossRef](#)]
80. Chiu, L.-H.; Chen, C.-C.; Yang, C.-F. Improvement of corrosion properties in an aluminum-sprayed AZ31 magnesium alloy by a post-hot pressing and anodizing treatment. *Surf. Coat. Technol.* **2005**, *191*, 181–187. [[CrossRef](#)]
81. Yoo, B.; Shin, K.R.; Hwang, D.Y.; Lee, D.H.; Shin, D.H. Effect of surface roughness on leakage current and corrosion resistance of oxide layer on AZ91 Mg alloy prepared by plasma electrolytic oxidation. *Appl. Surf. Sci.* **2010**, *256*, 6667–6672. [[CrossRef](#)]
82. Hwang, D.K.; Yoo, B.Y.; Cho, J.Y.; Lee, D.H.; Shin, D.H. Effect of surface roughness on corrosion resistance of oxide layer on AZ91 Mg alloy prepared by plasma electrolytic oxidation. In Proceedings of the 214th ECS Meeting, Honolulu, HI, USA, 12–17 October 2008.
83. Burstein, G.T.; Pistorius, P.C. Surface Roughness and the Metastable Pitting of Stainless Steel in Chloride Solutions. *Corros. Sci.* **1995**, *51*, 380–385. [[CrossRef](#)]
84. Parekh, R.B.; Shetty, O.; Tabassum, R. Surface Modifications for Endosseous Dental Implants. *Int. J. Oral Implantol. Clin. Res.* **2012**, *3*, 116–121. [[CrossRef](#)]
85. Lacefield, W.R. Materials Characteristics of Uncoated/Ceramic-Coated Implant Materials. *Adv. Dent. Res.* **1999**, *13*, 21–26. [[CrossRef](#)]

86. Suzuki, K.; Aoki, K.; Ohya, K. Effects of surface roughness of titanium implants on bone remodeling activity of femur in rabbits. *Bone* **1997**, *21*, 507–514. [[CrossRef](#)]
87. Von der Höh, N.; von Rechenberg, B.; Bormann, D.; Lucas, A.; Meyer-Lindenberg, A. Influence of different surface machining treatments of resorbable magnesium alloy implants on degradation—EDX-analysis and histology results. *Materialwiss. Werkstofftech.* **2009**, *40*, 88–93. [[CrossRef](#)]
88. Zhao, Y.; Jamesh, M.I.; Li, W.K.; Wu, G.; Wang, C.; Zheng, Y.; Yeung, K.W.K.; Chu, P.K. Enhanced antimicrobial properties, cytocompatibility, and corrosion resistance of plasma-modified biodegradable magnesium alloys. *Acta Biomater.* **2014**, *10*, 544–556. [[CrossRef](#)] [[PubMed](#)]
89. Mustafa, K.; Lopez, B.S.; Hultenby, K.; Wennerberg, A.; Arvidson, K. Attachment and proliferation of human oral fibroblasts to titanium surfaces blasted with TiO₂ particles. A scanning electron microscopic and histomorphometric analysis. *Clin. Oral Implants Res.* **1998**, *9*, 195–207. [[CrossRef](#)]
90. Soskolne, W.A.; Cohen, S.; Shapira, L.; Sennerby, L.; Wennerberg, A. The effect of titanium surface roughness on the adhesion of monocytes and their secretion of TNF-alpha and PGE₂. *Clin. Oral Implants Res.* **2002**, *13*, 86–93. [[CrossRef](#)] [[PubMed](#)]
91. Derhami, K.; Wolfaardt, J.F.; Wennerberg, A.; Scott, P.G. Quantifying the adherence of fibroblasts to titanium and its enhancement by substrate-attached material. *J. Biomed. Mater. Res.* **2000**, *52*, 315–322. [[CrossRef](#)]
92. Boyan, B.D.; Lohmann, C.H.; Dean, D.D.; Sylvia, V.L.; Cochran, D.L.; Schwartz, Z. Mechanisms Involved in Osteoblast Response to Implant Surface Morphology. *Ann. Rev. Mater. Res.* **2001**, *31*, 357–371. [[CrossRef](#)]
93. Höh, N.V.D.; Bormann, D.; Lucas, A.; Denkena, B.; Hackenbroich, C.; Meyer-Lindenberg, A. Influence of Different Surface Machining Treatments of Magnesium-based Resorbable Implants on the Degradation Behavior in Rabbits. *Adv. Eng. Mater.* **2009**, *11*, B47–B54. [[CrossRef](#)]
94. Alvarez, R.B.; Martin, H.J.; Horstemeyer, M.F.; Chandler, M.Q.; Williams, N.; Wang, P.T.; Ruiz, A. Corrosion relationships as a function of time and surface roughness on a structural AE44 magnesium alloy. *Corros. Sci.* **2010**, *52*, 1635–1648. [[CrossRef](#)]
95. Supplit, R.; Koch, T.; Schubert, U. Evaluation of the anti-corrosive effect of acid pickling and sol-gel coating on magnesium AZ31 alloy. *Corros. Sci.* **2007**, *49*, 3015–3023. [[CrossRef](#)]
96. Walter, R.; Kannan, M.B. Influence of surface roughness on the corrosion behaviour of magnesium alloy. *Mater. Des.* **2011**, *32*, 2350–2354. [[CrossRef](#)]
97. Sharma, A.K. *Text Book of Correlation and Regression*; Discovery Publishing House: New Delhi, Delhi, India, 2005; ISBN 978-81-7141-935-7.
98. *Characterisation of areal surface texture*; Leach, R. (Ed.) Springer: Berlin, Germany, 2013; ISBN 978-3-642-36458-7.
99. Jin, S.; Amira, S.; Ghali, E. Electrochemical Impedance Spectroscopy Evaluation of the Corrosion Behavior of Die Cast and Thixocast AXJ530 Magnesium Alloy in Chloride Solution. *Adv. Eng. Mater.* **2007**, *9*, 75–83. [[CrossRef](#)]
100. Song, G.L.; St John, D.H.; Abbott, T. Corrosion behaviour of a pressure die cast magnesium alloy. *Int. J. Cast Met. Res.* **2005**, *18*, 174–180. [[CrossRef](#)]
101. Nudelman, F.; Pieterse, K.; George, A.; Bomans, P.H.H.; Friedrich, H.; Brylka, L.J.; Hilbers, P.A.J.; de With, G.; Sommerdijk, N.A.J.M. The role of collagen in bone apatite formation in the presence of hydroxyapatite nucleation inhibitors. *Nat. Mater.* **2010**, *9*, 1004–1009. [[CrossRef](#)] [[PubMed](#)]
102. Mhaede, M.; Pastorek, F.; Hadzima, B. Influence of shot peening on corrosion properties of biocompatible magnesium alloy AZ31 coated by dicalcium phosphate dihydrate (DCPD). *Mater. Sci. Eng. C* **2014**, *39*, 330–335. [[CrossRef](#)] [[PubMed](#)]
103. Pompa, L.; Rahman, Z.U.; Munoz, E.; Haider, W. Surface characterization and cytotoxicity response of biodegradable magnesium alloys. *Mater. Sci. Eng. C* **2015**, *49*, 761–768. [[CrossRef](#)] [[PubMed](#)]
104. Bakhsheshi-Rad, H.R.; Idris, M.H.; Abdul-Kadir, M.R. Synthesis and in vitro degradation evaluation of the nano-HA/MgF₂ and DCPD/MgF₂ composite coating on biodegradable Mg-Ca-Zn alloy. *Surf. Coat. Technol.* **2013**, *222*, 79–89. [[CrossRef](#)]
105. Jamesh, M.; Wu, G.; Zhao, Y.; Chu, P.K. Effects of silicon plasma ion implantation on electrochemical corrosion behavior of biodegradable Mg-Y-RE Alloy. *Corros. Sci.* **2013**, *69*, 158–163. [[CrossRef](#)]
106. Almen, J.O. *Shot Blasting to Increase Fatigue Resistance*; SAE International: Warrendale, PA, USA, 1943.
107. Guagliano, M. Relating Almen intensity to residual stresses induced by shot peening: A numerical approach. *J. Mater. Process. Tech.* **2001**, *110*, 277–286. [[CrossRef](#)]

108. Denkena, B.; Lucas, A. Biocompatible Magnesium Alloys as Absorbable Implant Materials—Adjusted Surface and Subsurface Properties by Machining Processes. *CIRP Ann.-Manuf. Technol.* **2007**, *56*, 113–116. [[CrossRef](#)]
109. *American Society of Mechanical Engineers Surface Texture Symbols*; ASME: New York, 1996; ISBN 978-0-7918-2319-4.
110. Guo, Y.B.; Salahshoor, M. Process mechanics and surface integrity by high-speed dry milling of biodegradable magnesium–calcium implant alloys. *CIRP Ann.-Manuf. Technol.* **2010**, *59*, 151–154. [[CrossRef](#)]
111. Denkena, B.; Lucas, A.; Thorey, F.; Waizy, H.; Angrisani, N.; Meyer-Lindenberg, A. Biocompatible Magnesium Alloys as Degradable Implant Materials—Machining Induced Surface and Subsurface Properties and Implant Performance. In *Special Issues on Magnesium Alloys*; Monteiro, W.A., Ed.; Intech Open: London, UK, 2011; ISBN 978-953-307-391-0.
112. Dorozhkin, S.V. Calcium orthophosphate-based biocomposites and hybrid biomaterials. *J. Mater. Sci.* **2009**, *44*, 2343–2387. [[CrossRef](#)]
113. Dorozhkin, S.V. Calcium Orthophosphate Cements and Concretes. *Materials* **2009**, *2*, 221–291. [[CrossRef](#)]
114. Berzina-Cimdina, L.; Borodajenko, N. Research of Calcium Phosphates Using Fourier Transform Infrared Spectroscopy. In *Infrared Spectroscopy—Materials Science, Engineering and Technology*; Theophanides, T., Ed.; Intech Open: London, UK, 2012; ISBN 978-953-51-0537-4.
115. El Kady, A.M.; Mohamed, K.R.; El-Bassyouni, G.T. Fabrication, characterization and bioactivity evaluation of calcium pyrophosphate/polymeric biocomposites. *Ceram. Int.* **2009**, *35*, 2933–2942. [[CrossRef](#)]
116. *Introduction to Biomaterials*; Shi, D. (Ed.) Tsinghua University Press; World Scientific: Beijing, China; Singapore; Hackensack, NJ, USA, 2006; ISBN 978-7-302-10807-8.
117. Duan, H.; Yan, C.; Wang, F. Growth process of plasma electrolytic oxidation films formed on magnesium alloy AZ91D in silicate solution. *Electrochim. Acta* **2007**, *52*, 5002–5009. [[CrossRef](#)]
118. Novaes, A.B.; de Souza, S.L.S.; de Barros, R.R.M.; Pereira, K.K.Y.; Iezzi, G.; Piatelli, A. Influence of Implant Surfaces on Osseointegration. *Braz. Dent. J.* **2010**, *21*, 471–481. [[CrossRef](#)]
119. Wennerberg, A.; Albrektsson, T. Suggested guidelines for the topographic evaluation of implant surfaces. *Int. J. Oral Maxillofac. Implant.* **2000**, *15*, 331–344.
120. Sanchez, A.H.M.; Luthringer, B.J.C.; Feyerabend, F.; Willumeit, R. Mg and Mg alloys: How comparable are in vitro and in vivo corrosion rates? A review. *Acta Biomater.* **2015**, *13*, 16–31. [[CrossRef](#)]



© 2018 by the authors. Licensee MDPI, Basel, Switzerland. This article is an open access article distributed under the terms and conditions of the Creative Commons Attribution (CC BY) license (<http://creativecommons.org/licenses/by/4.0/>).

3 Motivation and objectives

Common manufacturing techniques like machining can modify the near-surface region of the material by inducing mechanical stress, heat impact and the insertion of impurities. The related effects on the microstructure and chemical composition may change the degradation behaviour of biodegradable Mg alloys in an unwanted and non-reproducible manner, often resulting in inhomogeneous degradation. Therefore, this study aims to eliminate these production-related issues by etching of the manufactured part, focussing on Mg-Gd alloys.

To obtain this goal the following objectives have to be addressed:

- Understanding the relation between etching, morphology and microstructure.
- Development of an objective method to evaluate the homogeneity of the degradation, which is defined as uniform distribution of pit formation over the complete sample with similar pit volume and area for each part of the sample surface.
- Determination of the factors influencing the degradation rate and homogeneity of degradation.
- Determination of the effects of etching on the homogeneity and rate of degradation, with such and understanding, the development a suitable etching process.

4 Materials and Methods

4.1 Material

Depending on the Mg-xGd alloy, either 2 wt.%, 5 wt.% or 10 wt.% Gd (>99.9%, Table 4.1) prorated on the Mg (99.97%, Dead Sea Magnesium Ltd) amount were added to the furnace (Nabertherm) for permanent mould direct chill casting.

Table 4.1 Elements analysed next to Gd with >99.9% purity.

Element	La	Nd	Sm	Tb	Dy	Y	Fe	W	Si	C	Ni	Mn
[ppm]	30	25	10	20	20	260	650	450	70	35	50	15

A T4 solution heat treatment was performed at 525 °C for 8 h to dissolve intermetallic phases. Before extrusion the cast ingot was extruded to billets with the dimension of 49 mm diameter and 150 mm length. Indirect extrusion (Figure 4.1) were carried out to an extrusion ratio of 1:25, using a temperature of 400 °C and an extrusion ram speed of 2 mm/s.

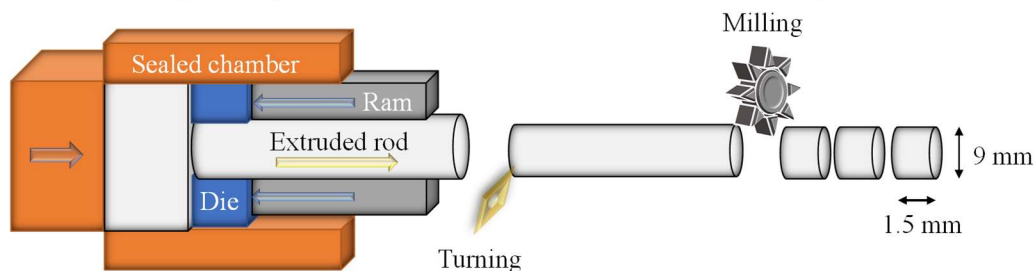


Figure 4.1 Schematic drawing of the extrusion processing, followed by machining.

The final diameter of the Mg-xGd rods were 10 mm. The rod was machined into 9 mm diameter to remove possible production contamination from the extrusion, followed by

milling to cut the rod into separate discs (Figure 4.1). The discs had a diameter of 9 mm and a height of 1.5 mm. The resulting surface after cutting has been defined as the as-received (AR) condition. The labeling and chemical composition of all Mg-xGd alloys produced are listed in Table 4.2. The amount of Gd was determined by X-ray fluorescence spectroscopy. Impurities like Fe, Cu and Ni were ascertained in as cast condition with atomic absorption spectroscopy (AAS). All following surface analyses were performed on one side of the sample.

Table 4.2 Label and chemical composition of all Mg-xGd alloys analysed by X-ray fluorescence spectroscopy and AAS.

Alloy	Label	Gd [wt.%]	Fe [ppm]	Cu [ppm]	Ni [ppm]	Mg [wt.%]
Mg-2Gd	G2	1.97	20	< 7	< 13	bal.
Mg-5Gd	G5	4.82	49	< 7	< 13	bal.
Mg-10Gd	G10	9.62	119	< 7	< 13	bal.

4.2 Etching procedure

The first step in the etching process was to prepare a 250 g/L HAc solution with glacial acetic acid (J.T. Baker, Avantor Performance Materials). Prior to etching, samples were cleaned in a test tube containing 3 mL hexane in an ultrasonic bath. Each Mg-xGd sample was then immersed with plastic tweezers into 5 mL or 10 mL HAc solution inside a watch glass (Figure 4.2).

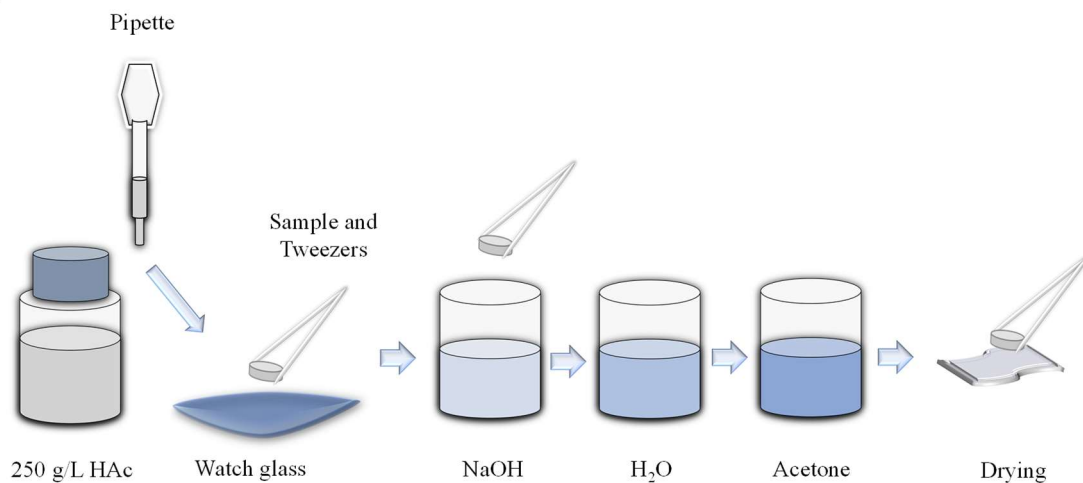


Figure 4.2 Illustration of the HAc etching procedure of the Mg-xGd alloys.

The curved watch glass was chosen to prevent direct contact between the sample bottom and the glass surface. After 1 s immersion, the samples were flipped and then etched for 15 or 150 s. During this time, the sample was inside the solution without the tweezers being in contact. After the etching time, the sample was removed from the solution and immersed in 40 mL of 1 mol NaOH for 30 s, followed by dipping into equal volumes of double distilled water and acetone successively, for 30 s. Acetone was used to accelerate drying. The solutions were chosen after a previous study of Gawlik et al. [56] and Nwaogu et al. [53]. To avoid corrosion of the samples, the samples were immediately pressed into a lint-free tissue for some seconds after acetone immersion (Figure 4.2). New HAc solution was used for every single sample, while NaOH, H₂O and acetone were changed after 6 samples. After etching, the samples were cleaned in 3 mL of hexane in an ultrasonic bath for 40 min [57].

The etching procedures are [57]:

- 250 g/L for 150 s in 5 mL HAc = 150_5
- 250 g/L for 150 s in 10 mL HAc = 150_10
- 250 g/L for 15 s in 5 mL HAc = 15_5

4.3 Ground samples for comparison

For comparison, grinding was used as a second method of material removal to compare etched samples with mechanically treated samples. The surfaces perpendicular to the extrusion direction of the AR samples were ground with P800 SiC paper for 2 s to remove the cutting marks on both sides of the sample. After grinding, the samples were cleaned with water and 100% ethanol and then dried under a blow dryer, followed by 40 min ultrasonic cleaning in hexane. Fifteen samples per alloy were prepared.

4.4 Calculation of material removal

The mean value and standard deviation of material removed after etching and grinding was calculated from the results of six samples per alloy. The material removed M was determined by mass loss, using AR after 40 min cleaning in hexane as mass before and after etching and cleaning or grinding and cleaning as final mass. M was defined as follows:

$$M = \frac{\Delta m}{\rho \cdot A} \cdot 10^4 \quad (14)$$

Where M is the material removal in μm ; Δm is the mass loss in g, measured by the weight before (AR+cleaning) and after etching+cleaning or after grinding+cleaning; ρ is the density in $\frac{\text{g}}{\text{cm}^3}$; A is the surface area in cm^2 [57].

4.5 Metallographic investigation

4.5.1 Sample preparation

For grinding and polishing, it was necessary to embed the discs in methyl methacrylate which was made up of 20 mg Demotec powder and 50 mL Demotec fluid (Demotec 30®, Demotec Demel e.K). After a hardening the embedded samples were ready for grinding. Five different SiC papers (P320, P500, P800, P1500, P2000) were used to remove material from the surface. The first four grinding steps were performed for one minute, while the last grinding step with P2000 SiC paper was performed for 10 min. Remaining scratches and grinding marks were removed by using an automatic polishing process, which used a polishing mixture composed of water-free oxide polishing suspension solution (OPS™, Cloeren Technology GmbH) a 1 μm diamond solution and ethylene glycol (Fisher Scientific UK) [57].

4.5.2 Optical microscopy

Microstructures cross-sections parallel to the extrusion direction were examined using an optical microscope (OM Leica DMI5000 M, Leica Microsystems GmbH, Wetzlar, Germany). The samples had been etched for 2 - 5 s in a picric acid solution. The picric acid solution consists of 200 mL ethanol, 20 mL distilled water, 20 g picric acid (Sigma-Aldrich) and 7 mL glacial acetic acid (J.T. Baker, Avantor Performance Materials). Afterwards the samples were cleaned in ethanol and dried under a blow dryer [57].

In order to analyse the near-surface region, three AR samples were prepared per alloy. Deformation zones (DZ) and twinning zones (TZ) were measured in the AR conditions by

use of “analySIS Pro” software (Olympus Soft Imaging Solutions GmbH). The deformation zone is defined as a zone, where no grain structure is identifiable. The thickness of deformation zone is measured from the edge of the surface to the point where grain structure starts to be observed. An extension line from this point to the end of twinning defines the twinning zone. The deformation zone and twinning zone were measured at fifteen different positions on one side of three AR samples. One micrograph for each etching condition was prepared for every alloy, to compare the remaining twinning with the calculated material removal [57].

4.5.3 Scanning electron microscopy

Scanning electron microscopy (SEM) was performed in the secondary electron (SE) and backscattered electron (BSE) modes using a Tescan Vega III SB scanning electron microscope (TESCAN). The analysis was carried out at a voltage of 15 kV and a working distance of around 15 mm. Energy-dispersive X-ray spectroscopy (EDS) (IXRF Sytems) was used to do elemental analysis on particles and the alloy matrix. The quantification of the elemental distribution was done using the software “Iridium Ultra” (version 2.4 F, IXRF Sytems). Element analysis was undertaken on cross sections (Chapter 4.5.1) parallel to extrusion direction of AR samples. The surface morphology for all alloys and conditions after etching was observed using SEM. The elemental distribution in wt.% of particles inside etching holes were determined for all etched surfaces for two samples of each alloy [57]. To investigate the initiation points of corrosion, particles were analyzed with EDS on one sample for every alloy on corrosion residues inside pits after fourteen days of degradation in physiological medium.

4.6 ToF-SIMS

Time-of-flight secondary ion mass spectrometry (ToF-SIMS) was performed with a dual beam TOF-SIMS5 instrument (ION-TOF GmbH, Münster, Germany) at Karlsruher Institut für Technologie (KIT), Germany. The spectrometer allows static secondary ion mass spectrometry (SIMS) with a Bi cluster primary ion source and dynamic SIMS with dual beam profiling, using a Bi cluster ion beam together with a Cs⁺ or O₂⁺ sputter ion beam. The secondary ions after several short pulses are detected inside a reflectron type time-of-flight analyzer (ION-TOF GmbH) with an ultra-high vacuum base pressure below 5 × 10⁻⁹ mbar. For this study the parameters used are listed in Table 4.3 and Table 4.4 [57].

Table 4.3 Overview of parameters used for primary Bi⁺ ions on Mg-xGd with ToF-SIMS.

Primary ion	Ion pulse Energy	Pulse length	Field of view	Data points	Lateral resolution	Target current	Repetition rate
Bi ⁺	25 keV	1.2 ns	500 x 500 μm ²	128 x 128	~4 μm	1.5 pA	14 kHz

Table 4.4 Overview of parameters used for sputtering with O₂⁺ ions on Mg-xGd with ToF-SIMS.

Sputter ion	Ion pulse Energy	Erosion length	Fiel of view	Target current	Angle of incidence
O ₂ ⁺	1 keV	6 s wit 0.3 s pause	750 x 750 μm ²	200 nA	45 °

Between the erosion steps, a surface area is scanned by the Bi⁺ primary ions and mass spectra are recorded. The lateral distribution of ion images is calculated for xy, xz and yz

planes out of the individual mass spectra, where 3D analysis can be visualized. For depth scale calibration, a pre-experiment was performed on polished Mg-xGd samples to calibrate the depth scale for the Mg-Gd system. On the basis of crater depths, determined by WLI, a mean sputter yield of 5.02 was calculated. For sputtering the crater, a low sputter ion dose was used to remove contamination from the surface. Contaminations were removed after about 25 nm. The eroded crater had an area of $250 \times 250 \mu\text{m}$ [57].

4.7 Interferometry

4.7.1 White light interferometry

White light interferometry (WLI) is a well-known non-destructive method used to determine the roughness and topography of surfaces. WLI was performed using a Contour GT-K WLI (Bruker Cooperation). The tilt of the surface raw data was removed by the F-Operator (Tilt removal filter) by use of the option “cylinder and tilt” (Vision64 5.41 update 1, Bruker Corporation). This filtering flattens the surface and highlights any surface deviations of a cylindrical sample with tilt [57]. By using a 3D Filter called Mask Data (Vision64 5.41 update 1, Bruker Corporation), the surface can be cut into an angular shape as presented in Figure 4.3.

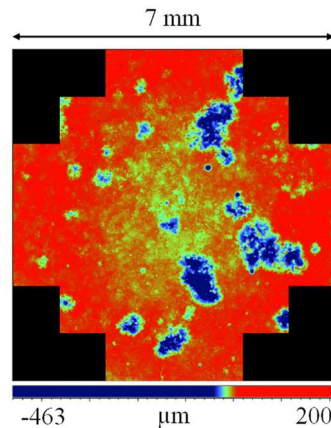


Figure 4.3 Topography of the G10 alloy after 30 days of degradation with removed edges.

The area of this surface was 37 mm^2 for reasons of comparability.

The roughness S_a was determined for the masked surfaces using the 3D analysis Tool “S Parameters - Height”. S_a was calculated for three samples per etching condition and alloy both before and after etching [57].

4.7.2 Etching pit

The 3D analysis tool “Multiple region” (Vision64 5.41 update 1, Bruker Corporation) was used for etching pit counting after placing the mask on the surface sample with an area of 37 mm^2 . A trial and error pre-experiment with different areas and depths for all etched samples led to the decision that pits with an area greater than $800 \mu\text{m}^2$ and a depth deeper than $15 \mu\text{m}$ below the reference plane (zero level) were ideally found to be counted. In the case of some pits white light was not reflected due to a deep narrow pit structure. The analysis tool could not count white spots, which were not reflected. These weak spots were counted manually. The mean value and standard deviation of the number of pits per mm^2 were determined for three samples for each alloy [57].

4.7.3 Homogeneity of the surface

V_v is determined by the 3D analysis “V-Parameter” (Vision64 5.41 update 1, Bruker Corporation). The homogeneity of the degradation was analyzed by separating the masked sample into 37 squares (Figure 4.4). The mean value “mean V_v” was calculated from the of 37 V_v values obtained from each 1 mm² square. Mean V_v defines the mean surface damage in μm³/μm². The standard deviation of the mean V_v, labelled as “V_v_dev”, in one sample defines the homogeneity of the pit distribution. The term “Homogeneity” is defined as uniform distributed pit forming over the complete sample with similar pit volume and area for each part of the sample surface or no pit formation, which is achieved by low V_v_dev values.

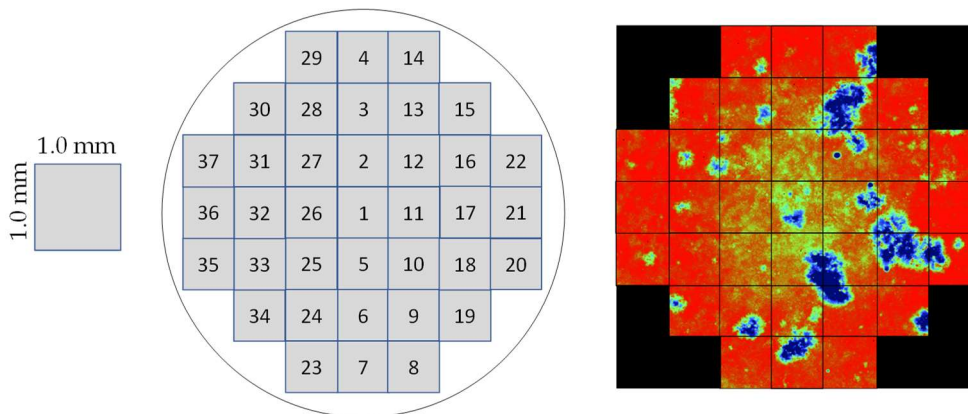


Figure 4.4 Schematic drawing of the original mask separated into 37 smaller squares.

4.7.4 Depth calibration of ToF-SIMS

The O₂⁺ sputtering depth for the depth calibration of the ToF-SIMS measurements was measured by WLI on polished (ground to P2000, followed by polishing for 20 min with 1 μm diamond solution and water-free OPS) Mg-xGd samples. O₂⁺ sputtering was performed with the same energy as shown in Table 4.4. For polished samples the F-Operator “Tilt only” (Vision64 5.41 update 1, Bruker Corporation) was used to remove the shift of grinding and polishing. The deepest point near to the central area was chosen inside the crater for the determination of the mean depth (Figure 4.5).

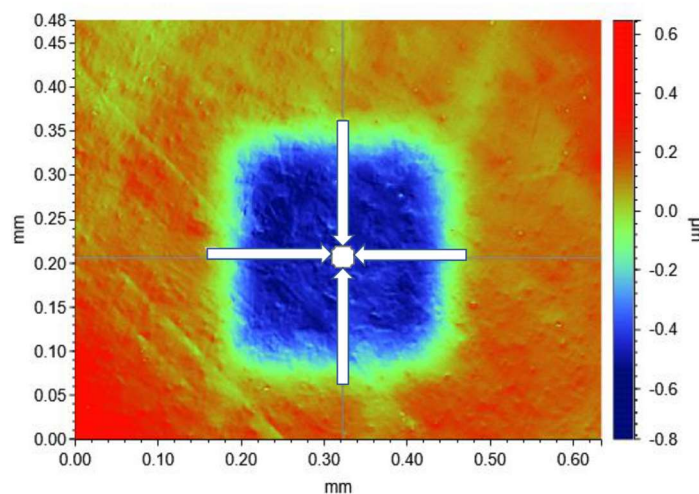


Figure 4.5 Topography of a O₂⁺ sputter crater to illustrate the calculation of mean crater depth.

The difference from the middle point to the top surface level was calculated for four different sidewalls of the crater. Following values were determined for each alloy [57]:

- G2 = $0.42 \pm 0.05 \mu\text{m}$
- G5 = $0.45 \pm 0.04 \mu\text{m}$
- G10 = $0.49 \pm 0.03 \mu\text{m}$

4.8 Degradation test

The degradation experiment tested different conditions (etched with acetic acid, ground and as-received) of the Mg-xGd alloys for degradation periods of up to 30 days. Table 4.5 shows an overview of the number of samples used for different surface conditions and degradation times.

Table 4.5 Overview of degradation time and number of Mg-xGd alloy samples with corresponding surface conditions.

Condition	Degradation time [d]	Number of samples investigated
As-received	30	15
Ground	30	15
HAc: 150_5	30	15
HAc: 150_10	14	8
HAc: 15_5	14	8

All samples were cleaned for 40 min in hexane and sterilized by submersion into 70 vol.% ethanol for 20 min in an ultrasonic bath. After one hour drying the samples were immersed in 2 mL of medium (described below and shown in Figure 4.6 in a sterile 24 well cell culture plate (Greiner bio-one, cellstar). The medium used was a combination of DMEM + Glutamax (Life TechnologiesTM, Gibco), 10 vol.% fetal bovine serum (FBS) (Biochrom GmbH) and 1 vol.% penicillin and streptomycin (Pen Strep) (Life TechnologiesTM, Gibco).

The degradation tests were performed under semi-static testing conditions at 37 °C, 5% CO₂, 20% O₂, 95% relative humidity inside an incubator. The medium inside the well plate was replaced three times per week with 2 mL of fresh medium. One sample was removed out of the medium each day for the first five days. Further samples were removed three times per week, starting from the second week.

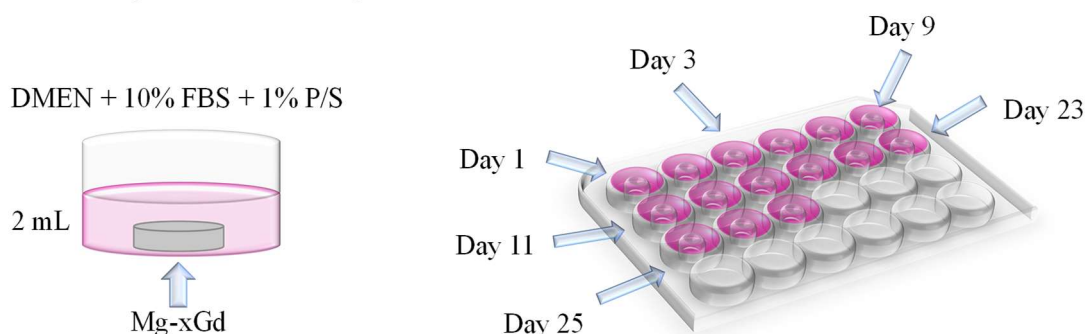


Figure 4.6 Drawing of fifteen Mg samples inside a 24 well cell culture plate.

After removal, the samples were washed with distilled water and 100% ethanol. Following drying, the samples were re-weighed. The degraded samples were treated with chromic acid for 20 min to remove the degradation layer.

The mean degradation depth was then determined from the weight loss using the formula:

$$d = \frac{\Delta m}{\rho \cdot A} \cdot 10^4 \quad (15)$$

Where d is the mean degradation depth in μm ; Δm is the mass loss in g, measured by the weight before degradation experiment and after removal of degradation products; ρ is the density in $\frac{\text{g}}{\text{cm}^3}$; A is the surface area in cm^2 . The calculated degradation depth for each specimen was plotted against degradation time. The slope of the linear fit is the mean degradation depth over time $d(t)$ according to the formula:

$$d(t) = D \cdot t + d_0 \quad (16)$$

which was introduced by [166]. Where $d(t)$ is the mean degradation depth at time point t in μm ; D is the degradation rate in $\mu\text{m}/\text{day}$; t is the time in days and d_0 is the intersection of the linear fit with the y-axis.

Generally, a constant degradation rate can be assumed, when after initial formation of a degradation layer material transport from this layer into the medium is in equilibrium with the degradation and diffusion through this layer. This is the case when the process conditions do not change. E.g., in a study of Zhao et al. [167] a dependency of pH to corrosion tendency was reported, due to the stabilisation of the $\text{Mg}(\text{OH})_2$ layer. A stable passivation layer is reported above a pH of 11.5 [91]. However, in this study a constant degradation rate over time is expected as an ideal case by changing the medium regularly. The medium change preserve the same pH [166] and volume inside the wells. A short degradation period of 30 days will lead to a negligible sample volume loss, which in turn leads to an approach of constant sample volume to medium volume ratio. Constant degradation rate means a linear increase of degradation depth. Thus, a linear regression fit is applied for the evaluation of the experimental data. An important characteristic value for a linear degradation progress is the coefficient of determination R^2 . R^2 is a measure for the quality of the linear regression fit with respect to the experimental points. Highest accuracy is assigned with $R^2 = 1$, when all calculated values are equal to the observed ones. R^2 represents the fraction of variation [168] in mean degradation depth values, determined in the performed degradation test. Within this study R^2 near to 1 is desired for an accurate prediction of the applied degradation progress over time. A constant degradation over time with high accuracy implies reproducible results.

5 Results

5.1 As-received microstructure

The cross section of as-received Mg-2Gd (G2) is shown in Figure 5.1 as an example for all alloys. In the near-surface region a smaller deformation zone (DZ) is visible, where no grains are identifiable. Below this region a deeper twinning zone (TZ) is present, where twins pervade the grain microstructure [57].

In Figure 5.2 the deformation depth, including deformation zone and twinning zone is shown for all alloys. The deformation zone is similar for Mg-2Gd (G2) and Mg-5Gd (G5), while the mean value of Mg-10Gd (G10) deformation zone is higher. The difference in deformation zone for all alloys is not significant, thus comparable, due to an overlap of all standard deviations. The twinning zone decreases with increasing Gd content, while the standard deviation of twinning zone is the highest for G2 [57].

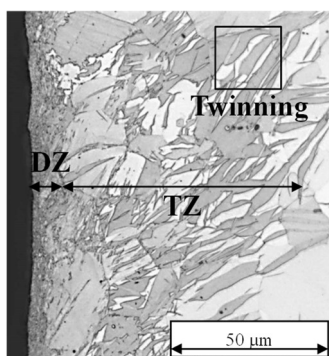


Figure 5.1 Micrograph of G2_AR cross section with deformation zone and twinning zone.

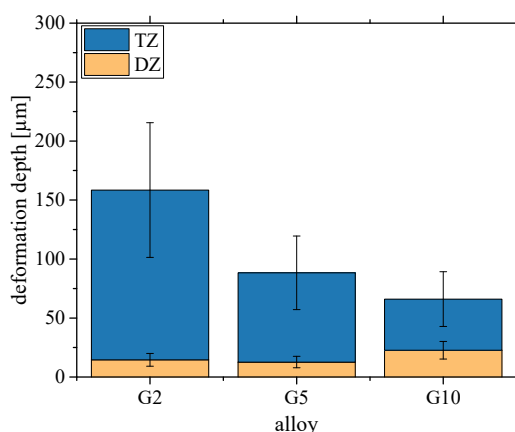


Figure 5.2 Plotted deformation depth with deformation zone and twinning zone for G2, G5 and G10. (modified and obtained from [57] with permission from Metals CC by 4.0)

Representative microstructural cross-sections of alloys G2, G5 and G10 are shown in Figure 5.3. Twinning inside the twinning zone is deepest for the lowest Gd containing alloy. Figure 5.3 a (alloy G2) shows regions, where twins are highly accumulated, separated by areas where the grains are not twinned as deeply. Alloy G5 shown in Figure 5.3 b has a similar deformation zone, but a less extended twinning zone, as determined in Figure 5.2.

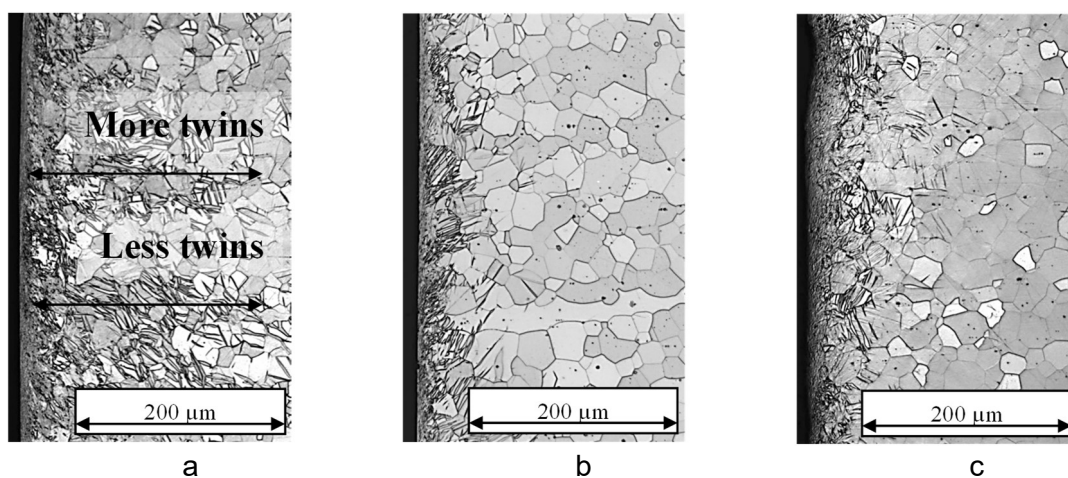


Figure 5.3 Micrographs of AR cross sections: a) G2 with deepest twinning zone, b) G5 with similar deformation zone compared to G2 and less extended twinning zone, c) G10 with deepest deformation zone and shortest twinning zone of all alloys.

In Figure 5.3 c, the deformation zone of G10 is slightly broader compared to G2 and G5 (Figure 5.3 a and b), while the width of twinning zone is comparable to that of G5. Additionally, some dark black particles were visible [57].

Small black particles were found in all alloys. G2 has some isolated particles, while G5 showed aligned particles. G10 had the highest number of particle accumulations, as seen for example in Figure 5.4. The aligned particles were partly stretched from one surface edge to the other, or locally accumulated. Between the groups of aligned particles, the grains were smaller compared to other grains [57].

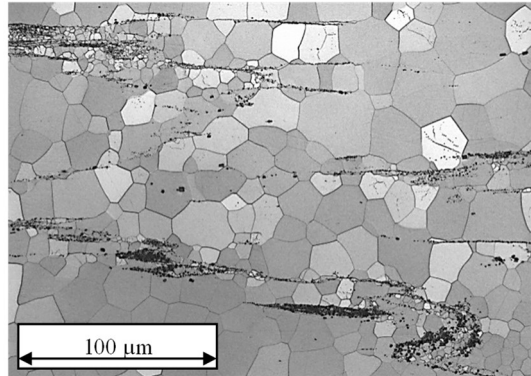


Figure 5.4 Micrograph of G10_AR microstructure perpendicular to the extrusion direction with accumulations of particles in the extrusion direction.

Particle lines in G10 are often bended in the deformation zone and twinning zone shown in Figure 5.5 a. The bright spots which can be seen are particles with higher Gd content (point 1: Gd = 30.5 wt.%), whereas the matrix (Point 2) has the measured expected value of 9.7 wt.% Gd for the alloy composition (Figure 5.5 b) [57].

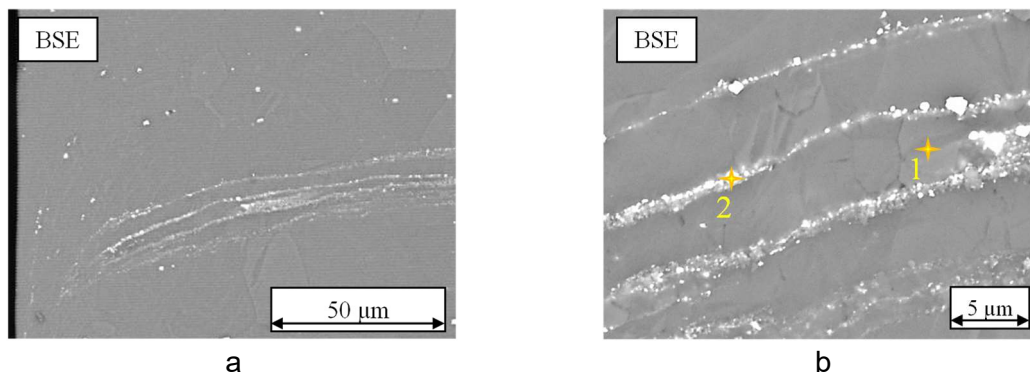


Figure 5.5 Micrographs of G10_AR observed on a section perpendicular to extrusion direction, obtained using the BSE mode: a) Particle lines are bended inside deformation zone and twinning zone, b) Higher Gd amount is determined on bright particles by EDS. (modified and obtained from [57] with permission from Metals CC by 4.0)

5.2 Microstructure and material removal after surface treatments

The material removal after grinding and after etching under different etching conditions is shown in Figure 5.6. Mg-2Gd (G2) and Mg-10Gd (G10) have the same mean value of removed material with a slightly higher standard deviation for G10 after grinding. Mg-5Gd (G5) has a significantly higher mean value of material removed after grinding and with a higher standard deviation compared to G2 and G10. It is determined, that the deformation zone is removed for all ground alloys. The twinning zone of G2 is still present after grinding. For alloys G5 and G10, there are grinded samples, where the twinning zone is assumed to

be removed or not removed, depending on the material removal per sample due to the range of standard deviation.

More material is removed, with increasing Gd amount for an etching treatment with 15 s in 5 mL (15_5) and 150 s in 10 mL (150_10) (Figure 5.6). For the condition 150 s in 5 mL (150_5) the mean value of removed material of G5 is slightly higher compared to G10. The amount of material removal is comparable for G10 after etching 150_5 and 150_10 in regard to the overlap of the standard deviation. Overall, the mean value of material removal is higher for 150_5, when compared with 150_10. Deformation zone and twinning zone are suspected to be extant after 15_5 etching. For 150 s etching, the deformation zone is removed for all alloys, while the twinning zone of G2 is assumed to remain. A complete removal of twinning zone is supposed for G5 and G10 [57].

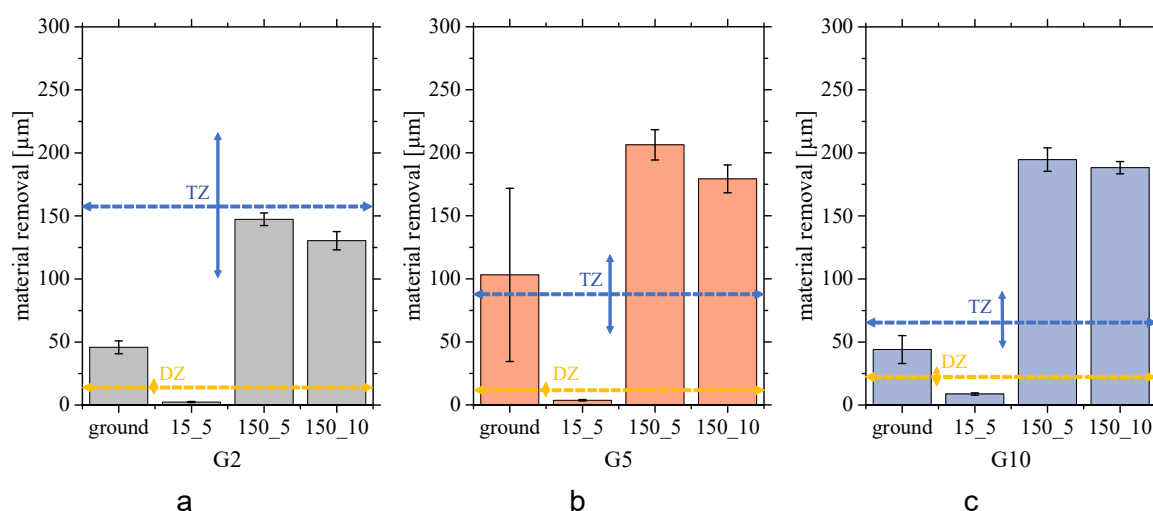


Figure 5.6 Diagrams of removed material after grinding and etching for 15 s or 150 s in 5 mL or 10 mL HAc solution: a) G2, b) G5, c) G10. (modified and obtained from [57] with permission from Metals CC by 4.0)

Figure 5.7 represents the cross sections of all alloys after etching for 150_5 HAc solution. As expected, due to the calculated material removal, no deformation zone is visible for all alloys in Figure 5.7. The accumulation of twins inside the twinning zone is decreasing with increasing Gd amount from G2 (Figure 5.7 a) to G10 (Figure 5.7 c). Some single twins are determined for G5 (Figure 5.7 b), while no twinning was visible for G10 (Figure 5.7 c). The direct surface region of G2 is more wavy on some parts of the sample (Figure 5.7 a) compared to G5 and G10. In G5 some single particle lines are visible, while G10 shows a higher appearance of particle lines [57].

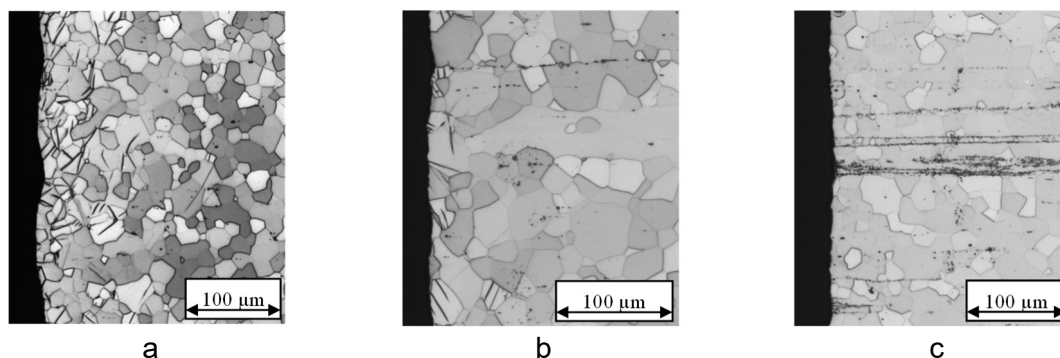


Figure 5.7 Micrographs of etched (150_5) cross sections: a) G2, b) G5, c) G10. (modified and obtained from [57] with permission from Metals CC by 4.0)

5.3 Morphology after etching

SEM investigations showing the morphology of all alloys after etching with characteristic etching pits. These etching pits are determined for 150 s etching with both volumes, while etching with 15_5 shows no pit formation. In nearly all etching pits were particles found inside the centre of these pits (Figure 5.8). Figure 5.8 a, shows a smaller pit at the sample edge of G2, where particles were clustered in the middle. In Figure 5.8 b an etching pit is shown, where two particle holes are found inside one etching pit. Both points are supposed to be connected with a particle line. Figure 5.8 c shows G10 with three single pits next to each other and single points with particles. An accumulation of Gd rich particles were also found e.g. in G2, where the particles are assumed to accumulate in a spherical shape (Figure 5.8 d).

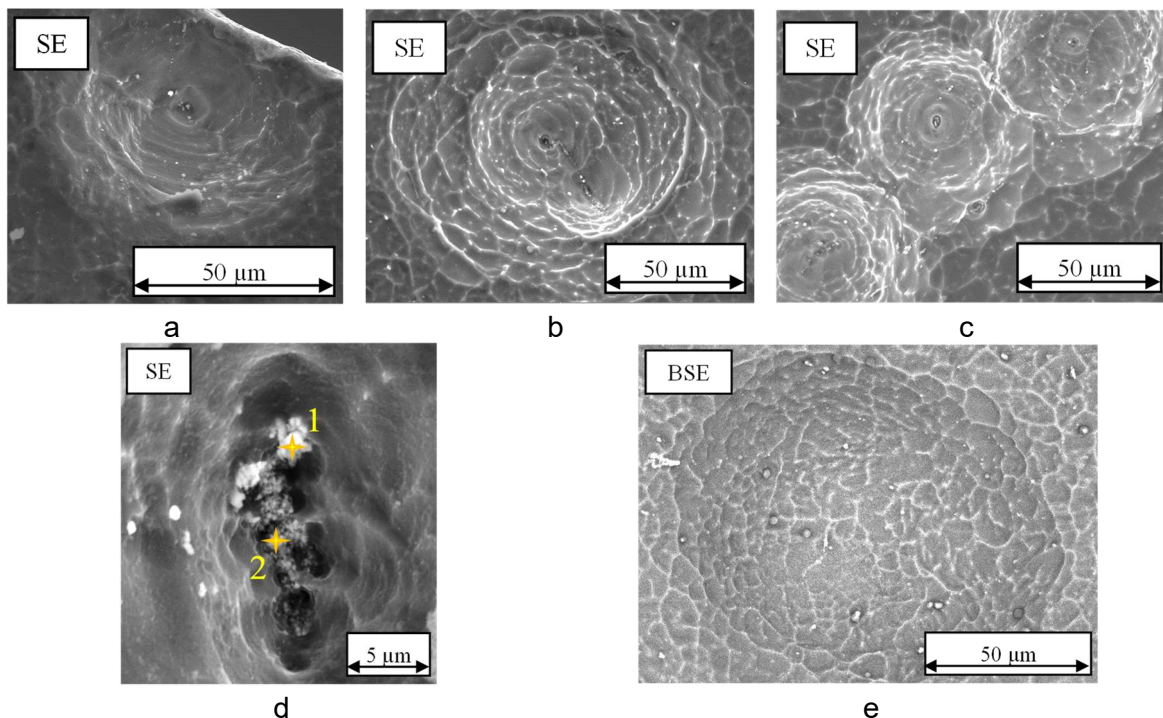


Figure 5.8 Etching pits observed by SEM: a) G2 etched for 150_10, b) G5 etched for 150_10, c) G10 etched for 150_10, d) G2 etched 150_5 (modified and obtained from [57] with permission from Metals CC by 4.0), e) G2 etched for 150_5 with no accumulation of particles.

The EDS results for point 1 show a higher Gd amount of 56.6 wt.% next to Mg. A higher Gd amount of 68.3 wt.% was determined for point 2, next to 10.3 wt.% O and residual Mg. Smaller etching pits were also found, especially for G2, where no or hardly any particles were found accumulated in the centre of the pit as shown e.g. in Figure 5.8 e.

The WLI topography of G5 before and after etching for 15_5 is plotted in Figure 5.9. Figure 5.9 a, shows the AR morphology with bold cutting marks. The deepest point (blue) is about 25 µm below the zero level, while the highest point (red) is at 95 µm above the zero level. After etching, the morphology did not change and no etching pits were determined. No significant variation in the deepest point is measured after etching, while the highest point was reduced to more than half of AR measurement. A slight reduction of Sa from 2.4 µm to 2.3 µm occurred after etching, due to removal of upper parts.

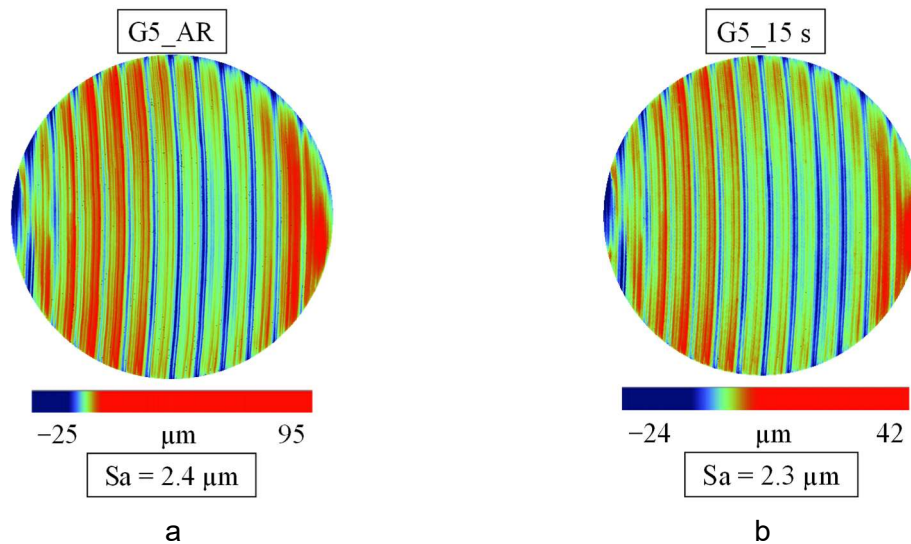


Figure 5.9 WLI topographies of G5 with corresponding peak-valley difference and surface roughness Sa: a) AR condition, b) same sample etched 15_5.

Bisected WLI topographies after 150 s etching of all alloys are shown in Figure 5.10. The left sample is etched in 5 mL and the right sample in 10 mL for each alloy. In general, small blue pits are visible more distinctive for 150_5 etching compared to 150_10. A higher material removal is assumed in the centre of the samples of each alloy for 10 mL etching. In particular, this is clearly visible for all etched G10 samples. G2 in Figure 5.10 a has residues of visible cutting marks for both etching volumes. The morphology does not differ strongly for 150_5 and 150_10. More pits are suggested for the 150_5 etching by comparing both surfaces. A higher Sa for 150_5 compared to 150_10 affirms a rougher surface by pit forming. The deepest point for 150_10 can originate from one deep single pit on different samples. After a 150_5 etching of G5 in Figure 5.10 b, the cutting marks are removed completely in contrast to 10 mL. A higher number of pits and bigger pits are visible for 150_5.

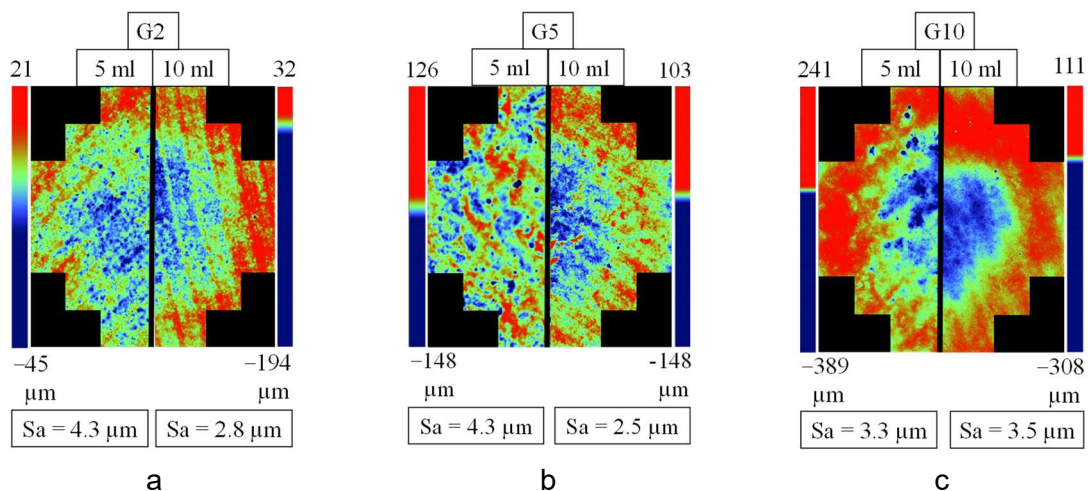


Figure 5.10 WLI topographies of 150 s etched alloys. The left sample is etched in 5 mL and the right sample is etched in 10 mL: a) G2, b) G5, c) G10. (modified and obtained from [57] with permission from Metals CC by 4.0)

The Sa after 150_5 etching is higher compared to G5, while highest and deepest points are similar. The etching of G10 in 150_5 lead to a lower peak valley difference in contrast to etching in 150_10 (Figure 5.10 c). The roughness of G10 does not vary strongly compared

to etching G2 and G5, more over there is a slight increase in Sa for 150_10 compared to 150_5. Cutting marks for G10 are nearly removed with both volumes [57]. It can be seen from the topography in Figure 5.9 that 15_5 etching did not cause pit formation. Etching pits per mm² for every alloy were determined after 150 s etching condition and are plotted in Figure 5.11.

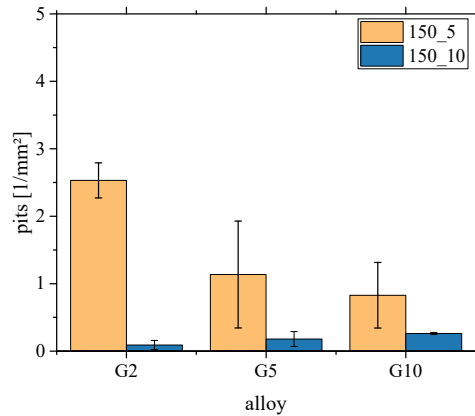


Figure 5.11 Mean value and standard deviation of etching pits per mm² for G2, G5 and G10 etched for 150_5 and 150_10.

The number of etching pits is decreasing with increasing Gd amount, when etching in 150_5. The standard deviation of pit number for G5 and G10 is higher compared to G2. When etching in 10 mL, there is a strong decrease in pit number visible for all alloys in contrast to 150_5 etching. No clear trend of pit number and Gd amount is predictable [57].

5.4 Analysis of Fe surface impurities

Two depth profiles of ToF-SIMS measurement were plotted as an example of as-received Mg-10Gd (G10_AR) in Figure 5.12 a. The initial increase in Fe arose from airborne contaminations. The maximum on Fe signal is shown around 30 nm in near-surface region. For G10_a_AR, the Fe intensity is lower compared to G10_b_AR. After erosion of about 30 nm material, the Fe intensity starts to decrease for both alloys, while G10_b_AR shows a lower decrease in Fe intensity after 340 nm erosion compared to G10_a_AR.

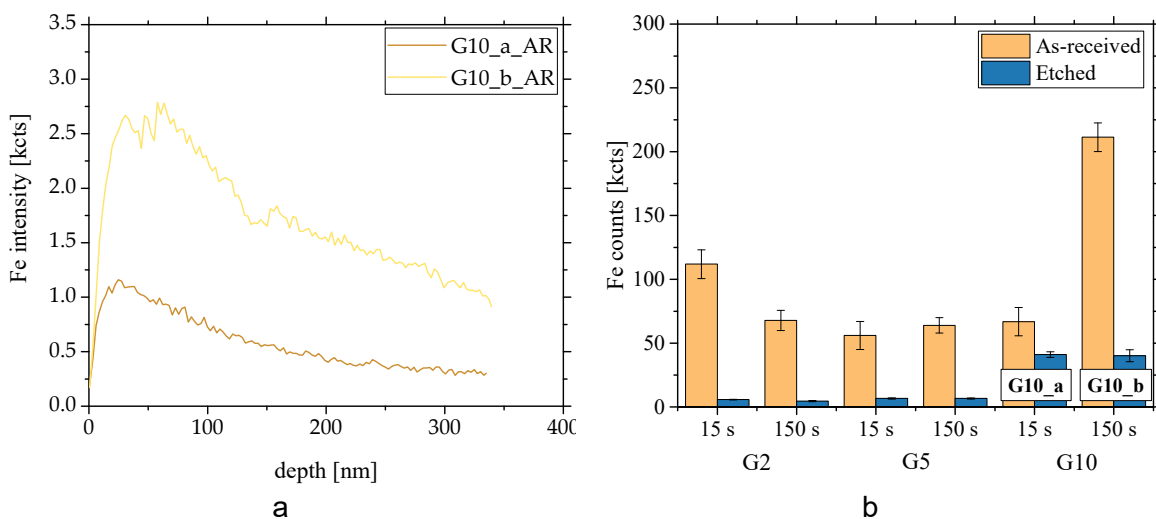


Figure 5.12 ToF-SIMS analysis: a) Depth profile of Fe for one position each of two G10_AR samples, b) Graph of mean value and standard deviation of Fe counts for G2, G5, and G10 before and after etching. (modified and obtained from [57] with permission from Metals CC by 4.0)

Figure 5.12 b shows the mean value of Fe counts for three eroded positions on one sample with corresponding standard deviation for as-received condition and after etching. The higher mean value of Fe counts for sample G10_b_AR, matches with the depth profile in Figure 5.12 a. After etching for 15 s and 150 s, the mean value and standard deviation of Fe counts decreased to the same level for both etching times, even if the Fe amount for sample G10_b_AR is much higher.




In comparison, the mean value and standard deviation of G2 and G5 for all AR samples is around the same level as G10_a. After etching for 15 s and 150 s, the Fe counts decreased nearly to zero for G2 and G5, in contrast to etched G10 (Figure 5.12 b) [57].

5.5 Additional etching results

Additional results and results, which are partly used in this thesis, are shown in following publication: “**Acetic Acid Etching of Mg-xGd Alloys**” [57]

Article

Acetic Acid Etching of Mg-xGd Alloys

Marcjanna Maria Gawlik ^{1,*}, Björn Wiese ¹ , Alexander Welle ², Jorge González ¹ ,
Valérie Desharnais ^{1,3}, Jochen Harmuth ¹, Thomas Ebel ¹ and Regine Willumeit-Römer ¹ 

¹ Helmholtz-Zentrum Geesthacht, Institute of Materials Research, 21502 Geesthacht, Germany; bjoern.wiese@hzg.de (B.W.); jorge.gonzalez@hzg.de (J.G.); valerie.desharnais@sympatico.ca (V.D.); jochen.harmuth@hzg.de (J.H.); thomas.ebel@hzg.de (T.E.); regine.willumeit@hzg.de (R.W.-R.)

² Karlsruhe Institute of Technology (KIT), Institute of Functional Interfaces, Karlsruhe Nano Micro Facility, 76344 Eggenstein-Leopoldshafen, Germany; alexander.welle@kit.edu

³ School of Computer Science, McGill University, Montréal, QC H3A 2T5, Canada

* Correspondence: marcjanna.gawlik@hzg.de; Tel.: +49-4152-87-1917

Received: 14 December 2018; Accepted: 21 January 2019; Published: 23 January 2019



Abstract: Mg-xGd alloys show potential to be used for degradable implants. As rare earth containing alloys, they are also of special interest for wrought products. All applications from medical to engineering uses require a low and controlled degradation or corrosion rate without pitting. Impurities from fabrication or machining, like Fe inclusions, encourage pitting, which inhibits uniform material degradation. This work investigates a suitable etching method to remove surface contamination and to understand the influence of etching on surface morphology. Acetic acid (HAc) etching as chemical surface treatment has been used to remove contamination from the surface. Extruded Mg-xGd ($x = 2, 5$ and 10) discs were etched with 250 g/L HAc solution in a volume of 5 mL or 10 mL for different times. The microstructure in the near surface region was characterized. Surface characterization was done by SEM, EDS, interferometry, and ToF-SIMS (time-of-flight secondary ion mass spectrometry) analysis. Different etching kinetics were observed due to microstructure and the volume of etching solution. Gd rich particles and higher etching temperatures due to smaller etchant volumes promote the formation of pits. Removal of 2–9 μm of material from the surface was sufficient to remove surface Fe contamination and to result in a plain surface morphology.

Keywords: Mg-Gd alloy; surface treatments; acetic acid etching; surface characterization

1. Introduction

The use of Mg alloys as biocompatible and degradable materials has been described as innovative research field [1–4]. Mg alloys have stimulating effects on osseointegration and osteoconduction [5–7]. Additionally, Mg can efficiently be alloyed with elements that are non-toxic to the human body [8,9]. For load-bearing implants that are used in fracture fixation, Mg alloys have Young's moduli closer to those of human bone [10], unlike Ti alloys, steels and most of the other medical alloys. Mg alloys with rare earth additions have been gaining importance in the field of degradable Mg alloys [11]. For biocompatible Mg alloys, the highly soluble elements Dy and Gd are advantageous due to the possibility of avoiding the formation of secondary phases [12]. Rare earth secondary phases with high electrochemical differences to Mg provoke localized galvanic corrosion [13–18]. In Mg alloys with rare earth additions of Gd, Dy, and Nd, for example, rectangular hydrides were found within the material. Rare earths have a higher affinity to H₂ compared to Mg and will form rare earth hydrides in the presence of water or hydrogen. Hence the formation of GdH₂ in Mg occurs rather easily [19]. These hydrides are reported to form in the material via different pathways during fabrication and preparation [11,19–21]. Mg-Gd and Mg-Dy alloys are already under investigation [11,22–26]. Gd plays no role in human metabolism. However, Feyerabend et al. [9] performed an in vitro study

of cytotoxicity and inflammatory response and found the best cytocompatible rare earth alloying additions to be Dy and Gd. Mg-10Gd typically had the slowest material degradation rate, as reported in a study that investigated Mg-2Gd, Mg-5Gd, Mg-10Gd, and Mg-15Gd alloys [11]. In vivo studies showed good healing and bone implant integration, when investigating the degradation behavior of Mg-Gd alloys [27–29].

Acid etching as surface treatment is used to remove galvanic corrosion inducing impurities like Fe and processing deformation from the surface [30–33]. Fe impurities have to be removed from the surface to avoid galvanic corrosion [34]. Deformation from machining change, e.g. grain size, defect density and internal stress in the subsurface [30,35,36], which has a direct influence on mechanical properties and corrosion resistance [37–40]. Most of the studies on etching were performed on AZ alloys, which are reported not to be suitable in biodegrading environments due to the Al content. The neurotoxicity of Al has been discussed and is thought to increase the risk of Alzheimer's disease [41–44]. Thus introducing Al in the human body via AZ based implants should be avoided. To date, etching Al-free Mg alloys have been rarely studied. However, the studies on AZ alloys are a good basis for the development of suitable etching treatments for biocompatible Al-free Mg alloys and Mg-RE alloys in bio-structural applications. The advantage of acid etching on Mg-5Gd alloys has been demonstrated by in vitro degradation testing [45].

Nwaogu et al. [31,32] used organic (acetic acid, oxalic acid, citric acid) and inorganic acids (sulfuric acid, nitric acid, phosphoric acid) to clean AZ31 sheets of impurities such as Fe and Ni. A greater amount of material was removed as the etching time was increased, which led to more impurities being removed. The greatest layer thickness removed from the surface layer was 20 μm . Acetic acid etching showed the highest degradation resistance as tested by electrochemical impedance spectroscopy (EIS) and salt spray in 5 wt.% NaCl [31]. Gray-Munro et al. [33] studied acid etching (90% H_3PO_4) on AZ31 foils as a pretreatment for calcium, phosphate, and polymer coatings. After etching, the passive surface oxide layer was thicker compared to that of the as-received condition. The surface morphology was also more uniform as post-production marks were removed by etching [33]. Song and Xu [30] studied sulfuric acid etching (10% H_2SO_4 for 20 s) on AZ31 sheets. By etching the surface, Fe impurities and the deformed surface layer that resulted from sandblasting were removed. Compared to the as-received and heat-treated conditions, etching increases the degradation resistance as measured by mass loss, hydrogen evolution, potentiodynamic polarisation (PDP) and EIS [30]. Supplit et al. [46] used acetic, nitric, phosphoric, and hydrofluoric acid etching solutions to decrease the degradation rate of AZ31 sheets. They achieved a decrease in the degradation rate by a factor of 60 on testing in 5 wt.% NaCl and measured by hydrogen evolution. They used a combination of acetic acid as a pretreatment and a sol-gel coating afterwards. Phosphoric acid was the second most effective acid in this experiment, while hydrofluoric acid etching resulted in the fastest degradation of testing in 5 wt.% NaCl [46].

Thus, etching is a potential way to remove impurities and deformed material from the surface, however, the wrong choice of etching agent and processing parameters can lead to undesirable degradation effects or an unnecessary loss of bulk material. The current work aims to understand which parameters of the etching process affect material degradation and to find a suitable etching treatment for Mg-xGd alloys using acetic acid. The etching treatment has to uniformly remove material without localized etching pits, and also eliminate harmful contaminants from the fabrication process. The positive influence of HAc etching on the degradation rate of Mg-5Gd has been presented in a previous study [45].

2. Materials and Methods

2.1. Material Casting and Processing

Three different Mg-Gd alloys were used in this study. Melting was performed using an Ar + 3 vol.% SF_6 shielding gas in an induction furnace, (Nabertherm GmbH, Lilienthal, Germany). Gd was added to a Mg melt that was held at 710 $^{\circ}\text{C}$. The alloys produced had 2, 5, and 10 wt.% Gd

additions. The alloys were cast into preheated molds at 550 °C. The cast ingots were then solution heat treated at 515 °C for 6 h and then processed by indirect extrusion (ratio 1:25) at a temperature of 400 °C and extrusion ram speed of 2 mm/s. The resulting extrusions had round profiles with a 10 mm diameter. A more detailed description is published in Harmuth et al. [47]. The round extruded rods were machined to a diameter of 9 mm, and then milled and cut into discs with a height of 1.5 mm (Figure 1). This initial state will be referred to the as as-received (AR) condition. Atomic absorption spectroscopy (AAS) measurements were performed in [47] to compare the Fe amount of AR bulk material for Mg-2Gd (Fe 20 ppm), Mg-5Gd (Fe 49 ppm), and Mg-10Gd (Fe 119 ppm).

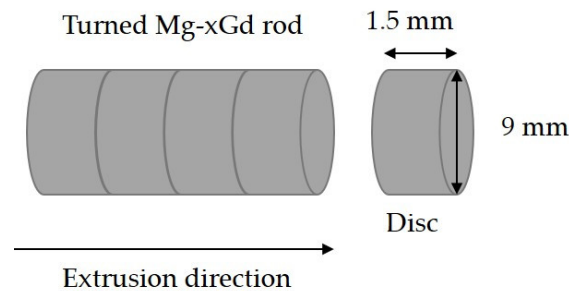


Figure 1. Charting of an extruded Mg-xGd rod after machining to a diameter of 9 mm. Discs in cylindrical form with a diameter of 9 mm and a height of 1.5 mm were cut off by milling.

2.2. Etching Procedure

Before etching, the density and weight of the samples were determined (using an electronic balance “RADWAG MYA 2.4 Y” (RADWAG, Radom, Poland) with an accuracy of 0.01 mg) and measured (using calipers with an accuracy of 0.01 mm). The discs were ultrasonically cleaned in 3 mL n-hexane for 40 min to remove organic contaminants, subsequently dried for 30 min in a fume cupboard and re-weighed. The etching solution was prepared using double distilled water and acetic acid (HAc) (J.T. Baker, Avantor Performance Materials, Inc, Center Valley, PA, USA). Etching of the samples, shown in Figure 1, was performed in 5 mL or 10 mL of HAc etchant solution, corresponding to 2.9 or 5.9 mL/cm². The concentration of HAc was chosen after a previous study of Gawlik et al. [45]. Acid etching was performed by first pouring 250 g/L HAc solution into a watch glass. Cleaned samples were dipped for one second into the solution, flipped over and then re-submerged in the solution for a certain time varying between 15 s and 150 s. To stop the reaction, the samples were first immersed in 40 mL of 1 mol/L NaOH for 30 s, then into 40 mL of double distilled water for 30 s and finally into 40 mL of acetone for 30 s. The samples were then dried using a lint-free tissue. Finally, the samples were again ultrasonically cleaned in 3 mL of n-hexane for 40 min.

2.3. Determination of Material Removal

Etching was performed for 15 s in 5 mL, 150 s in 5 mL, and 150 s in 10 mL of the HAc solution. Six samples of each alloy were etched for each condition and the mean and standard deviation of removed material was calculated. For every etched sample, the material removal M in μm normalized to the surface area was calculated by the following formula:

$$M = \frac{\Delta m}{\rho \cdot A} \cdot 10^4 \quad (1)$$

where Δm is the mass loss in g as measured by the difference in mass before and after HAc etching, ρ is the alloy density in g/cm³ and A is the disc surface area in cm².

2.4. Determination of the Temperature and pH

Before etching, the pH of the HAc solution was measured with a miniFET pH probe (Sentron Europe BV, VD Leek, The Netherlands) with an accuracy of 0.01. A thermocouple (MT2/ST) (otom

Group GmbH, Bräunlingen, Germany) was used to measure the initial and final temperatures of each sample during etching. This was done by applying a thermocouple immediately onto the sample surface after flipping over for the full duration of the etching. An additional three samples of each Mg-xGd alloy were etched in 5 mL and 10 mL of 250 g/L HAc for 15 s, 120 s, and 150 s. Only one additional sample was etched in 5 mL and 10 mL per duration of 30 s, 60 s, and 90 s. After etching of the samples was complete, 200 μ L of the remaining HAc solution was used to measure the pH. The pH was measured for solutions after 15 s etching in 5 mL and 150 s etching in 5 mL and 10 mL. Mean value and standard deviation of three samples and solutions were calculated for temperature (15 s, 120 s, and 150 s) and pH difference.

2.5. Interferometry

White light interferometry (WLI), performed with a non-contact interferometer (Contour GT-K, Bruker Corporation, Billerica, MA, USA) was used to analyze the topography after etching. The data from these measurements were analyzed using "Vision64" software (version 5.41 update 1, Bruker Corporation, Billerica, MA, USA). The raw data was fitted with an F-operator to correct the cylindrical form and tilt of the samples. A 3D Filter, "Mask Data" (Vision64 5.41 update 1, Bruker Corporation, Billerica, MA, USA), was then used to crop a circle with a diameter of 8 mm out of the data to avoid including the damaged edges arising from the machining process in the etching pit analysis. Peak-Valley difference and the surface roughness S_a (arithmetic mean of the absolute value of the height within sample area [48]) were determined with the 3D Analysis Tool "S Parameters-Height" (Vision64 5.41 update 1, Bruker Corporation, Billerica, MA, USA). Pits were then counted using the 3D Analysis Tool "Multiple Region" (Vision64 5.41 update 1, Bruker Corporation, Billerica, MA, USA) by searching for surface depressions with areas $>800 \mu\text{m}^2$ and depths greater than 15 μm below the mean surface height. These identification parameters were determined by a trial and error process of testing different values to find those capable of separating the valleys from the reference plane. Three samples from each of the etching conditions were measured to calculate the average and standard deviation for the number of pits per mm^2 .

2.6. Micrographs

Micrographs were taken from cross-sections that were orientated parallel to the extrusion direction. The samples were embedded in methyl methacrylate (Demotec 30®, Demotec Demel e.K, Nidderau, Germany) and after hardening were ground with SiC papers of P320, P500, P800, P1200, and P2000 until half of the disc diameters. After grinding, a water-free 1 μm oxide polishing suspension solution (OPSTM, Cloeren Technology GmbH, Wegberg, Germany), 1 μm diamond solution and ethylene glycol were used for polishing. The embedded samples were immersed for a few seconds into a picric acid solution (VWR International, Radnor, PA, USA) to be able to observe the microstructure under a standard optical microscope (OM Leica DMI5000 M, Leica Microsystems GmbH, Wetzlar, Germany). Three micrographs per AR sample from each alloy were prepared. Two different sections were determined as they were either of a deformation zone (DZ) or a twinning zone (TZ) originating from the edge of the sample into the bulk material. The thicknesses of these zones were measured with the software "analySIS Pro" (version 5, Olympus Soft Imaging Solutions GmbH, Münster, Germany). Mean thickness value and standard deviation of the DZs and TZs were calculated from fifteen measurements per sample. One micrograph per etched (150 s in 5 mL) sample from each alloy was prepared to analyze the change in microstructure.

2.7. SEM and EDS

The surface of etched Mg-xGd specimens was analyzed both parallel and perpendicular to the extrusion direction. Particle traces of cross sections, which were seen in the micrographs, were analyzed for one sample of Mg-10Gd with Energy-dispersive X-ray spectroscopy (EDS) (IXRF Sytems, Austin, TX, USA). The cross sections were prepared in the same way as described above. The morphology perpendicular to the extrusion direction was observed using the secondary electron

(SE) and backscattered electron (BSE) modes in a Tescan Vega III SB scanning electron microscope (TESCAN, Kohoutovice, Czech Republic) operating at 15 kV with a working distance of 15 mm. Particle element analysis was done using EDS and quantified using the “Iridium Ultra” (version 2.4 F, IXRF Systems, Austin, TX, USA) software.

2.8. ToF-SIMS

ToF-SIMS (time-of-flight secondary ion mass spectrometry) was performed on a TOF.SIMS5 instrument (ION-TOF GmbH, Münster, Germany). This spectrometer is equipped with a Bi cluster primary ion source and a reflectron type time-of-flight analyzer (ION-TOF GmbH, Münster, Germany). Ultra-high vacuum base pressure was $<5 \times 10^{-9}$ mbar. For high mass resolution the Bi source was operated in “high current bunched” mode providing short Bi⁺ primary ion pulses at 25 keV energy, a lateral resolution of approx. 4 μm , and a target current of approx. 1.5 pA at 14 kHz repetition rate. The short pulse length of 1.2 ns allowed for high mass resolution. Spectra were calibrated on the omnipresent ²⁶Mg⁺, ¹⁵⁸Gd⁺ and GdMgO₂⁺ peaks, mass deviations were <10 ppm. For depth profiling a dual beam analysis was performed in non-interlaced mode: The primary ion source was operated in “high current bunched” mode with a scanned area of 500 \times 500 μm^2 (3 frames with 128 \times 128 data points) and a sputter gun (operated with O₂⁺ ions, 1 keV, scanned over a concentric field of 750 \times 750 μm^2 , target current 200 nA, 45° angle of incidence) was applied to erode the sample for 6 s followed by a 0.3 s pause. Stable analysis conditions were ensured, for 6 subsequently performed depth profiles on two different Mg-2Gd samples the total Gd signal intensities varied less than 2.5% (mean value / standard deviation). To calibrate the depth scale for the dynamic SIMS (secondary ion mass spectrometry) experiments one polished specimen of each alloy was briefly precleaned with a low sputter ion dose density and subsequently eroded with a 1 keV oxygen beam in a 250 \times 250 μm^2 crater with a controlled sputter ion dose density of 3×10^{18} 1/cm² \pm 0.5%. During these erosions Mg and Gd signals were found to be constant from a depth of 25 nm onwards as soon as the sputter/oxygen implantation equilibrium was reached and a very thin non-metallic contamination layer was removed. Crater depths were measured by White light interferometry (WLI) (Contour GT-K, Bruker Corporation, Billerica, MA, USA). All alloys had eroded to a depth of 3.5 $\mu\text{m} \pm 10\%$. Based on these data a mean sputter yield of 5.02 was determined, being in good agreement with semi-empirical calculations from Yamamura et al. [49] indicating for pure Mg a sputter yield of 5.38.

In contrast to other surface analysis techniques, like X-Ray Photoelectron Spectroscopy, SIMS is semi-quantitative. Hence, absolute atom ratios can only be achieved by using external calibration standards and by taking the matrix effect into account. This effect is based on different sputter rates and different ionization yields for the elements to be studied in different matrices. Based on the known Mg/Gd ratios (Gd content varying from 2 to 10 wt.%, corresponding to 0.34 to 1.7 at.%) the linearity of the measured Gd⁺ signal intensities obtained from depth profiles was good. With all instrument parameters held constant relative Gd⁺ signal intensities of 1:2.5:4.5 were found for the Mg-2Gd, Mg-5Gd, and Mg-10Gd samples. This means that the investigated sample set showed no varying matrix effect for the different alloys, since Mg is the dominating matrix element with >98 to >99 at.%.

3. Results

3.1. Micrographs

Deformed grains and twins (see Figure 2a) were observed in the near surface region. Within DZ the grain structure was not visible. Inside TZ many twins (straight black lines inside of the grains) were observed. Additional particles were partly clustered and aligned in the extrusion direction. They are curved inside the DZ and TZ, this is a result of the milling process (see Figure 2b). The aligned particles are mainly clustered in Mg-10Gd, while all other alloys, show scattered distribution of particles and particle lines.

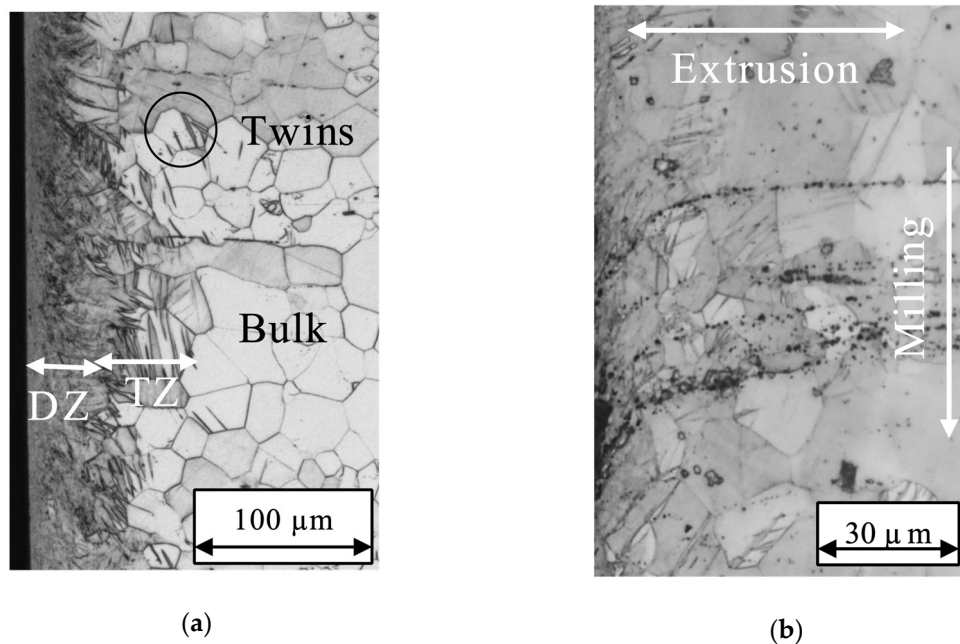


Figure 2. Micrographs of Mg-10Gd cross sections: (a) As received surface edge with deformed layer including a deformation zone (DZ) and twinning zone (TZ); (b) linear particle cluster are curved inside TZ.

After 150 s HAc etching in 5 mL solution, the surface edge in Figure 3 is more even with increasing Gd amount. The number of clustered particles is increasing with Gd amount. In Figure 3a, some single particles and lines are visible for Mg-2Gd, whereas Mg-10Gd in Figure 3c has accumulations of particle lines. With decreasing Gd amount the number of twins is increasing. For Mg-2Gd some deformed grains and a significant part of the TZ are still visible after the etching procedure. For Mg-5Gd the most of grains are deformation-free and some single twins are still visible. Mg-10Gd has a completely deformation-free surface edge.

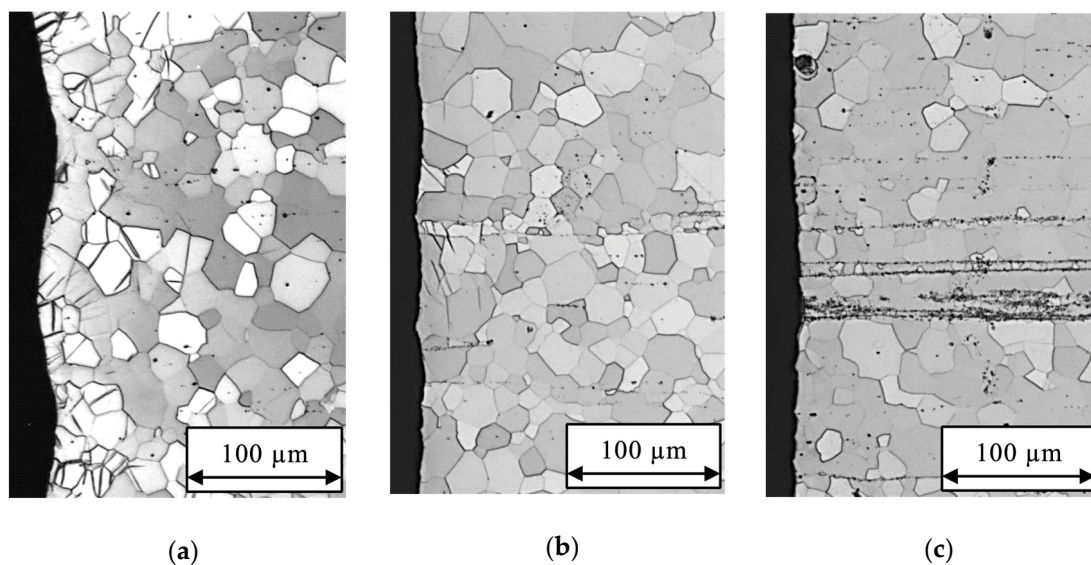


Figure 3. Micrographs cross sections after etching with 250 g/L for 150 s in 5 mL acetic acid (HAc) solution: (a) uneven surface edge of Mg-2Gd with partly non-deformed grains and grains including twins, some single black particles are visible; (b) mainly deformation free surface edge of Mg-5Gd with some single twins and partly visible particle lines; (c) deformation free surface edge of Mg-10Gd with linear particle cluster.

Within the standard deviation all alloys showed similar deformation zone (DZ) widths (Figure 4a), while mean value and standard deviation of TZ decreased with increasing Gd content. A high standard deviation of TZ arise from strong variation in twin depth for different positions, especially for Mg-2Gd. With increasing Gd amount the twin depth is shorter and more clustered.

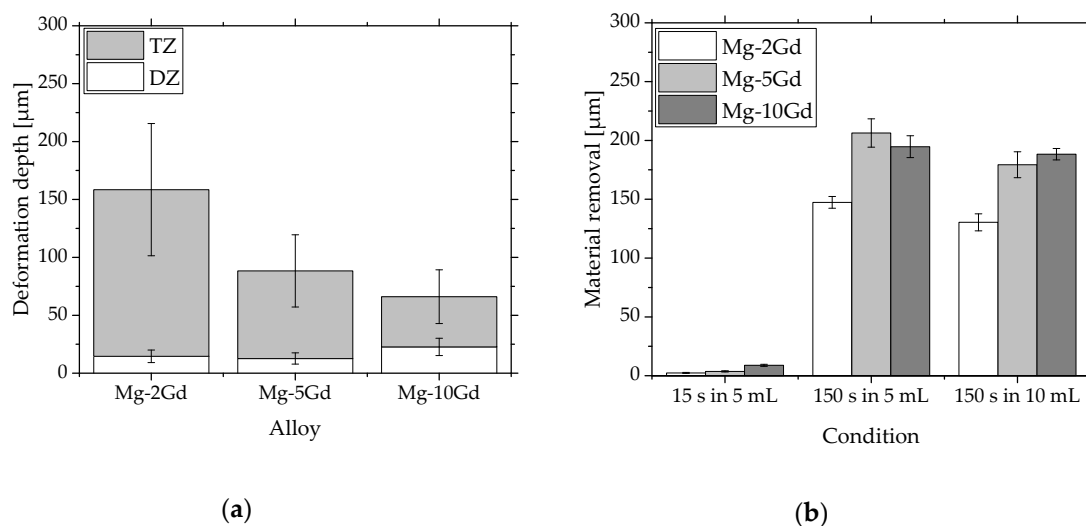


Figure 4. Diagrams of: (a) Mean value and standard deviation of DZ and TZ calculated for fifteen different regions per sample. Three samples per alloy were measured; (b) mean value and standard deviation of six samples for the amount of material removed from the Mg-xGd alloys after each etching treatment. The material removal increases with higher Gd content for all etching conditions. For each alloy the material removal after etching for 150 s in 5 mL and 10 mL solution are comparable.

3.2. Material Removal

Figure 4b and Table 1 indicate that basically more material is removed when the Gd content of the alloy is increased. After 15 s HAc etching, deformation and twins are still existing in all alloys. Using a longer etching time of 150 s, DZ is removed completely for all alloys and volumes. The calculations of material removal suggest a TZ free material for Mg-5Gd and Mg-10Gd for both etching volumes.

Table 1. Mean value of removed material and standard deviation of six samples for the Mg-xGd alloys after each etching.

Condition	Mg-2Gd	Mg-5Gd	Mg-10Gd
M after 15 s in 5 mL [μm]	2.4 ± 0.4	3.6 ± 0.5	8.9 ± 0.9
M after 150 s in 5 mL [μm]	147.4 ± 5.0	206.3 ± 12.1	194.7 ± 9.4
M after 150 s in 10 mL [μm]	130.4 ± 7.2	179.3 ± 11.0	188.3 ± 4.9

3.3. SEM and EDX

Etching pits were observed for all alloys after 150 s etching in the 5 mL and 10 mL of 250 g/L HAc solutions. At the center of some deeper etching pits, Gd rich particles were detected (see Figure 5a,b with white spots). The Gd rich particles, identified by EDS, are either accumulated in a spot or clustered in lines. Next to Gd hydrides which were mentioned before, Kubásek and Vojtěch [50] found also oxides, which are assumed as Gd₂O₃ or GdMg₂O₄, formed during melting and casting. Hort et al. [11] ascertain a formation of Gd₂O₃ or GdMg₂O₄ during casting as well. Due to the small size of the particles it was not possible to determine the specific rectangular shape of hydrides. For this reason, it is not possible to distinguish between Gd oxides and hydrides and the mentioned particles are defined as Gd rich particles within this study.

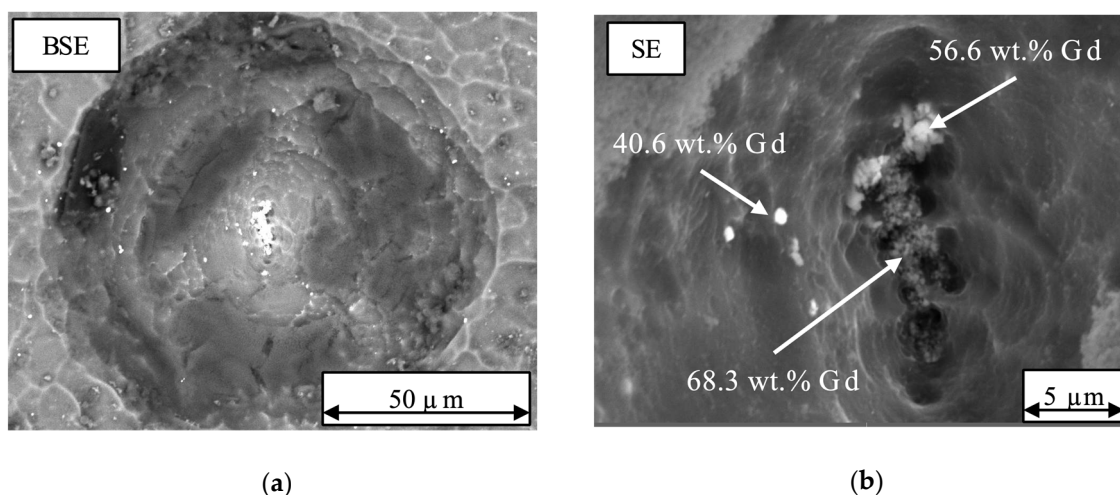


Figure 5. SEM picture of one etching pit on the surface of the Mg-2Gd alloy after etching for 150 s in a 5 mL solution of 250 g/L HAC: (a) backscattered electron (BSE)-mode, formation of an etching pit inside the matrix with particles at the center; (b) secondary electron (SE) mode: higher magnification of accumulated Gd rich particles (white spots) at the center of an etching pit.

Using EDS it has been shown that the visible lines of particles are enriched with Gd (Table 2). In Figure 6 the corresponding points measured by EDS are marked. Inside the matrix at point 3, 9.7 wt.% Gd was measured, very similar to the nominal 10 wt.%. At the other positions marked 1 and 2, 62.8 wt.% and 30.5 wt.% of Gd was measured, respectively.

Table 2. EDS analysis from three spots shown in Figure 6.

Element	1	2	3
Mg [wt.%]	37.2	69.5	90.3
Gd [wt.%]	62.8	30.5	9.7

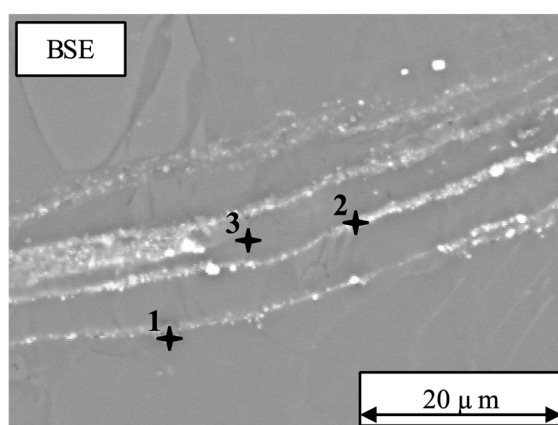


Figure 6. SEM micrograph obtained using the BSE mode of the as-received Mg-10Gd. Several lines of particles are curved inside the TZ and DZ of the Mg-10Gd material. EDS analysis was done at the three positions indicated to determine the Gd content.

3.4. Temperature and pH

Immersion in 5 mL for 15 s resulted in similar pH changes for all the Mg-xGd alloys (see Table 3). After etching for 150 s the change in pH is higher for the 5 mL experiments compared to 10 mL experiments. In contrast to the 5 mL experiments, immersion in 10 mL shows that the change in pH is

increasing slightly with increasing Gd content. However, systematic errors in the pH measurement setup lead to the assumption, that pH changes for all alloys in 10 mL are comparable.

Table 3. Δ pH of HAc solution after etching the Mg-xGd alloys in 5 and 10 mL solution.

Condition	Mg-2Gd	Mg-5Gd	Mg-10Gd
Δ pH after 15 s in 5 mL	0.07 ± 0.06	0.00 ± 0.00	0.20 ± 0.10
Δ pH after 150 s in 5 mL	1.47 ± 0.12	1.40 ± 0.00	1.47 ± 0.06
Δ pH after 150 s in 10 mL	0.73 ± 0.12	0.83 ± 0.06	1.00 ± 0.00

Figure 7 indicates an increase in temperature with immersion time for all alloys and solution volumes. For the Mg-2Gd and Mg-5Gd alloys etched in 5 mL, the temperature rises linearly with time while the other conditions show a constant value of temperature change after around 120 s and longer. Additionally, the change of temperature is higher for etching in 5 mL compared to 10 mL.

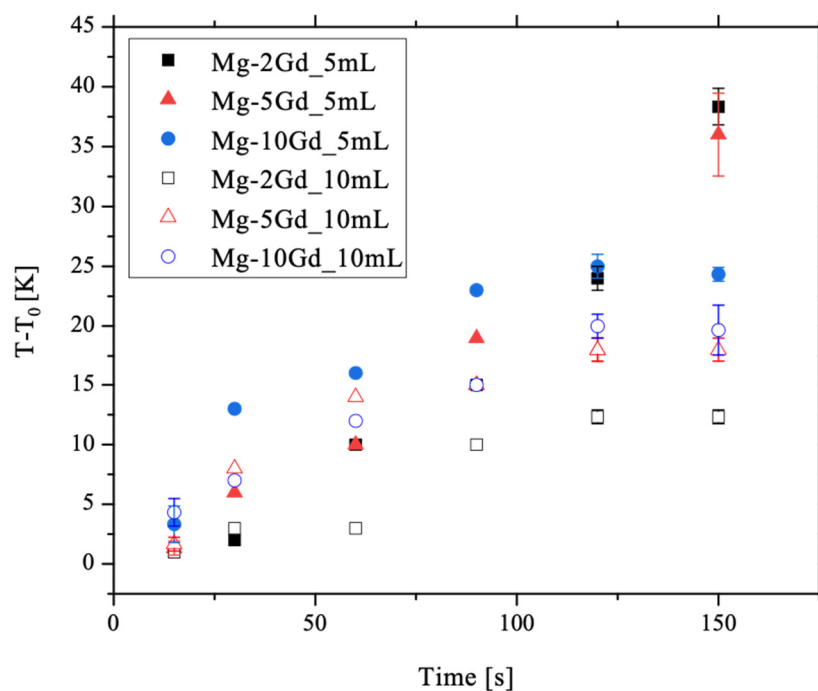


Figure 7. Diagram of $T-T_0$ plotted against time. $T-T_0$ increases with increasing time. Temperature increases are greater on etching in 5 mL compared to 10 mL solutions. Mean value and standard deviation of 3 samples were calculated for the time steps 15 s, 120 s, and 150 s.

3.5. Interferometry

Marks resulting from the machining with a wavelike structure were characteristic for the AR surface, as shown in Figure 8a. The color scale in Figure 8 shows the difference between the highest and lowest point of the surface for a Mg-2Gd specimen, as an example. After etching for 15 s in 5 mL the milling marks remained and no etching pits were formed (Figure 8b). However, the peak height as well as the difference in height of peak to valley are reduced. A slight decrease in S_a is also measurable after etching for 15 s compared to the AR condition. After etching for 150 s in 5 mL and 10 mL HAc solution, the surface morphology is very different compared to the AR surface as visible in Figure 9. The roughness S_a is higher after treatment in the 5 mL solution compared to 10 mL.

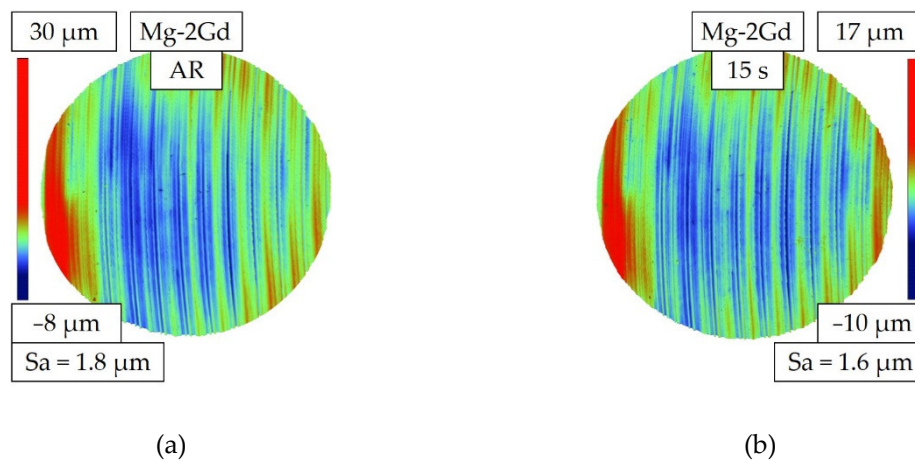


Figure 8. Topographies of the Mg-2Gd alloy as measured by white light interferometry (WLI): (a) Topography in as-received (AR) state with machining marks and a peak-valley difference of 38 (30 μm to $-8 \mu\text{m}$) (b) Topography after etching with 250 g/L HAc for 15 s in 5 mL of solution. Machining marks are still visible and the peak-valley difference of 27 μm (17 μm to $-10 \mu\text{m}$) is reduced in as compared to the AR state.

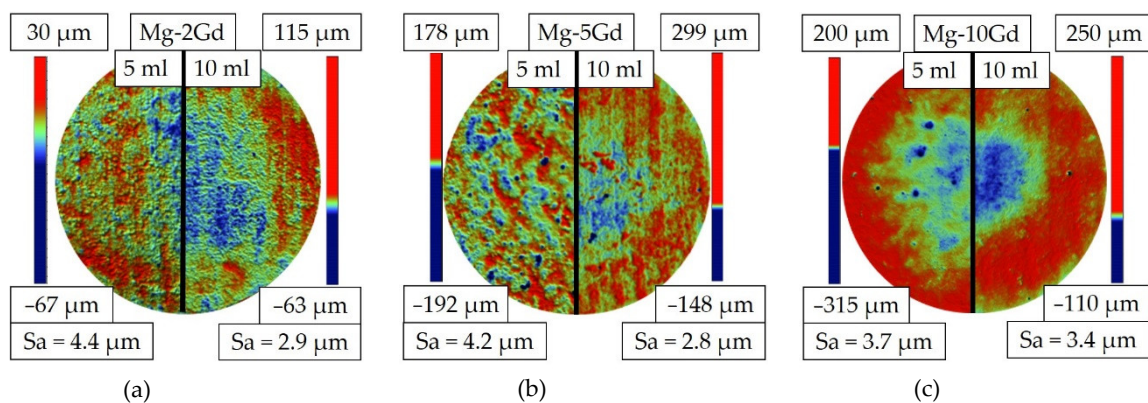


Figure 9. Topographies and their describing parameters of Mg-xGd alloys measured using WLI after etching with 250 g/L HAc for 150 s; left half image: 5 mL, right half image: 10 mL etching volume, (a) topographies of Mg-2Gd; (b) topographies of Mg-5Gd; (c) topographies of Mg-10Gd.

Figure 9 compares the etching effect after 150 s for different Gd contents and two different volumes of etching solution each. The left half shows the result after etching in 5 mL, the right one in 10 mL solution. For the Mg-2Gd specimens (Figure 9a) the machining marks are much less obvious compared to the AR state (Figure 8a). Etching pits have been formed with etching in 5 mL leading to a higher number of pits/ mm^2 (Table 4) compared to etching in 10 mL. For Mg-5Gd (Figure 9b), the machining marks are still visible after the 10 mL etching in contrast to 5 mL etching and the number of pits/ mm^2 (Table 4) is lower accompanied by smaller standard deviation. Almost no machining marks are visible for the Mg-10Gd (Figure 9c). Here, using 5 mL solution led to more pits/ mm^2 (Table 4) than using 10 mL solution. Table 4 shows that for 5 mL volume of etching solution the number of pits clearly decreases with increasing Gd content, while for 10 mL solution the number of pits is comparable within the standard deviation. It should be noted, that the color code refers to different absolute heights depending on the image.

Table 4. Number of etching pits formed in the Mg-*x*Gd alloys after etching for 150 s in 5 and 10 mL solutions.

Condition	Mg-2Gd	Mg-5Gd	Mg-10Gd
pits/mm ² for 5 mL	2.66 ± 0.51	1.70 ± 1.11	0.99 ± 0.41
pits/mm ² for 10 mL	0.21 ± 0.30	0.20 ± 0.00	0.52 ± 0.46

3.6. ToF-SIMS

Dynamic SIMS measurements were used to analyze the depth distribution of Fe impurities in the topmost 0.3 μm of the untreated, as received samples. For this, on each of two samples for Mg-2Gd, Mg-5Gd and Mg-10Gd, three depth profiles were analyzed. As example for a depth profile, only one profile of each alloy (Mg-2Gd, Mg-5Gd, Mg-10Gd_a) is shown in Figure 10. The depth profiles of the as-received Mg-*x*Gd samples, indicate a higher intensity of Fe measured in near surface region as compared to the bulk of the alloys. After a maximum Fe signal at around 30 nm of erosion, a decrease in Fe⁺ counts was observed. The initial increase of the Fe signals is based on airborne contaminations, shielding effectively signals from deeper layers due to the low probing depth of SIMS. As soon as this contamination layer is removed, and the sputter/implantation equilibrium of oxygen reached, the Fe signals are dropping as shown in Figure 10. A second profile of Mg-10Gd_b (Figure 10) is plotted as further example, where next to Fe as surface contamination, also Fe particles inside the bulk are detected (Figure 11 d–f). For this reason, the decrease in Fe intensity is not as strong as shown for Mg-10Gd_a after 340 nm.

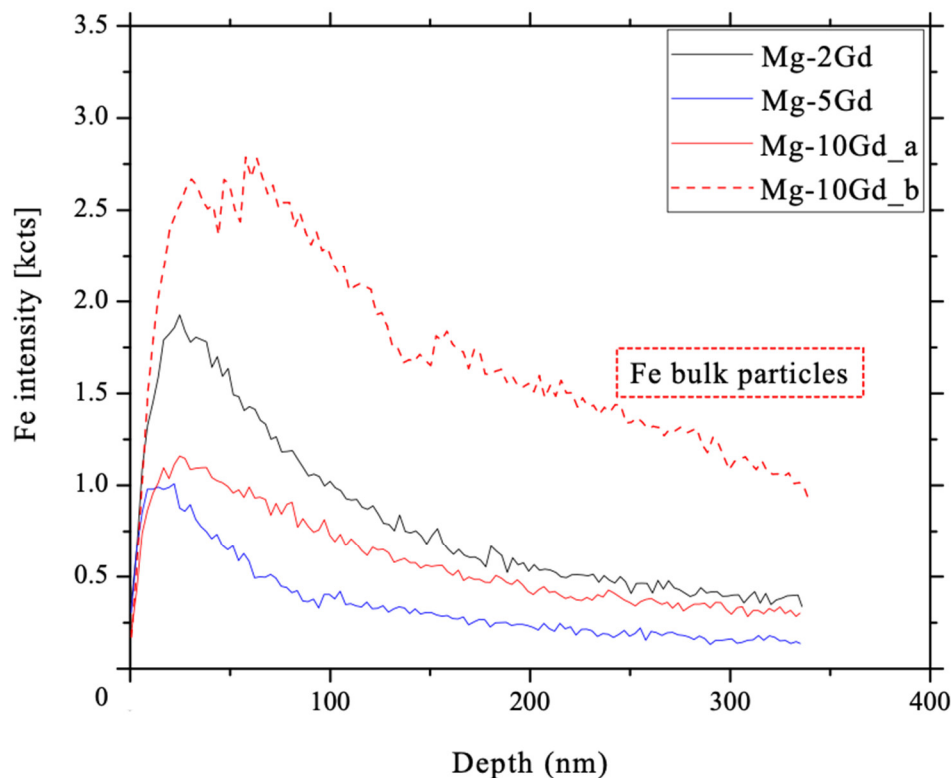


Figure 10. Depth profiles for Fe in the sub-surface of as-received Mg-*x*Gd alloys. The Fe intensity decreases at a depth around 30 nm. One profile of each alloy (Mg-2Gd, Mg-5Gd, Mg-10Gd_a) is plotted and show the decrease of Fe intensity to be virtually zero for the case of Fe surface contamination. The decrease of Mg-10Gd_b is not virtually zero after around 340 nm, due to additional bigger Fe particles inside the bulk.

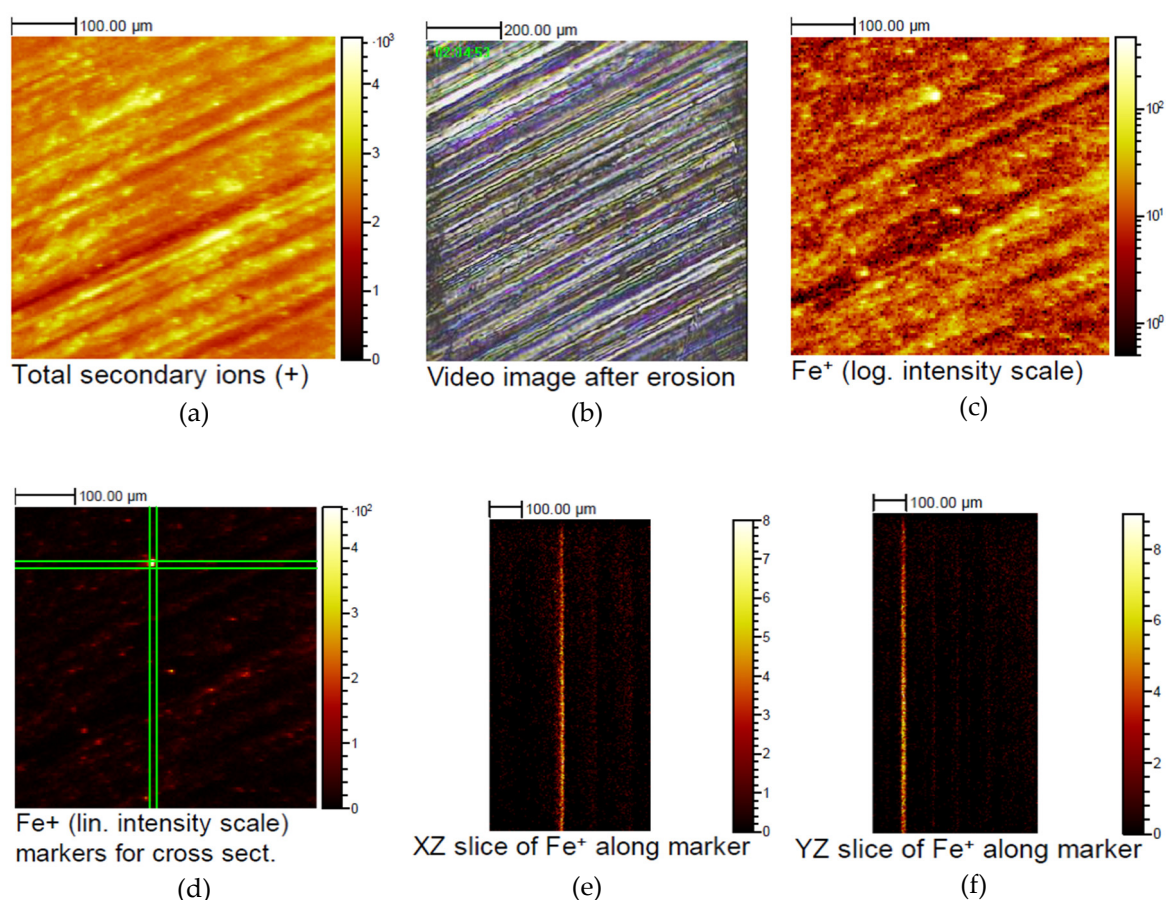


Figure 11. Lateral distribution of the Fe containing inclusions in Mg-10Gd corresponding to the depth profile: (a) total secondary ion image; (b) micrograph showing the measurement position; (c) depth-integrated lateral distribution of Fe with a log intensity scale; (d) integrated Fe signal with linear intensity scale, highlighting an individual Fe particle; (e) calculated cross sections in the XZ plane along the green indicators centered on the Fe particle; (f) calculated cross sections in the YZ plane along the green indicators centered on the Fe particle.

Analyzing the lateral distribution of the Fe containing inclusions two contributions are detectable: (a) is a weak Fe background correlated with the surface structure from the sample preparation, and (b) some rare individual Fe particles of several μm size. Figure 11 shows data corresponding to the depth profile shown in Figure 10. Mg-10Gd_b with the highest Fe intensity in Figure 10 shows the total secondary ion image (Figure 11a), a video image showing the measurement position (Figure 11b), and in Figure 11c the depth-integrated lateral distribution of Fe is given with a log intensity scale. In Figure 11d, the depth-integrated Fe signal is shown again, here with linear intensity scale, highlighting an individual Fe particle bracketed by green lines. Both panels in Figure 11e and f are calculated cross sections in the XZ and YZ plane along the green indicators centered on the Fe particle. As seen from the cross sections, the Fe particle is not eroded by the ion bombardment and is responsible for the remarkably strong Fe signal (Mg-10Gd_b) decreasing only very slowly during depth profiling in Figure 10.

After etching with HAc, much more material is removed than during the dynamic SIMS experiments reaching only $0.34 \mu\text{m}$ depth. At the etched surface (15 s and 150 s) of the alloys Fe almost completely disappeared in case of the Mg-2Gd and Mg-5Gd alloys (Figure 12). Here, the intensity of Fe on the surface after etching was found to be rather uniform as indicated by analysis of several positions. In contrast, a slightly greater local variation of the Fe signal was observed in the etched Mg-10Gd alloy. However, after etching the Gd rich samples the scatter of the Fe detected at different

measurement positions decreased in comparison to the AR samples. The remaining Fe content after etching of Mg-10Gd was reduced but still higher as compared to the samples with lower Gd content.

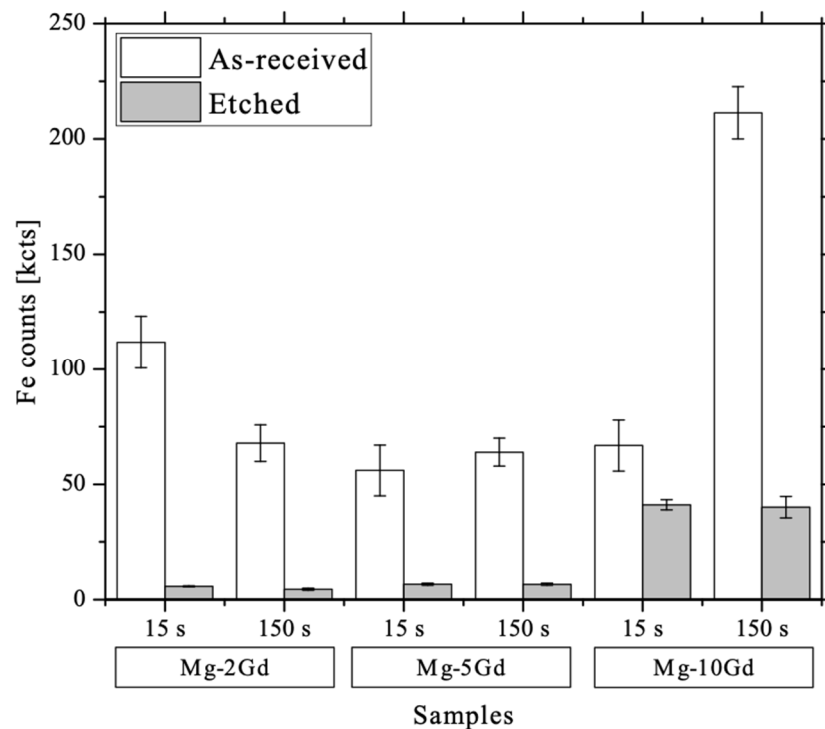


Figure 12. Graph showing Fe counts at the surface before and after etching the different alloys, obtained using ToF-SIMS.

4. Discussion

The sum of DZ and TZ depths (Figure 4a) is decreasing with increasing Gd amount, due to the higher strength of the material [47]. Higher Gd amounts strengthen the material by solid solution strengthening [51]. Higher strength lead to lower deformation depths, which results in reaching the bulk material earlier by etching for Mg-10Gd than for the other alloys. A higher dependency of TZ than of DZ on Gd content is expected, due to the not significant difference of DZ between different Gd amounts. Kaynak et al. [37] also reported a segmentation into three different microstructures after machining, whose thicknesses correlate with the mechanical properties of the alloy and the cutting conditions and parameters. Severe plastic deformation is described for refined and transition layer in near surface region, followed by the bulk material. Lu et al. [52] described a stress layer depth in near surface region of AZ31, visible by varying microstructure in contrast to the bulk material. The stress layer depth increased with decreased cutting speed. In the present study, all alloys are separated into two zones. The DZ is a strong deformation in direct surface region, where grains are not visible by SEM. It is assumed, that the original grain structure is damaged by the cutting tool. For the reason, that DZ is similar for all Gd content, it is supposed that the strength of the alloys has a lower effect on DZ. The cutting parameters are equal, which means the same force is introduced into the material and grains are crushed and shifted similarly, despite higher tensile strength of the alloys. With higher strength, dislocations are slipping less, which is why, TZ is more affected on depth than DZ. The second zone TZ in the sub-surface is the accumulation of twins, where twinning is a process to enable more material plasticity [53]. After twinning, the bulk material with non-deformed grains follows, similar to Kaynak et al. [37]. Residual stress is expected in the direct and sub-surface, which is not further investigated in this study.

More surface material is removed during the etching process with a higher Gd content (Figure 4b). The thicker TZ for alloys with lower Gd content (Figure 4a) might slow down dissolution at early

stages. For Mg-10Gd, the twinned surface region is removed earlier as compared to alloys with lower Gd contents. Hence the un-twinned bulk material is reached faster, due to a smaller TZ thickness. Some studies [54–56] reported the corrosion resistance to be increased by reduced grain size, and due to grain boundaries acting as borders between grains [54]. Corrosion in neutral and acid solutions are both electrochemical processes, for what the principle of mentioned corrosion studies are assumed to be transferable on HAc etching. Under the assumption that a higher twinning density results in higher number of twin boundaries, which act similar to grain boundaries, it would be expected that the material dissolution rate would be reduced in twinned material compared to un-twinned bulk.

By etching for 15 s only, less material is removed (Figure 4b) and no pit formation occurs (Figure 8b). Pit forming is observed for etching with 150 s duration (Figure 9, Table 4), associated with higher material removal. A chemical or structural difference inside an Mg alloy can result in a potential difference, where different parts of the material show either anodic or cathodic behavior. Grains and grain boundaries, as well as deformed and non-deformed areas, different crystallographic orientation or secondary phases can thus all lead to inhomogeneous dissolution [57–61]. It is assumed that Gd particles act as cathodes as well, due to Gd rich accumulations inside the etching pits (Figure 5). The visible accumulation of Gd after etching is possibly justified by the non-dissolution of Gd rich particles in HAc. The more material is removed by etching the more particles are freed from the matrix and can serve as potential initiators for pit forming. Pit forming in 5 mL solution etching is intensified in contrast to 10 mL solution. It is reported, that pit forming is released at a specific temperature for metals [62] and in general the corrosion rate increased with increasing temperature [63]. Hence, the temperature plays a pivotal role during pit formation in acid solution, the material removal is not the only limiting factor for pit forming.

It is reported, that the amount of Gd rich particles like GdH_2 is increasing with Gd addition inside the alloy [20]. For that reason, a higher number of pits would be expected, by considering Gd rich particles as the only initiation. Owing to a contrary pit forming behavior (Figure 9 and Table 4), it is assumed, that a temperature increase during etching for Mg-2Gd and Mg-5Gd has a higher influence on pit forming than hydrides. For this reason, it is expected that by regulating the etching temperature, pit forming will be reduced or avoided. The etching procedure may be then transferred to other RE systems.

The acceleration of the reaction, despite the neutralization of acetic acid leading to an increase of the pH of the solution (Table 3) is explained by the strong temperature increase measured directly at the metal surface in solution (in that case from 16 °C at the beginning to 56 °C after 150 s etching, Figure 7). The exothermic nature of the etching reactions leads to a temperature increase during the process. Neglecting the heat loss to the surrounding, the temperature difference observed during the etching process is dependent on the etch rate and the heat capacity of the setup, mainly the etchant solution. During etching with 5 mL of solution, the temperature increase is higher and more pits are formed compared to etching 15 s or 150 s in 10 mL etching (Figure 7).

Removal of the DZ and TZ is assumed to generate more heat compared to the removal of un-twinned bulk material. The Mg-2Gd alloy with highest temperature increase (Figure 7) had the highest twinning depth which was not completely removed even after the longest etching time in 5 mL solution (Figure 4a,b). Comparable material removal between samples etched in 5 mL and 10 mL of solution after the same time, suggest similar dissolution rates of the material. Etching in 10 mL solution did not show the same strong increase, due to higher thermal capacity of 10 mL solution compared to 5 mL.

After pits form, the roughness increases compared to the AR condition and 15 s etched samples (Figures 8 and 9). In particular, the Mg-2Gd alloy with the highest number of pits, exhibited the highest surface roughness S_a (Figure 9a). Higher roughness is attributed to pit formation, resulting in higher difference between peaks and valleys. The roughness of a surface may have influence of the initial degradation of an implant or improve cell density or is even useful to vary the morphology of

coatings [64–67]. For this reason, a variation of etching parameter allows the formation of a required morphology, dependent on the application.

Nwaogu et al. [31] reported that a rougher surface after etching arises from the dissolution of grain boundaries. Hou et al. [68] determined a higher attack of hydrofluoric acid (HF) for microstructure that contained more twins compared to less twinned specimens. The roughness of a sample with a high twinning density increased after dipping in HF for longer times. More heavily twinned samples gave rise to a higher surface roughness [68]. Because of that, twinning is assumed to influence pit forming, associated in higher surface roughness. Wang et al. [59] suggest that galvanic corrosion can take place between twinned and un-twinned microstructural regions due to different crystallographic orientations. Aung and Zhou [54] reported higher inter-granular corrosion in twinned regions, but more pits forming within un-twinned microstructure. The density of twins is higher within the material at the near surface region. Pit forming is expected for regions with less dense twinning, where galvanic corrosion can occur between twinned and un-twinned regions. As shown in Figure 3c, after etching of Mg-10Gd, only the bulk material is visible, while for Mg-2Gd there are areas of twinning, bulk material and a more uneven etched surface after 150 s etching (Figure 3a). The standard deviation of TZ is increasing with decreasing Gd amount (Figure 4a), because of strong varying twin depth on different positions in Mg-2Gd. The TZ of Mg-10Gd is more accumulated and flatter (Figure 2a). By removing less material for Mg-2Gd, deeper twins are still visible, next to areas, where flat TZ are already removed (Figure 3a). With a higher number of pits in Mg-2Gd it is expected, that the suggestions of Wang et al. [59] coincidences with the results in this study. It is expected that pits can occur due to the dissolution of the matrix between grain boundaries inside DZ and TZ area. It is assumed, that non-deformed grains dissolve locally faster compared to twinned grains as supposed before with different material dissolutions rates of DZ, TZ and bulk material.

The milling process introduces Fe impurities on the outer surface. This is shown by the ToF-SIMS experiments which indicate higher Fe ion counts near the surface region compared to those obtained inside the bulk material (Figure 10). Fe impurities must be removed from the surface to avoid galvanic corrosion, resulting in non-homogenous corrosion and fast material removal especially in the initial state [34]. By reducing the initial corrosion rate, mechanical integrity and ongrowth of the implant is ensured. Gawlik et al. [45] reported that HAc etching reduce the scattering of degradation results compared to untreated samples. This can be explained by the results of the reduction of Fe contamination in the present study. Using HAc etching for 15 s on the Mg-xGd alloys resulted in the surfaces being free of Fe contaminants (Figure 12) once a layer of around 2–9 μm thickness was removed from the surface. Supplit el al. [46] support the use of acid treatments as a surface cleaning method [46]. Nwaogu et al. [31] showed that removing 4 μm material was enough to reduce the number of contaminants present, including Fe and Ni, and resulted in lower corrosion rates. It can be assumed that acetic acid etching is able to remove contaminants such as Fe from the material surfaces, by removing the near surface region due to the solubility of Fe in acid [69–71]. The etching time had no influence on the amount of Fe on the surfaces, the number of Fe counts was similarly reduced after 15 s and 150 s (Figure 12). As a result, it is not necessary to remove more than 9 μm from the surface, achieved by longer etching times. The lateral distribution of Fe in the near surface region after etching is assumed to be homogenous for the Mg-2Gd and Mg-5Gd alloys, as there was a lower standard deviation in the number of counts measured at different positions on the specimen. Etching the Mg-10Gd greatly reduced the intensity of Fe counts obtained for different samples, even if the intensity varied strongly in the as-received condition. These results indicate that the etching process is advantageous in removing surface Fe. Due to higher number of Fe counts obtained in the Mg-10Gd compared to the other alloys, it is assumed, that Fe particles are more numerous at the surface and distributed to deeper regions within the alloy. This assumption is confirmed by AAS measurements of Harmuth et al. [47], which shows higher Fe bulk content of Mg-10Gd compared to Mg-2Gd and Mg-5Gd.

5. Conclusions

Acetic acid etching works of Mg-Gd alloys for biological and engineer applications and is expected to be used as surface treatment for other RE-alloys as well. The following should be considered:

- Short etching durations like 15 s induce no pit formation and are suitable for smooth surfaces like rolled sheets.
- Rougher surfaces are generated by use of longer etching time of 150 s or an etching volume of 5 mL instead of 10 mL and can encourage cell adhesion.
- HAc is capable to reliably remove surface contaminations like Fe after 15 s and 150 s, which is why a minor material removal of 2–9 μm is sufficient. According to previous reported research, material removal can reduce the scatter of degradation results.
- The removal of deformed material from processing is enabled by use of higher etching time. The deformation depth depends on the amount of Gd.
- Different etching kinetics are expected from deformed to non-deformed microstructure, which are regulated by the heat dissipation into the environment.
- The number of Gd rich particles is not the leading reason for pitting, but Gd particles and twins act as an initiator for pit forming, caused by an increase in temperature. The temperature of the exothermic reaction has the highest impact on pit formation.

Author Contributions: M.M.G. and B.W. conceived and designed the experiments; M.M.G., V.D., J.G., J.H. and A.W. performed the experiments; M.M.G., B.W., V.D. and A.W. analyzed the data; B.W., A.W. and J.H. contributed reagents/materials/analysis tools; M.M.G. wrote the initial manuscript; B.W., J.G., V.D., T.E., A.W., and R.W.-R. revised the manuscript; M.M.G. prepared the final paper.

Funding: This research was financially supported by the Helmholtz Virtual Institute VH-VI-523 (In vivo studies of biodegradable Mg based implant materials).

Acknowledgments: The authors would like to thank the department of Corrosion and Surface Technology, Helmholtz-Zentrum Geesthacht, Germany and Karlsruhe Nano Micro Facility (KNMF), Germany.

Conflicts of Interest: The authors declare no conflict of interest. The funders had no role in the design of the study; in the collection, analyses, or interpretation of data; in the writing of the manuscript, and in the decision to publish the results.

References

1. Mao, L.; Shen, L.; Chen, J.; Zhang, X.; Kwak, M.; Wu, Y.; Fan, R.; Zhang, L.; Pei, J.; Yuan, G.; et al. A promising biodegradable magnesium alloy suitable for clinical vascular stent application. *Sci. Rep.* **2017**, *7*, 46343. [[CrossRef](#)] [[PubMed](#)]
2. Persaud-Sharma, D.; McGoron, A. Biodegradable Magnesium Alloys: A Review of Material Development and Applications. *J. Biomim. Biomater. Tissue Eng.* **2012**, *12*, 25–39. [[CrossRef](#)] [[PubMed](#)]
3. Witte, F.; Hort, N.; Vogt, C.; Cohen, S.; Kainer, K.U.; Willumeit, R.; Feyerabend, F. Degradable biomaterials based on magnesium corrosion. *Curr. Opin. Solid State Mater. Sci.* **2008**, *12*, 63–72. [[CrossRef](#)]
4. Witte, F.; Kaese, V.; Haferkamp, H.; Switzer, E.; Meyer-Lindenberg, A.; Wirth, C.J.; Windhagen, H. In vivo corrosion of four magnesium alloys and the associated bone response. *Biomaterials* **2005**, *26*, 3557–3563. [[CrossRef](#)] [[PubMed](#)]
5. Galli, S.; Stocchero, M.; Andersson, M.; Karlsson, J.; He, W.; Lilin, T.; Wennerberg, A.; Jimbo, R. The effect of magnesium on early osseointegration in osteoporotic bone: A histological and gene expression investigation. *Osteoporos. Int.* **2017**, *28*, 2195–2205. [[CrossRef](#)] [[PubMed](#)]
6. Castellani, C.; Lindtner, R.A.; Hausbrandt, P.; Tschegg, E.; Stanzl-Tschegg, S.E.; Zaroni, G.; Beck, S.; Weinberg, A.-M. Bone-implant interface strength and osseointegration: Biodegradable magnesium alloy versus standard titanium control. *Acta Biomater.* **2011**, *7*, 432–440. [[CrossRef](#)] [[PubMed](#)]
7. Liu, C.; Ren, Z.; Xu, Y.; Pang, S.; Zhao, X.; Zhao, Y. Biodegradable Magnesium Alloys Developed as Bone Repair Materials: A Review. *Scanning* **2018**, *2018*, 15. [[CrossRef](#)] [[PubMed](#)]
8. Feyerabend, F.; Wendel, H.-P.; Mihailova, B.; Heidrich, S.; Agha, N.A.; Bismayer, U.; Willumeit-Römer, R. Blood compatibility of magnesium and its alloys. *Acta Biomater.* **2015**, *25*, 384–394. [[CrossRef](#)]

9. Feyerabend, F.; Fischer, J.; Holtz, J.; Witte, F.; Willumeit, R.; Drücker, H.; Vogt, C.; Hort, N. Evaluation of short-term effects of rare earth and other elements used in magnesium alloys on primary cells and cell lines. *Acta Biomater.* **2010**, *6*, 1834–1842. [[CrossRef](#)]
10. Li, J.; Tan, L.; Wan, P.; Yu, X.; Yang, K. Study on microstructure and properties of extruded Mg–2Nd–0.2Zn alloy as potential biodegradable implant material. *Mater. Sci. Eng. C* **2015**, *49*, 422–429. [[CrossRef](#)]
11. Hort, N.; Huang, Y.; Fechner, D.; Störmer, M.; Blawert, C.; Witte, F.; Vogt, C.; Drücker, H.; Willumeit, R.; Kainer, K.U. Magnesium alloys as implant materials—Principles of property design for Mg–RE alloys. *Acta Biomater.* **2010**, *6*, 1714–1725. [[CrossRef](#)] [[PubMed](#)]
12. Rokhlin, L.L. *Magnesium Alloys Containing Rare Earth Metals: Structure and Properties*; Advances in Metallic Alloys; Taylor & Francis: London, UK; New York, NY, USA, 2003; ISBN 978-0-415-28414-1.
13. Hamdy Makhoulouf, A.S.; Hussien, H.M. Deposition, Characterization and Electrochemical Properties of Permanganate-Based Coating Treatments Over ZE41 Mg–Zn–Rare Earth Alloy. *Int. J. Electrochem. Sci.* **2013**, *8*, 11386–11402.
14. Hamdy Makhoulouf, A.S.; Hussien, H.M. The effect of solution pH of permanganate coating on the electrochemical characteristics of ZE41 magnesium alloy in chloride media. *Int. J. Electrochem. Sci.* **2014**, *9*, 2682–2695.
15. Hamdy Makhoulouf, A.S. Intelligent Stannate-Based Coatings of Self-Healing Functionality for Magnesium Alloys. In *Intelligent Coatings for Corrosion Control*; Tiwari, A., Rawlins, J., Hihara, L.H., Eds.; Butterworth-Heinemann: Boston, MA, USA, 2015; pp. 537–555. ISBN 978-0-12-411467-8.
16. Hamdy, A.S.; Doench, I.; Möhwald, H. Vanadia-based coatings of self-repairing functionality for advanced magnesium Elektron ZE41 Mg–Zn–rare earth alloy. *Surf. Coat. Technol.* **2012**, *206*, 3686–3692. [[CrossRef](#)]
17. Hamdy, A.S.; Doench, I.; Möhwald, H. Assessment of a one-step intelligent self-healing vanadia protective coatings for magnesium alloys in corrosive media. *Electrochim. Acta* **2011**, *56*, 2493–2502. [[CrossRef](#)]
18. Hamdy, A.S.; Butt, D.P. Corrosion mitigation of rare-earth metals containing magnesium EV31A–T6 alloy via chrome-free conversion coating treatment. *Electrochim. Acta* **2013**, *108*, 852–859. [[CrossRef](#)]
19. Peng, Q.; Huang, Y.; Meng, J.; Li, Y.; Kainer, K.U. Strain induced GdH₂ precipitate in Mg–Gd based alloys. *Intermetallics* **2011**, *19*, 382–389. [[CrossRef](#)]
20. Huang, Y.; Yang, L.; You, S.; Gan, W.; Kainer, K.U.; Hort, N. Unexpected formation of hydrides in heavy rare earth containing magnesium alloys. *J. Magnes. Alloy.* **2016**, *4*, 173–180. [[CrossRef](#)]
21. Zhu, S.M.; Nie, J.F.; Gibson, M.A.; Easton, M.A. On the unexpected formation of rare earth hydrides in magnesium–rare earth casting alloys. *Scr. Mater.* **2014**, *77*, 21–24. [[CrossRef](#)]
22. Yang, L.; Feyerabend, F.; Kainer, K.U.; Willumeit, R.; Hort, N. Corrosion Behavior of As-Cast Binary Mg–Dy Alloys. *Mater. Sci. Forum* **2011**, *690*, 417–421. [[CrossRef](#)]
23. Yang, L.; Huang, Y.; Peng, Q.; Feyerabend, F.; Kainer, K.U.; Willumeit, R.; Hort, N. Mechanical and corrosion properties of binary Mg–Dy alloys for medical applications. *Mater. Sci. Eng. B* **2011**, *176*, 1827–1834. [[CrossRef](#)]
24. Yang, L.; Huang, Y.; Feyerabend, F.; Willumeit, R.; Kainer, K.U.; Hort, N. Influence of ageing treatment on microstructure, mechanical and bio-corrosion properties of Mg–Dy alloys. *J. Mech. Behav. Biomed. Mater.* **2012**, *13*, 36–44. [[CrossRef](#)] [[PubMed](#)]
25. Yang, L.; Hort, N.; Laipple, D.; Höche, D.; Huang, Y.; Kainer, K.U.; Willumeit, R.; Feyerabend, F. Element distribution in the corrosion layer and cytotoxicity of alloy Mg–10Dy during in vitro biodegradation. *Acta Biomater.* **2013**, *9*, 8475–8487. [[CrossRef](#)] [[PubMed](#)]
26. Yang, L.; Huang, Y.; Feyerabend, F.; Willumeit, R.; Mendis, C.; Kainer, K.U.; Hort, N. Microstructure, mechanical and corrosion properties of Mg–Dy–Gd–Zr alloys for medical applications. *Acta Biomater.* **2013**, *9*, 8499–8508. [[CrossRef](#)] [[PubMed](#)]
27. Willumeit-Römer, R.; Moosmann, J.; Zeller-Plumhoff, B.; Florian Wieland, D.C.; Krüger, D.; Wiese, B.; Wennerberg, A.; Peruzzi, N.; Galli, S.; Beckmann, F.; et al. Visualization of Implant Failure by Synchrotron Tomography. In *TMS 2018 147th Annual Meeting & Exhibition Supplemental Proceedings*; The Minerals, Metals & Materials Society, Ed.; Springer: Cham, Switzerland, 2018; pp. 275–284. ISBN 978-3-319-72525-3.
28. Moosmann, J.; Zeller-Plumhoff, B.; Florian Wieland, D.C.; Galli, S.; Krüger, D.; Dose, T.; Burmester, H.; Wilde, F.; Bech, M.; Peruzzi, N.; et al. Biodegradable magnesium-based implants in bone studied by synchrotron radiation microtomography. In *Proceedings of the Developments in X-Ray Tomography XI*; Müller, B., Wang, G., Eds.; SPIE: San Diego, CA, USA, 2017.

29. Galli, S.; Hammel, J.U.; Herzen, J.; Damm, T.; Jimbo, R.; Beckmann, F.; Wennerberg, A.; Willumeit-Römer, R. Evaluation of the degradation behavior of resorbable metal implants for in vivo osteosynthesis by synchrotron radiation based X-ray tomography and histology. In *Developments in X-Ray Tomography X*; Stock, S.R., Müller, B., Wang, G., Eds.; SPIE: San Diego, CA, USA, 2016.
30. Song, G.-L.; Xu, Z. The surface, microstructure and corrosion of magnesium alloy AZ31 sheet. *Electrochim. Acta* **2010**, *55*, 4148–4161. [[CrossRef](#)]
31. Nwaogu, U.C.; Blawert, C.; Scharnagl, N.; Dietzel, W.; Kainer, K.U. Effects of organic acid pickling on the corrosion resistance of magnesium alloy AZ31 sheet. *Corros. Sci.* **2010**, *52*, 2143–2154. [[CrossRef](#)]
32. Nwaogu, U.C.; Blawert, C.; Scharnagl, N.; Dietzel, W.; Kainer, K.U. Influence of inorganic acid pickling on the corrosion resistance of magnesium alloy AZ31 sheet. *Corros. Sci.* **2009**, *51*, 2544–2556. [[CrossRef](#)]
33. Gray-Munro, J.E.; Seguin, C.; Strong, M. Influence of surface modification on the in vitro corrosion rate of magnesium alloy AZ31. *J. Biomed. Mater. Res. Part A* **2009**, *91A*, 221–230. [[CrossRef](#)]
34. Höche, D.; Blawert, C.; Lamaka, S.V.; Scharnagl, N.; Mendis, C.; Zheludkevich, M.L. The effect of iron re-deposition on the corrosion of impurity-containing magnesium. *Phys. Chem. Chem. Phys.* **2016**, *18*, 1279–1291. [[CrossRef](#)]
35. Denkena, B.; Lucas, A. Biocompatible Magnesium Alloys as Absorbable Implant Materials—Adjusted Surface and Subsurface Properties by Machining Processes. *CIRP Ann. Manuf. Technol.* **2007**, *56*, 113–116. [[CrossRef](#)]
36. Denkena, B.; Lucas, A.; Thorey, F.; Waizy, H.; Angrisani, N.; Meyer-Lindenberg, A. Biocompatible Magnesium Alloys as Degradable Implant Materials—Machining Induced Surface and Subsurface Properties and Implant Performance. In *Special Issues on Magnesium Alloys*; Monteiro, W.A., Ed.; InTech: London, UK, 2011; ISBN 978-953-307-391-0.
37. Kaynak, Y.; Lu, T.; Jawahir, I.S. Cryogenic Machining-Induced Surface Integrity: A Review and Comparison with Dry, MQL, and Flood-Cooled Machining. *Mach. Sci. Technol.* **2014**, *18*, 149–198. [[CrossRef](#)]
38. Liu, Y.; Liu, D.; You, C.; Chen, M. Effects of grain size on the corrosion resistance of pure magnesium by cooling rate-controlled solidification. *Front. Mater. Sci.* **2015**, *9*, 247–253. [[CrossRef](#)]
39. Ahmadkhaniha, D.; Fedel, M.; Heydarzadeh Sohi, M.; Deflorian, F. Corrosion behavior of severely plastic deformed magnesium based alloys: A review. *Surf. Eng. Appl. Electrochem.* **2017**, *53*, 439–448. [[CrossRef](#)]
40. Pu, Z.; Outeiro, J.C.; Batista, A.C.; Dillon, O.W.; Puleo, D.A.; Jawahir, I.S. Enhanced surface integrity of AZ31B Mg alloy by cryogenic machining towards improved functional performance of machined components. *Int. J. Mach. Tools Manuf.* **2012**, *56*, 17–27. [[CrossRef](#)]
41. Marchkesbery, W.R.; Ehmann, W.D.; Hossain, T.I.M.; Alauddin, M.; Goodin, D.T. Instrumental neutron activation analysis of brain aluminum in Alzheimer’s disease and aging. *Ann. Neurol.* **1981**, *10*, 511–516. [[CrossRef](#)] [[PubMed](#)]
42. Crapper, D.R.; Krishnan, S.S.; Quittkat, S. Aluminium, neurofibrillary degeneration and alzheimer’s disease. *Brain* **1976**, *99*, 67–80. [[CrossRef](#)]
43. Mirza, A.; King, A.; Troakes, C.; Exley, C. Aluminium in brain tissue in familial Alzheimer’s disease. *J. Trace Elem. Med. Biol.* **2017**, *40*, 30–36. [[CrossRef](#)]
44. Tomljenovic, L. Aluminum and Alzheimer’s Disease: After a Century of Controversy, Is there a Plausible Link? *J. Alzheimers Dis.* **2011**, *23*, 567–598. [[CrossRef](#)]
45. Gawlik, M.M.; Steiner, M.; Wiese, B.; González, J.; Feyerabend, F.; Dahms, M.; Ebel, T.; Willumeit-Römer, R. The effects of HAC etching on the degradation behavior of Mg-5Gd. *J. Med. Mater. Technol.* **2017**, *1*, 22–25.
46. Supplit, R.; Koch, T.; Schubert, U. Evaluation of the anti-corrosive effect of acid pickling and sol-gel coating on magnesium AZ31 alloy. *Corros. Sci.* **2007**, *49*, 3015–3023. [[CrossRef](#)]
47. Harmuth, J.; Wiese, B.; Bohlen, J.; Ebel, T.; Willumeit-Römer, R. Tailoring of Material Properties of Mg-Gd Alloys for Biomedical Applications. In *Magnesium 2018: Proceedings of the 11th International Conference on Magnesium Alloys and Their Applications*; Brunel University: London, UK, 2018; ISBN 978-1-908549-37-2.
48. *Characterisation of Areal Surface Texture*; Leach, R. (Ed.) Springer: Berlin/Heidelberg, Germany, 2013; ISBN 978-3-642-36457-0.
49. Yamamura, Y.; Tawara, H. Energy dependence of ion-induced sputtering yields from monatomic solids at normal incidence. *At. Data Nucl. Data Tables* **1996**, *62*, 149–253. [[CrossRef](#)]
50. Kubásek, J.; Vojtěch, D. Structural and corrosion characterization of biodegradable Mg-RE (RE = Gd, Y, Nd) alloys. *Trans. Nonferrous Met. Soc. China* **2013**, *23*, 1215–1225. [[CrossRef](#)]

51. Askeland, D.R. *Essentials of Materials Science and Engineering*; Third Edition, SI.; Cengage Learning: Stamford, CT, USA, 2014; ISBN 978-1-111-57686-8.
52. Lu, L.; Hu, S.; Liu, L.; Yin, Z. High speed cutting of AZ31 magnesium alloy. *J. Magnes. Alloy.* **2016**, *4*, 128–134. [[CrossRef](#)]
53. Barnett, M.R. Twinning and the ductility of magnesium alloys. *Mater. Sci. Eng. A* **2007**, *464*, 1–7. [[CrossRef](#)]
54. Aung, N.N.; Zhou, W. Effect of grain size and twins on corrosion behaviour of AZ31B magnesium alloy. *Corros. Sci.* **2010**, *52*, 589–594. [[CrossRef](#)]
55. Alvarez-Lopez, M.; Pereda, M.D.; del Valle, J.A.; Fernandez-Lorenzo, M.; Garcia-Alonso, M.C.; Ruano, O.A.; Escudero, M.L. Corrosion behaviour of AZ31 magnesium alloy with different grain sizes in simulated biological fluids. *Acta Biomater.* **2010**, *6*, 1763–1771. [[CrossRef](#)] [[PubMed](#)]
56. Birbilis, N.; Ralston, K.D.; Virtanen, S.; Fraser, H.L.; Davies, C.H.J. Grain character influences on corrosion of ECAPed pure magnesium. *Corros. Eng. Sci. Technol.* **2010**, *45*, 224–230. [[CrossRef](#)]
57. Bergmann, W.; Leyens, C.; Fleck, C. *Werkstofftechnik: Grundlagen und Anwendung. Teil 1: Grundlagen*; Hanser: München, Germany, 2013; ISBN 978-3-446-43581-0.
58. Merkel, M.; Thomas, K.-H. *Taschenbuch der Werkstoffe*; 7 Verbesserte Auflage; Fachbuchverlag Leipzig im Carl Hanser Verlag: München, Germany, 2008; ISBN 978-3-446-41194-4.
59. Wang, B.J.; Xu, D.K.; Dong, J.H.; Ke, W. Effect of the crystallographic orientation and twinning on the corrosion resistance of an as-extruded Mg–3Al–1Zn (wt.%) bar. *Scr. Mater.* **2014**, *88*, 5–8. [[CrossRef](#)]
60. Zou, G.; Peng, Q.; Wang, Y.; Liu, B. The effect of extension twinning on the electrochemical corrosion properties of Mg–Y alloys. *J. Alloy. Compd.* **2015**, *618*, 44–48. [[CrossRef](#)]
61. Pawar, S.; Slater, T.J.A.; Burnett, T.L.; Zhou, X.; Scamans, G.M.; Fan, Z.; Thompson, G.E.; Withers, P.J. Crystallographic effects on the corrosion of twin roll cast AZ31 Mg alloy sheet. *Acta Mater.* **2017**, *133*, 90–99. [[CrossRef](#)]
62. Frankel, G.S. Pitting Corrosion of Metals. *J. Electrochem. Soc.* **1998**, *145*, 2186. [[CrossRef](#)]
63. *Corrosion: Fundamentals, Testing and Prevention*; ASM Handbook; ASM International; Cramer, S.D.; Covino, B.S., Jr. (Eds.) ASM International: Materials Park, OH, USA, 2003; ISBN 978-0-87170-705-5.
64. Gawlik, M.; Wiese, B.; Desharnais, V.; Ebel, T.; Willumeit-Römer, R. The Effect of Surface Treatments on the Degradation of Biomedical Mg Alloys—A Review Paper. *Materials* **2018**, *11*, 2561. [[CrossRef](#)] [[PubMed](#)]
65. Lorenz, C.; Brunner, J.G.; Kollmannsberger, P.; Jaafar, L.; Fabry, B.; Virtanen, S. Effect of surface pre-treatments on biocompatibility of magnesium. *Acta Biomater.* **2009**, *5*, 2783–2789. [[CrossRef](#)] [[PubMed](#)]
66. Yoo, B.; Shin, K.R.; Hwang, D.Y.; Lee, D.H.; Shin, D.H. Effect of surface roughness on leakage current and corrosion resistance of oxide layer on AZ91 Mg alloy prepared by plasma electrolytic oxidation. *Appl. Surf. Sci.* **2010**, *256*, 6667–6672. [[CrossRef](#)]
67. Walter, R.; Kannan, M.B.; He, Y.; Sandham, A. Effect of surface roughness on the in vitro degradation behaviour of a biodegradable magnesium-based alloy. *Appl. Surf. Sci.* **2013**, *279*, 343–348. [[CrossRef](#)]
68. Hou, Y.; Li, Y.; Zhang, C.; Koizumi, Y.; Chiba, A. Effects of cold working on corrosion resistance of Co-modified Ni–16Cr–15Mo alloy in hydrofluoric acid solution. *Corros. Sci.* **2014**, *89*, 258–267. [[CrossRef](#)]
69. McCafferty, E. *Introduction to Corrosion Science*; Springer: New York, NY, USA, 2010; ISBN 978-1-4419-0454-6.
70. Chen, H.; Grassian, V.H. Iron Dissolution of Dust Source Materials during Simulated Acidic Processing: The Effect of Sulfuric, Acetic, and Oxalic Acids. *Environ. Sci. Technol.* **2013**, *47*, 10312–10321. [[CrossRef](#)] [[PubMed](#)]
71. *Allgemeines zur Pharmakologie der Metalle—Eisen—Mangan—Kobalt—Nickel*; Heffter, A. (Ed.) Springer: Berlin/Heidelberg, Germany, 1934; ISBN 978-3-642-51955-0.



5.6 Degradation test

Exemplary results of the degradation test for all alloys in AR and 150 s in 5 mL (150_5) condition are shown in Figure 5.13. R^2 was analysed to predict the reliability of the degradation process over time. Simple linear fit in Equation (16) was used to evaluate the degradation rate between day 1 and 30 for AR, ground and 150_5 samples, and between 1 and 14 days for 150_10 and 150_5 respectively. It can be seen from the data in Figure 5.13 a that as-received Mg-2Gd (G2_AR) has the most linear degradation progress with time in contrast to as-received Mg-5Gd (G5_AR) and G10_AR. Figure 5.13 b shows the degradation progress after 150_5 etching. A linear degradation process is determined for all alloys with a reduction in degradation rate for G10. The next section gives an overview of R^2 , and the degradation rate D , mentioned in Chapter 4.8 for alloys and conditions from day 1 to the last day of degradation (14 days or 30 days). A clear benefit of etching before degradation could be identified in this analysis already within 14 days. For this reason, the etching experiments 150_10 and 150_5 were performed for 14 days only in contrast to the other conditions.

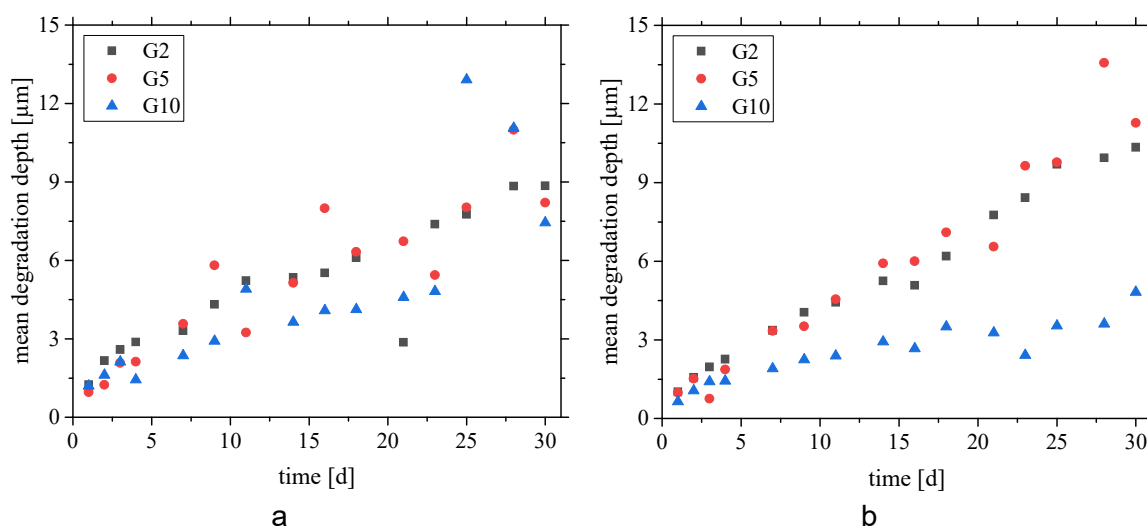


Figure 5.13 Mean degradation depth plotted over time after 30 days degradation for a) as-received G2, G5 and G10, b) etched (150_5) G2, G5 and G10.

The R^2 in Table 5.1 shows an improvement of R^2 after etching compared to AR and ground condition for all alloys. Degradation rate D in Table 5.2 is comparable for all alloys in AR and ground condition. Etched samples showed a higher degradation rate for G2 and G5 compared to G10.

Table 5.1 Overview of R^2 for all alloys and conditions from day 1 to last degradation day (14 or 30 days).

Condition	AR_30	Ground_30	150_5_30	150_10_14	15_5_14
Alloy					
G2	0.81	0.95	0.99	0.97	0.99
G5	0.82	0.75	0.95	0.87	0.98
G10	0.68	0.75	0.86	0.93	0.91

Table 5.2 Overview of degradation rate D for all alloys and conditions from day 1 to last degradation day (14 or 30 days).

Condition	AR_30	Ground_30	150_5_30	150_10_14	15_5_14
Alloy					
G2	0.23 $\mu\text{m}/\text{d}$	0.26 $\mu\text{m}/\text{d}$	0.32 $\mu\text{m}/\text{d}$	0.30 $\mu\text{m}/\text{d}$	0.35 $\mu\text{m}/\text{d}$
G5	0.27 $\mu\text{m}/\text{d}$	0.29 $\mu\text{m}/\text{d}$	0.39 $\mu\text{m}/\text{d}$	0.39 $\mu\text{m}/\text{d}$	0.34 $\mu\text{m}/\text{d}$
G10	0.29 $\mu\text{m}/\text{d}$	0.21 $\mu\text{m}/\text{d}$	0.11 $\mu\text{m}/\text{d}$	0.20 $\mu\text{m}/\text{d}$	0.17 $\mu\text{m}/\text{d}$

5.7 Homogeneity after degradation

5.7.1 Homogeneity of all conditions

As-received

The purpose of the interferometry experiment was to determine the homogeneity after degradation. Figure 5.14 a show the topography of as-received Mg-5Gd (G5_AR) morphology. The cutting marks after milling are visible over the entire sample surface. Figure 5.14 b presents the same sample after three days of degradation. Pits which are formed, destroy the recurring cutting structure. Pit formation lead to an increase in mean valley void volume (Vvv). A pit formation, which is not homogenous distributed like the cutting marks, lead to an increase in standard deviation of mean Vvv, defined as Vvv_dev. A low Vvv_dev corresponds to similar mean Vvv for every square, which defines a homogenous degradation behaviour. A high Vvv_dev implies single deep pit formation. A combination of mean Vvv and standard deviation describes the strength and distribution of the degradation damage.

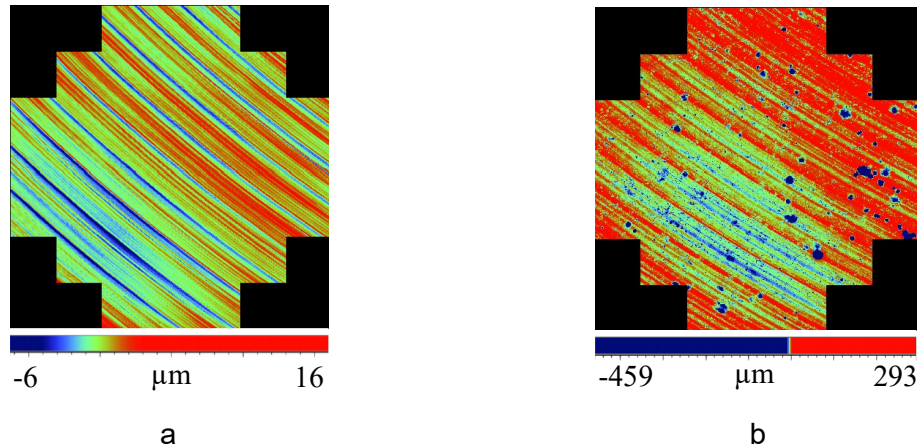


Figure 5.14 WLI topographies of mean Vvv and Vvv_dev determined surface: a) G5_AR before degradation, b) identical G5_AR after 3 days degradation.

The mean Vvv of as-received conditions with the corresponding Vvv_dev is plotted over time in Figure 5.15. The lowest mean Vvv value is determined at day 0 (without degradation) for as-received conditions. The sample on day 3 is the same sample of day 0 after 3 days of degradation for all alloys. By comparing for example day 0 and day 3 of G5, it is visible, that mean Vvv is higher after degradation due to the pit forming, as shown in Figure 5.14 b).

In general, mean Vvv and Vvv_dev of Mg-10Gd (G10) are smaller compared to Mg-2Gd (G2) and G5 until day 11. Starting with day 14, mean Vvv of G10 is mostly in the range of G2 and G5. However, the Vvv_dev after 14 days of G10 is always higher compared to G5 and except of day 23 and 25 also higher than G2. The mean Vvv in the range from 21 to 30 days is around the mean Vvv of day 14 and Vvv_dev is comparable inside this time

range for all alloys. In case of day 14 and day 23 (Figure 5.15) the V_{vv_dev} is even greater than mean V_{vv} . The following text and Figure 5.16 explain the reason for a higher V_{vv_dev} than mean V_{vv} or a V_{vv_dev} in the same range of mean V_{vv} . Figure 5.16 a and b show the comparison between the morphology of G5 and G2 after 23 days degradation. G5 has a lower mean V_{vv} and V_{vv_dev} compared to G2 in Figure 5.15.

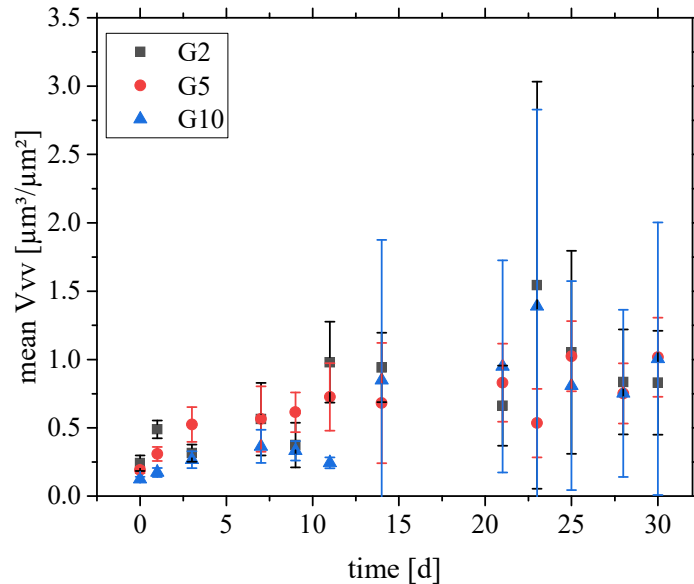


Figure 5.15 Mean V_{vv} of as-received conditions plotted with V_{vv_dev} over time for G2, G5 and G10.

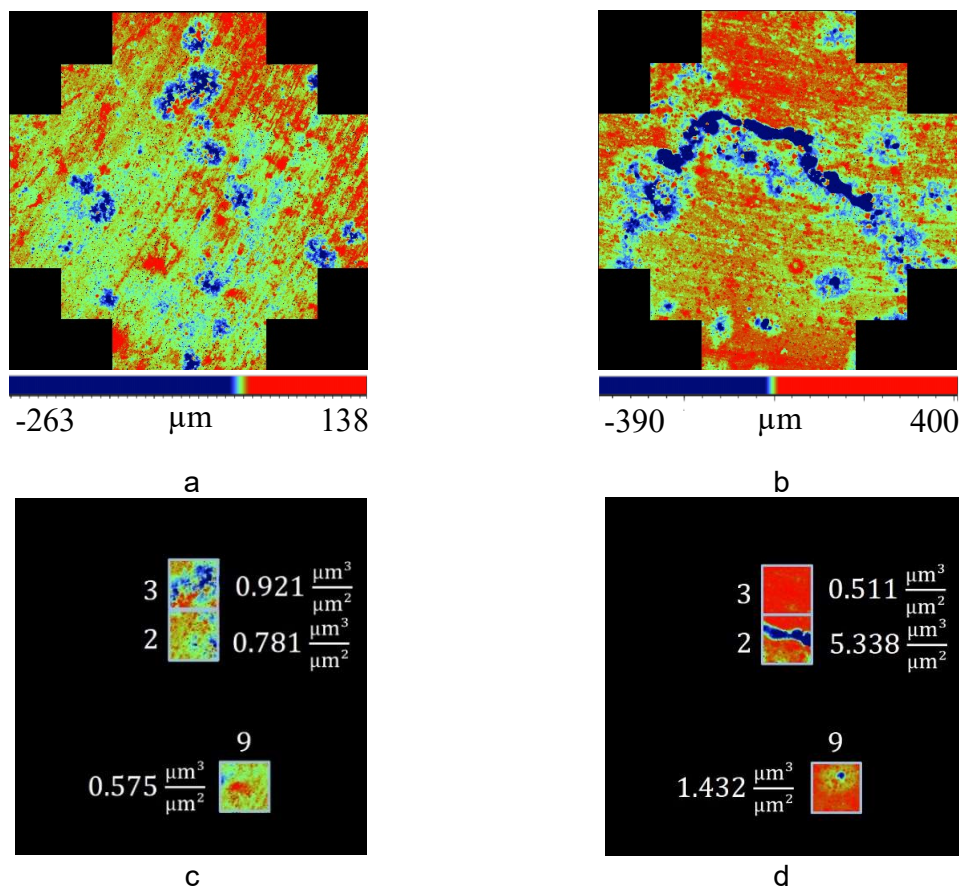


Figure 5.16 WLI topographies of mean V_{vv} and V_{vv_dev} determined surface after 23 days of degradation: a) G5, b) G2, c) cut G5 squares for the regions 2,3 and 9, d) cut G2 squares with severe damage in region 2, nearly no attack in region 3 and a deeper single pit in region 9.

Pits are formed overall the surface, but mostly accumulated in the middle region from top to the bottom in Figure 5.16 a. Especially the left side of G5 is less damaged compared to the middle part. Figure 5.16 b shows a similar pit formation over all the sample of G2. In addition, a strong attack to the surface is visible by removed material in a line shape in the centre of the sample. By comparing the same regions in Figure 5.16 c and d, it is visible that mean V_{vv} of regions 2, 3 and 9 in Figure 5.16 c are more comparable than the same regions of G2 in Figure 5.16 d. In the middle region 2, mean V_{vv} of G2 is highly increased ($5.338 \mu\text{m}^3/\mu\text{m}^2$), while other parts like region 9 are less damaged with single pits ($1.432 \mu\text{m}^3/\mu\text{m}^2$) or nearly not attacked ($0.511 \mu\text{m}^3/\mu\text{m}^2$). The height difference from a square with deeper pits in line shape and a square with no pitting lead to a higher V_{vv_dev} than the mean V_{vv} .

Ground

The mean V_{vv} of ground conditions with the corresponding V_{vv_dev} is plotted over time in Figure 5.17. The lowest mean V_{vv} value and V_{vv_dev} is determined at day 0 for ground condition for all alloys, whereby the mean V_{vv} of all alloys is equal. More linear progress in mean V_{vv} is given for G2 and G5 compared to G10 within the first 14 days. Between day 21 to 30, mean V_{vv} and V_{vv_dev} of G2 and G5 is comparable to day 11 and 14.

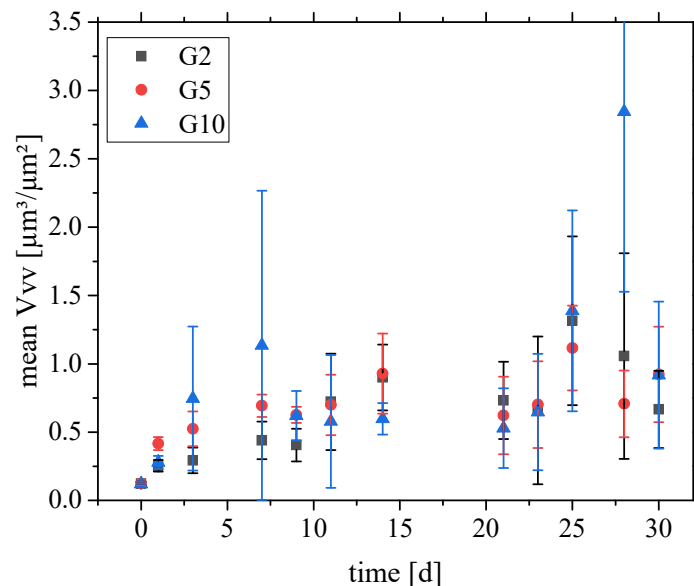


Figure 5.17 Mean V_{vv} of the ground conditions plotted with V_{vv_dev} over time for G2, G5 and G10 before (day 0) and after degradation (day 1 – 30).

There is no further increase with time. G10 showed the strongest variation in mean V_{vv} and V_{vv_dev} from day to day. Figure 5.18 shows the topography of degraded G10 samples after 3, 7, 14 and 28 days. In Figure 5.18 a, bigger pits are illustrated in near-centre region, while some smaller pits are distributed overall the sample. After 7 days degradation, a big hole is formed in the left lower corner of Figure 5.18 b. Besides this, several pits are also distributed over the sample. Compared to Figure 5.18 a, pits after 7 days degradation are bigger in contrast to 3 days degradation. Due to stronger and non-homogenous pit formation after 7 days, the mean V_{vv} and V_{vv_dev} of day 7 is higher than day 3 in Figure 5.17. Instead of further pit size increase, smaller pits compared to day 7 are distributed over the complete samples after 14 days. Even if there are some bigger pits, they are not accumulated on one position, as seen in Figure 5.18 a. Day 28 has the highest mean V_{vv} and V_{vv_dev} in Figure 5.17. Figure 5.18 d shows the morphology of day 28 with strong surface attack. Mean V_{vv} is increased by the strong pit formation, while V_{vv_dev} is increased especially by the accumulation of holes on the left side of the morphology in Figure 5.18 d. On the left side of

the sample, there are more regions with higher mean V_v, while the right side has squares, which are nearly not influenced by pit formation. This pit formation behaviour of all samples from all alloys explain the strong variations in V_v_dev from day to day.

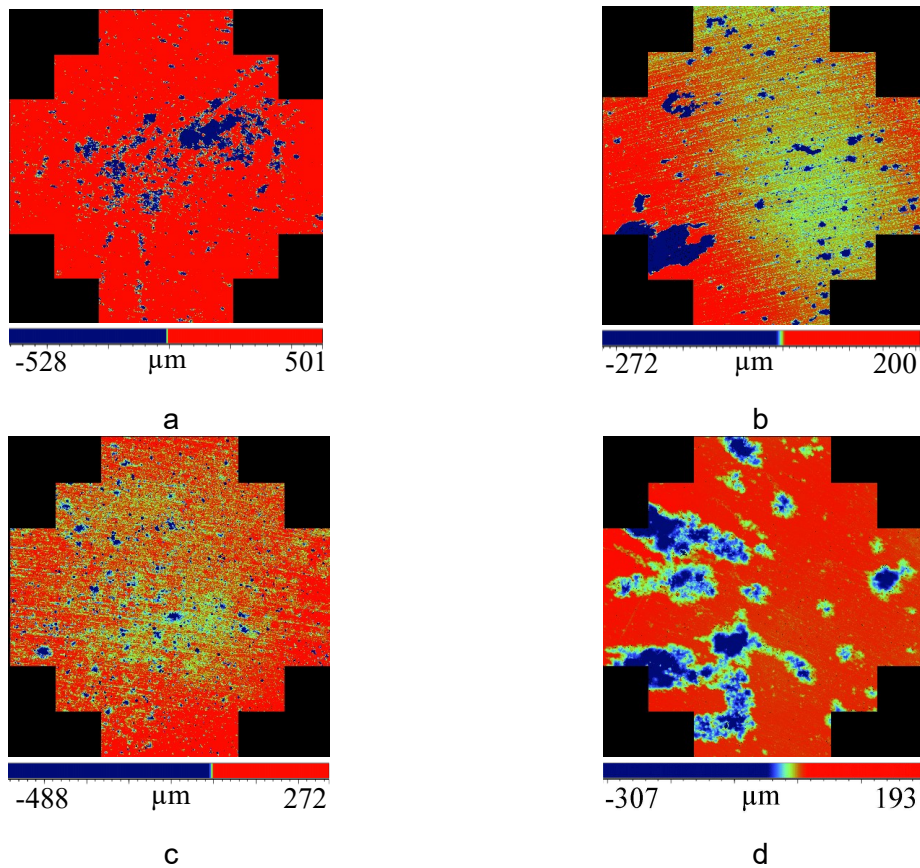


Figure 5.18 WLI topographies of G10 surface after degradation, which was ground before: a) after 3 days, b) after 7 days, c) after 14 days, d) after 28 days.

Etched_150_5

The mean V_v of etched (150_5) conditions with the corresponding V_v_dev is plotted over time in Figure 5.19.

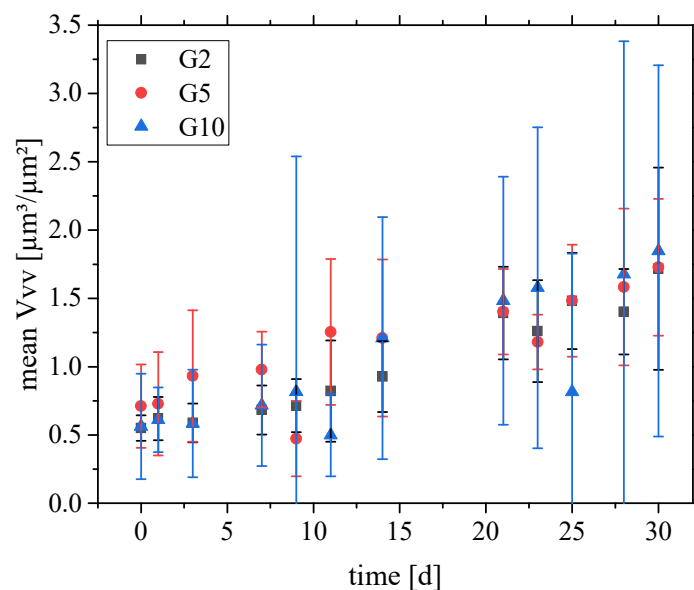


Figure 5.19 Mean V_v of the etched (150_5) conditions plotted with V_v_dev over time for G2, G5 and G10 before (day 0) and after degradation (day 1 – 30).

The mean V_{vv} value and V_{vv_dev} is determined at day 0 for etched condition. Conspicuously, the mean V_{vv} and V_{vv_dev} of day 0 is not the lowest for all alloys and samples, in contrast to Figure 5.15 and Figure 5.17. The reason for this is the formation of pits by the etching process, visible in Figure 5.20 a. After 3 days degradation the degradation progress of G10 is determined with $0.58 \pm 0.39 \mu\text{m}^3/\mu\text{m}^2$ compared to day 0, which amounts to $0.56 \pm 0.39 \mu\text{m}^3/\mu\text{m}^2$. The comparison of Figure 5.20 a and b shows no obvious formation of new pits after 3 days degradation. For this reason, the distribution of pits remains the same. In general, there is an increasing trend with time, with some exceptions for all alloys until day 30. V_{vv_dev} of G2 is lower compared to G5 and G10 inside the time range 0-14 days. V_{vv_dev} is the lowest for G5, when compared with G2 and G10 within day 21 to 30. G10 showed the strongest variation in mean V_{vv} and V_{vv_dev} from day to day. Starting from day 14 the V_{vv_dev} of G10 is dramatically higher compared to G2 and G5. In the case of day 9, 25 and 28 the V_{vv_dev} is even higher than mean V_{vv} of each sample.

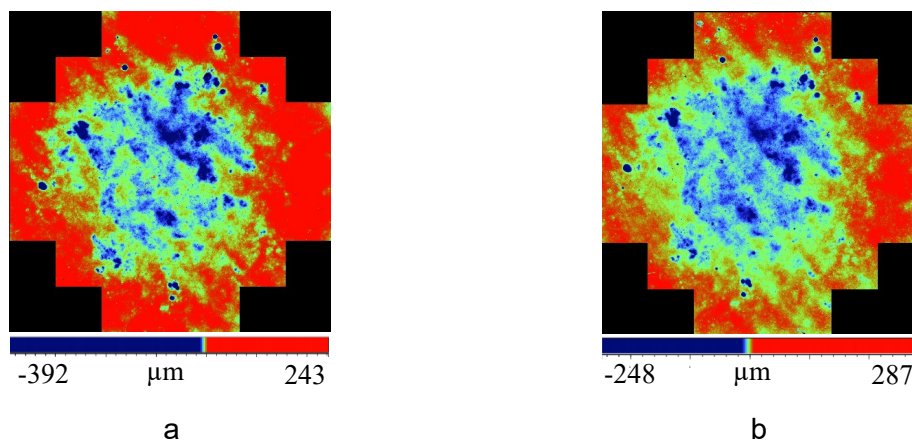


Figure 5.20 WLI topographies: a) G10 – day 0 (150_5), b) G10 – after 3 days degradation.

Etched_150_10

The mean V_{vv} for all alloys is similar at day 0, 1 and 3 in Figure 5.21. Mean V_{vv} of all alloys after three days is comparable with day 0. However, the V_{vv_dev} of all alloys is increasing after three days. A higher increase in mean V_{vv} with time is determined for G5, when compared with G2. Both alloys, G2 and G5 show a more linear behaviour in mean V_{vv} in contrast to G10. In general, G10 has the highest V_{vv_dev} except of day 1 and 11 and the strongest variation in V_{vv_dev} from day to day compared to the other alloys.

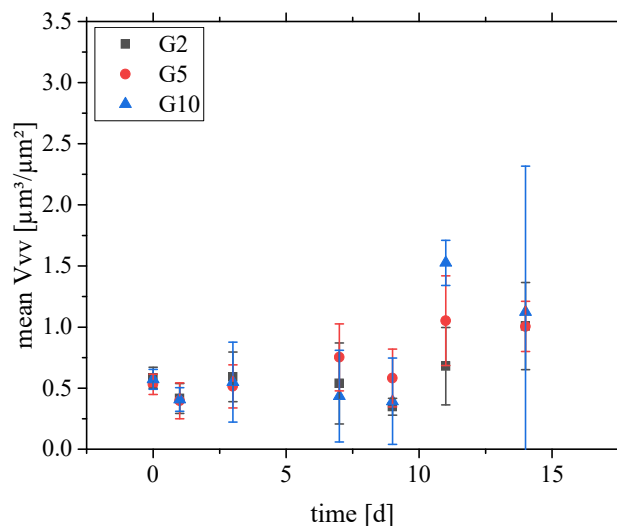


Figure 5.21 Mean V_{vv} and V_{vv_dev} after 150_10 etching and degradation for G2, G5 and G10.

Etched_15_5

The lowest mean V_{vv} and V_{vv_dev} for all alloys is measured for day 0, while the highest mean V_{vv} and V_{vv_dev} is measured for day 14 for all alloys. A trend of decreasing mean V_{vv} with increasing Gd amount is observed in Figure 5.22. The highest mean V_{vv} progress after HAc etching with 15_5 is measured for G2 with the exception of day 7, followed respectively by G5 and G10. Strongest variation in V_{vv_dev} is measured for G10. Except of day 7 and 9, the V_{vv_dev} of G2 is higher compared to G5.

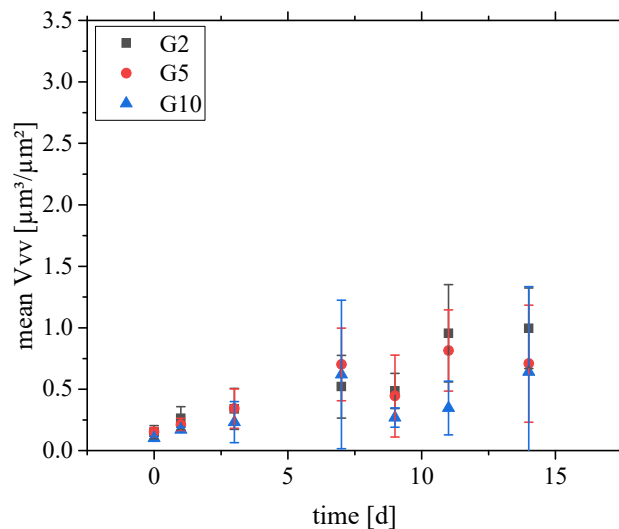


Figure 5.22 Mean V_{vv} and V_{vv_dev} after 15_5 etching and degradation for G2, G5 and G10.

5.7.2 Selected topographies

Figure 5.23 - Figure 5.25 show an overview of all alloys and some exemplary conditions after 14 days degradation with corresponding mean V_{vv} and V_{vv_dev} . In general, the mean V_{vv} and V_{vv_dev} of G2 for all conditions is comparable in a range from 0.90 – 1.01 $\mu\text{m}^3/\mu\text{m}^2$ and 0.24 – 0.36 $\mu\text{m}^3/\mu\text{m}^2$, respectively. The highest mean V_{vv} is measured for G5 and G10, when etched before degradation for 150 s. G2 and G5 show a more similar pit forming behaviour with clustered degradation residues inside the pits compared to G10. The pit development of as-received samples for each alloy (Figure 5.23 a-c) and 15_5 etched samples (Figure 5.25 a-c) are comparable. Likewise, both 150 s etched conditions exemplarily shown on 5 mL in Figure 5.24 a-c, are similar in kind of pit formation, when comparing the same alloy.

As-received

For the as-received samples, the cutting marks are still visible after 14 days degradation for all alloys Figure 5.23 a – c). G2 has the highest amount of pit formation, which is distributed over the complete sample (Figure 5.23 a). For this reason, the mean V_{vv} is the highest for all as-received alloys. Due to a spreading of pits over the complete samples, the V_{vv_dev} is smaller compared to G5 and G10. Red spots are detected inside the blue valleys. G5 has a lower mean V_{vv} and higher V_{vv_dev} , based on lower and widely spaced pit development. Some red plateaus inside the blue parts are shown (Figure 5.23 b). The mean V_{vv} of G10 is in-between G2 and G5 but has the highest V_{vv_dev} . Bigger and more elongated holes are formed often inside the grooves of the cutting marks (Figure 5.23 c). The holes are more crowded on one side of the sample. The irregular pitforming lead to a non-homogenous degradation in (Figure 5.23 c), visible in a V_{vv_dev} of 1.03 $\mu\text{m}^3/\mu\text{m}^2$.

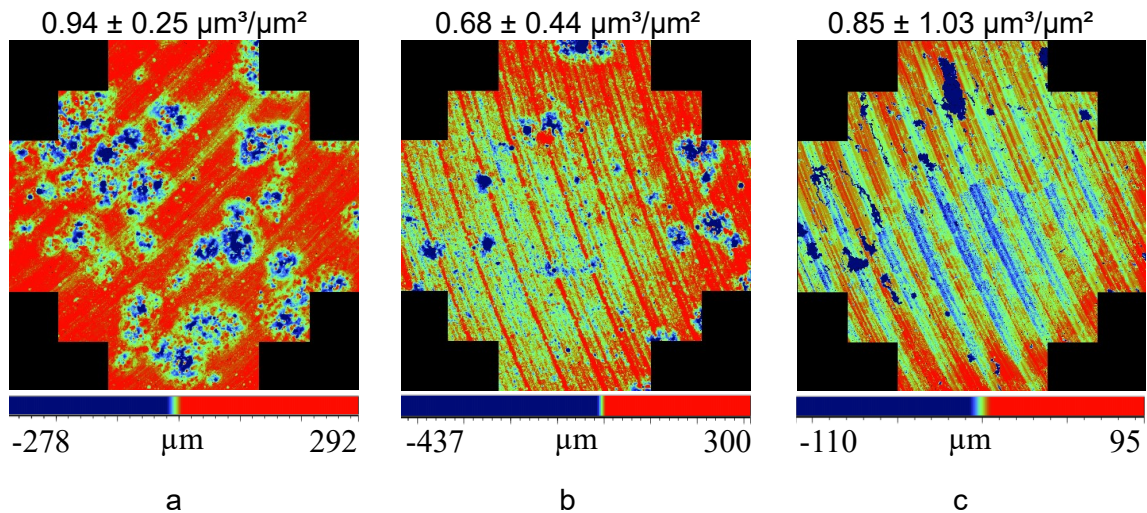


Figure 5.23 WLI topographies of AR samples after 14 days of degradation: a) G2 with highest amount of degradation pits, b) G5 with lower number and widely distributed degradation pits, c) G10 with bigger and irregular degradation pit forming.

Etched_150_5

The mean V_{vv} and V_{vv_dev} is rising with higher Gd amount for etched (150_5) samples in Figure 5.24 a – c. G2 has the lowest mean V_{vv} and V_{vv_dev} with smaller pits. The degradation of G5 seems to be more homogenous compared to G2, due to a pit distribution over the complete sample. However, deeper and bigger etching pits, which are still visible in Figure 5.24 b lead to a less homogenous surface dispersion in contrast to G2 (Figure 5.24 a). G10 has the highest V_{vv_dev} through the formation of bigger, irregular distributed holes (Figure 5.24 c). Red spots inside the valleys are less recognizable compared to AR samples in Figure 5.23.

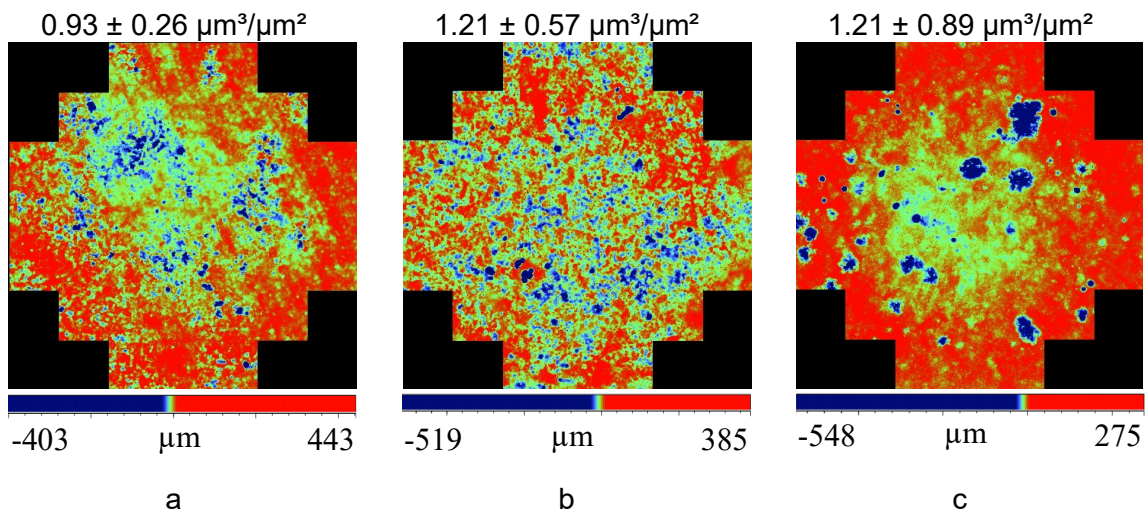


Figure 5.24 WLI topographies of etched (150_5) samples after 14 days degradation: a) G2 with smaller pits distributed over the surface, b) G5 with optical more homogenous distribution than G2, c) G10 with a formation of deeper and more irregular distributed degradation pits.

Etched_15_5

For 15_5 etching, the mean V_{vv} is decreasing with higher Gd amount, while the V_{vv_dev} is increasing with higher Gd amount. Mean V_{vv} is decreasing with less pits, but V_{vv_dev} increasing, due to irregular pit surface distribution (Figure 5.25 a – c).

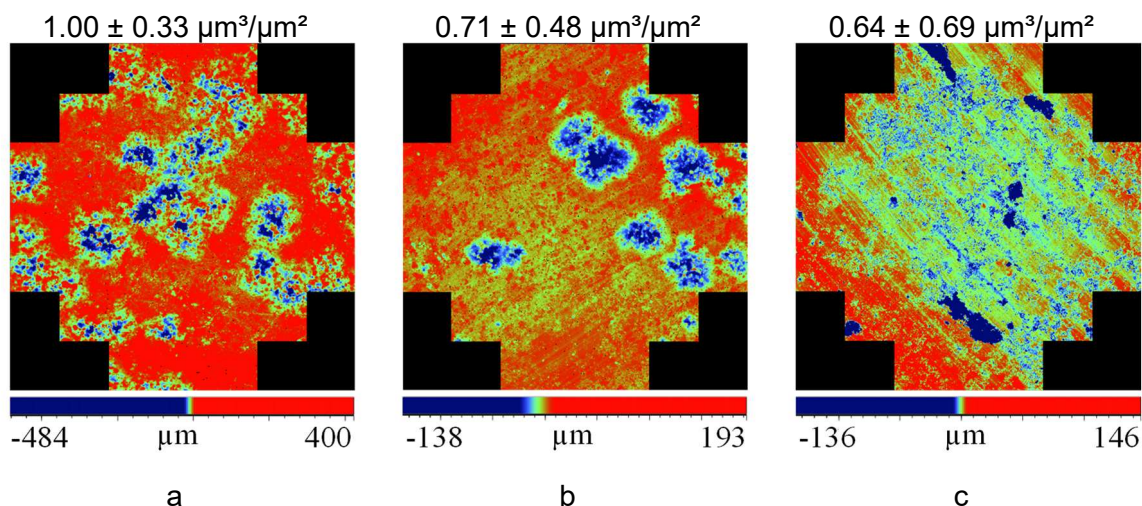


Figure 5.25 WLI topographies of etched (15_5) samples after 14 days degradation: a) G2 with degradation pits spread over the complete surface, b) G5 with with some bigger and clustered degradation pits; c) G10 with bigger elongated holes.

5.8 Particle induced micro-galvanic degradation

Comparing all mean V_{vv} results, it can be seen that mean V_{vv} is increasing in most cases during the first 14 days. The comparison to mean V_{vv} values between day 21 to 30 with mean V_{vv} of 14 days shows, that mean V_{vv} are often equal or in the same range. In addition to that, plateau forming is starting to develop with day 11 and day 14, which are observed inside developed pits (Figure 5.26).

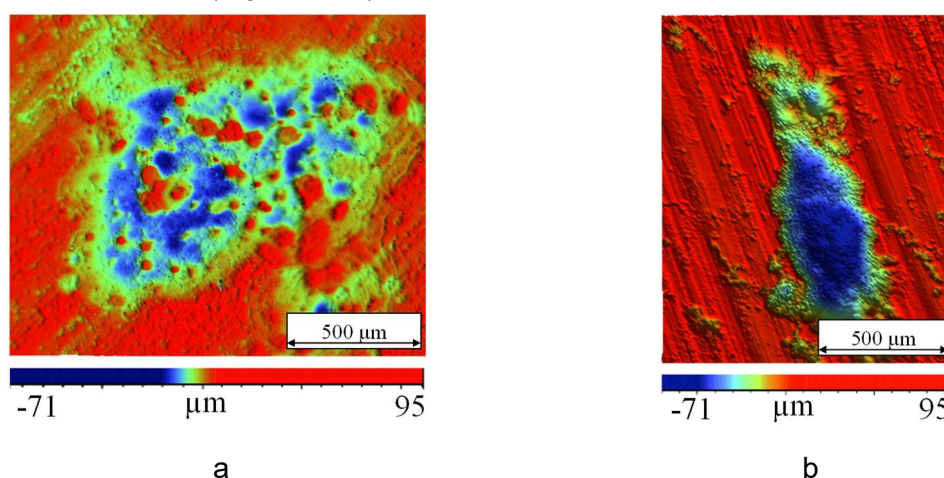


Figure 5.26 WLI topographies of pits after 14 days degradation: a) G2 with red higher plateaus, b) G20 with a bigger pit without plateaus.

SEM and EDX analysis were done for samples after 14 days degradation to investigate the reason for the pit formation around plateau or volcano shaped degradation residues. Different particles were determined in near-centre of these pits, which are shown in Figure 5.27. This phenomenon is defined as particle induced micro-galvanic degradation (PID) in this study. As examples typical plateau shaped degradation residues inside degradation pits are shown for G2 and G5. Rectangular shaped particles are found in all G2 conditions, which often stick together (Figure 5.27 a and b). Next to Mg, these particles consist of a high amount of Gd (49.8 – 68.9 wt.% in Table 5.3 a and b) and Si (12.5 - 15.3 wt.% in Table 5.3 a and b).

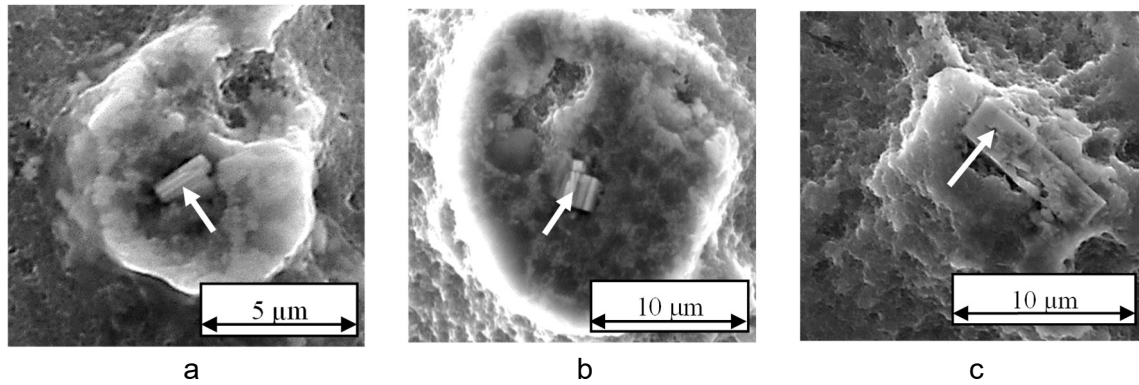


Figure 5.27 Gd rich and rectangular shaped particles on plateau shaped degradation residues inside: a) G2_AR, b) G2_150_10, c) G5_AR.

This kind of joined cuboids were only seen in G2. Single cuboids were found in all G5 conditions inside the plateaus (Figure 5.27 c) with a higher content of Gd (73.2 wt.% in Table 5.3 c) and Si (15.6 wt.% in Table 5.3 c) next to Mg.

Table 5.3 Element distribution of Gd rich particles located on plateau shaped degradation residues.

Elements	G2_AR (a)	G2_150_10 (b)	G5_AR (c)
Mg [wt.%]	37.7	15.8	11.2
Gd [wt.%]	49.8	68.9	73.2
Si [wt.%]	12.5	15.3	15.6
Gd [at.%]	13.7	26.8	31.4
Si [at.%]	19.3	33.3	37.4
Gd/Si [at.%/at.%]	0.71	0.80	0.84

For further analysis, the morphology after 14 days degradation was measured by WLI and compared to the SEM for 14 days degraded samples. As an example, one degraded sample of G10, which was etched for 150 s and 10 ml before degradation, is shown in Figure 5.28.

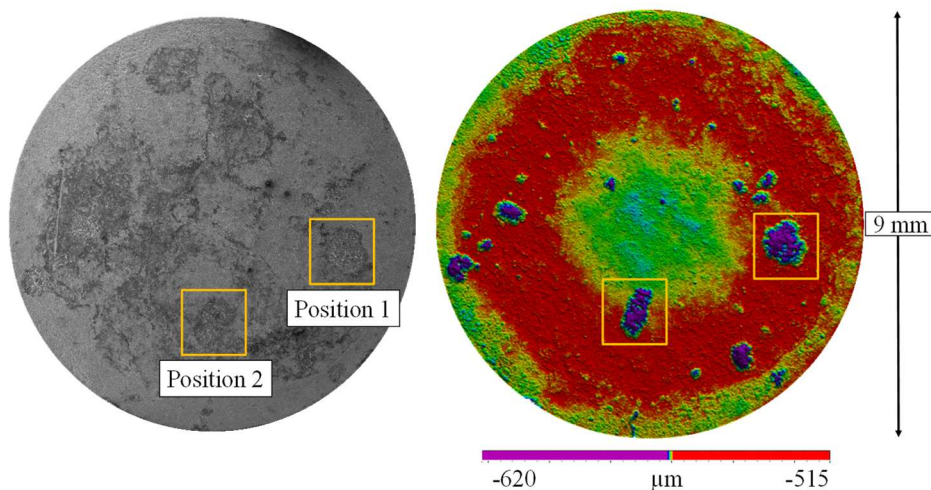


Figure 5.28 Surface morphology determined by SEM and WLI topography measured by WLI for etched (150_10) G10 after 14 days degradation.

This condition was chosen, due to huge holes and less plateaus. In general, every condition and alloy showed a plateau forming, except of G10_AR after 14 days degradation. The left side in Figure 5.28 shows the morphology, measured by SEM, while the right sight is

determined by WLI. Typical pits were found, which had plateau shaped degradation residues inside in Figure 5.28. Two position were chosen to analyse particles by SEM/EDS.

A plateau was analysed in Position 1 (Figure 5.29). Near the centre of the degradation residue was a single rectangular shaped particle, which had a crack inside.

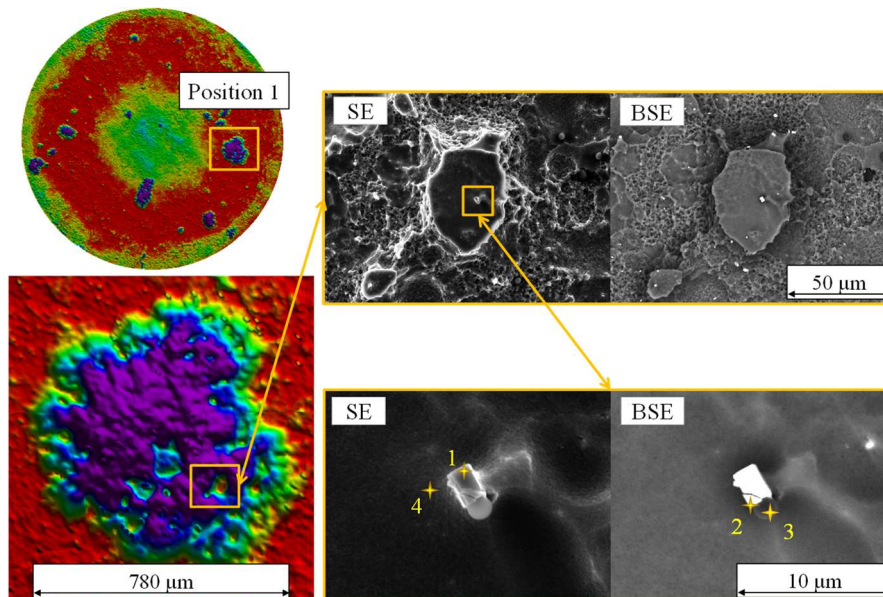


Figure 5.29 Magnified Gd rich rectangular shaped particle (SEM) on a plateau at position 1 (WLI) for the etched (150_10) and degraded (14 days) G10 alloy.

EDS measured for point 1 next to Mg, a high Gd content (70.8 wt.%) and a higher amount of Si (14.4 wt.%). For point 2, a higher amount of O (16.8 wt.%) was found, while the amount of Gd (32.7 wt.%) and Si (7.63 wt.%) was lower compared to point 1. Point 3 was taken on a bubble-like structure. For this point, the O (22.8 wt.%) amount was higher than the Gd (7.0 wt.%) and Si (0.5 wt.%) amount. An EDS taken on the plateau next to the particle (point 4), revealed an amount of 9.3 wt.% Gd next to Mg, which coincides with the expected Gd matrix amount of 9.6 wt.% (Table 4.2).

A smaller plateau was additionally found in position 1 (Figure 5.30). Two bright particles were seen on it.

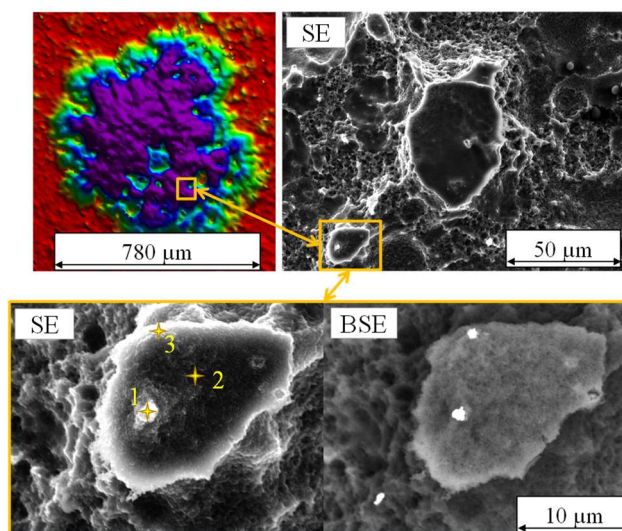


Figure 5.30 Determined particles (SEM) on a plateau on position 1 (WLI) for the etched (150_10) and degraded (14 days) G10 alloy.

The particle on point 1 does not have a rectangular shape and was not located directly on the flat plateau surface like in Figure 5.29. Moreover, it is assumed that the particle is inside a degradation residue. Inside this particle on point 1, a higher amount of Gd (22.9 wt.%) was found again. Next to Mg and Gd, also Fe (23.6 wt.%), Al (3.4 wt.%) and Si (2.6 wt.%) were detected. An amount of 8.6 wt.% Gd was measured directly on the plateau on point 2, where no particles were observed. The second bright particle on point 3, which is shown in the BSE picture of Figure 5.30, has a high Gd (26.6 wt.%) content, but no rectangular shape was detected.

Position 2 showed also several plateau shaped degradation residues in the WLI topography and SEM (Figure 5.31). On one spot several rectangular shaped particles were found on a volcano shaped residue. The surface was not flat, as seen before in Figure 5.29 and Figure 5.30. It is assumed, that the particles inside the matrix lead to a complete dissolution around the particles. The particles (Figure 5.31) inside (point 1 -3) had next to Mg a higher Gd (48.0 – 62.9 wt.%) and O (7.2 – 13.3 wt.%) amount. Point 4 showed again an expected Gd amount of 15.9 wt.% closer to the matrix material.

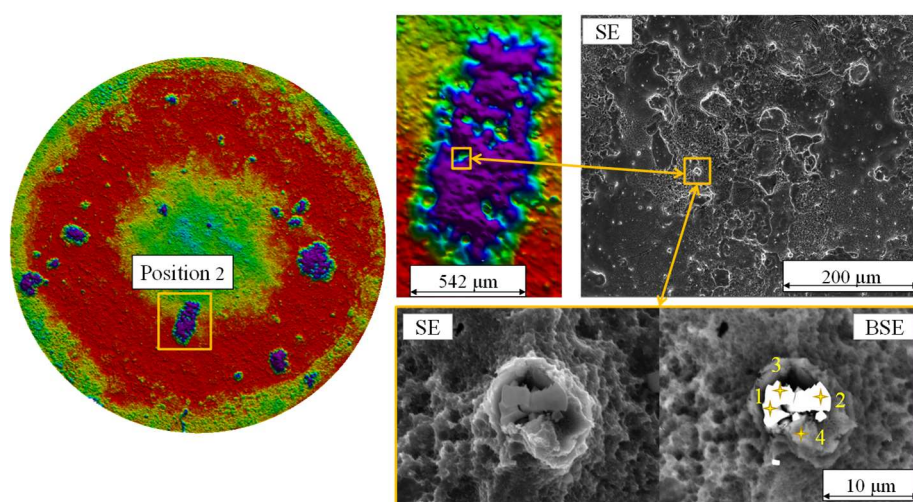


Figure 5.31 WLI topographies and SEM images of etched (150_10) and 14 days degraded G10 alloy. Accumulation of Gd rich and rectangular particles inside a degradation residue.

A bigger plateau shaped deposit in pit position 2 showed a non-rectangular shaped particle (Figure 5.32). The particle is located on a tip of triangular first plateau, whereas the right side next to the particle is degraded and a deeper second plateau is formed.

One measurement on the particle (point 1) detected a higher Gd (48.3 wt.%) amount, followed by a combination of Fe (4.9 wt.%), Al (1.9 wt.%) and Si (8.3 wt.%). The Si amount in Figure 5.32 is higher and the Fe amount distinctly lower compared to point 1 in Figure 5.30.

Altogether, rectangular shaped particles with high Gd amount were found for all alloys and conditions after 14 days degradation, except G10_AR as determined exemplary in Figure 5.27. There were also Gd rich particles, where it was not possible to identify the shape of the particle due to a small size. Only G10 showed Gd rich particles, where Fe was additionally detected by EDS (Figure 5.30 and Figure 5.32).

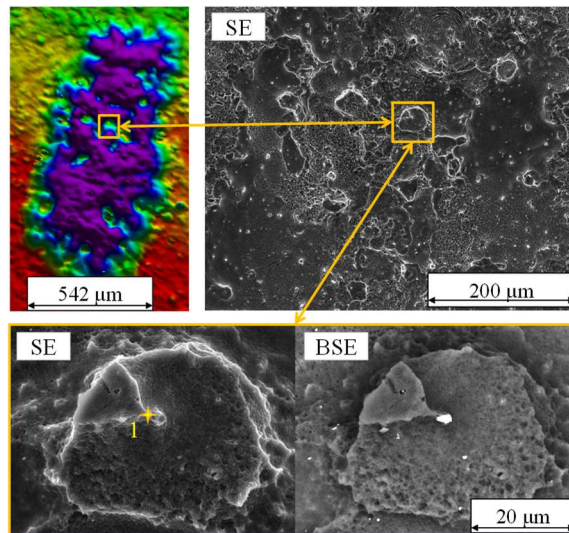


Figure 5.32 WLI topography and SEM images of etched (150_10) and 14 days degraded G10 alloy with one particle.

5.9 Effect of HAc etching on the degradation behaviour

Further degradation experiments on HAc etched Mg-5Gd samples were shown in following publication:

“The Effects of HAc Etching on the Degradation Behavior of Mg-5Gd” [56]

The Effects of HAc Etching on the Degradation Behavior of Mg-5Gd

¹*Marcjanna Maria Gawlik, ¹Markus Steiner, ¹Björn Wiese, ¹Jorge González, ¹Frank Feyerabend, ²Michael Dahms, ¹Thomas Ebel, ¹Regine Willumeit-Römer

¹ Institute of Materials Research, Division Metallic Biomaterials, Helmholtz-Zentrum Geesthacht, Germany

²Hochschule Flensburg, Germany

*Corresponding author (marcjanna.gawlik@hzg.de)

Abstract – The effects of different acetic acid (HAc) etching procedures were investigated using Mg-5Gd samples in as-extruded and T4 conditions in order to achieve defined surfaces and homogenous degradation behavior. Samples were dipped into HAc solution with five different concentrations for three durations. In total, fifteen different etching conditions were tested with regard to the degradation resistance in physiological solution. The cell culture medium consisted of Dulbecco's Modified Eagle Medium (DMEM), Glutamax, 10 Vol.-% fetal bovine serum (FBS) and 1 Vol.-% Streptomycin/Penicillin solution. A screening test was performed to select the etching combinations with the lowest initial mean degradation depth. The most promising etching procedures were chosen for further long term degradation tests lasting up to 30 days in cell culture medium. The surfaces of the etched samples and for selected samples after degradation were characterized by interferometry, OM, SEM, and XRD to correlate the influence of morphology, roughness and microstructure on the degradation rate. Etching with 250 g/L HAc and 150 s leads to the most uniform degradation with low degradation rate compared to non-etched Mg-5Gd.

Keywords – acetic acid etching, biodegradable magnesium, degradation rate, surface characterization

1. INTRODUCTION

Mg degrades in aqueous solutions and produces a layer of magnesium hydroxide and hydrogen gas [1]. Aqueous salt solutions, including for example chloride ions, are particularly able to dissolve the protective magnesium hydroxide layer which leads to an acceleration of the degradation process [2]. Furthermore, impurities like Fe, Ni, Co and Cu or phases with high electrochemical potential difference to the Mg-matrix increase the degradation rate due to micro or macro galvanic corrosion [3]. To adjust the mechanical and degradation properties alloying elements and different processing steps are introduced. Mg alloys containing specific rare earth (RE) elements including Gd are used because their solubility increases with temperature which allows mechanical and degradation properties to be tailored by heat treatments. With a high solid solubility secondary phases are avoided, which improves the degradation behavior [4]. However, some Mg-RE alloys also contain hydride particles which can react with the Mg as galvanic cell and produce Mg(OH)₂ phases around these particles. Higher RE content in the alloy increases the amount of hydrides produced [5]. But it has been also reported that a content of Gd < 15.-wt % reduces the degradation rate [4]. Furthermore Gd was reported as an appropriate element in terms of cytotoxicity for biodegradable materials [6]. Some reports confirm that the degradation behavior of Mg alloys can be improved by chemical surface treatments. Etching for example is an effective method for removing surface contaminations resulting from the production process [7, 8]. In addition, it removes twins near the surface region. Twins

act as additional weak points on the surface due to the reduction of the equilibrium potential at these locations [9]. Moreover, chemical surface treatments are able to improve the initial condition of the entire surface. This is necessary to achieve reproducible results regarding homogeneous degradation and linear degradation rate.

Aims of the study:

- Analyse the effects of acetic acid (HAc) etching on the morphology and microstructure of Mg-5Gd
- Evaluate the ideal surface treatment regardless of the processing route
- Ensure a reproducible degradation rate

2. MATERIAL AND METHODS

Material

For this study Mg-5Gd was used. Direct chill casting was performed with high purity Mg (99.95 %, Supplier: Magnesium Elektron) and Gd (>99.9 %) at 650 °C in a preheated mold. Afterwards the material was solution heat treated at 550 °C for 6 hours. The material was extruded at a speed of 3-4 mm/s at 430 °C. The diameter after extrusion was 12.0 mm. After machining, the rods were milled into discs with a diameter of 10.0 mm and a height of 1.5 mm. In the following, these discs are referred to as as-received samples (AR).

Etching procedure

The as-received samples were immersed in 3 ml hexane for 40 min in an ultrasonic bath to degrease the samples and to remove contaminations originating from production. HAc

solutions with concentrations of 100 g/L, 150 g/L, 200 g/L, 250 g/L and 300 g/L were prepared. The samples were immersed into a clock glass filled with 5 ml of HAc solution and samples were immersed for durations of 90 s, 120 s or 150 s. To stop the reaction, the samples were immersed in 40 mL of 1 mol/L NaOH for 30 s, followed by dipping these into 40 mL distilled water. After another dip into 40 mL of acetone and drying the sample with a piece of lint-free tissue, the samples were cleaned again in hexane for 40 min in an ultrasonic bath. After that, each sample was put into a falcon tube and filled with 3 ml of 70 % ethanol. The sterilization with ethanol necessary for the immersion tests under cell culture conditions was performed for 20 min in an ultrasonic bath. All specimens were weighed before and after cleaning and etching using an electronic balance (Sartorius, accuracy: 0.1 mg). To calculate the etching depth, the diameter and height of the discs were also measured before and after etching using callipers.

Degradation

- Short-term degradation test: To compare the effects of etching on the degradation behavior, 15 different testing series were analyzed by using a 24 h short term degradation test (n=6). The degradation behavior of the different samples was analyzed by immersing the samples into Dulbecco's Modified Eagle Medium (DMEM), Glutamax, 10 Vol.-% fetal bovine serum (FBS) and 1 Vol.-% of Streptomycin and Penicillin under cell culture conditions (37 °C, 5 % CO₂, 20 % O₂, 95 % relative humidity). After one day, six samples of each test series were taken out, washed with distilled water and dried for 24 h in a vacuum chamber. Following drying, the samples were weighed again. The degraded samples were treated with chromic acid for 20 min to remove the degradation layer. Afterwards, the specimens were dried for one hour and weighed again to calculate the weight of the corrosion layer. The mean degradation depth which can be considered the amount of surface removed was evaluated from mass loss using the formula:

$$d = \frac{\Delta m}{\rho \cdot A} \cdot 10^4 \quad (1)$$

Here, d is the degradation depth in μm ; Δm is the mass loss in g, measured by the weight before degradation and after removal of degradation products; ρ is the density in $\frac{\text{g}}{\text{cm}^3}$; A is the surface area in cm^2 .

- Long-term degradation test: After evaluating the short-term degradation results, the etching methods with lowest mean degradation depths and standard deviations were used for the 30-day degradation tests. The preparation, degradation and removal processes were identical to those of the short-term test. In order to verify if etching with HAc affects the degradation behavior, as-received samples were also used for the degradation experiments. As-received samples received a minor additional treatment. They were put into falcon tubes filled with ethanol and then moved to the clean bench for further preparation. This procedure was executed to preserve the sterile area of the clean bench, where the degradation experiments were arranged. In the 30-day degradation test, one sample per day was removed out of the medium within the first week. Further samples were removed after every second day starting from the second week. In total

15 samples were measured per test series. The degradation depth was plotted over time. A linear fit was calculated over 15 measurement points. The slope of the linear fit is the degradation rate D. The degradation rate D was fitted linearly according to this formula as introduced by [10]:

$$d(t) = D \cdot t + d_0 \quad (2)$$

Here, d(t) is the degradation depth at time point t in μm ; D is the degradation rate in $\mu\text{m}/\text{day}$; t is the time in days; d_0 is the intersection of the linear fit with the y-axis.

Microstructure and surface characterization

- Microstructure: Metallographic preparation of cross sections was performed to analyze the deformation and twinning zone by optical microscopy (Leica DMI 5000 M). The twinning depth was measured by length measurement from the surface edge inwards into the sample by use of the Software analySIS pro. A mean value and standard deviation was calculated for as-received conditions using 18 positions.

- Interferometry: The surfaces of the samples were investigated at 5x magnification by an Interferometer (Bruker Contour GT-K) after etching and after the 30-day degradation period for one as-received sample and the evaluated combination of conditions. The surface topography and roughness was analyzed by the software Vision64. For surface characterization, the raw data was fitted using the F-Operator (cylinder and tilt) to remove the nominal shape. Afterwards the measured area was cut by use of the 3D Filter Mask Data into a measurement area of 8 mm to avoid effects from the surface edge region on the roughness. This was necessary due to the fact that some edges of the samples were damaged by the milling process.

- X-ray diffraction: Glancing angle x-ray diffraction was performed by Bruker D8 ADVANCED at an angle of 3°. Parallel beam setup was used with an aperture size of 0.6 μm . The measurements were carried out by a Cu anode (0.15418 nm). 2 θ was set between 3° and 80°. Diffraction patterns were interpreted by the software DIFFRAC.EVA and Pearsons Crystal Data [11].

- SEM and EDX: The morphology was determined by Tescan Vega III SB after 2 days of degradation and removal of the degradation layer of the chosen combination of etching conditions. The analysis was carried out using 15 kV. The EDX point analysis and quantification was performed with the software Iridium Ultra.

3. RESULTS AND DISCUSSION

After 24 hours of short-term degradation it is visible in Figure 1 that the HAc etching reduces the mean degradation depth of Mg-5Gd in most cases. Only a combination of 100 g/L and 150 s does not decrease the mean degradation depth. The value of the mean degradation of the as-received Mg-5Gd samples is $3.1 \pm 1.5 \mu\text{m}$. The standard deviation of the as-received samples is higher compared to the etched conditions. Particularly, etching with a concentration of 150 g/L for 150 s leads to a reduction of the mean degradation depth. The combinations of 150 g/L for 150 s, 250 g/L for 150s and 300 g/L for 90 s were chosen for further long-term degradation testing due to their lowest mean degradation depth and standard deviation. Further results and

discussions were carried out on the samples of these chosen conditions.

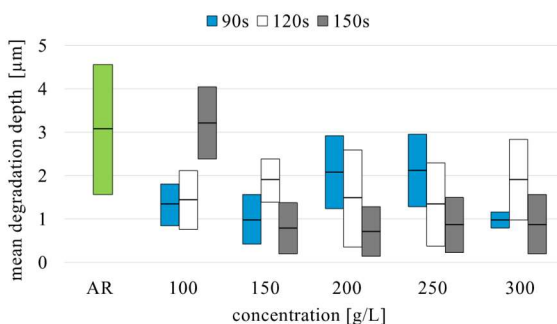


FIGURE 1
DIAGRAM OF THE MEAN DEGRADATION DEPTHS (ACCURACY: 0.3 µm) AND STANDARD DEVIATIONS OF 6 SAMPLES FOR EACH CONDITION AFTER 24 H SHORT-TERM DEGRADATION.

As-received samples show a difference in microstructure in regions near the surface and bulk material. Figure 2 illustrates the near-surface regions of one as-received sample and the etched samples. For the as-received sample, the grain structure is deformed, followed by high accumulation of twins. After etching it is visible that, for all etching conditions, the deformation zone is removed. Stronger twinning is only detectable for etching conditions of 150 g/L for 150 s and 300 g/L for 90 s. Comparison of the microstructures and the calculated etching depths reveals that the condition of 250 g/L for 150 s has the highest etching depth. It is the only condition that completely removes the microstructural changes originating from the production process whereas the conditions of 150 g/L for 150 s and 300 g/L for 90 s remove a similar amount of material corresponding to a comparable amount of remaining twins.

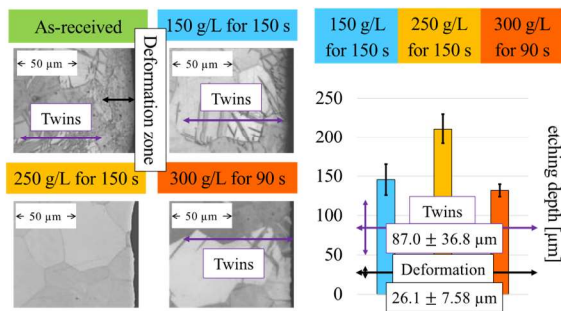


FIGURE 2
MICROSTRUCTURE OF THE CROSS SECTION OF ONE AS-RECEIVED SAMPLE AND ONE ETCHED SAMPLE PER CONDITION AND COMPARISON WITH THE CALCULATED ETCHING DEPTH.

White light interferometry measurements on the remaining cutting marks of the milling process confirm similar etching depths for the etching parameters 150 g/L for 150 s and 300 g/L for 90 s as visible in Figure 3. Compared to the as-received sample in Figure 3, the roughness of etched samples described by Sa (arithmetic mean height) and Sq (the root mean square height) [12] is higher due to pit formation. The pit formation for the condition 250 g/L for 150 s is stronger but more uniformly distributed. Moreover, milling marks are completely removed. The roughness of the samples increases

after 30 days of degradation due to degradation and stronger pit formation. For all 30-day samples no milling marks are visible anymore. Figure 3 shows after degradation that the pits of the as-received sample and the samples with conditions of 150 g/L for 150 s and 250 g/L for 150 s are more homogeneously distributed compared to the conditions of 300 g/L for 90 s.

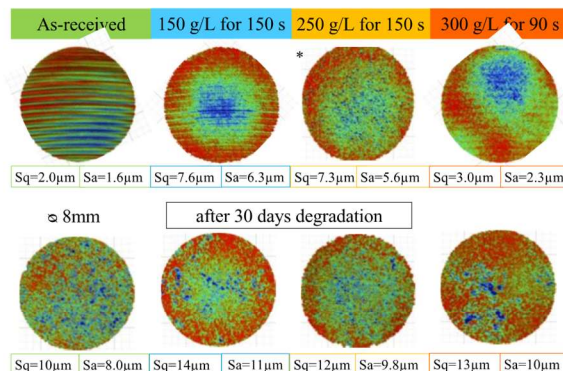


FIGURE 3
3D SURFACE PROFILES OF AS-RECEIVED, ETCHED AND DEGRADED SAMPLES MEASURED BY WHITE LIGHT INTERFEROMETRY (WLI).
* MEASUREMENT NOT COMPLETED DUE TO HEIGHT RANGE PROBLEMS, ROUGHNESS VALUES CAN VARY ± 0.7 µm.

Further surface investigations were performed before and after etching with XRD measurements. Figure 4 shows that at a glancing angle of 3° no GdH₂ peaks are detectable for all the as-received samples investigated.

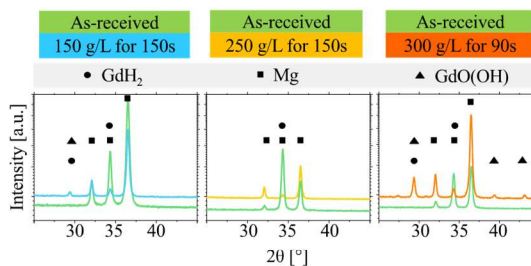


FIGURE 4
XRD PATTERN OF MEASUREMENTS AT A GLANCING ANGLE OF 3° BEFORE (AS-RECEIVED) AND AFTER ETCHING.

After 150 g/L for 150 s etching, the GdH₂ main peak is detectable, which confirms that GdH₂ is formed by etching. After 250 g/L etching, no GdH₂ is found in these samples. Therefore, it can be assumed that this etching procedure removes material from the surface without producing high amounts of GdH₂. It is visible that after the etching procedure 300 g/L for 90 s Gd rich particles like GdH₂ and GdO(OH) were formed. Gd rich particles within the etching holes were also found by SEM as seen in Figure 5 after 2 days of degradation. Rectangular shaped particles with high amounts of Gd are reported as GdH₂ [13]. However, due to the small sizes of the particles inside the etching holes, it is not possible to distinguish between GdH₂ and GdO(OH) by SEM. Figure 5 shows the difference in the amount of Gd rich particles inside the etching holes of different etching conditions. It is assumed that Gd rich particles are formed

during the etching process inside the holes and that particles already present beforehand are not dissolved by etching and falls into the etching pit.

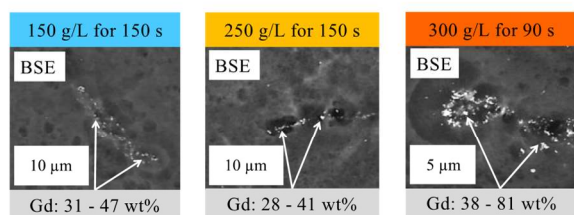


FIGURE 5
SEM/EDX ANALYSIS OF ONE ETCHING PIT AFTER 2 DAYS OF DEGRADATION FOR EVERY CONDITION. GD RICH PARTICLES ARE FOUND ON THE BOTTOM OF THE ETCHING PIT.

In terms of degradation rate, it is visible in Figure 6 that acetic acid etching leads to a reduction of the degradation rate and to a minor scattering of single measurement points. The standard deviation of the mean degradation depth ($\pm 0.3 \mu\text{m}$) was excluded out of Figure 6 for clarity. For as-received samples the degradation rate amounts to $0.50 \mu\text{m}/\text{day}$ with a non-linear degradation behavior. In comparison, the degradation rate of etched samples amounts to a value of around $0.30 \mu\text{m}/\text{day}$.

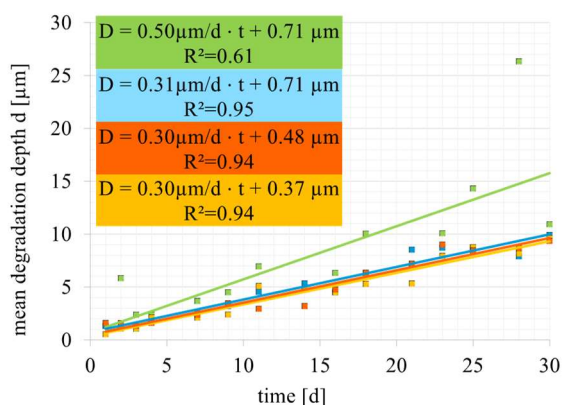


FIGURE 6
GRAPH OF PLOTTED DEGRADATION DEPTH OVER TIME. THE SLOPE OF THE LINEAR FIT IS EQUAL TO THE DEGRADATION RATE.

Due to the fact that all etched conditions lead to a similar linear degradation rate with high linear regression ($R^2 \sim 0.94$), it is assumed that the morphology and roughness after etching does not contribute to the degradation rate. It is reported that twins have an influence on the degradation resistance [9]. Therefore, it is presumed that the removal of the deformation zone, of the high accumulation of twins and of possible impurities permit to avoid differences in electrochemical potential between bulk material and defects in near-surface regions in order to induce a linear degradation. Besides a linear degradation rate, it is also important to sustain a homogeneous degradation. It is supposed that an accumulation of Gd rich particles and remains of accumulated twins can influence a uniform degradation. Additionally, impurities resulting from milling like Fe lead to micro galvanic corrosion and influence the

degradation resistance. Further analysis of surfaces with ToF-SIMS, SEM, Interferometry and EBSD are planned to find more differences in microstructure, morphology and impurities between as-received and singly-etched conditions. To investigate the homogeneity of degraded surfaces, further surface analyses are planned, including the analysis of pit volumes, bearing areas and fast Fourier transformation.

4. CONCLUSIONS

- A specific amount of material removal is necessary to avoid different degradation kinetics between deformed grains, twins and the microstructure of the bulk material.
- The etching procedures reduces the scattering of degradation results compared to as-received samples.
- HAc etching of Mg-5Gd represents a good compromise between practicality and effective results in terms of reduction of the degradation rate.
- Accumulation of Gd rich particles and its effects on degradation behavior need further study.

Acknowledgment

We like to express sincere appreciation and deep gratitude to Helmholtz Virtual Institute (Grant agreement no. VH-VI-523) and the department of Corrosion and Surface Technology, Helmholtz-Zentrum Geesthacht, Germany.

5. REFERENCES

- [1] Ghali, E, "Corrosion and protection of magnesium alloys", *Materials Science Forum*, 350-351, August 2000, 261-272.
- [2] Song, GL, Atrens, A, St John, DH, Wu, X, Naim, J, "The anodic dissolution of magnesium in chloride and sulphate solutions", *Corrosion Science*, 39, No 10-11., October-November 1997, 1981-2004.
- [3] Song, GL, Atrens, A, "Corrosion mechanisms of magnesium alloys", *Adv. Eng. Mater.*, 1, No 1., September 1999, 11-33.
- [4] Hort, N, Huang, Y, Fechner, D, Störmer, M, Blawert, C, "Magnesium alloys as implant materials – Principles of property design for Mg-RE alloys", *Acta Biomaterialia*, 6, No 5., May 2010, 1714-1725.
- [5] Huang, Y, Yang, L, You, S, Gan, W, Kainer, KU, et al., "Unexpected formation of hydrides in heavy rare earth containing magnesium alloys", *Journal of Magnesium and Alloys*, 4, No 3., September 2016, 173-180.
- [6] Feyerabend, F, Fischer, J, Holtz, J, Witte, F, Willumeit, R, et al., "Evaluation of short-term effects of rare earth and other elements used in magnesium alloys on primary cells and cell lines", *Acta Biomaterialia*, 6, No 5., May 2010, 1834-1842.
- [7] Nwaogu, UC, Blawert, C, Schamagl, N, Dietzel, W, Kainer, KU, "Influence of inorganic acid pickling on the corrosion resistance of magnesium alloy AZ31 sheet", *Corrosion Science*, 51, No 11., November 2009, 2544-2556.
- [8] Nwaogu, UC, Blawert, C, Schamagl, N, Dietzel, W, Kainer, KU, "Effects of organic acid pickling on the corrosion resistance of magnesium alloy AZ31 sheet", *Corrosion Science*, 52, No 6., June 2010, 2143-2154.
- [9] Aung, NN, Zhou, W, "Effect of grain size and twins on corrosion behaviour of AZ31B magnesium alloy", *Corrosion Science*, 52, No 2., February 2010, 589-594.
- [10] Nidadavolu, EPS, Feyerabend, F, Ebel, T, Willumeit-Römer, R, Dahms, M, "On the determination of magnesium degradation rates under physiological conditions", *Materials*, 9, No 8., July 2016, 627.
- [11] Villars, P, Cenzual, K, "Pearson's Crystal Data – Crystal Structure Database for Inorganic Compounds", *ASM International*, 2015/16.
- [12] Leach, R, Brown, L, Jiang, X, Blunt, R, Conroy, M, et al., "Guide for the Measurement of Smooth Surface Topography using Coherence Scanning Interferometry" *National physical laboratory*, No 108, 2008.
- [13] Peng, Q, Huang, Y, Meng, J, Li, Y, Kainer, KU, "Strain induced GdH₂ precipitate in Mg-Gd based alloys", *Intermetallics*, 19, No 3., March 2011, 382-389.

6 Discussion

6.1 Origin of influencing factors

6.1.1 Fe surface impurities

It was shown in Figure 5.12 b that Fe is completely removed for Mg-2Gd (G2) and Mg-5Gd (G5), while the Fe amount of Mg-10Gd (G10) is reduced after 15 s in 5 mL (15_5) and 150 s in 5 mL (150_5) etching. This means that all AR alloys contained Fe surface impurities, which are assumed to arise from the use of Fe containing tools at milling the samples into discs.

6.1.2 Gd rich particles

It is interesting to note that in all alloys of this study, Gd rich particles were found. One unanticipated finding was that Gd rich particles were accumulated in the bottom of most of the etching pits (Figure 5.8). Some uncertainty exists with respect to the source of these particles. In accordance with the present results, a previous study [33] has demonstrated a formation of rectangular shaped Gd rich particles in Mg-Gd. Gd is formed to GdH_2 (hydrides) during solidification and by grinding and polishing in watery environments [33]. However, in accordance with some higher oxygen amounts in particles measured by EDS in this work, previous studies [31,87] have demonstrated that Gd oxides are found, which are assumed as Gd_2O_3 or $GdMg_2O_4$, formed during melting and casting [31,87]. The origin and composition of Gd rich particles therefore needs to be interpreted with caution. The oxygen detected in the particles shown in Chapter 5.8 can also originate from oxide residues after degradation. Gd rich particles in this study are suggested to be already present before etching and degradation, due to their existence in the AR microstructure, oriented in lines parallel to the extrusion direction (Figure 5.4, Figure 5.7 b and Figure 5.7 c). Gd rich particles with higher amount of Si were additionally detected. Table 4.1 shows a Si contamination with 70 ppm in the Gd raw material. A binary Gd-Si phase formation is expected due to a stoichiometric composition ratio of around 0.72 – 0.84 measured by EDS (Table 5.3). Possible binary GdSi phases like GdSi or βGd_3Si_5 are shown in the GdSi phase diagram [169], assumed from comparable atomic ratio of Gd and Si (Figure 6.1).

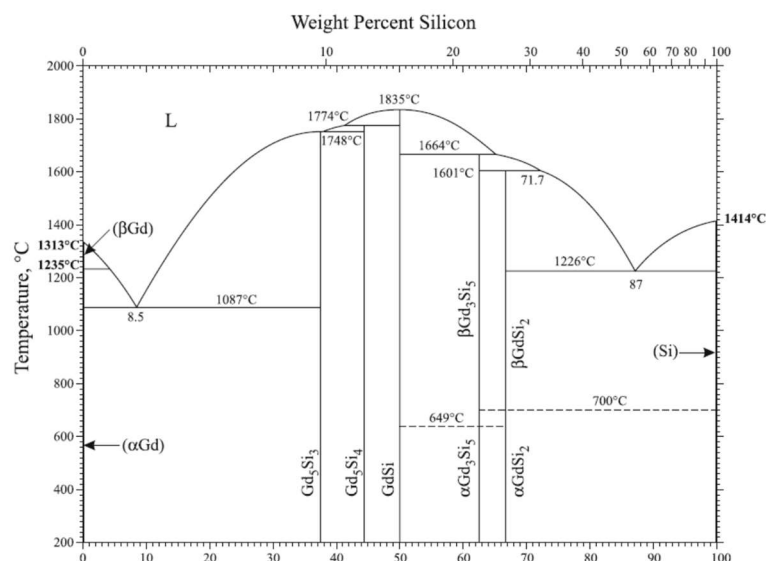


Figure 6.1 Binary GdSi phase diagram. (obtained from [169] with permission from Springer Nature)

These binary phases are temperature stable far beyond 1000 °C. As a result, Gd-Si phases from the Gd raw material remain stable at 710 °C during alloy production or at 525 °C during T4 heat treatment.

Gd rich particles with Fe showed less amount of Si. It has been shown in Table 4.2 that the Fe amount in the bulk increased with increasing Gd content in the as cast condition. A distinct higher amount of bulk Fe was measured by ToF-SIMS for G10 compared to G2 and G5 after removing the direct near-surface region (Figure 5.12 b). This implicates a higher Fe amount with increasing Gd addition. Fe (650 ppm) is shown in Table 4.1 as an impurity of the Gd raw material. Around 430 ppm [at.%] is the maximum solid solubility of Fe in Mg [170], which implies that only small amounts of Fe are dissolved in Mg. Increasing content of alloying elements typically decreases the solubility further. Thus, due to the rather low Fe content in G2 and G5 compared to G10, Fe can almost completely be dissolved in the matrix, while at higher Gd amount solubility exceeding Fe forms precipitates.

All variations of Gd containing particles with and without enrichment of Si are defined as hydrides for further discussion, due to their reported typical rectangular shape [40,171]. The oxide amount, which was detected at rectangular particles (Figure 5.29 and Figure 5.31) are attributed to the oxide residues after degradation and are not considered as Gd oxides. Higher oxide amount inside etching pits at spherical shaped particles (Figure 5.8 d) are assumed to be Gd oxides. Gd particles with Fe enrichments are labelled as GdFe bulk particles. The hydrides and Gd oxides cannot be distinctly identified as initiation point of all etching pits. GdFe bulk particles were not determined in etching pits so far. In some cases, no particle accumulations were found inside the pit bottom (Figure 5.8 e).

6.1.3 Deformation

The depth of the deformed area including deformation zone and twinning zone is correlated with the amount of Gd. With increasing Gd amount, the deformed area in total is decreased, essentially depending on the depth of twinning zone (Figure 5.2). It is reported, that solid solution strengthening is the reason for an increase in strength with higher Gd amount, due to different atomic radii of Gd and Mg [26]. Harmuth et al. [86] and Kim et al. [25] confirmed that the strength of the alloy is associated with the Gd amount [25,86]. There are similarities between the deformed area mentioned in this study and those described by Pu et al. [58,114,115] and Lu. et al. [113]. Comparison of the findings with those of Pu et al. [114] confirms the deformed zone directly in near-surface region of AZ31 as featureless, where the grain size is not identifiable by optical microscope. These findings showed, that deformation is dependent on the machining process and the strength of the alloy. Cottom et al. [172] and Agnew et al. [173] reported a higher activity of non-basal slip modes, with increasing Y addition. In a study of Schlüter et al. [174] a similar solute solution strengthening for Mg-Gd and Mg-Y alloys is suggested [174], due to a comparable atomic radius and shear modulus of Gd and Y, which in turn lead to comparable interaction parameters with Mg [174,175]. For this reason, a higher activity of non-basal slip modes is conceivable with increasing Gd, which would inhibit the twinning mechanism more, in particular for G10.

6.2 Effect of etching on the morphology and microstructure

An initial objective of the project was to identify the effect of precipitates and impurities on surface morphology after etching. Hydrides and oxides are still present after etching (Figure 5.8). According to this, it is provided, that hydrides and oxides are not dissolved in HAc. The accumulation of hydrides and oxides inside the etching pit assume hydrides and oxides acting as cathode to the Mg matrix. With higher material removal, more particles are released. It can therefore be supposed that with higher material removal and more residual

particles, the number of pits would increase [57]. However, a similar material removal of etching in 5 mL and 10 mL contradicts this suggestion, due to a lower etching pit number in 10 mL (Figure 5.11). A higher Gd hydride amount with increasing Gd content in Mg is reported by Peng et al. [40], which would suggest more pits with more Gd. The findings of the current study support the previous research in terms of rectangular shaped hydrides, which can be seen in the microstructure (Figure 5.4 and Figure 5.7 c). However, despite higher hydride amount, the number of etching pits is not increasing with increasing Gd content (Figure 5.11). Etched surfaces are less likely to suffer from pit forming when the etching volume is doubled to 10 mL (Figure 5.10 and Figure 5.11). A 10 mL etching solution has a higher thermal capacity compared to 5 mL. Frankel [176] reported that pit forming is temperature dependent. It may be assumed, that pit forming is then more activated in 5 mL etching solution.

All etching procedures lead to a removal of surface-near material. Depending on the depths of deformation zone and twinning zone as well as on etching time the microstructure is varying for each condition. The current study found that by etching 15 s instead of 150 s the morphology of the surface does not change (Figure 5.9), while longer etching time leads to pit formation (Figure 5.10 and Figure 5.11). It is interesting to note that in all alloys of this study the deformation zone is still existent after 15 s in 5 mL (15_5) etching. For all alloys, using different etching volumes for 150 s etching leads to pit forming in both cases, but with a difference in pit number, while deformation zone is removed completely. Etching for 150 s in 5 mL (150_5) leads to more etching pits in comparison with 150 s in 10 mL etching (150_10) due to temperature activated pit forming. For the same reason, 150_5 leads to a slightly higher material removal compared to 150_10. Due to still visible twins at the surface edge of G5 in Figure 5.7 b when etched with 150_5, it is suspected, that the material removal calculated by mass loss does not coincide exactly with the removed surface depth. The microstructure after 150_5 etching of G10 in Figure 5.7 c shows no indication of twinning, despite similar deformation depth and material removal. A formation of more etching pits in G5 compared to G10 leads to a higher mass loss. This is proven by an equal amount of removed material volume for G5 ($38 \pm 2.2 \text{ mm}^3$) and G10 ($36 \pm 2.0 \text{ mm}^3$), while G5 showed a distinct higher mass loss than G10. Another reason for single visible twins could be an effect of grinding and polishing. Twins of AR samples shown in Figure 5.3 exhibit a preferential direction, while the twins of G5_150_5 in Figure 5.7 b are distributed in different directions. This leads to the assumption that some visible twins in G5 after 150 s etching in Figure 5.7 b are introduced by preparation. It has been shown that with higher Gd content, the formation of twinning is reduced (Figure 5.2). Thus, Mg-xGd alloys with lower Gd content are more affected by twinning induced by grinding and polishing. Moreover, the edges of the surface sustain more deformation than the centre bulk material after grinding and polishing, which could explain the single twinning observed on the edge of the sample in Figure 5.7 b. Wang et al. [112] assumed galvanic corrosion between twinned and non-twinned regions owing to different crystallographic orientation as initiator. Degradation processes of material in both neutral and acid solution are electrochemical reactions. Therefore, the study of Wang et al. [112] is taken to compare these results with corrosive etching mechanism in this work. The twinning zone in the near of G2 bulk is not continuous as seen in Figure 5.3 a. There are alternating deeper twins and more non-twinned regions. For this reason, galvanic corrosion is expected between these areas. It can thus be suggested, that the development of higher pit number in G2 arose from the galvanic corrosion between twinned and non-twinned regions in addition to hydride initiated etching pits.

This study has demonstrated, that HAc etching removes Fe impurities from milling in near-surface region in Figure 5.12 b. One unanticipated finding in the results was that Fe is removed by etching after 15 s and 150 s in exactly the same way for all alloys. It can thus

be suggested that a removal between 2 – 9 μm (Figure 5.6) is enough to clean the surface. This finding was supported by Nwagou et al. [53], who observed a reduction in degradation rate related to a reduction of Fe and Ni with a removal of around 4 μm . It is somewhat surprising that the Fe amount in G10 does not decrease to zero in contrast to G2 and G5 (Figure 5.12 b). Contrary to expectations, the Fe levels after etching in G10 for both etching times were equal even with a higher AR Fe level in one sample before etching for 150 s (Figure 5.12 b). Therefore, it can be concluded that these differences arose from GdFe bulk particles or dissolved Fe and not from Fe surface contaminations. The depth profile in Figure 5.12 a showed a lower decrease of Fe with increasing erosion depth for G10_b_AR compared to G10_a_AR, due to detected Fe bulk particles. A higher Fe bulk amount was also determined by AAS in G10 than in G2 and G5 (Table 4.2). GdFe bulk particles were only found in G10 by use of the EDX analysis in Figure 5.30 and Figure 5.32. These results indicate that Fe bulk particles are only present in G10.

6.3 Factors influencing the degradation behaviour

6.3.1 Particle induced micro-galvanic degradation

The results of this study indicate that hydrides and GdFe particles in the bulk cause particle induced micro-galvanic degradation (PID). Oxide particles (Figure 5.8 d) were not detected as PID initiator after degradation. Hydrides and GdFe particles in the bulk were found on plateaus of remaining matrix material (Figure 5.27- Figure 5.32). These results reflect those of Cao et al. [34] who detected Y as rare earth rich particles on the top of volcano shaped degradation residues. They explained a formation of Mg(OH) around the particle, which prevents the attack of the surrounding surface. These findings cannot be applied to all particles for Cao et al. [34] and this study. Cao et al. [34] point out that only around 2% of the number of particles causes the surrounding degradation. As seen in Figure 5.31, an accumulation of hydrides does not form a typical plateau. Moreover, the particles are included inside a volcano shaped residue. This formation is in agreement with Kalb et al. [108] findings which showed Fe and Zr rich particles inside volcano shaped residues. In contrast to Cao et al. [34], Kalb et al. [108] argue that volcano shaped residues are formed as Mg(OH) directly around the particles. It may be the case therefore that an accumulation of several hydrides has a similar cathodic effect on degradation as pure Fe particles. The reason for this is not clear but it may be connected to an electrochemical potential difference of the particle – matrix system. Fe is known to have a high potential difference to Mg [91]. It is somewhat surprising that G2 showed strong particle induced micro-galvanic degradation for AR and 15_5 condition in contrast to G10 with no or less indication to plateau forming (Figure 5.23, Figure 5.25 and Figure 5.26). Peng et al. [40] demonstrated higher accumulation of Gd hydrides at grain boundaries and an influence of deformation and dislocation on the formation of reported hydrides. A similar finding was also reported by Viček et al. [33], who reported accumulations of hydrides in deformed areas. It is therefore likely that such connections exist between hydrides and deformation, considering that G2 has the highest grade of deformation, visible on higher twinning zone (Figure 5.2). Pu et al. [114] showed by AFM that the grain size in deformed area decreased from μm to nm range. These findings are not detectable in this study with optical microscope or SEM. Overall, these studies might be a possible explanation for the high amount of particle induced micro-galvanic degradation in G2_AR and G2_15_5, suggesting that a link may exist between deformation and Gd induced micro-galvanic degradation. Further observations of the topographies etched for 150 s, may support the hypothesis that a removal of deformation zone lead to less particle induced micro-galvanic degradation.

6.3.2 Effect on homogeneity

Despite an expected higher particle induced micro-galvanic degradation (PID), G2 shows a more homogenous material dissolution due to lower standard deviation of mean valley void volume (V_{vv_dev}) within the first 14 days compared to G5 and G10 (Figure 5.23). An implication of this is the possibility that the high amount of PID leads to a more homogenous distribution of particle induced micro-galvanic degradation compared to deep single pit forming. In reviewing the literature, no data was found on the association between micro-galvanic degradation and homogeneity. According to the valley void volume (V_{vv}) results with including topography in Figure 5.28 - Figure 5.32, it is inferred that particle induced micro-galvanic degradation causes non-homogeneity of the sample surface in the case of G10 when etched for 150 s. The most interesting finding was that V_{vv_dev} of G10_AR is the lowest compared to other alloys up to day 14, followed by a strong increase in V_{vv_dev} afterwards (Figure 5.15). Figure 6.2 displays the correlation between removed surface and V_{vv_dev} of G10.

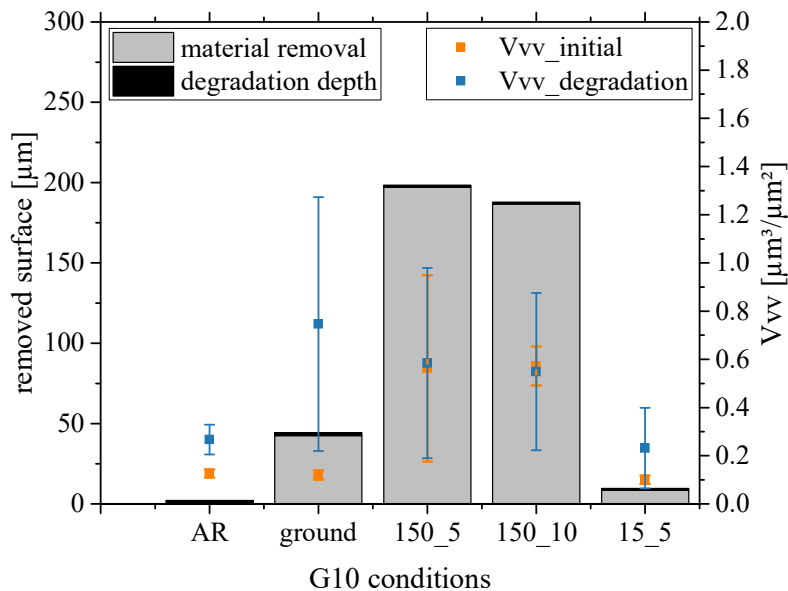


Figure 6.2 Plotted material removal from surface treatments with the addition of the removed mean degradation depth after 3 days in comparison with mean V_{vv} and V_{vv_dev} before and after 3 days degradation of G10.

The blue dots represent the mean value $V_{vv_initial}$ before degradation, while the yellow dots show the mean value of $V_{vv_degradation}$ of the same sample after three days degradation as a representative example. The V_{vv_dev} is higher for all surface treated samples after degradation compared to AR. As expected, the V_{vv_dev} is lowest for ground samples before degradation, due to the effect of flattening. After three days of degradation, a strong increase in V_{vv_dev} is calculated for ground samples. This indicates a non-uniform corrosive attack in contrast to AR and etched samples, despite less material removal compared to 150 s etching. A higher V_{vv_dev} after 150_5 occurred due to the formation of etching pits. Only V_{vv_dev} of 150_5 etching did not increase after degradation in contrast to the other surface conditions. The condition 150_10 showed a lower V_{vv_dev} before degradation due to less pits, which increased after degradation. A slightly attack occurred also for samples etched with 15_5.

Some of the issues emerging from this finding relate specifically to material removal and particles. The AR condition may have a passivation layer on the surface. After etching 15_5, the passivation layer and the first μm of the deformation zone are removed, which does not affect the homogeneity strongly. With higher material removal particle induced micro-

galvanic degradation occurred. It is assumed that with higher material removal, more hydrides and GdFe bulk particles are freed, which leads to single distributed particle induced micro-galvanic degradation and rises non-homogeneity. A scheme of microstructure and particle/impurity distribution is drawn in Figure 6.3. The oxides were neglected, because no oxides were found as particle induced micro-galvanic degradation initiator after degradation. Hydrides are suggested to be predominant in near-surface microstructure. A possible reason of higher V_{vv_dev} after degradation for the ground sample is that by grinding more hydrides are formed. Some studies [32,33,40] report the formation of hydrides, when the surface is deformed in aqueous solution. With an increase in hydrides, more initiations points for corrosive attack are formed, which worsen the degradation homogeneity.

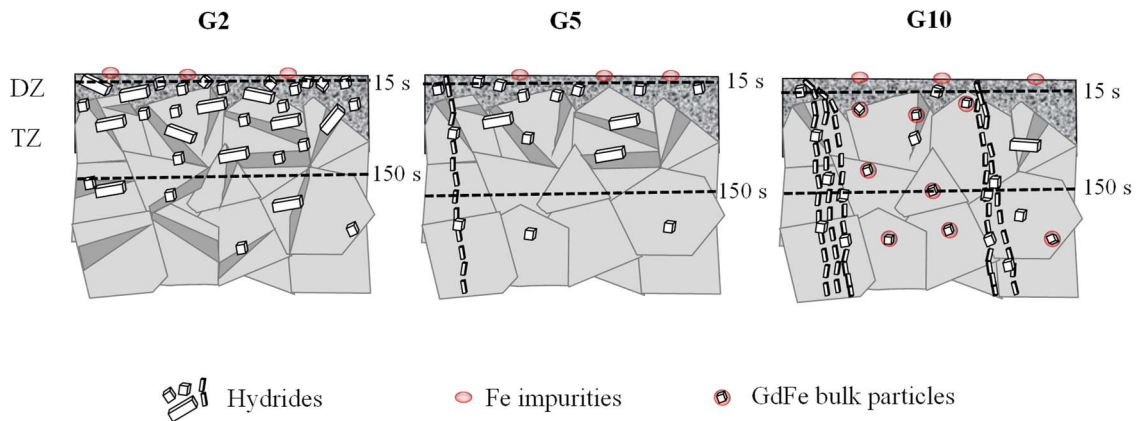


Figure 6.3 Drawing of the assumptions of particle distribution after the evaluation of the results in near-surface microstructure of all alloys.

6.3.3 Effect on degradation rate and reproducibility

This study found that Mg-2Gd (G2) had the highest R^2 of 0.95 or higher for all surface conditions, except of AR. This is explainable by the outlier on day 21 of AR, while other mean degradation depths are located in the near of the trend line. This explains the higher difference (-0.14) between the R^2 of 1-30 days (Δ_{30}) subtracted with R^2 of 1-14 days (Δ_{14}) (Table 6.1).

Table 6.1 Overview of difference in R^2 for all alloys between the degradation rate 1-14 days and 1-30 days.

Alloy	Condition	AR_Δd	Ground_Δd	150_5_Δd
G2		-0.14	-0.01	0
G5		0.09	0.07	-0.01
G10		-0.07	0.08	-0.11

The difference in R^2 is nearly zero, when compared with grinded and 150_5 etched conditions (Table 6.1). A value of $R^2 = 0.98$ for G2_AR is calculated, by removing the outlier from the evaluated data. In this case, the difference in R^2 amounts to 0.03, which showed that a high R^2 is determined for every degradation time and surface condition of G2 in comparison to Mg-5Gd (G5) and Mg-10Gd (G10). This result may be explained by keeping specific microstructure zones after degradation.

Figure 6.4 shows an overview of removed material by surface treatment and degradation of the G2 material after 14 days degradation with corresponding mean value of valley void

volume (mean V_{vv}) and standard deviation of mean V_{vv} (V_{vv_dev}). A high R^2 is achieved for all conditions after 14 days degradation.

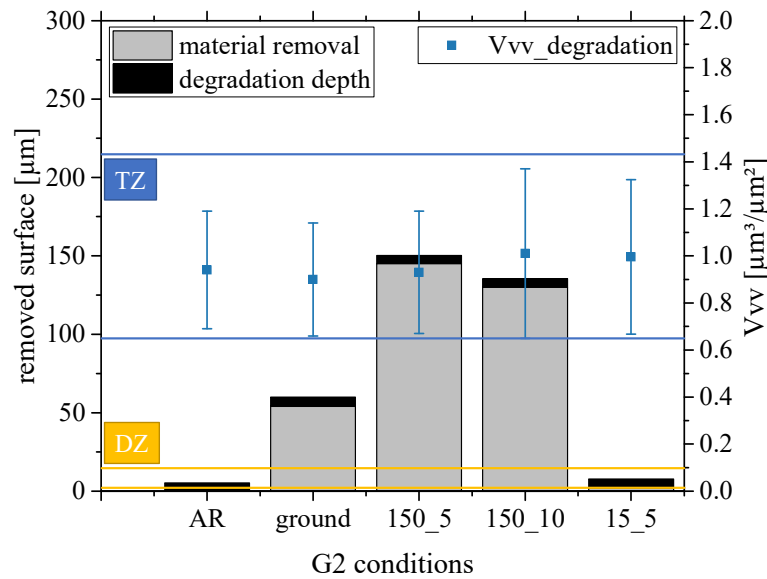


Figure 6.4 Plotted material removal from surface treatments with the addition of the removed mean degradation depth after 14 days in comparison with mean V_{vv} and V_{vv_dev} after 14 days degradation of G2.

After 14 days degradation the deformation zone is assumed to be still present in AR and 15_5 samples. Aung and Zhou [109] showed a faster material dissolution for twinned regions, with intergranular corrosion. Pu et al. [114] determine a microstructure in nm range inside the deformation layer in contrast to μm sized bulk microstructure. It can be suggested that each zone and bulk material has a different degradation kinetic, due to different microstructural features inside. When suggesting different degradation kinetics for different microstructural zones, each condition had the same near-surface microstructure from first to last day of degradation test for G2. It can thus be suggested that a high R^2 is enabled by the congruence of the near-surface microstructure during degradation. All conditions of G2 have a comparable mean V_{vv} and V_{vv_dev} , which demonstrate a similar homogeneity for all conditions. In Figure 5.23 a and Figure 5.25 a similar particle induced micro-galvanic degradation behaviour was determined because of degrading within deformation zone. The morphology of 150_5 in Figure 5.24 a was not impaired by particle induced micro-galvanic degradation as strong as the other both conditions, but smaller pits were distributed homogenously, which can be explained less hydrides in twinning zone compared to deformation zone as suggested in Figure 6.3. Even if each microstructure zone has their own pit forming and distribution, in the case that the sample for each timestep have the same near-surface microstructure for all degradation days, a constant degradation over time is feasible, which may be a reason for high R^2 for all conditions.

G5_AR has more deviations in Figure 5.13 a in comparison with G2, with a lower difference in R^2 between both time ranges. The lower difference arose from existing deviations within $\Delta 14$ and within $\Delta 30$ for G5, while G2 showed a R^2 of 0.95 within 14 days and a lower R^2 of 0.81 within $\Delta 30$. Even if both alloys showed a similar R^2 , G2 showed a more reproducible progress. G10 has the lowest R^2 with stronger deviations of measurement points after 14 days degradation than before. The deformation zone is assumed to be still present after 30 days degradation for all AR alloys when comparing the mean degradation depths in Figure 5.13 a with deformation zone values in Figure 5.2. This shows clearly, that a consistent near-surface microstructure alone does not guarantee highest R^2 . Instead, more

influence factors have to be considered. The mean V_{vv} and V_{vv_dev} increased starting with day 14, due to strong particle induced micro-galvanic degradation, initiated by GdFe particles and hydrides from the bulk. There is no correlation between outliers in Figure 5.13 and Figure 5.15. However, it is shown that the G10 samples of longer degradation days suffer from non-homogeneity and less alignment to the linear approximation.

There is nearly no difference of R^2 for 150_5 etched G2 and G5, when comparing 14 days to 30 days degradation. This implies a sufficient prediction of degradation rate and reliability of the degradation process after 14 days. For this reason, it is possible to reduce the time of degradation testing and save material when the required reliability is given. All etching conditions on G10 lead to an increase in R^2 compared to AR and ground samples, even if 15_5 did not show the highest R^2 as observed in G2 and G5 (Table 5.1). G10 showed in comparison to G2 and G5 a higher difference between $\Delta 14$ and $\Delta 30$. This discrepancy is attributed to a higher R^2 inside the range $\Delta 14$ and lower R^2 after 14 days. An increase in mean V_{vv} and V_{vv_dev} is shown in Figure 5.19 beginning with day 14, which originates from the enlargement of particle induced micro-galvanic degradations to deep and broad holes.

Mean V_{vv} and V_{vv_dev} of G2_150_5 and G5_150_5 after 14 days degradation are more comparable with volume parameters before 14 days degradation. Here, smaller pits with more homogenous distribution are observed and especially particle induced micro-galvanic degradation formation was not as distinct as reported for AR samples after 14 days. Etching pits were still visible (Figure 5.24) on the samples after 14 degradation in particular for 150_5 etched G5. The etching pits are identifiable by a typical roundish shape. As an example, etched and degraded samples after 7 days degradation of G5 are shown in Figure 6.5. It is clearly visible, that etching pits remain mainly after degradation. This could be an explanation in particular for the constancy of mean V_{vv} . Mean V_{vv} is increasing slightly with time with more degradation and remaining etching pits. It is assumed, that the surface around the etching pits is degraded firstly in most cases. This effect fades, when the material around the etching pit is removed.

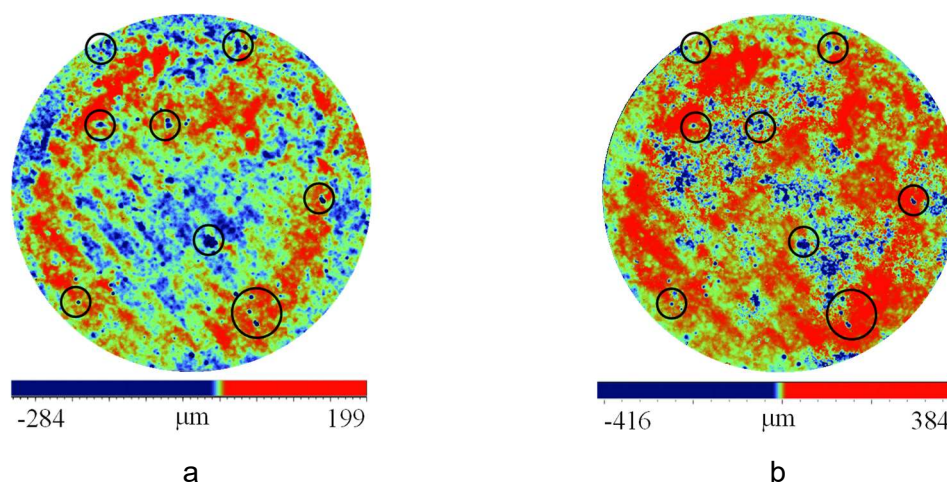


Figure 6.5 WLI topographies of G5 with corresponding peak-valley difference: a) etched (150_5), b) same sample etched 150_5 and 7 days degraded.

Comparing 150 s in 5 mL (150_5) with 150 s in 10 mL (150_10) etching showed that mean pit number per area and standard deviation of 150_5 are higher (Figure 5.11) for all alloys. This indicates that the pit number varied strongly for 150_5 and the etching process itself is related to uncontrolled pit formation compared to 150_10. Contrary to expectations, the non-reproducibility of etching pits for each sample surface did not affect the R^2 . Instead, the uneven etching by 150_10, where more material is removed in the centre of sample for some

samples, might be a possible explanation for a lower R^2 . By etching for 150_10 and a visible higher dissolution in the centre of the sample (Figure 6.6), deformation zone or twinning zone could remain on the outer part of the sample.

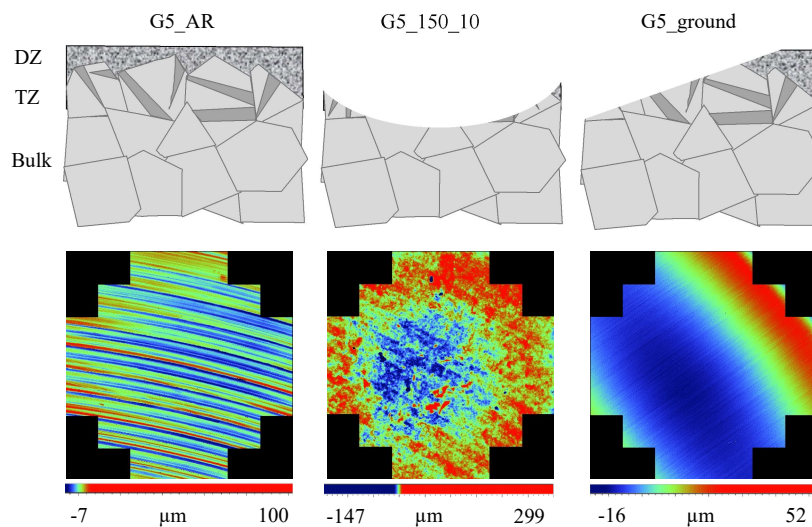


Figure 6.6 Drawing of supposed microstructure changes after etching 150_10 and grinding in correlation to measured WLI topographies of G5.

The reason for the higher removal in the centre is not clear. A possible reason may be a slower motion of the sample inside the etching solution, when etched with 10 mL solution due to less reactivity. Thus, a faster motion inside 5 mL could arise a more homogenous dissolution. This effect was not visible on all samples, but samples with higher Gd amount were stronger affected. Due to a lower degradation rate of G10 (Table 5.2), less reactivity is assumed in comparison with G2 and G5. A lower motion of the sample inside the etching solution, dependent on the reactivity of the material, is assumed higher material removal in the centre. R^2 of G10_150_10 is suggested to shift closer to 1 than G5_150_10, because of a higher number of equivalent samples for the degradation testing of G10_150_10 with similar near-surface microstructure (more material removal in the centre of the samples). This observation supports the hypothesis that a well-defined initial surface condition is important to achieve highest R^2 .

Ground G5 and G10 showed equal R^2 and also comparable differences in R^2 between both time ranges. In contrast to G2, where the twinning zone is assumed to exist for all ground samples, the standard deviation of material removal by grinding overlapped with the twinning zone standard deviation of G5 and G10. The near-surface microstructure is supposed to vary strongly for each sample. Grinding by hand affects the accuracy of material removal in a non-reproducible manner, which is especially visible on e.g. the standard deviation of removed material of ground G5 (Figure 5.6). The non-reproducible ground surface may be a reason for lower R^2 , due to a strong variation in microstructure from sample to sample. Another source of uncertainty is the tilt of several ground samples. Grinding by hand leads to a surface tilt, where parts of deformation zone and twinning zone could still exist for one side of the sample (Figure 6.6). This would lead to different degradation kinetics on the sample surface. It may be the case therefore that these variations could be a reason for a non-uniform material removal. Despite a lower reproducibility of ground G5 compared to G10, the V_{vv_dev} of G5 is significantly lower than of G10. These results indicate that R^2 is barely sufficient to describe the overall degradation behaviour.

It is obvious that the removal of Fe impurities is not the only influencing factor. On the other hand, as shown in some studies, a Fe amount over a tolerance limit will initiate severe

degradation [15,62]. The etching 15_5 proved that removing Fe lead to an increase in R^2 for all alloys, due to a retained near-surface microstructure and morphology equal to AR.

It is suggested that the degradation rate of etched samples is more reliable due to higher R^2 . The degradation rate of G2 and G5 is higher after etching in comparison to G10. This result corroborates the findings of a previous work of Hort et al. [31], where an addition of 10 wt.% Gd led to lowest degradation rate, when tested as cast Mg-xGd (x=2, 5, 10, 15). The results of this study did not show any significant difference in degradation rate, which is varying between 0.21 – 0.29 $\mu\text{m}/\text{d}$ for all alloys in AR and ground condition (Table 5.2).

. These relationships may partly be explained by higher spreading of measurement points or AR and ground conditions. The linear fits are overlapping for all alloys, which in turn lead to similar slope and degradation rate. The reasons for scattering of mean degradation depths with lower R^2 are already explained before.

6.4 Summary of influencing factors

This study sets out the aim at assessing the importance of etching in relation to the degradation behaviour. It was found that an etching process can influence the microstructure and the morphology of the surface in a controllable and useful manner if the mechanisms behind are well understood. An overview of results is shown in Figure 6.7.

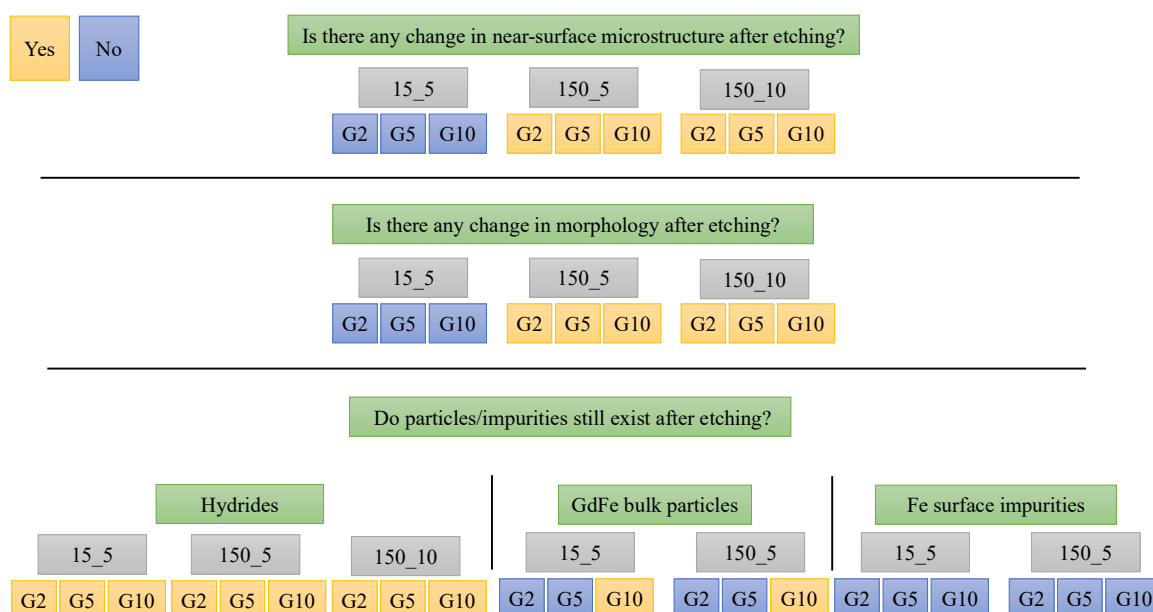


Figure 6.7 Overview of all alloys and etching conditions and their influence on microstructure and morphology.

In the current study, comparing different etching times and volumes showed that etching by 15 s in 5 mL (15_5) solution does not change the near-surface microstructure. The deformation zone is still existing for all alloys after a material removal between 2 – 9 μm , depending on the Gd amount. With longer etching time, a similar material removal is achieved for etching in 150 s in 5 mL (150_5) and in 150 s in 10 mL (150_10) for all alloys. After 15_5 etching no pit forming and removal of cutting marks were determined, which proved no change in morphology. Etching for 150 s leads to pit formation for both volumes, while the pit forming inside 5 mL is more distinct. To avoid non-uniform pit distribution after etching a temperature increase should be suppressed by low etching times, low ratio of sample volume to etching volume or set-ups with temperature control. This is an issue for future research.

Hydrides are not dissolved in HAc. For this reason, hydrides are still located on the surface for each etching condition. The Fe surface contaminations are decreased on the direct surface for all alloys, due to a solubility of Fe in HAc. However, the amount of Fe in Mg-10 Gd (G10) is higher compared to Mg-2Gd (G2) and Mg-5Gd (G5) for all etching methods. This indicates Fe impurities inside the bulk material of G10, which is a problem of alloying and raw material contamination and not of surface contamination. GdFe bulk particles revealed no influence on R^2 .

The results of this study show that with all etching conditions a linear degradation rate is achievable. A slightly higher linearity after etching with 15_5 leads to the assumptions that the microstructure and morphology change has a minor influence on the linearity of degradation rate.

Severe particle induced micro-galvanic degradation was observed at day 14 in the case of G2 and G5 for AR and 15_5. The formed pits were spread more uniform over the complete sample, independent of the etching condition. Deeper and more non-uniform distributed pits in G10 led to worst homogeneity within the investigated alloys, especially for higher material removal. This study confirms that non-homogeneity is associated with the hydrides and GdFe bulk impurities. It has been not possible to correlate quantitatively an increasing number of hydrides with increasing Gd amount. However more hydride lines were apparent in the micrographs of cross-sections.

These findings have important implications for developing etching procedures for several REE alloys, including REE hydrides or enrichments. This experiment did not detect any evidence for a correlation of linear degradation rate and homogeneity in particular for G10. This result suggests that it is not enough to calculate only degradation values to predict an entire degradation behaviour for Mg implants. Also homogeneity assessment has to be done.

7 Conclusion

From the results of this work seven main conclusions can be drawn:

- HAc etching is an effective method to clean the surface from Fe impurities

It is sufficient to remove the first 2 – 9 μm top surface in order to achieve this objective to clean the surface from Fe contaminations of the machining with Fe containing tools like used in a milling process.

- A short etching time maintains the original near-surface microstructure and morphology

The morphology after etching Mg-xGd alloys is dependent on the amount of Gd related to different microstructural features and particles/impurities. A short etching time is for example useful for complex implant geometries like screws and stents in order to maintain narrow geometrical tolerances. This is achievable by etching for 15 s only, when using 5 mL solution of 250 g/L in the same set up.

- Higher R^2 is attained by all etching conditions

The parameter R^2 , being characteristic for a linear progression of the degradation process, is increased for all etching conditions compared to the as-received milled surface. The etching experiments performed confirmed the possibility of a constant degradation rate over time, which ensured a transferable and reproducible degradation behaviour.

- Homogeneity of degradation can be meaningfully evaluated by valley void volume

One aim of this work was to develop a time-efficient method capable of processing a large quantity of samples in order to reduce the total workload necessary. Prior to the gained results, it was difficult to make predictions about the uniformity of material dissolution over the entire surface. In this work a method was evaluated using the valley void volume “Vvv”,

determined by white light interferometry (WLI). Mean value (mean V_{vv}) and standard deviation (V_{vv_dev}) of 37 square positions on the surface were calculated to ascertain the distribution of surface damage taken.

- Particle induced micro-galvanic degradation is initiated by hydrides and GdFe bulk particles and influence the homogeneity

Particle induced micro-galvanic degradation for as-received and etched (15 s in 5 mL) condition decreased with increasing Gd amount within 14 days of degradation. Mg-2Gd showed a more homogenous material dissolution visible by lower V_{vv_dev} compared to Mg-5Gd and Mg-10Gd, due to a more homogenous particle induced micro-galvanic degradation distribution overall the surface. By etching with 150 s in 5 mL and 150 s in 10 mL, particle induced micro-galvanic degradation is reduced for Mg-2Gd and Mg-5Gd because of removing deformed surface with expected higher amount of hydrides. Mg-10Gd showed the opposite degradation behaviour. The removal of material by etching worsens the homogeneity with increasing V_{vv_dev} by releasing instead more deteriorative accumulations of hydrides and GdFe bulk particles. For this case no homogenous degradation of Mg-10Gd was possible by etching.

- Determination of both homogeneity and R^2 is important for implant predictions

The mean V_{vv} and V_{vv_dev} results do not support recommendations to determine degradation rate only for predictions of Mg alloy implants live time. Even if the degradation rate appears constant, which assumes a uniform weight loss over time, the degradation itself can be non-homogenous, as especially shown for Mg-10Gd. The relevance of determination of homogeneity in addition to the degradation rate is clearly supported by the current findings.

- Prediction of degradation characteristics is possible for HAc cleaning of hydride containing REE alloys

The present research enables better prediction of the impact of particles, impurities and microstructure on the morphology after etching and non-homogeneity after degradation. The findings achieved from this study facilitate HAc etching as cleaning method for several REE alloys. The results will be of particular interest to REE alloys with determined REE rich hydride particles.

References

1. Agarwal, S.; Curtin, J.; Duffy, B.; Jaiswal, S. Biodegradable magnesium alloys for orthopaedic applications: A review on corrosion, biocompatibility and surface modifications. *Materials Science and Engineering: C* **2016**, *68*, 948–963.
2. Zhao, D.; Witte, F.; Lu, F.; Wang, J.; Li, J.; Qin, L. Current status on clinical applications of magnesium-based orthopaedic implants: A review from clinical translational perspective. *Biomaterials* **2017**, *112*, 287–302.
3. Sankar, M.; Vishnu, J.; Gupta, M.; Manivasagam, G. Magnesium-based alloys and nanocomposites for biomedical application. In *Applications of Nanocomposite Materials in Orthopedics*; Elsevier, 2019; pp. 83–109 ISBN 978-0-12-813740-6.
4. Chen, Y.; Dou, J.; Yu, H.; Chen, C. Degradable magnesium-based alloys for biomedical applications: The role of critical alloying elements. *Journal of Biomaterials Applications* **2019**.
5. Kraus, T.; Fischerauer, S.; Treichler, S.; Martinelli, E.; Eichler, J.; Myrissa, A.; Zötsch, S.; Uggowitzner, P.J.; Löffler, J.F.; Weinberg, A.M. The influence of biodegradable magnesium implants on the growth plate. *Acta Biomaterialia* **2018**, *66*, 109–117.
6. Zhang, C.; Lin, J.; Liu, H. Magnesium-based Biodegradable Materials for Biomedical Applications. *MRS Advances* **2018**, *3*, 2359–2364.
7. Zeng, R.; Dietzel, W.; Witte, F.; Hort, N.; Blawert, C. Progress and Challenge for Magnesium Alloys as Biomaterials. *Advanced Engineering Materials* **2008**, *10*, B3–B14.
8. Gu, X.; Zheng, Y.; Cheng, Y.; Zhong, S.; Xi, T. In vitro corrosion and biocompatibility of binary magnesium alloys. *Biomaterials* **2009**, *30*, 484–498.
9. Heublein, B.; Rohde, R.; Kaese, V.; Niemeyer, M.; Hartung, W.; Haverich, A. Biocorrosion of magnesium alloys: a new principle in cardiovascular implant technology? *Heart* **2003**, *89*, 651.
10. Witte, F.; Ulrich, H.; Rudert, M.; Willbold, E. Biodegradable magnesium scaffolds: Part 1: Appropriate inflammatory response. *Journal of Biomedical Materials Research Part A* **2007**, *81A*, 748–756.
11. Witte, F.; Hort, N.; Vogt, C.; Cohen, S.; Kainer, K.U.; Willumeit, R.; Feyerabend, F. Degradable biomaterials based on magnesium corrosion. *Current Opinion in Solid State and Materials Science* **2008**, *12*, 63–72.
12. Vormann, J. Magnesium: nutrition and metabolism. *Molecular Aspects of Medicine* **2003**, *24*, 27–37.
13. Seal, C.K.; Vince, K.; Hodgson, M.A. Biodegradable surgical implants based on magnesium alloys – A review of current research. *IOP Conference Series: Materials Science and Engineering* **2009**, *4*, 012011.
14. Gawlik, M.; Wiese, B.; Desharnais, V.; Ebel, T.; Willumeit-Römer, R. The Effect of Surface Treatments on the Degradation of Biomedical Mg Alloys – A Review Paper. *Materials* **2018**, *11*, 2561.
15. Song, G.L.; Atrens, A. Corrosion Mechanisms of Magnesium Alloys. *Advanced Engineering Materials* **1999**, *1*, 11–33.
16. Weber, C.R.; Knörnschild, G.; Dick, L.F.P. The negative-difference effect during the localized corrosion of magnesium and of the AZ91HP alloy. *Journal of the Brazilian Chemical Society* **2003**, *14*, 584–593.
17. Thomas, S.; Medhekar, N.V.; Frankel, G.S.; Birbilis, N. Corrosion mechanism and hydrogen evolution on Mg. *Current Opinion in Solid State and Materials Science* **2015**, *19*, 85–94.
18. Noviana, D.; Paramitha, D.; Ulum, M.F.; Hermawan, H. The effect of hydrogen gas evolution of magnesium implant on the postimplantation mortality of rats. *Journal of Orthopaedic Translation* **2016**, *5*, 9–15.
19. Kraus, T.; Fischerauer, S.F.; Hänzli, A.C.; Uggowitzner, P.J.; Löffler, J.F.; Weinberg, A.M. Magnesium alloys for temporary implants in osteosynthesis: In vivo studies of their degradation and interaction with bone. *Acta Biomaterialia* **2012**, *8*, 1230–1238.

20. Yang, L.; Feyerabend, F.; Kainer, K.U.; Willumeit, R.; Hort, N. Corrosion Behavior of As-Cast Binary Mg-Dy Alloys. *Materials Science Forum* **2011**, *690*, 417–421.
21. Yang, L.; Huang, Y.; Peng, Q.; Feyerabend, F.; Kainer, K.U.; Willumeit, R.; Hort, N. Mechanical and corrosion properties of binary Mg–Dy alloys for medical applications. *Materials Science and Engineering: B* **2011**, *176*, 1827–1834.
22. Yang, L.; Huang, Y.; Feyerabend, F.; Willumeit, R.; Kainer, K.U.; Hort, N. Influence of ageing treatment on microstructure, mechanical and bio-corrosion properties of Mg–Dy alloys. *Journal of the Mechanical Behavior of Biomedical Materials* **2012**, *13*, 36–44.
23. Yang, L.; Hort, N.; Laipple, D.; Höche, D.; Huang, Y.; Kainer, K.U.; Willumeit, R.; Feyerabend, F. Element distribution in the corrosion layer and cytotoxicity of alloy Mg–10Dy during in vitro biodegradation. *Acta Biomaterialia* **2013**, *9*, 8475–8487.
24. Yang, L.; Huang, Y.; Feyerabend, F.; Willumeit, R.; Mendis, C.; Kainer, K.U.; Hort, N. Microstructure, mechanical and corrosion properties of Mg–Dy–Gd–Zr alloys for medical applications. *Acta Biomaterialia* **2013**, *9*, 8499–8508.
25. Kim, S.-H.; Jung, J.-G.; You, B.S.; Park, S.H. Microstructure and texture variation with Gd addition in extruded magnesium. *Journal of Alloys and Compounds* **2017**, *695*, 344–350.
26. Gao, L.; Chen, R.S.; Han, E.H. Effects of rare-earth elements Gd and Y on the solid solution strengthening of Mg alloys. *Journal of Alloys and Compounds* **2009**, *481*, 379–384.
27. Stanford, N.; Barnett, M.R. The origin of “rare earth” texture development in extruded Mg-based alloys and its effect on tensile ductility. *Materials Science and Engineering: A* **2008**, *496*, 399–408.
28. Jung, I.-H.; Sanjari, M.; Kim, J.; Yue, S. Role of RE in the deformation and recrystallization of Mg alloy and a new alloy design concept for Mg–RE alloys. *Scripta Materialia* **2015**, *102*, 1–6.
29. Al-Samman, T.; Li, X. Sheet texture modification in magnesium-based alloys by selective rare earth alloying. *Materials Science and Engineering: A* **2011**, *528*, 3809–3822.
30. Xu, Y.; Gensch, F.; Ren, Z.; Kainer, K.U.; Hort, N. Effects of Gd solutes on hardness and yield strength of Mg alloys. *Progress in Natural Science: Materials International* **2018**, *28*, 724–730.
31. Hort, N.; Huang, Y.; Fechner, D.; Störmer, M.; Blawert, C.; Witte, F.; Vogt, C.; Drücker, H.; Willumeit, R.; Kainer, K.U. Magnesium alloys as implant materials – Principles of property design for Mg–RE alloys. *Acta Biomaterialia* **2010**, *6*, 1714–1725.
32. Huang, Y.; Yang, L.; You, S.; Gan, W.; Kainer, K.U.; Hort, N. Unexpected formation of hydrides in heavy rare earth containing magnesium alloys. *Journal of Magnesium and Alloys* **2016**, *4*, 173–180.
33. Vlček, M.; Čížek, J.; Lukáč, F.; Hruška, P.; Smola, B.; Stulíková, I.; Kudrnová, H.; Minárik, P.; Kmječ, T.; Vlasák, T. Hydrogen absorption in Mg-Gd alloy. *International Journal of Hydrogen Energy* **2017**, *42*, 22598–22604.
34. Cao, F.; Zheng, D.; Song, G.-L.; Shi, Z.; Atrens, A. The Corrosion Behavior of Mg5Y in Nominally Distilled Water. *Advanced Engineering Materials* **2018**, *20*, 1700986.
35. Liu, M.; Schmutz, P.; Uggowitzer, P.J.; Song, G.; Atrens, A. The influence of yttrium (Y) on the corrosion of Mg–Y binary alloys. *Corrosion Science* **2010**, *52*, 3687–3701.
36. Zhu, S.M.; Nie, J.F.; Gibson, M.A.; Easton, M.A. On the unexpected formation of rare earth hydrides in magnesium–rare earth casting alloys. *Scripta Materialia* **2014**, *77*, 21–24.
37. Xie, D.H.; Li, P.; Zeng, C.X.; Sun, J.W.; Qu, X.H. Effect of substitution of Nd for Mg on the hydrogen storage properties of Mg₂Ni alloy. *Journal of Alloys and Compounds* **2009**, *478*, 96–102.
38. Kamegawa, A.; Goto, Y.; Kakuta, H.; Takamura, H.; Okada, M. High-pressure synthesis of novel hydrides in Mg–RE–H systems (RE=Y, La, Ce, Pr, Sm, Gd, Tb, Dy). *Journal of Alloys and Compounds* **2006**, *408–412*, 284–287.

39. Gan, W.; Huang, Y.; Yang, L.; Kainer, K.U.; Jiang, M.; Brokmeier, H.-G.; Hort, N. Identification of unexpected hydrides in Mg–20 wt% Dy alloy by high-brilliance synchrotron radiation. *Journal of Applied Crystallography* **2012**, *45*, 17–21.
40. Peng, Q.; Huang, Y.; Meng, J.; Li, Y.; Kainer, K.U. Strain induced GdH₂ precipitate in Mg–Gd based alloys. *Intermetallics* **2011**, *19*, 382–389.
41. Cui, L.-Y.; Zeng, R.-C.; Guan, S.-K.; Qi, W.-C.; Zhang, F.; Li, S.-Q.; Han, E.-H. Degradation mechanism of micro-arc oxidation coatings on biodegradable Mg–Ca alloys: The influence of porosity. *Journal of Alloys and Compounds* **2017**, *695*, 2464–2476.
42. Prakash, C.; Singh, S.; Pabla, B.S.; Uddin, M.S. Synthesis, characterization, corrosion and bioactivity investigation of nano-HA coating deposited on biodegradable Mg–Zn–Mn alloy. *Surface and Coatings Technology* **2018**, *346*, 9–18.
43. Rezk, A.I.; Mousa, H.M.; Lee, J.; Park, C.H.; Kim, C.S. Composite PCL/HA/simvastatin electrospun nanofiber coating on biodegradable Mg alloy for orthopedic implant application. *Journal of Coatings Technology and Research* **2019**, *16*, 477–489.
44. Castro, Y.; Durán, A. Control of degradation rate of Mg alloys using silica sol–gel coatings for biodegradable implant materials. *Journal of Sol-Gel Science and Technology* **2018**, *90*, 198–208.
45. Shahri, Z.; Allahkaram, S.R.; Soltani, R.; Jafari, H. Study on corrosion behavior of nano-structured coatings developed on biodegradable as cast Mg–Zn–Ca alloy by plasma electrolyte oxidation. *Surface and Coatings Technology* **2018**, *347*, 225–234.
46. Wang, C.; Yi, Z.; Sheng, Y.; Tian, L.; Qin, L.; Ngai, T.; Lin, W. Development of a novel biodegradable and anti-bacterial polyurethane coating for biomedical magnesium rods. *Materials Science and Engineering: C* **2019**, *99*, 344–356.
47. Yang, G.; Chen, T.; Feng, B.; Weng, J.; Duan, K.; Wang, J.; Lu, X. Improved corrosion resistance and biocompatibility of biodegradable magnesium alloy by coating graphite carbon nitride (g-C₃N₄). *Journal of Alloys and Compounds* **2019**, *770*, 823–830.
48. Jin, W.; Wang, G.; Qasim, A.M.; Mo, S.; Ruan, Q.; Zhou, H.; Li, W.; Chu, P.K. Corrosion protection and enhanced biocompatibility of biomedical Mg–Y–RE alloy coated with tin dioxide. *Surface and Coatings Technology* **2019**, *357*, 78–82.
49. Makkar, P.; Kang, H.J.; Padalhin, A.R.; Park, I.; Moon, B.-G.; Lee, B.T. Development and properties of duplex MgF₂/PCL coatings on biodegradable magnesium alloy for biomedical applications. *PLOS ONE* **2018**, *13*, e0193927.
50. Yu, W.; Sun, R.; Guo, Z.; Wang, Z.; He, Y.; Lu, G.; Chen, P.; Chen, K. Novel fluoridated hydroxyapatite/MAO composite coating on AZ31B magnesium alloy for biomedical application. *Applied Surface Science* **2019**, *464*, 708–715.
51. Gray-Munro, J.E.; Seguin, C.; Strong, M. Influence of surface modification on the *in vitro* corrosion rate of magnesium alloy AZ31. *Journal of Biomedical Materials Research Part A* **2009**, *91A*, 221–230.
52. Song, G.-L.; Xu, Z. The surface, microstructure and corrosion of magnesium alloy AZ31 sheet. *Electrochimica Acta* **2010**, *55*, 4148–4161.
53. Nwaogu, U.C.; Blawert, C.; Scharnagl, N.; Dietzel, W.; Kainer, K.U. Effects of organic acid pickling on the corrosion resistance of magnesium alloy AZ31 sheet. *Corrosion Science* **2010**, *52*, 2143–2154.
54. Nwaogu, U.C.; Blawert, C.; Scharnagl, N.; Dietzel, W.; Kainer, K.U. Influence of inorganic acid pickling on the corrosion resistance of magnesium alloy AZ31 sheet. *Corrosion Science* **2009**, *51*, 2544–2556.
55. Supplit, R.; Koch, T.; Schubert, U. Evaluation of the anti-corrosive effect of acid pickling and sol–gel coating on magnesium AZ31 alloy. *Corrosion Science* **2007**, *49*, 3015–3023.
56. Gawlik, M.M.; Steiner, M.; Wiese, B.; González, J.; Feyerabend, F.; Dahms, M.; Ebel, T.; Willumeit-Römer, R. The Effects of HAc Etching on the Degradation Behavior of Mg–5Gd. *Journal of Medical Materials and Technologies* **2017**, *1*, 22–25.
57. Gawlik, M.M.; Wiese, B.; Welle, A.; González, J.; Desharnais, V.; Harmuth, J.; Ebel, T.; Willumeit-Römer, R. Acetic Acid Etching of Mg–xGd Alloys. *Metals* **2019**, *9*, 117.

58. Pu, Z.; Dillon, O.W.; Jawahir, I.S.; Puleo, D.A. Microstructural Changes of AZ31 Magnesium Alloys Induced by Cryogenic Machining and Its Influence on Corrosion Resistance in Simulated Body Fluid for Biomedical Applications. In Proceedings of the ASME 2010 International Manufacturing Science and Engineering Conference, Volume 1; ASME: Erie, Pennsylvania, USA, 2010; pp. 271–277.
59. Pu, Z.; Song, G.-L.; Yang, S.; Dillon, O.W.; Puleo, D.A.; Jawahir, I.S. Cryogenic Burnishing of AZ31B Mg Alloy for Enhanced Corrosion Resistance. In *Magnesium Technology 2011*; Sillekens, W.H., Agnew, S.R., Neelameggham, N.R., Mathaudhu, S.N., Eds.; Springer International Publishing: Cham, 2011; pp. 513–518 ISBN 978-3-319-48568-3.
60. Pu, Z.; Song, G.-L.; Yang, S.; Outeiro, J.C.; Dillon, O.W.; Puleo, D.A.; Jawahir, I.S. Grain refined and basal textured surface produced by burnishing for improved corrosion performance of AZ31B Mg alloy. *Corrosion Science* **2012**, *57*, 192–201.
61. Matsubara, H.; Ichige, Y.; Fujita, K.; Nishiyama, H.; Hodouchi, K. Effect of impurity Fe on corrosion behavior of AM50 and AM60 magnesium alloys. *Corrosion Science* **2013**, *66*, 203–210.
62. Yang, L.; Liu, G.; Ma, L.; Zhang, E.; Zhou, X.; Thompson, G. Effect of iron content on the corrosion of pure magnesium: Critical factor for iron tolerance limit. *Corrosion Science* **2018**, *139*, 421–429.
63. Höche, D.; Blawert, C.; Lamaka, S.V.; Scharnagl, N.; Mendis, C.; Zheludkevich, M.L. The effect of iron re-deposition on the corrosion of impurity-containing magnesium. *Physical Chemistry Chemical Physics* **2016**, *18*, 1279–1291.
64. Eddy Jai Poinern, G.; Brundavanam, S.; Fawcett, D. Biomedical Magnesium Alloys: A Review of Material Properties, Surface Modifications and Potential as a Biodegradable Orthopaedic Implant. *American Journal of Biomedical Engineering* **2013**, *2*, 218–240.
65. Staiger, M.P.; Pietak, A.M.; Huadmai, J.; Dias, G. Magnesium and its alloys as orthopedic biomaterials: A review. *Biomaterials* **2006**, *27*, 1728–1734.
66. Moravej, M.; Mantovani, D. Biodegradable Metals for Cardiovascular Stent Application: Interests and New Opportunities. *International Journal of Molecular Sciences* **2011**, *12*, 4250–4270.
67. Aljihmani, L.; Alic, L.; Boudjemline, Y.; Hijazi, Z.M.; Mansoor, B.; Serpedin, E.; Qaraqe, K. Magnesium-Based Bioresorbable Stent Materials: Review of Reviews. *Journal of Bio- and Tribo-Corrosion* **2019**, *5*, 26.
68. Galli, S.; Stocchero, M.; Andersson, M.; Karlsson, J.; He, W.; Lilin, T.; Wennerberg, A.; Jimbo, R. The effect of magnesium on early osseointegration in osteoporotic bone: a histological and gene expression investigation. *Osteoporosis International* **2017**, *28*, 2195–2205.
69. Castellani, C.; Lindtner, R.A.; Hausbrandt, P.; Tschegg, E.; Stanzl-Tschegg, S.E.; Zanoni, G.; Beck, S.; Weinberg, A.-M. Bone–implant interface strength and osseointegration: Biodegradable magnesium alloy versus standard titanium control. *Acta Biomaterialia* **2011**, *7*, 432–440.
70. Liu, C.; Ren, Z.; Xu, Y.; Pang, S.; Zhao, X.; Zhao, Y. Biodegradable Magnesium Alloys Developed as Bone Repair Materials: A Review. *Scanning* **2018**, *2018*, 1–15.
71. Lee, J.-W.; Han, H.-S.; Han, K.-J.; Park, J.; Jeon, H.; Ok, M.-R.; Seok, H.-K.; Ahn, J.-P.; Lee, K.E.; Lee, D.-H.; et al. Long-term clinical study and multiscale analysis of in vivo biodegradation mechanism of Mg alloy. *Proceedings of the National Academy of Sciences* **2016**, *113*, 716–721.
72. Grünewald, T.A.; Ogier, A.; Akbarzadeh, J.; Meischel, M.; Peterlik, H.; Stanzl-Tschegg, S.; Löffler, J.F.; Weinberg, A.M.; Lichtenegger, H.C. Reaction of bone nanostructure to a biodegrading Magnesium WZ21 implant – A scanning small-angle X-ray scattering time study. *Acta Biomaterialia* **2016**, *31*, 448–457.
73. Robinson, D.A.; Griffith, R.W.; Shechtman, D.; Evans, R.B.; Conzemius, M.G. In vitro antibacterial properties of magnesium metal against *Escherichia coli*, *Pseudomonas aeruginosa* and *Staphylococcus aureus*. *Acta Biomaterialia* **2010**, *6*, 1869–1877.
74. Li, Y.; Liu, G.; Zhai, Z.; Liu, L.; Li, H.; Yang, K.; Tan, L.; Wan, P.; Liu, X.; Ouyang, Z.; et al. Antibacterial Properties of Magnesium *In Vitro* and in an *In Vivo* Model of Implant-

- Associated Methicillin-Resistant Staphylococcus aureus Infection. *Antimicrobial Agents and Chemotherapy* **2014**, *58*, 7586–7591.
75. Liu, Z.; Schade, R.; Luthringer, B.; Hort, N.; Rothe, H.; Müller, S.; Liefelth, K.; Willumeit-Römer, R.; Feyerabend, F. Influence of the Microstructure and Silver Content on Degradation, Cytocompatibility, and Antibacterial Properties of Magnesium-Silver Alloys In Vitro. *Oxidative Medicine and Cellular Longevity* **2017**, *2017*, 1–14.
76. Friedrich, H.E.; Mordike, B.L. *Magnesium technology: metallurgy, design data, applications*; Springer: Berlin ; New York, 2006; ISBN 978-3-540-20599-9.
77. Mises, R.V. Mechanik der plastischen Formänderung von Kristallen. *ZAMM - Zeitschrift für Angewandte Mathematik und Mechanik* **1928**, *8*, 161–185.
78. Rösler, J.; Harders, H.; Bäker, M. *Mechanisches Verhalten der Werkstoffe: mit 31 Tabellen und 34 Aufgaben und Lösungen*; Lehrbuch Maschinenbau; 2., durchges. und erw. Aufl.; Teubner: Wiesbaden, 2006; ISBN 978-3-8351-0008-4.
79. Haasen, P. *Physikalische Metallkunde*; Springer Berlin Heidelberg: Berlin, Heidelberg, 1984; ISBN 978-3-662-12703-2.
80. Robert E. Reed-Hill; William D. Robertson Deformation of magnesium single crystals by nonbasal slip. *JOM* **1957**, *9*, 496–502.
81. Robert E. Reed-Hill; William D. Robertson Pyramidal slip in magnesium. *Trans. Met. Soc. AIME* **1958**, 256.
82. Rokhlin, L.L. *Magnesium alloys containing rare earth metals: structure and properties*; Advances in metallic alloys; Taylor & Francis: London ; New York, 2003; ISBN 978-0-415-28414-1.
83. Hamdy Makhlof, A.S.; M. Hussien, H. Deposition, Characterization and Electrochemical Properties of Permanganate-Based Coating Treatments Over ZE41 Mg-Zn-Rare Earth Alloy. *Int. J. Electrochem. Sci.* **2013**, *8*, 11386–11402.
84. Hamdy, A.S.; Doench, I.; Möhwald, H. Vanadia-based coatings of self-repairing functionality for advanced magnesium Elektron ZE41 Mg-Zn-rare earth alloy. *Surface and Coatings Technology* **2012**, *206*, 3686–3692.
85. Hamdy, A.S.; Butt, Darryl.P. Corrosion mitigation of rare-earth metals containing magnesium EV31A-T6 alloy via chrome-free conversion coating treatment. *Electrochimica Acta* **2013**, *108*, 852–859.
86. Harmuth, J.; Wiese, B.; Bohlen, J.; Ebel, T.; Willumeit-Römer, R. Tailoring of Material Properties of Mg-Gd Alloys for Biomedical Applications. In *Magnesium 2018: Proceedings of the 11th International Conference on Magnesium Alloys and Their Applications*; BRUNEL UNIVERSITY: S.I., 2018 ISBN 978-1-908549-37-2.
87. Kubásek, J.; Vojtěch, D. Structural and corrosion characterization of biodegradable Mg-RE (RE=Gd, Y, Nd) alloys. *Transactions of Nonferrous Metals Society of China* **2013**, *23*, 1215–1225.
88. Wang Xuemin; Wu Weidong; Tang Yongjian; Zeng Xiaoqin; Yao Shoushan Early high temperature oxidation behaviors of Mg-10Gd-3Y alloys. *Journal of Alloys and Compounds* **2009**, *474*, 499–504.
89. Brar, H.S.; Berglund, I.S.; Allen, J.B.; Manuel, M.V. The role of surface oxidation on the degradation behavior of biodegradable Mg-RE (Gd, Y, Sc) alloys for resorbable implants. *Materials Science and Engineering: C* **2014**, *40*, 407–417.
90. Gu, X.-N.; Zheng, Y.-F. A review on magnesium alloys as biodegradable materials. *Frontiers of Materials Science in China* **2010**, *4*, 111–115.
91. Ghali, E.; Dietzel, W.; Kainer, K.-U. General and localized corrosion of magnesium alloys: A critical review. *Journal of Materials Engineering and Performance* **2004**, *13*, 7–23.
92. Ghali, E. Corrosion and Protection of Magnesium Alloys. *Materials Science Forum* **2000**, *350–351*, 261–272.
93. Yun, Y.; Dong, Z.; Lee, N.; Liu, Y.; Xue, D.; Guo, X.; Kuhlmann, J.; Doepke, A.; Halsall, H.B.; Heineman, W.; et al. Revolutionizing biodegradable metals. *Materials Today* **2009**, *12*, 22–32.

94. Zeng, R.; Zhang, J.; Huang, W.; Dietzel, W.; Kainer, K.U.; Blawert, C.; Ke, W. Review of studies on corrosion of magnesium alloys. *Transactions of Nonferrous Metals Society of China* **2006**, *16*, s763–s771.
95. Zheng, Y.F.; Gu, X.N.; Witte, F. Biodegradable metals. *Materials Science and Engineering: R: Reports* **2014**, *77*, 1–34.
96. Witte, F.; Kaese, V.; Haferkamp, H.; Switzer, E.; Meyer-Lindenberg, A.; Wirth, C.J.; Windhagen, H. In vivo corrosion of four magnesium alloys and the associated bone response. *Biomaterials* **2005**, *26*, 3557–3563.
97. Xu, L.; Yu, G.; Zhang, E.; Pan, F.; Yang, K. In vivo corrosion behavior of Mg-Mn-Zn alloy for bone implant application. *Journal of Biomedical Materials Research Part A* **2007**, *83A*, 703–711.
98. Willumeit, R.; Fischer, J.; Feyerabend, F.; Hort, N.; Bismayer, U.; Heidrich, S.; Mihailova, B. Chemical surface alteration of biodegradable magnesium exposed to corrosion media. *Acta Biomaterialia* **2011**, *7*, 2704–2715.
99. Fischer, J.; Prosenč, M.H.; Wolff, M.; Hort, N.; Willumeit, R.; Feyerabend, F. Interference of magnesium corrosion with tetrazolium-based cytotoxicity assays☆. *Acta Biomaterialia* **2010**, *6*, 1813–1823.
100. Merkel, M.; Thomas, K.-H. *Taschenbuch der Werkstoffe*; 7., verbesserte Auflage.; Fachbuchverlag Leipzig im Carl Hanser Verlag: München, 2008; ISBN 978-3-446-41194-4.
101. Birbilis, N.; Easton, M.A.; Sudholz, A.D.; Zhu, S.M.; Gibson, M.A. On the corrosion of binary magnesium-rare earth alloys. *Corrosion Science* **2009**, *51*, 683–689.
102. Jiang, Q.; Lv, X.; Lu, D.; Zhang, J.; Hou, B. The corrosion behavior and mechanical property of the Mg–7Y–xNd ternary alloys. *Journal of Magnesium and Alloys* **2018**, *6*, 346–355.
103. Reddy Tiyyagura, H.; Petovar, B.; Finšgar, M.; Willumeit-Römer, R.; Luthringer, B.J.C.; Mohan, M.K.; Kokol, V. Degradation behaviour of Mg-4Ag and Mg-5Gd alloys under in-vitro conditions and different time-frames. *Journal of Alloys and Compounds* **2019**, *774*, 980–987.
104. Zidane, N.; Albrimi, Y.A.; Addi, A.A.; Akbour, R.A.; Douch, J.; Nahle, A.; Hamdani, M. Effect of Gadolinium Content on the Corrosion Behavior of Magnesium Alloys in 1 wt.% NaCl Solution: *Portugaliae Electrochimica Acta* **2015**, *33*, 289–304.
105. Taheri, M.; Phillips, R.C.; Kish, J.R.; Botton, G.A. Analysis of the surface film formed on Mg by exposure to water using a FIB cross-section and STEM–EDS. *Corrosion Science* **2012**, *59*, 222–228.
106. Curioni, M.; Scenini, F.; Monetta, T.; Bellucci, F. Correlation between electrochemical impedance measurements and corrosion rate of magnesium investigated by real-time hydrogen measurement and optical imaging. *Electrochimica Acta* **2015**, *166*, 372–384.
107. Gennero de Chialvo, M.R.; Chialvo, A.C. The Tafel–Heyrovsky route in the kinetic mechanism of the hydrogen evolution reaction. *Electrochemistry Communications* **1999**, *1*, 379–382.
108. Kalb, H.; Rzany, A.; Hensel, B. Impact of microgalvanic corrosion on the degradation morphology of WE43 and pure magnesium under exposure to simulated body fluid. *Corrosion Science* **2012**, *57*, 122–130.
109. Aung, N.N.; Zhou, W. Effect of grain size and twins on corrosion behaviour of AZ31B magnesium alloy. *Corrosion Science* **2010**, *52*, 589–594.
110. Hamu, G.B.; Eliezer, D.; Wagner, L. The relation between severe plastic deformation microstructure and corrosion behavior of AZ31 magnesium alloy. *Journal of Alloys and Compounds* **2009**, *468*, 222–229.
111. Zou, G.; Peng, Q.; Wang, Y.; Liu, B. The effect of extension twinning on the electrochemical corrosion properties of Mg–Y alloys. *Journal of Alloys and Compounds* **2015**, *618*, 44–48.
112. Wang, B.J.; Xu, D.K.; Dong, J.H.; Ke, W. Effect of the crystallographic orientation and twinning on the corrosion resistance of an as-extruded Mg–3Al–1Zn (wt.%) bar. *Scripta Materialia* **2014**, *88*, 5–8.

113. Lu, L.; Hu, S.; Liu, L.; Yin, Z. High speed cutting of AZ31 magnesium alloy. *Journal of Magnesium and Alloys* **2016**, *4*, 128–134.
114. Pu, Z.; Outeiro, J.C.; Batista, A.C.; Dillon, O.W.; Puleo, D.A.; Jawahir, I.S. Enhanced surface integrity of AZ31B Mg alloy by cryogenic machining towards improved functional performance of machined components. *International Journal of Machine Tools and Manufacture* **2012**, *56*, 17–27.
115. Pu, Z.; Umbrello, D.; Dillon, O.W.; Lu, T.; Puleo, D.A.; Jawahir, I.S. Finite element modeling of microstructural changes in dry and cryogenic machining of AZ31B magnesium alloy. *Journal of Manufacturing Processes* **2014**, *16*, 335–343.
116. Mostaed, E.; Vedani, M.; Hashempour, M.; Bestetti, M. Influence of ECAP process on mechanical and corrosion properties of pure Mg and ZK60 magnesium alloy for biodegradable stent applications. *Biomatter* **2014**, *4*, e28283.
117. Argade, G.R.; Panigrahi, S.K.; Mishra, R.S. Effects of grain size on the corrosion resistance of wrought magnesium alloys containing neodymium. *Corrosion Science* **2012**, *58*, 145–151.
118. Lu, Y.; Bradshaw, A.R.; Chiu, Y.L.; Jones, I.P. Effects of secondary phase and grain size on the corrosion of biodegradable Mg–Zn–Ca alloys. *Materials Science and Engineering: C* **2015**, *48*, 480–486.
119. Ahmadkhaniha, D.; Fedel, M.; Heydarzadeh Sohi, M.; Deflorian, F. Corrosion behavior of severely plastic deformed magnesium based alloys: A review. *Surface Engineering and Applied Electrochemistry* **2017**, *53*, 439–448.
120. Song, Y.; Shan, D.; Chen, R.; Han, E.-H. Corrosion characterization of Mg–8Li alloy in NaCl solution. *Corrosion Science* **2009**, *51*, 1087–1094.
121. Chiu, L.-H.; Chen, C.-C.; Yang, C.-F. Improvement of corrosion properties in an aluminum-sprayed AZ31 magnesium alloy by a post-hot pressing and anodizing treatment. *Surface and Coatings Technology* **2005**, *191*, 181–187.
122. Xin, Y.; Huo, K.; Tao, H.; Tang, G.; Chu, P.K. Influence of aggressive ions on the degradation behavior of biomedical magnesium alloy in physiological environment. *Acta Biomaterialia* **2008**, *4*, 2008–2015.
123. Tian, P.; Liu, X.; Ding, C. In vitro degradation behavior and cytocompatibility of biodegradable AZ31 alloy with PEO/HT composite coating. *Colloids and Surfaces B: Biointerfaces* **2015**, *128*, 44–54.
124. Gaur, S.; Singh Raman, R.K.; Khanna, A.S. In vitro investigation of biodegradable polymeric coating for corrosion resistance of Mg-6Zn-Ca alloy in simulated body fluid. *Materials Science and Engineering: C* **2014**, *42*, 91–101.
125. Zhang, E. Phosphate treatment of magnesium alloy implants for biomedical applications. In *Surface Modification of Magnesium and its Alloys for Biomedical Applications*; Elsevier, 2015; pp. 23–57 ISBN 978-1-78242-078-1.
126. Qiu, X.; Wan, P.; Tan, L.; Fan, X.; Yang, K. Preliminary research on a novel bioactive silicon doped calcium phosphate coating on AZ31 magnesium alloy via electrodeposition. *Materials Science and Engineering: C* **2014**, *36*, 65–76.
127. Razavi, M.; Fathi, M.; Savabi, O.; Hashemi Beni, B.; Vashaei, D.; Tayebi, L. Surface microstructure and in vitro analysis of nanostructured akermanite (Ca₂MgSi₂O₇) coating on biodegradable magnesium alloy for biomedical applications. *Colloids and Surfaces B: Biointerfaces* **2014**, *117*, 432–440.
128. da Conceicao, T.F.; Scharnagl, N.; Blawert, C.; Dietzel, W.; Kainer, K.U. Surface modification of magnesium alloy AZ31 by hydrofluoric acid treatment and its effect on the corrosion behaviour. *Thin Solid Films* **2010**, *518*, 5209–5218.
129. Walter, R.; Kannan, M.B. Influence of surface roughness on the corrosion behaviour of magnesium alloy. *Materials & Design* **2011**, *32*, 2350–2354.
130. Walter, R.; Kannan, M.B.; He, Y.; Sandham, A. Effect of surface roughness on the in vitro degradation behaviour of a biodegradable magnesium-based alloy. *Applied Surface Science* **2013**, *279*, 343–348.
131. Liu, H. The effects of surface and biomolecules on magnesium degradation and mesenchymal stem cell adhesion. *Journal of Biomedical Materials Research Part A* **2011**, *99A*, 249–260.

132. Maier, P.; Peters, R.; Mendis, C.L.; Müller, S.; Hort, N. Influence of Precipitation Hardening in Mg-Y-Nd on Mechanical and Corrosion Properties. *JOM* **2016**, *68*, 1183–1190.
133. Petra, M.; Kelim, H.; Gabor, S.; Carla, V.; Norbert, H. Qualitative and quantitative analysis during corrosion of biodegradable magnesium-silver wires. *Frontiers in Bioengineering and Biotechnology* **2016**, *4*.
134. Maier, P.; Gentsch, L.; Hort, N. Voltammetric Studies of Extruded Pure Magnesium in Different Electrolytes and Its Corrosion Morphology. In *Magnesium Technology 2017*; Solanki, K.N., Orlov, D., Singh, A., Neelameggham, N.R., Eds.; Springer International Publishing: Cham, 2017; pp. 429–437 ISBN 978-3-319-52391-0.
135. Martin, H.J.; Horstemeyer, M.F.; Wang, P.T. Comparison of corrosion pitting under immersion and salt-spray environments on an as-cast AE44 magnesium alloy. *Corrosion Science* **2010**, *52*, 3624–3638.
136. Martin, H.J.; Horstemeyer, M.F.; Wang, P.T. Structure–property quantification of corrosion pitting under immersion and salt-spray environments on an extruded AZ61 magnesium alloy. *Corrosion Science* **2011**, *53*, 1348–1361.
137. Song, W.; Martin, H.J.; Hicks, A.; Seely, D.; Walton, C.A.; Lawrimore II, W.B.; Wang, P.T.; Horstemeyer, M.F. Corrosion behaviour of extruded AM30 magnesium alloy under salt-spray and immersion environments. *Corrosion Science* **2014**, *78*, 353–368.
138. Walton, C.A.; Martin, H.J.; Horstemeyer, M.F.; Wang, P.T. Quantification of corrosion mechanisms under immersion and salt-spray environments on an extruded AZ31 magnesium alloy. *Corrosion Science* **2012**, *56*, 194–208.
139. Chen, Y.; Ju, L.-K. Method for Fast Quantification of Pitting Using 3D Surface Parameters Generated with Infinite Focus Microscope. *CORROSION* **2015**, *71*, 1184–1196.
140. Guan, L.; Zhang, B.; Wang, J.Q.; Han, E.-H.; Ke, W. The reliability of electrochemical noise and current transients characterizing metastable pitting of Al–Mg–Si microelectrodes. *Corrosion Science* **2014**, *80*, 1–6.
141. Espinosa, C.; Veleva, L.P.; Lopez, J.L. Power Spectral Density Analysis of the Corrosion Potential Fluctuation of Stainless Steel 316L in Early Stages of Exposure to Caribbean Sea Water. *ECS Transactions* **2015**, *66*, 3–11.
142. Park, C.J.; Rao, V.S.; Kwon, H.S. Effects of Sigma Phase on the Initiation and Propagation of Pitting Corrosion of Duplex Stainless Steel. *CORROSION* **2005**, *61*, 76–83.
143. Holme, B.; Lunder, O. Characterisation of pitting corrosion by white light interferometry. *Corrosion Science* **2007**, *49*, 391–401.
144. Petzing, J.; Coupland, J.; Leach, R. *The Measurement of Rough Surface Topography using Coherence Scanning Interferometry*; Measurement Good Practice Guide No.116; National Physical Laboratory: Hampton Road, Teddington, Middlesex, TW11 0LW; ISBN ISSN 1368-6550.
145. O Mahony, C.; Hill, M.; Brunet, M.; Duane, R.; Mathewson, A. Characterization of micromechanical structures using white-light interferometry. *Measurement Science and Technology* **2003**, *14*, 1807–1814.
146. de Groot, P. Coherence Scanning Interferometry. In *Optical Measurement of Surface Topography*; Leach, R., Ed.; Springer Berlin Heidelberg: Berlin, Heidelberg, 2011; pp. 187–208 ISBN 978-3-642-12011-4.
147. Raja, J.; Muralikrishnan, B.; Fu, S. Recent advances in separation of roughness, waviness and form. *Precision Engineering* **2002**, *26*, 222–235.
148. Blateyron, F. The Areal Field Parameters. In *Characterisation of Areal Surface Texture*; Leach, R., Ed.; Springer Berlin Heidelberg: Berlin, Heidelberg, 2013; pp. 15–43 ISBN 978-3-642-36457-0.
149. Whitehouse, D.J. *Surfaces and their measurement*; Kogan Page Science paper edition; Kogan Page Science: London, 2004; ISBN 978-1-903996-60-7.
150. Deepak Lawrence, K.; Shanmugamani, R.; Ramamoorthy, B. Evaluation of image based Abbott–Firestone curve parameters using machine vision for the characterization of cylinder liner surface topography. *Measurement* **2014**, *55*, 318–334.

151. Singh, M.; Dong, S.; Koch, D.; Shimamura, K.; Clauss, B.; Heidenreich, B.; Akedo, J. *Advances in high temperature ceramic matrix composites and materials for sustainable development*; Ceramic transactions; Wiley: Hoboken, New Jersey, 2017; ISBN 978-1-119-40728-7.
152. ISO 25178 part 2: 2012 Geometrical product specification (GPS) - Surface texture: areal - Part 2: Terms, definitions and surface texture parameters, International Organization for Standardization.
153. Leach, R. *Fundamental principles of engineering nanometrology*; Micro & nano technologies series; Second edition.; Elsevier, William Andrew: Amsterdam, 2014; ISBN 978-1-4557-7753-2.
154. ISO 25178 part 3: 2012 Geometrical product specification (GPS) - Surface texture: areal - Part 3: Specification operators, International Organization for Standardization.
155. Fearn, S. *An Introduction to Time-of-Flight Secondary Ion Mass Spectrometry (ToF-SIMS) and its Application to Materials Science*; IOP Publishing, 2015; ISBN 978-1-68174-088-1.
156. Wittmaack, K. Oxygen-concentration dependence of secondary ion yield enhancement. *Surface Science* **1981**, *112*, 168–180.
157. Winters, H.F.; Coburn, J.W. Influence of the altered layer on depth profiling measurements. *Applied Physics Letters* **1976**, *28*, 176–179.
158. Yamamura, Y.; Tawara, H. Energy dependence of ion-induced sputtering yields from monatomic solids at normal incidence. *Atomic Data and Nuclear Data Tables* **1996**, *62*, 149–253.
159. Jin, W.; Wu, G.; Li, P.; Chu, P.K. Improved corrosion resistance of Mg-Y-RE alloy coated with niobium nitride. *Thin Solid Films* **2014**, *572*, 85–90.
160. Jamesh, M.; Wu, G.; Zhao, Y.; Chu, P.K. Effects of silicon plasma ion implantation on electrochemical corrosion behavior of biodegradable Mg-Y-RE Alloy. *Corrosion Science* **2013**, *69*, 158–163.
161. Jamesh, M.; Wu, G.; Zhao, Y.; Jin, W.; McKenzie, D.R.; Bilek, M.M.M.; Chu, P.K. Effects of zirconium and nitrogen plasma immersion ion implantation on the electrochemical corrosion behavior of Mg-Y-RE alloy in simulated body fluid and cell culture medium. *Corrosion Science* **2014**, *86*, 239–251.
162. Li, M.; Cheng, Y.; Zheng, Y.F.; Zhang, X.; Xi, T.F.; Wei, S.C. Surface characteristics and corrosion behaviour of WE43 magnesium alloy coated by SiC film. *Applied Surface Science* **2012**, *258*, 3074–3081.
163. Wendler-Kalsch, E.; Gräfen, H. Grundlagen der Korrosion. In *Korrosionsschadenkunde*; Springer Berlin Heidelberg: Berlin, Heidelberg, 1998; pp. 10–46 ISBN 978-3-662-22074-0.
164. Holzner, D.; Holzner, K. *Chemie für Technische Assistenten in der Medizin und in der Biologie*; 2018; ISBN 978-3-527-80949-3.
165. Bjerrum, N.; Ebert, L. *Kurzes Lehrbuch der Anorganischen Chemie*; Springer Berlin Heidelberg, 2013; ISBN 978-3-642-91147-7.
166. Nidadavolu, E.; Feyerabend, F.; Ebel, T.; Willumeit-Römer, R.; Dahms, M. On the Determination of Magnesium Degradation Rates under Physiological Conditions. *Materials* **2016**, *9*, 627.
167. Zhao, M.-C.; Liu, M.; Song, G.-L.; Atrens, A. Influence of pH and chloride ion concentration on the corrosion of Mg alloy ZE41. *Corrosion Science* **2008**, *50*, 3168–3178.
168. Schneider, A.; Hommel, G.; Blettner, M. Linear Regression Analysis. *Deutsches Ärzteblatt Online* **2010**.
169. Okamoto, H. Gd-Si (Gadolinium-Silicon). *Journal of Phase Equilibria and Diffusion* **2009**, *30*, 213–214.
170. Nayeb-Hashemi, A.A.; Clark, J.B.; Swartzendruber, L.J. The Fe-Mg (Iron-Magnesium) system. *Bulletin of Alloy Phase Diagrams* **1985**, *6*, 235–238.
171. Čížek, J.; Hruška, P.; Vlasák, T.; Vlček, M.; Janeček, M.; Minárik, P.; Krajňák, T.; Šlapáková, M.; Dopita, M.; Kužel, R.; et al. Microstructure development of ultra fine

-
- grained Mg-22 wt%Gd alloy prepared by high pressure torsion. *Materials Science and Engineering: A* **2017**, *704*, 181–191.
172. Cottam, R.; Robson, J.; Lorimer, G.; Davis, B. Dynamic recrystallization of Mg and Mg–Y alloys: Crystallographic texture development. *Materials Science and Engineering: A* **2008**, *485*, 375–382.
173. Agnew, S.R.; Yoo, M.H.; Tomé, C.N. Application of texture simulation to understanding mechanical behavior of Mg and solid solution alloys containing Li or Y. *Acta Materialia* **2001**, *49*, 4277–4289.
174. Schlüter, K.; Shi, Z.; Zamponi, C.; Cao, F.; Quandt, E.; Atrens, A. Corrosion performance and mechanical properties of sputter-deposited MgY and MgGd alloys. *Corrosion Science* **2014**, *78*, 43–54.
175. Holleman, A.F.; Wiberg, E.; Wiberg, N. *Lehrbuch der anorganischen Chemie*; 91.-100., verb. u. stark erw. Aufl.; de Gruyter: Berlin, 1985; ISBN 978-3-11-007511-3.
176. Frankel, G.S. Pitting Corrosion of Metals. *Journal of The Electrochemical Society* **1998**, *145*, 2186.

Figures

Figure 2.1 Mg lattice structure. The illustration is drawn and modified after [76].	2
Figure 2.2 A reduction of Fe particles leads to a formation of cathodic active dark area, which increases the hydrogen evolution reaction: a) cross sectional view; b) top view. (obtained from [63], published by the PCCP Owner Societies CC by 3.0)	5
Figure 2.3 Drawing showing the principle of the Michelson interferometer.	9
Figure 2.4 Top view and profile of a surface with a single pit and the corresponding Abbot-Firestone curve.	10
Figure 2.5 Setup of ToF-SIMS analysis in this study.	11
Figure 4.1 Schematic drawing of the extrusion processing, followed by machining.	43
Figure 4.2 Illustration of the HAc etching procedure of the Mg-xGd alloys.	44
Figure 4.3 Topography of the G10 alloy after 30 days of degradation with removed edges.	47
Figure 4.4 Schematic drawing of the original mask separated into 37 smaller squares.	48
Figure 4.5 Topography of a O_2^+ sputter crater to illustrate the calculation of mean crater depth.	48
Figure 4.6 Drawing of fifteen Mg samples inside a 24 well cell culture plate.	49
Figure 5.1 Micrograph of G2_AR cross section with deformation zone and twinning zone.	51
Figure 5.2 Plotted deformation depth with deformation zone and twinning zone for G2, G5 and G10. (modified and obtained from [57] with permission from Metals CC by 4.0)	51
Figure 5.3 Micrographs of AR cross sections: a) G2 with deepest twinning zone, b) G5 with similar deformation zone compared to G2 and less extended twinning zone, c) G10 with deepest deformation zone and shortest twinning zone of all alloys.	51
Figure 5.4 Micrograph of G10_AR microstructure perpendicular to the extrusion direction with accumulations of particles in the extrusion direction.	52
Figure 5.5 Micrographs of G10_AR observed on a section perpendicular to extrusion direction, obtained using the BSE mode: a) Particle lines are bended inside deformation zone and twinning zone, b) Higher Gd amount is determined on bright particles by EDS. (modified and obtained from [57] with permission from Metals CC by 4.0)	52
Figure 5.6 Diagrams of removed material after grinding and etching for 15 s or 150 s in 5 mL or 10 mL HAc solution: a) G2, b) G5, c) G10. (modified and obtained from [57] with permission from Metals CC by 4.0)	53
Figure 5.7 Micrographs of etched (150_5) cross sections: a) G2, b) G5, c) G10. (modified and obtained from [57] with permission from Metals CC by 4.0)	53
Figure 5.8 Etching pits observed by SEM: a) G2 etched for 150_10, b) G5 etched for 150_10, c) G10 etched for 150_10, d) G2 etched 150_5 (modified and obtained from [57] with permission from Metals CC by 4.0), e) G2 etched for 150_5 with no accumulation of particles.	54
Figure 5.9 WLI topographies of G5 with corresponding peak-valley difference and surface roughness Sa: a) AR condition, b) same sample etched 15_5.	55
Figure 5.10 WLI topographies of 150 s etched alloys. The left sample is etched in 5 mL and the right sample is etched in 10 mL: a) G2, b) G5, c) G10. (modified and obtained from [57] with permission from Metals CC by 4.0)	55
Figure 5.11 Mean value and standard deviation of etching pits per mm^2 for G2, G5 and G10 etched for 150_5 and 150_10.	56
Figure 5.12 ToF-SIMS analysis: a) Depth profile of Fe for one position each of two G10_AR samples, b) Graph of mean value and standard deviation of Fe counts for G2, G5, and G10 before and after etching. (modified and obtained from [57] with permission from Metals CC by 4.0)	56

Figure 5.13 Mean degradation depth plotted over time after 30 days degradation for a) as-received G2, G5 and G10, b) etched (150_5) G2, G5 and G10.	77
Figure 5.14 WLI topographies of mean V _v and V _v _dev determined surface: a) G5_AR before degradation, b) identical G5_AR after 3 days degradation.....	78
Figure 5.15 Mean V _v of as-received conditions plotted with V _v _dev over time for G2, G5 and G10.	79
Figure 5.16 WLI topographies of mean V _v and V _v _dev determined surface after 23 days of degradation: a) G5, b) G2, c) cut G5 squares for the regions 2,3 and 9, d) cut G2 squares with severe damage in region 2, nearly no attack in region 3 and a deeper single pit in region 9.	79
Figure 5.17 Mean V _v of the ground conditions plotted with V _v _dev over time for G2, G5 and G10 before (day 0) and after degradation (day 1 – 30).	80
Figure 5.18 WLI topographies of G10 surface after degradation, which was ground before: a) after 3 days, b) after 7 days, c) after 14 days, d) after 28 days.	81
Figure 5.19 Mean V _v of the etched (150_5) conditions plotted with V _v _dev over time for G2, G5 and G10 before (day 0) and after degradation (day 1 – 30).	81
Figure 5.20 WLI topographies: a) G10 – day 0 (150_5), b) G10 – after 3 days degradation.	82
Figure 5.21 Mean V _v and V _v _dev after 150_10 etching and degradation for G2, G5 and G10.	82
Figure 5.22 Mean V _v and V _v _dev after 15_5 etching and degradation for G2, G5 and G10.	83
Figure 5.23 WLI topographies of AR samples after 14 days of degradation: a) G2 with highest amount of degradation pits, b) G5 with lower number and widely distributed degradation pits, c) G10 with bigger and irregular degradation pit forming.....	84
Figure 5.24 WLI topographies of etched (150_5) samples after 14 days degradation: a) G2 with smaller pits distributed over the surface, b) G5 with optical more homogenous distribution than G2, c) G10 with a formation of deeper and more irregular distributed degradation pits.	84
Figure 5.25 WLI topographies of etched (15_5) samples after 14 days degradation: a) G2 with degradation pits spread over the complete surface, b) G5 with with some bigger and clustered degradation pits; c) G10 with bigger elongated holes.	85
Figure 5.26 WLI topographies of pits after 14 days degradation: a) G2 with red higher plateaus, b) G20 with a bigger pit without plateaus.	85
Figure 5.27 Gd rich and rectangular shaped particles on plateau shaped degradation residues inside: a) G2_AR, b) G2_150_10, c) G5_AR.....	86
Figure 5.28 Surface morphology determined by SEM and WLI topography measured by WLI for etched (150_10) G10 after 14 days degradation.....	86
Figure 5.29 Magnified Gd rich rectangular shaped particle (SEM) on a plateau at position 1 (WLI) for the etched (150_10) and degraded (14 days) G10 alloy.	87
Figure 5.30 Determined particles (SEM) on a plateau on position 1 (WLI) for the etched (150_10) and degraded (14 days) G10 alloy.....	87
Figure 5.31 WLI topographies and SEM images of etched (150_10) and 14 days degraded G10 alloy. Accumulation of Gd rich and rectangular particles inside a degradation residue.	88
Figure 5.32 WLI topography and SEM images of etched (150_10) and 14 days degraded G10 alloy with one particle.....	89
Figure 6.1 Binary GdSi phase diagram. (obtained from [169] with permission from Springer Nature)	94

Figure 6.2 Plotted material removal from surface treatments with the addition of the removed mean degradation depth after 3 days in comparison with mean V_{vv} and V_{vv_dev} before and after 3 days degradation of G10. 98

Figure 6.3 Drawing of the assumptions of particle distribution after the evaluation of the results in near-surface microstructure of all alloys. 99

Figure 6.4 Plotted material removal from surface treatments with the addition of the removed mean degradation depth after 14 days in comparison with mean V_{vv} and V_{vv_dev} after 14 days degradation of G2. 100

Figure 6.5 WLI topographies of G5 with corresponding peak-valley difference: a) etched (150_5), b) same sample etched 150_5 and 7 days degraded. 101

Figure 6.6 Drawing of supposed microstructure changes after etching 150_10 and grinding in correlation to measured WLI topographies of G5. 102

Figure 6.7 Overview of all alloys and etching conditions and their influence on microstructure and morphology..... 103

Tables

Table 4.1 Elements analysed next to Gd with >99.9% purity.	43
Table 4.2 Label and chemical composition of all Mg-xGd alloys analysed by X-ray fluorescence spectroscopy and AAS.	44
Table 4.3 Overview of parameters used for primary Bi ⁺ ions on Mg-xGd with ToF-SIMS. .	46
Table 4.4 Overview of parameters used for sputtering with O ₂ ⁺ ions on Mg-xGd with ToF-SIMS.	46
Table 4.5 Overview of degradation time and number of Mg-xGd alloy samples with corresponding surface conditions.	49
Table 5.1 Overview of R ² for all alloys and conditions from day 1 to last degradation day (14 or 30 days).	77
Table 5.2 Overview of degradation rate D for all alloys and conditions from day 1 to last degradation day (14 or 30 days).	78
Table 5.3 Element distribution of Gd rich particles located on plateau shaped degradation residues.	86
Table 6.1 Overview of difference in R ² for all alloys between the degradation rate 1-14 days and 1-30 days.	99

Appendix

1. Definitions

- **Coefficient of determination $R^2 = R^2$** is a measure for the quality of the linear regression fit with respect to the experimental points. Highest accuracy is assigned with $R^2 = 1$, when all calculated values are equal to the observed ones. R^2 represents the fraction of variation [168] in mean degradation depth values, determined in the performed degradation test.
- **Hydrides** = Gd enriched particles with rectangular shape.
- **Gd rich particles** = Particles with higher amount of Gd e.g Gd hydrides with and without Si enrichments and GdFe bulk particles.
- **Vvv** = Valley void volume of voids per unit area, which are calculated by integrating the volume between two heights x_1 and x_2 in the material ratio curve. In ISO 25178-3 the heights are set by standard at $x_1 = 80\%$ material fraction and $x_2 = 100\%$ material fraction for Vvv.
- **Mean Vvv** = The mean valley void volume calculated out of 37 squares with a size of $1 \times 1 \text{ mm}^2$, which are cut out of the sample topography after degradation. The mean Vvv defines the severity of the degradation.
- **Vvv_dev** = The standard deviation of 37 mean valley void volumes for one sample, which are cut out of sample topography after degradation. Vvv_dev defines if the sample is more or less homogenous degraded.
- **Homogeneity**: Low Vvv_dev values, which indicate homogenous distribution of pit formation over the complete sample with similar pit volume and area for each part of the sample surface or no pit formation.
- **PID** = Pit formation around a plateau or volcano shaped degradation residue including a particle inside or in near-centre region.

2. Abbreviations

15_5	Etching with 250 g/L HAc in 5 mL for 15 s
150_5	Etching with 250 g/L HAc in 5 mL for 150 s
150_10	Etching with 250 g/L HAc in 10 mL for 150 s
A	Surface area
AAS	Atomic absorption spectroscopy
AFM	Atomic force microscope
Ag	Silver
Al	Aluminium
AM50	Mg-5Al-0.5>Mn
AM60	Mg-6Al-0.5>Mn
AR	As-received
AZ31	Mg-3Al-1Zn
AZ31B	Mg-3Al-1Zn extruded bar
AZ31B-H24	Mg-3Al-1Zn sheet/plate medium strength
BSE	Backscattered electrons
Ca	Calcium
$\text{CaCl}_2 \cdot 2\text{H}_2\text{O}$	Calcium chloride
CCM	Cell culture medium

Ce	Cerium
CH ₃ COOH	Acetic acid
Cl	Chloride
CO ₂	Carbon dioxide
Cu	Copper
DMEM	Dulbecco's Modified Eagle's Medium
D	Degradation rate
d(t)	Mean degradation depth at time point t
Dy	Dysprosium
DZ	Deformation zone
E	Energy
ECAP	Equal channel angular pressing
EDS	Energy dispersive X-ray spectroscopy
e.g.	exempli gratia
EIS	Electrochemical impedance spectroscopy
FBS	Fetal bovine serum
Fe	Iron
FSP	Friction stir processing
Gd	Gadolinium
G2	Mg-2Gd
G5	Mg-5Gd
G10	Mg-10Gd
GdH ₂	Gadolinium hydride
Gd ₂ O ₃	Gadolinium(III) oxide
H ₂	Hydrogen
H ₂ CO ₃	Carbonic acid
H ₂ O	Water
H ₃ O ⁺	Hydronium
HAc	Acetic acid
HAp	Hydroxyapatite
hcp	Hexagonal closed packed
i _{corr}	Current density
La	Lanthanum
M	Material removal
m	mass
m/z	Mass to charge ratio
Mg	Magnesium
MgCO ₃	Magnesium carbonate
Mg(CH ₃ COO) ₂	Magnesium acetate
MgCl ₂	Magnesium chloride
MgH ₂	Magnesium hydride
MgO	Magnesium oxide
Mg(OH) ₂	Magnesium hydroxide
N	Nitrogen
NaCl	Sodium chloride

NaHCO ₃	Sodium bicarbonate
NaH ₂ PO ₄ ·2H ₂ O	Sodium phosphate monobasic
NaOH	Sodium hydroxide
NbN	Niobium nitride
Nd	Neodymium
Ni	Nickel
O	Oxygen
OES	Optical emission spectrometry
O ₂	Oxygen gas
OH ⁻	Hydroxide ion
OPS	Oxide polishing suspension
PID	Particle induced micro-galvanic degradation
PECVD	Plasma enhanced chemical vapour deposition
Pen Strep	Penicillin and streptomycin
PSD	Power Spectral Density
ρ	Density
R ²	Coefficient of determination
REE	Rare earth element
S	Sulphur
s	Seconds
Sa	Arithmetic mean of the height within a surface area
SBF	Simulated body fluid
SE	Secondary electron
SEM	Scanning electron microscopy
SFE	Stacking fault energy
Si	Silicon
SiC	Silicon carbide
SIMS	Secondary ion mass spectrometry
Sr	Strontium
t	Time
T4	Solution heat treated and naturally aged
Ti	Titanium
ToF-SIMS	Time-of-flight secondary ion mass spectrometry
TZ	Twinning zone
V	Volume
V _{mc}	Core material volume
V _{mp}	Peak material volume
V _v	Void volume
V _{vv}	Valley void volume
WE43	Mg-4Y-3RE
WLI	White light interferometry
wt. %	Weight percentage
XPS	X-ray photoelectron spectroscopy
XRD	X-ray diffraction
Y	Yttrium

ZEK100	Mg-1Zn-0.5>RE-0.5>Zr
Zn	Zinc
Zr	Zirconium

Acknowledgements

I would like to thank Prof. Dr. Willumeit – Römer for giving me the possibility to work at her institute. I appreciate the feedback after several meetings with new suggestions and corrections. I really enjoyed to be a part of her group. The work in my department has given me the opportunity to be able to develop constantly in the topic surface treatments and surface characterisation.

I want to thank Prof. Dr. Rainer Adelung to be the second reviewer of my thesis. I also want to thank for a nice and productive meeting about acid etching methods and morphologies.

I would like to show my warm thank to my supervisors Dr. Thomas Ebel and Dr. Björn Wiese. Both were greatly supportive. Discussion were very helpful and encourage to start one thinking. Without their guidance this dissertation would not have been possible.

I have greatly benefited from the knowledge of Dr. Alexander Welle. I would like to thank for the invitation to the KNMF Meeting in Karlsruhe, the ToF-SIMS measurements and the good explanations of all my questions.

I want to express my gratitude to all members of WBM and WBB. I want to thank for the nice meetings, discussions and ideas. I am particularly grateful for the assistance given by Dr. Bérengère Luthringer - Feyerabend, Dr. Heike Helmholtz, Andreas Dobernowsky, Anke Schuster, Alexandra Amherd Hidalgo and Jorge González. I want to thank Jochen Harmuth for material supply and the evaluation of suitable picric acid solution for micrographs.

I am particularly grateful for the assistance given by Petra Fischer and Gert Wiese, whose help turned my research a success.

My deepest heartfelt appreciation goes to Florian Riedlberger. Thank you for the emotional support.

Lists of publications and conferences

Publications:

1. **Gawlik, M.M.**; Steiner, M.; Wiese, B.; González, J.; Feyerabend, F.; Dahms, M.; Ebel, T.; Willumeit-Römer, R. The Effects of HAc Etching on the Degradation Behaviour of Mg-5Gd. *J. Med. Mater. Tech.* **2017**, *1*, 22–25.
 - **Die Experimente in diesem Paper wurden von Marcjanna Maria Gawlik (M.M.G) unter Absprache zuständiger Betreuer konzipiert und durchgeführt. Ideen und Herangehensweisen wurden eigenständig von M.M.G entwickelt. Degradationsergebnisse wurden entsprechend nach angegebener Referenz ausgewertet. Die Essigsäureätzungen wurden zusammen mit dem Masterstudenten Markus Steiner durchgeführt. Die Erstellung der Diskussion entstand durch eigene Gedankengänge von M.M.G. Das Manuskript wurde von M.M.G eigenständig vorbereitet und geschrieben und nach einer Prüfung der Betreuer und Co-Autoren eingereicht.**
2. **Gawlik, M.M.**; Wiese, B.; Desharnais, V.; Ebel, T.; Willumeit-Römer, R. The Effect of Surface Treatments on the Degradation of Biomedical Mg Alloys - A Review Paper. *Materials* **2018**, *11*, 2561
 - **Ideen und Herangehensweisen des Review Papers wurden eigenständig von M.M.G entwickelt. Die Literaturrecherche in diesem Paper wurde von M.M.G durchgeführt. Tabellen und Bilder wurden von M.M.G erstellt. Die Erstellung der Diskussion entstand durch eigene Gedankengänge von M.M.G. Das Manuskript wurde von M.M.G eigenständig vorbereitet und geschrieben und nach einer Prüfung der Betreuer und Co-Autoren mit Verbesserungsvorschlägen eingereicht.**
3. **Gawlik, M.M.**; Wiese, B.; Welle, A.; González, J.; Desharnais, V.; Harmuth, J.; Ebel, T.; Willumeit-Römer, R. Acetic Acid Etching of Mg-xGd Alloys. *Metals* **2019**, *9*, 117
 - **Teile dieser Veröffentlichung wurden in dieser Doktorarbeit modifiziert und verwendet. Dazu gehören teilweise Material/Methoden (Kapitel 4.1, 4.2, 4.4, 4.5 4.6, 4.7.1 und 4.7.2), Ergebnisse (Kapitel 5.1 und 5.2) und Ideen in der Diskussion (Kapitel 6.1, 6.2 und 6.4). Die Experimente in diesem Paper wurden von Marcjanna Maria Gawlik (M.M.G) unter Absprache zuständiger Betreuer konzipiert und durchgeführt. Ideen und Herangehensweisen wurden eigenständig von M.M.G entwickelt. ToF-SIMS Analysen wurden von Herrn Dr. Welle ausgeführt, die Auswertung der Fe-Analyse wurden danach selbstständig von M.M.G nach dementsprechender Einführung dargestellt. M.M.G wurde von Jochen Harmuth bei der Politur und Erstellung der Pikrinsäurelösung unterstützt, um optimale Mikroschliffe herzustellen. Bei der Essigsäureätzung durfte eine Praktikantin helfen. Die Erstellung der Diskussion entstand durch eigene Gedankengänge von M.M.G. Das Manuskript wurde von M.M.G**

eigenständig vorbereitet und geschrieben und nach einer Prüfung der Betreuer und Co-Autoren eingereicht.

Conference Abstracts:

1. **Gawlik, M.M.**; Steiner, M.; Wiese, B.; González, J.; Feyerabend, F.; Dahms, M.; Ebel, T.; Willumeit-Römer, R. The Effects of HAc Etching on the Degradation Behaviour of Mg-5Gd, 4th Euro BioMAT - European Symposium and Exhibition on Biomaterials and Related Areas, May 2017, Weimar, Germany.
2. **Gawlik, M.M.**; Wiese, B, Steiner, M.; Lamaka, S.; Welle, A.; Dahms, M.; Ebel, T.; Willumeit-Römer, R. The influence of surface treatments on the degradation behaviour of Mg-5Gd, 3rd Intelligent Materials, June 2017, Kiel, Germany